Time-Resolved Single Frequency Infrared Absorption Spectroscopy on Photosystem II

Im Fachbereich Physik
der Freien Universität Berlin
eingereichte

Dissertation

zur Erlangung des Grades eines
Doktors der Naturwissenschaften
vorgelegt von

Philipp Stefan Simon

Berlin 2018

Time-Resolved Single Frequency Infrared Absorption Spectroscopy on Photosystem II

Im Fachbereich Physik
der Freien Universität Berlin
eingereichte

Dissertation

zur Erlangung des Grades eines
Doktors der Naturwissenschaften
vorgelegt von

Philipp Stefan Simon

Berlin 2018

1. Gutachter: Prof. Dr. Holger Dau
2. Gutachterin: Prof. Dr. Karsten Heyne
Tag der Disputation: 25.01.2019

Abstract

In spite of recent advancements in structure elucidation of Photosystem II (PSII), by far not the complete catalytic cycle of photosynthetic water oxidation is sufficiently well understood. Open questions concern the type of O-O bond formation mechanism, the nature of the substrate water molecules, the role of protein-internal H-bond networks and the sites of proton release and exit. Time-resolved infrared (IR) spectroscopy provides information about protonation states, H-bonding networks and bond strengths. On oxygen-evolving PSII, there have been less than five reports of time-resolved IR spectroscopy, but either they presented only a few wavenumbers of pure spectral resolution (16 cm^{-1}) or were not free of distortion by a laser-induced heat artefact.

In this thesis, a new alternative experiment is described that employs a continuous-wave Quantum-Cascade-Laser for single-frequency IR (SFIR) detection of absorption transients induced by a series of nanosecond laser flashes (532 nm). It became possible to detect IR absorption smaller than 10^{-5} OD in the time domain from 40 ns to s at wavenumbers ranging from 1300 to 1650 cm^{-1}. The setup comprises automatic sample exchange, data recording, a temperature control system and an adapted measurement protocols. The latter includes a flash sequence that drives the PSII synchronously through its reaction cycle (the S-state cycle PSII) and allows to correct for the flash-induced heat artefact, reproducibly. Reliable data now can be recorded at ten wavenumbers per day.

(1) First, FTIR steady-state measurements, variable chlorophyll fluorescence and the SFIR experiment were combined to track the electron transfer from the first (Q_A) to the second (Q_B) quinone electron-acceptor of PSII. The decay kinetics of Q_A^- were found to be identical in the SFIR transients at 1478 cm^{-1} and the variable fluorescence yield. This finding and the analysis of the "connectivity" resulting from inter-PSII excitation energy transfer revealed that connectivity-corrected fluorescence traces the Q_A-Q_B electron transfer very well, thereby verifying assumptions and models used thousands of times in physiological studies.

(2) I contributed to an ongoing discussion about the position of the CO stretching vibration of the redox active tyrosine radical $Y_Z^{\bullet ox}$. Using the high spectral resolution, a clear signal assignable to $Y_Z^{\bullet ox}$ could be identified at 1512.5-1515 cm^{-1}. The band formed faster than 40 ns and decayed with the known Mn oxidation kinetics. Its position is the same as in Mn depleted samples, surprisingly suggesting similar H-bond properties.

(3) I could show that the symmetric stretching region of carboxylates senses almost all kinetic components of the previously proposed extended reaction cycle of PSII water oxidation, which is characterized by alternating removal of electrons and protons from the catalytic site of water oxidation. Moreover, three so far unidentified bands showing either a 300 ns or a 30 µs phase are found in the $S_2 \rightarrow S_3$ and $S_3 \rightarrow S_0$ transitions.

(4) With Richard Debus (UC Riverside), we established a protocol to investigate PSII core complexes extracted from *Synechocystis* with time-resolved SFIR. First, it was verified that the kinetics of the reaction cycle of the cyanobacterial PSII are identical to that of spinach PSII. Then I obtained the very first time-resolved IR transients on genetically modified PSII. Introducing an alanine instead of an aspartate at the crucial 61 position of the D1 protein did not slow down the fast proton release phase in $S_2 \rightarrow S_3$ and $S_3 \rightarrow S_0$, but the Mn oxidation – especially in $S_3 \rightarrow S_0$. This excludes a direct involvement of the D61 residue in the early proton release but creates new questions on the mechanism of water oxidation.

In summary, the development of a new (superior) experimental approach for time-resolved tracking of the events in the PSII reaction cycle has facilitated new insights and opens up a variety of new avenues in PSII research.

Contents

List of Abbreviations

BCT	bicarbonate, HCO^-
β-dm	n-Dodecyl-β-D-Maltoside
brc	bacterial reaction center
DCMU	inhibitor, 3-(3,4-dichlorophenyl)-1,1-dimethylurea
$\delta(xy)$	bending vibration including atoms x and y
FeCy	ferricyanide, $[Fe(III)CN_6]^{3-}$, electron acceptor
FTIR	Fourier Transform Infrared (Spectroscopy)
LHC	Light harvesting complexes – the membrane bound antenna proteins in chloroplasts
MES	2-(N-Morpholino)ethanesulfonic acid, buffer
PSIIcc	Photosystem II core complexes, surrounded by detergent
P_{680}	Central chlorophyll made of four chlorophyll molecules
OEC	Oxygen Evolving Complex
$\nu_{AS/S}(xy)$	symmetric or asymmetric stretch vibration between atoms x and y
PPBQ	**p**ara-**p**henyl-**B**enzo**q**uinone, electron acceptor
P_{680}	Four central chlorophyll molecules where charge separation is initiated
PSI / PSII	Photosystem I / II
Q_A	PSII bound plastoquinone
Q_B	loosely bound plastoquinone, exchanged from plastoquinone pool
QCL	Quantum Cascade Laser, *here* cw, 1300-1650 cm^{-1}
SFIR	Single frequency infrared (absorption experiment)
Y_D	redox active tyrosine D2-Y160, slow reactions
Y_Z	redox active tyrosine D1-Y161

1 Introduction

Opposed to human technology, natural evolution has mastered the demanding task of transforming the sun's energy into store-able chemical energy. The huge and complex protein assembly Photosystem II (PSII) developed as the first component in the electron transfer chain of oxygenic photosynthesis. It harbors the catalytic center - a Mn_4Ca-oxo-cluster, where the substrate water is decomposed into molecular oxygen, protons and electrons. During the four-step accumulation of light energy in units of oxidizing equivalents at the cluster, protons are transported over large distances of up to 30 Å involving a sequence of alternating steps of electron and proton removal from the catalytic site.

The leading motivation of the scientific community studying psII is ultimately the development of new catalysts and even bio-inspired solar cells, that will produce clean and sustainable energy for the world. And indeed, it is the very confined environment created by mostly carboxylic amino acids and four waters directly ligating the cluster, that appeals and allows to formulate reaction mechanisms including the site of oxidation of single atoms and the movement of individual protons.

However, hidden beneath this function is a complex machine with variable protein subunits, that reacts on its environment and even contains feedback loops with other metabolic systems. Its transmembrane part functions with more than 30 chlorophyll molecules as a big antenna. Also, the two quinones bind here. One of these, the quinone Q_B, serves as a membrane-based electron and proton shuttle. The huge protein surrounding the Mn cluster shields the very same from its environment and transports the substrate and products. How these aspects merge into one big view, is the target of research, that will not only serve in understanding the catalytic reaction, but the basis of photosynthetic and dependent organisms.

With the following thesis I want to contribute to this research by introducing a new transient absorption infrared setup. Infrared spectroscopy tracks the vibrations of single bonds or molecules, thereby gaining access to the bond strength, which is closely coupled to the environment and molecular interactions like hydrogen bonds. This sensitivity makes IR spectroscopy an invaluable tool to tackle the open questions of photosynthetic water oxidation: the type of O-O bond formation mechanism, the nature of the substrate water molecules, the role of protein-internal H-bond networks, the sites of proton release and the exit pathways of the protons.

This thesis begins with a review of decades of – not reaction-time-resolved – IR studies on PSII, including the various cofactors and an overview of genetically modified PSII, relevant to water oxidation.

Then the new cw Quantum-Cascade-Laser based setup will be introduced in detail, comprising technical details, the automatic sample exchange, data recording and the temperature control system. Peculiarities as the measurement protocol or the excitation laser induced heat-artefact will be discussed.

First results were obtained on measurements, targeting the membrane bound electron shuttles, the plastoquinones. Because the signals of these are strong, they are ideal test targets. The details of the proton coupled electron transfer to the exchangeable quinone Q_B will be

investigated. One focus is also the comparison with a common, but never unambiguously verified technique in PSII research - the variable chlorophyll fluorescence.

The second target is the proton coupled electron transfer from a redox active tyrosine Y_Z to the place of charge separation - the chlorophyll unit P_{680}. The nature of the multiphasic sequence of events taking place, when the Mn cluster and its environment are positively charged, is unknown, but the processes do involve proton movements. To resolve the full picture of water oxidation, these intermediates need to be understood as well.

The third investigation focuses directly on the events of the extended reaction cycle of the Mn cluster. Only recently has the community agreed on the general sequence of alternating electron and proton release events. These will be investigated and compared between spinach and cyanobacterial samples.

Because IR spectroscopy is not site selective and many vibrations couple or alter even on greater distance, it is necessary to implement probes into PSII. The last chapter, therefore, will investigate a genetically altered PSII. To do so, first a new sample preparation protocol needs to be implemented. The D1-D61 residuum is proposed to be crucial for proton transfer events preceding the Mn oxidation. First time resolved IR measurements on mutated PSII will be shown on an alanine at this position.

2 Photosystem II - a very short overview

2.1 Photosystem II: a water plastoquinone oxidoreductase

In Photosynthesis the molecular redox driving forces of NADPH are created by photochemical energy-conversion of both photosystems. Additional photosynthetic energy is provided in quanta of ATP, whose formation is driven by a proton gradient established by the photosystems and the cytochrome-b_6f complex. The main role of photosystem II is the extraction of electrons from water and the reduction of plastoquinone to plastoquinol, which serves as an intermediate electron transporter through the thylakoid membrane:

$$2H_2O + 2Q + 4H^+_{stroma} \xrightarrow{4Photons} 2Q^{(2-)}H_2^{(+)} + O_2 + 4H^+_{Lumen} \tag{2.1}$$

To accumulate sufficient energy to oxidize water four photons are needed. Following the absorption of such a redox equivalent is stored mainly in the form of an increased oxidation state of manganese atoms of the catalytic center: a Mn_4-μ-oxo-Ca cluster. In order to keep the positive charge small an alternating electron and proton release model has been suggested ([Klauss et al., 2015]). The protons released are transferred into the lumen, thus these protons contribute to the driving force of the ATP-synthase. Also at the quinone side of PSII protons are taken up from the stroma and later released at the Cyt-b_6f into the lumen. To understand PSII means to understand the interrelation of the electron and proton transfer events. The electron transfer steps and the involved cofactors have been well studied (see figure 2.1 for a complete overview of the involved steps). Also numerous publications exist on the proton dynamics, but up to date only little structural insights at the level of the environment of the Mn-cluster and the single amino acids involved in the proton transfer is known.

In total PSII extracts in a full cycle four electrons from water and pumps four protons from the stroma to the lumen. Additional four protons are transferred with the doubly reduced Q_B towards the cytochrome b6f complex.

2.2 PSII structure

PSII in its dimeric form is embedded in the thylakoid membranes of the plant or algal chloroplast and cyanobacteria. Usually a large antenna system is bound to it. The antenna system in cyanobacteria is the phycobyllisome. It attaches to the membrane. The antenna system in plants are the light harvesting complexes and are membrane intrinsic. The PSII dimer consists of about 30 subunits and 100 bound cofactors. Whereas the vicinity around the Mn cluster is highly conserved between species, other parts as the extrinsic subunits may vary ([Nelson and Yocum, 2006]).

Important structural aspects related to the single investigations will be introduced in each chapter.

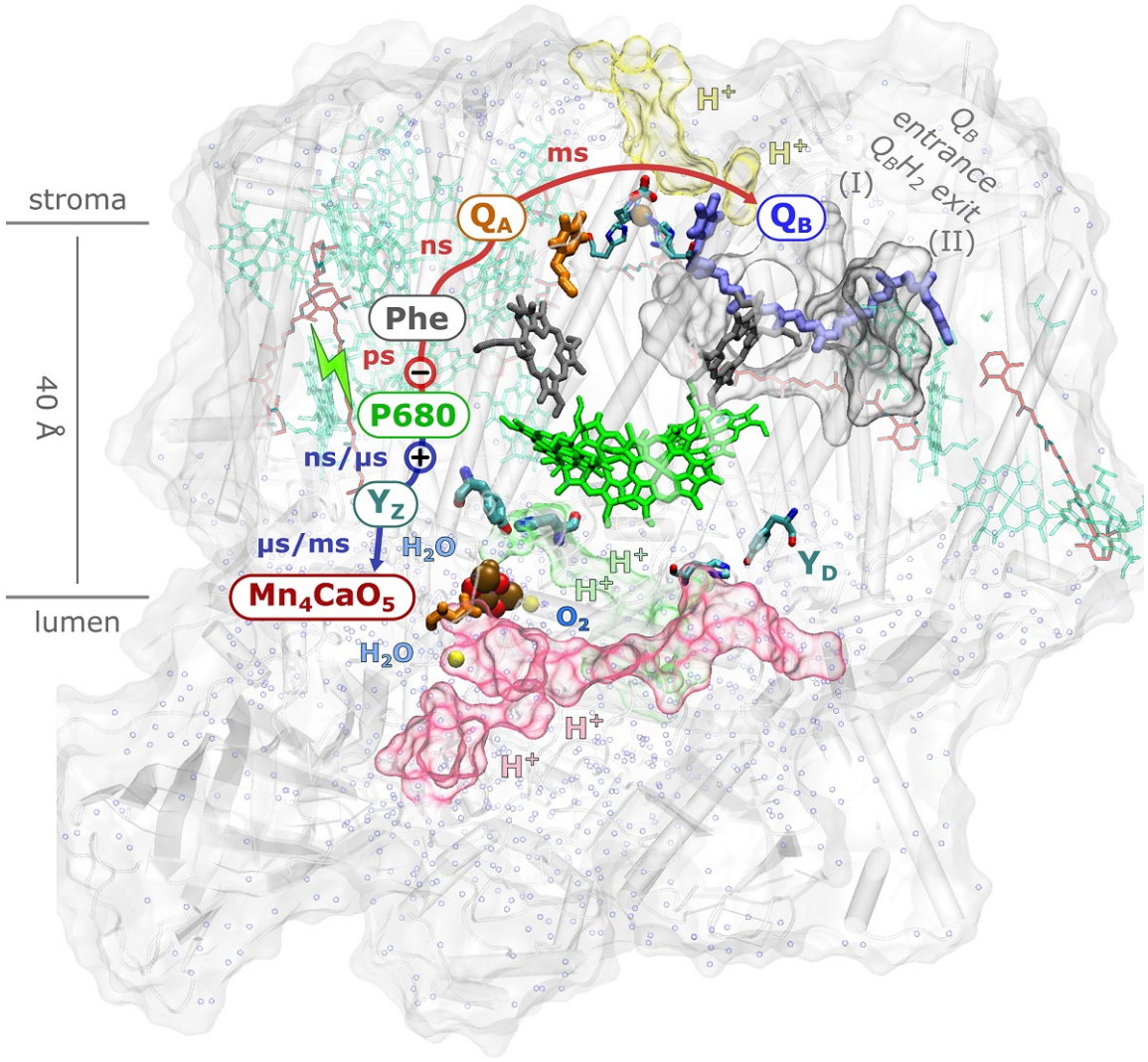

Figure 2.1: PSII monomer and redox cofactors of the electron transfer chain.
If any of the intrinsic or antenna chlorophylls is excited, the energy is transferred rapidly via FRET to the central special chlorophyll unit P_{680}. Here, charge separation takes place. The negative charge is conducted within about 300 ps via a pheophytin (Phe) to the first tightly bound quinone Q_A, which most likely induces the uptake of a proton (yellow pathes). From Q_A^- the electron is brought to a mobile quinone Q_B with multi phasic characteristics. Possibly this involves an iron atom held by four histidines located on four different transmembrane helices of the D1 and D2 protein and a bicarbonate which might function in a metabolistic feedback loop. After a second photon is absorbed and a second proton is taken up from the stroma the doubly reduced and protonated Q_BH_2 is exchanged via one of the suggested pathways (I) or (II).
At the lumenal side, the positive charge is transferred from P_{680}^+ to the redox active tyrosine Y_Z forming a functional unit with the strongly H-bonded histidine D1-H190. This happens within 30 ns but µs stabilizing phases are known. The redox potential of $Y_Z^{\bullet ox}$ is high enough to oxidize the Mn_4Ca-µoxo- cluster, the catalytic center. The kinetics depend on the redox state of the cluster, the so called S states. Our group proposed a strictly alternating sequence of electron and proton removal. After the accumulation of four redox equivalents a O-O bond can be formed from the oxygens of two water molecules. The released protons are transferred to the lumenal bulk via one of the many proposed channels (pink and green).
(crystal: 4UB6 from [Suga et al., 2015]), picture inspired by Ivelina Zahrievas

2.3 Quinone reactions

The mobile electron carrier Q_B can take up two electrons. A detailed introduction to the involved reactions will be given in chapter 7. For the understanding of the following sections, it is enough to know, that the main component of electron transfer from Q_A^- to either Q_B or Q_B^- lasts between 200 µs and 1 ms ([Muh et al., 2012]). The amount of available plastoquinones in the membranes is limited, and therefore it is necessary to add electron acceptors, when one wants to study the reactions of the oxygen evolving complex. Many of the added acceptors can oxidize the non-heme iron from Fe^{2+} to Fe^{3+}. The electron transfer from Q_A^- to Fe^{3+} is with 15 µs much faster than to Q_B ([Chernev et al., 2011]).

2.4 The extended reaction cycle of the oxygen evolving cluster

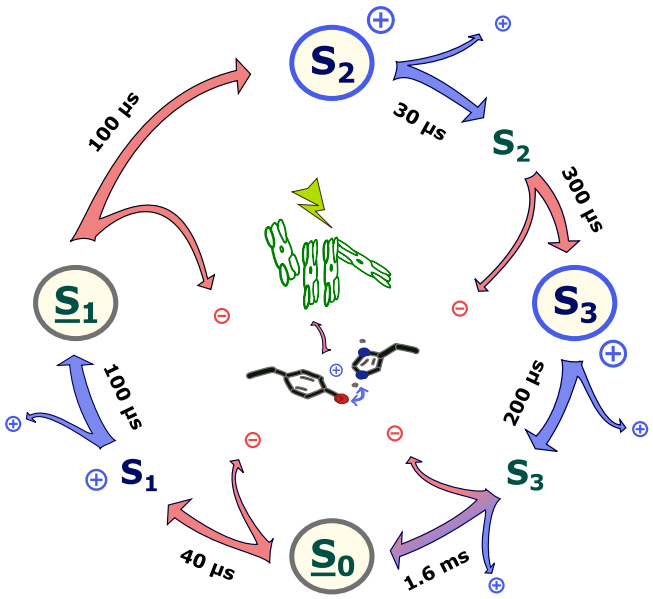

Figure 2.2: Extended reaction cycle of the oxygen evolving complex. The Mn cluster cycles through four stable S-states (encircled). During longer dark adaption higher S-states decay back to the S_0 or S_1 states, which remain stable in the dark. After an absorbed photon is transferred to the central chlorophyll unit P_{680}, the charges are separated. Then the redox active tyrosine Y_Z-His190 unit becomes oxidized, which is concerted by a proton shift from Y_Z to the histidine. The redox potential of $Y_Z^{\bullet ox}$ advances the Mn cluster through its S-state reaction cycle of strictly alternating electron and proton releases (time constants taken from [Klauss et al., 2015]). Red arrows represent electron transfer events from the Mn cluster to Y_Z and blue errors proton release. The environment of the cluster in the S_2 and S_3 as well as in the transient S_1 $^+$ is positively charged.

The current state of knowledge about the catalytic cycle is presented in figure 2.2. A detailed introduction to the structural changes and reactions accompanying each transition will be given in chapter 9. The multi-phasic stabilization reaction during the process of Y_Z oxidation in S_2 and S_3 is still under discussion. Known time constants include a 30 ns, a 300 ns and a 30 µs phase ([Renger, 2004]). A deeper introduction to recent studies will be given in chapter 8.

3 Infrared spectroscopy on PSII

Decades of PSII research has yielded a wealth of knowledge that no student can fully gasp. The only way to access the necessary information are well written reviews or theses.

While some reviews on infrared studies on proteins, photosystems in general or photosystem II exist, there is one problem: none of them provides you with the needed overview about vibrational assignments[1] and most focus on the authors' own works. Here are some of them:

- [Barth, 2007], [Barth and Zscherp, 2002] and [Barth, 2000]: overview of amino acid and protein backbone absorption modes
- [Berthomieu and Hienerwadel, 2009]: general approach to IR studies of proteins
- [Mezzetti and Leibl, 2017]: overview over recent time resolved studies of photosynthetic systems
- [Chu, 2013]: studied low wavenumber vibrations of the Mn-oxide below 1000 cm^{-1} in PSII
- [Noguchi, 2015]: electron and proton transfer in PSII including FTIR on typical additives such as FeCy or MES
- [Okubo and Noguchi, 2007]: a summary of some of the PSII cofactors measured by this group
- [Noguchi, 2008]: overview over high wavenumber water vibrations, the influence of pH and sample humidity on PSII and the mechanism of water oxidation studied by IR spectroscopy
- [Debus, 2015]: a summary of FTIR results on some of his large variety of point mutations in PSII

Unfortunately[2], there is nearly no literature on time resolved IR data on PSII. The noteworthy exceptions are three papers by the group of Takumi Noguchi, in which they presented the transients of three wavenumbers for all S-state transitions ([Noguchi et al., 2012]), six different wavenumbers for two transitions ([Sakamoto et al., 2017]) or two wavenumbers for the $S_0 \rightarrow S_1$ transition ([Shimizu et al., 2018]).

Additionally, the reader shall refer to the FTIR step scan results from Matthias Schönborn, that might help to assign processes based on their dynamics ([Schönborn, 2017]). Here caution needs to be taken in the heat artefact rich spectral region between 1530 and 1730 cm^{-1}.

The following chapter is an attempt to review the current knowledge on PSII infrared difference spectra in the region between 1100 and 1800 cm^{-1}. Much of the information stems from the great work of the above mentioned authors.

[1] still mainly tentative assignments

[2] or maybe rather luckily for us

3.1 Introduction to Infrared Spectroscopy on proteins

First, I want to shortly introduce the reader to the basic and simplified principles of infrared absorption and how to identify the approximate absorption frequency[3] of a certain molecular vibration. The chapter starts with basic knowledge from text books, but shall quickly proceed to questions relevant to the work on PSII, as for example the influence of Mn ligation on the carboxylate vibration, large scale coupling and obtainable knowledge from IR spectra about the H-bonding environment.

To understand the basic absorption principles of infrared light, the electronic wavefunctions and energy levels need to be known. Considering vibrations only around the equilibrium core distance R_0, independent rotations and vibrations, and assuming that the cores are much more inert than electrons and their movements are uncoupled, the total wavefunction ϕ can be split into the one of the electrones and the one of the cores: $\phi(\vec{r}_j, \vec{R}_i) = \phi_{el}(\vec{r}_j, \vec{R}_i) \cdot \phi_c(\vec{r}_j, \vec{R}_i)$. This **Born-Oppenheimer approximation** will lead to the energies in Schrödinger's equation of diatomic molecules:

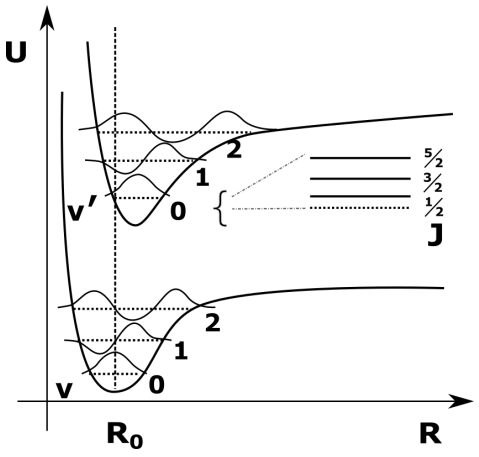

Figure 3.1: Potential curves of two electronic states filled with vibrational energy levels. Rotational splitting of the vibrational levels depends on spin and angular momentum coupling.

$$\begin{aligned} E &= E_{el} + E_{vib} + E_{rot} \\ &= E_{el}(R_0) + \hbar\sqrt{\frac{k}{\mu}}(v + 1/2) + \frac{\hbar^2 J(J+1)}{2\mu R_0^2}. \end{aligned} \tag{3.1}$$

E_{el} describes the interaction of the electrons and the cores, E_{vib} the vibrational energy in an parabolic potential with the quantum number ν, the binding strength k and the reduced mass μ. The rotational energy depends on the quantum number of the total angular momentum J. Details about this can be found in e.g. Demtröder Molekülphysik.

A typical potential energy diagram is presented in figure 3.1. Shown are the electronic ground state potential as well as one excited state potential of a diatomic molecule (E_{el}). These wells are filled with (in first order) equidistant vibrational energy levels (E_{vib}). Corresponding wavefunctions are drawn as well. Every vibrational energy level is split into many levels due to the rotational energies (E_{rot}). In solution these **rotational levels** are not resolved, in proteins they **can be neglected** completely.

When measuring infrared absorption, electronic transitions are not involved and in proteins only the allowed **normal modes of vibration** need to be taken into account. The thermal energy of room temperature is in terms of wavenumbers of the order of

$$\frac{k_B T}{hc} \approx 200\, cm^{-1},$$

[3] in IR spectroscopy the frequency unit of wavenumbers $\bar{\nu} = 1/\lambda_{vac}$ in cm^{-1} is used.

meaning nearly all electrons are in the **vibrational ground state** if the wavenumber observed is much greater. Absorption at multiples of the wavenumber are possible but only if the potential is anharmonic. Finding higher harmonic absorption bands will therefore give an idea about the nature of anharmonicity of the potential[4] (*Colthub, Introduction to infrared and raman spectroscopy, 3rd edition, Academic Press,inc., p.28,ch1*).

From $E_{vib} = hc\bar{\nu}(\nu + 1) \propto \sqrt{\frac{k}{\mu}}$ in equation 3.1 one can already follow:

I) **Heavier molecules** absorb at **lower wavenumbers**
This mass dependence one can use to identify bands in feature rich spectra by global, amino acid or side specific **isotope labeling**.

II) **Stronger bonds** lead to **higher wavenumbers**
We can for example learn how strong an amino acid side chain is involved in an **H-bond**. If, for example, the oxygen of a carbonyl group is involved in a strong H-bond the double bond to the carbon will be weakened and the wavenumber of the $\nu(C = O)$ vibration downshifted. If in a transition the H-bond is broken the $C = O$ bond will be strengthened and the wavenumber upshifted.

As for all interactions between matter and light, the strength of IR absorption is proportional to the transition dipole moment:

$$A_{vv'} \propto \left| \int \psi_v(R) \vec{\mu} \psi'_{v'}(R) dR \right|^2 . \tag{3.2}$$

This means the **higher the change of the dipole moment** of a vibration the easier the induction by the electric field of the photon and **the stronger the IR absorption**. As of course these are vectorial units, the relative direction of the fields (of a laser) and the transition dipole moments are of importance as well. Another line of argumentation works on symmetry aspects of the molecules, for which the reader may find details in *Colthub, Introduction to infrared and raman spectroscopy.*

In anharmonic potentials, where $\Delta\nu = \pm 2, 3, ...$ it is possible these overtone vibration can become strongly absorbing when they are coupled to the $\Delta\nu = 1$ vibration of groups close by. Then the position of both bands will shift and instead of one very strong and one very weak band two strong bands can be observed. This is called **Fermi resonance**. Noguchi suggests this explanation for the fine modulation of bands around 2800 cm^{-1} visible in the first and reversed in the third flash data[5]. He suggests that the $\nu(NH)$ vibration of strongly H-bonded histidines couple to not further specified overtone and combination bands of the imidazole ring [Noguchi et al., 1999] [Nakamura and Noguchi, 2017].

The width of IR bands of amino acids in solution are reported to be between 8 cm^{-1} (for the tyrosine ring vibration) and 30-50 cm^{-1} (form most other side chains) (full width at half maximum, [Venyaminov and Kalnin, 1990]).

An overview of the aproximate positions of the vibration of different chemical groups can be found in figure 3.2. This scheme only shows the group frequencies' approximate positions. Their actual position in a protein spectrum depends on their close environment. Some examples will be given below.

[4] selection rule $\Delta\nu = \pm 1$ in harmonic potentials
[5] reversed during the catalytic photocycle

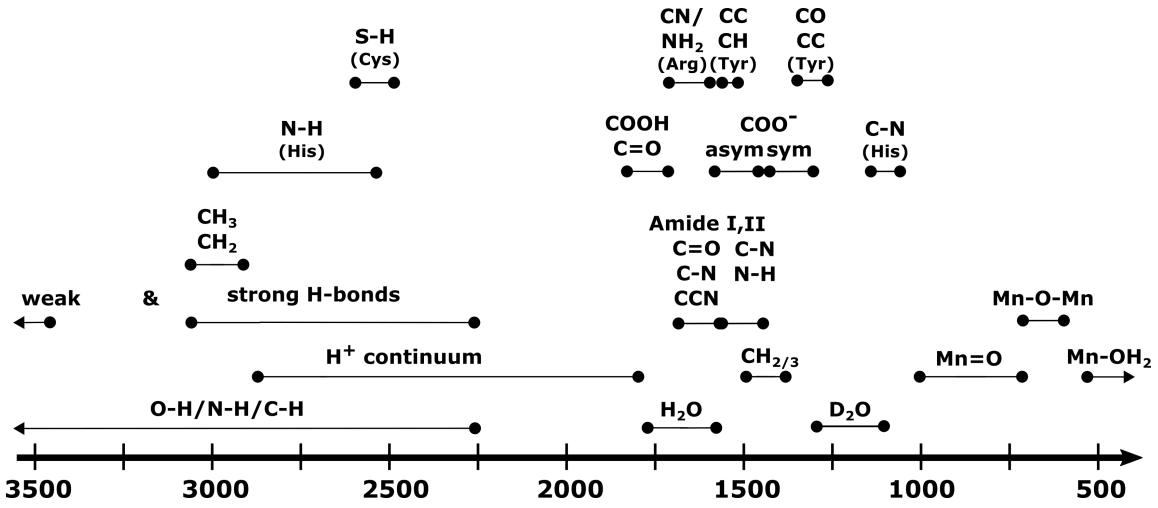

Figure 3.2: Position of chemical group frequencies relevant to PSII. Only the most prominent vibrations are shown. The positions are taken from various literature presented in this chapter.

- **Protein backbone vibration**
  The backbone vibration is classified into numerous groups. Relevant to this thesis are the amide I and II vibrations. Amide I includes mainly the $\nu(C=O)$ and weakly the CN out-of-phase stretch, the NH in-plane bend as well as the CCN deformation of the peptide bond. It is very sensitive to the secondary structure. The amide II vibrations consists mainly of the out of phase combination of the CN stretch and the NH in plane bend. It is not straightforward assignable to the secondary structure ([Barth, 2007]).

- 1250 to 1800 cm^{-1}: **Carboxylates**
  When they are protonated, the $\nu(CO)$ absorbs between 1710 and 1760 cm^{-1}, a region that is free of other amino acid vibrations ([Barth, 2000]). These vibration are very sensitive to H-bonding (detailed study by [Takei et al., 2008]).

  The $\nu(COO)$ vibration is split into an asymmetric and a symmetric band, which are found around 1570 and 1400 cm^{-1}, respectively ([Barth, 2000]). Upon ligation of a metal ion, the band position may shift considerably (for ν_S down to 1270 cm^{-1} [Kimura et al., 2005a]). The wavenumber difference between ν_{AS} and ν_S was found by: $\Delta\overline{\nu} = \overline{\nu}_{\nu(COO^-)_{asym}} - \overline{\nu}_{\nu(COO^-)_{sym}} \approx 200$ cm^{-1}: unidentate coordination, ≈ 160 cm^{-1}: ionic, ≈ 160 cm^{-1}: bridging bidentate structure, ≈ 100 cm^{-1}: chelating bidentate coordination [Shimada et al., 2009]. However, in PSII studies many ligands of Mn atoms, that undergo oxidation, are silent (see tables below). [Sproviero et al., 2008] found, that the charge of the cluster is strongly delocalized and no straightforward correlation of the ligating carboxylates and the oxidation state of the cluster can be drawn, unless the carboxylate is coordinated along the Jahn-Teller axis.

- **Proton continuum band**
  A delocalized proton gives rise to a broad continuum band and can be found in many proteins, also in PSII. It can be found in between 1000-3000 cm^{-1} ([Barth, 2007]) and depends on the number of sharing molecules and their 3d conformation ([Daldrop et al., 2018]).

- **Other amino acids**
  The guanidyl group of arginines absorbs at 1630-1690 cm^{-1} in their protonated state and at 1550-1600 cm^{-1} in their deprotonated state ([Shimada et al., 2011]).

  The IR modes of lysine are very weak with two modes around 1625 and 1525 cm^{-1} ([Barth, 2000]).

  The $\nu(C = O)$ modes of asparagine and glutamine are located around 1680 cm^{-1} but depend on the H-bonding. The amino groups absorb weakly around 1610 cm^{-1} ([Barth, 2000]).

  The absorption modes of serine and threonine are located between 1000 and 1420 cm^{-1}. Their $\nu(CO)$ contributes mainly around 1075 to 1150 cm^{-1} ([Barth, 2000]).

- **Lipids**
  The $\nu_{S/AS}(CH_2)$ of lipids absorbs around 2900 cm^{-1}. Methyl vibration absorb in between 1300 and 1500 cm^{-1}. Carbonyl stretching modes are expected from 1720 to 1750 cm^{-1}. The phosphate $\nu_{as}(PO^{2-})$ modes appear around 1220 to 1240 cm^{-1} and the $\nu_s(PO^{2-})$ modes around 1080 and 1090 cm^{-1} and both are sensitive to H-bonding and cation bonding. Lipids possessing carboxyl groups absorb additionally around 1600 to 1650 cm^{-1} [Tamm and Tatulian, 1997].

3.2 Steady state difference spectra of the S-state cycling in intact PSII

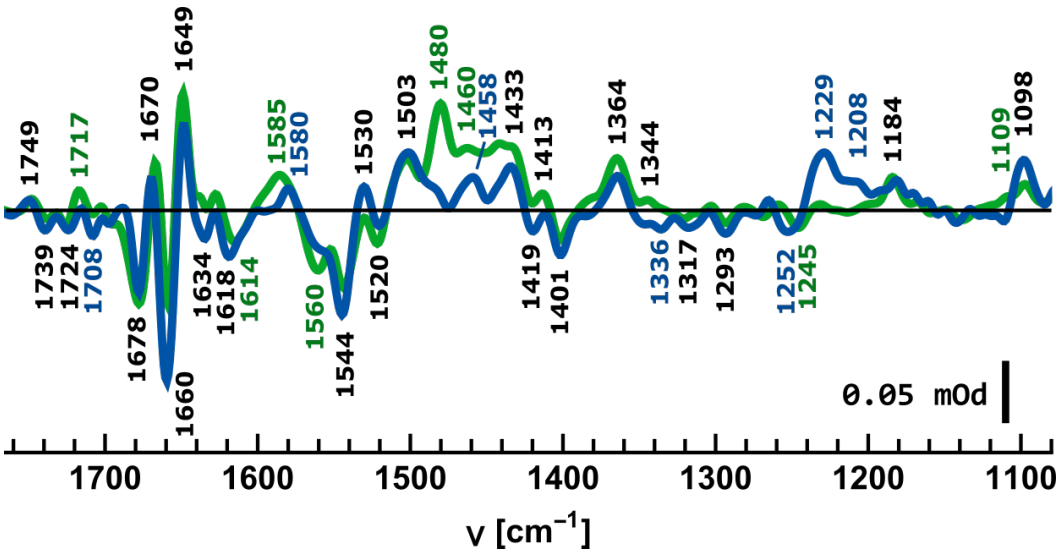

Figure 3.3: First flash steady state difference spectrum with (*blue*) and without PPBQ (*green*) of PSII membrane particles from spinach measured at pH 6.2 and 20 °C. Differences show up due to reduced quinone bands (e.g. 1410-1480 cm^{-1}) and non-heme iron reduction (e.g. 1229 cm^{-1}).

Figure 3.3 shows the steady state difference spectra recorded on PSII membranes at pH 6.2 and room temperature after excitation with one ns flash. In the green spectrum only the native quinones are present. The blue spectrum is measured with the addition of PPBQ as

an exogenous electron acceptor. Although the two spectra are similar over a broad spectral range, strong differences appear in others. The green peak around 1480 cm^{-1} is assigned to the reduced quinones, while the blue peaks around 1230 cm^{-1} stem from the oxidation of iron ($Fe^{2+} \rightarrow Fe^{3+}$). This figure emphasizes that when studying water oxidation by the means of time resolved IR spectroscopy, it is not enough to know the position of bands reflecting the S-state transition, but the spectra of all other involved cofactors - also the once transiently formed - need to be known.

Global isotope labeling on S-state difference spectra

Through global isotope labeling one can assign bands of a difference spectrum to vibrations of the labeled element. Furthermore, one can label specific atoms of one type of amino acid. To do that, the organism needs to be fed with the element or labeled amino acid. Amino acids will only be incorporated when the metabolic pathways for their synthesis are silenced. This can only be achieved for certain amino acids.

Here, only the bands assigned by global labeling shall be discussed. Bands of labeled tyrosine are discussed below in section 3.3 and the ones related to other specific amino acids in section 3.4.

Figure 3.4 shows the band positions of the four transitions in the photocycle of the Mn cluster taken from [Noguchi and Sugiura, 2003]. The data was not deconvoluted and especially the $S_0 \rightarrow S_1$ transition may be masked. The measurement was done on core complexes from *T. elongatus*. Presented was only the data down to 1200 cm^{-1}. All bands have been assigned – based on their shift upon ^{13}C or ^{15}N labeling – to either the $\nu(C=O)$ vibration of COOH groups ($\Delta\nu_C \approx 45cm^{-1}$), $\nu(C=O)$ of Gln or Asn or amide I of the backbone ($\Delta\nu_N \approx 1-5cm^{-1}$ and $\Delta\nu_C \approx 40cm^{-1}$), amide II of the backbone ($\Delta\nu_N \approx 10-15cm^{-1}$ and ($\Delta\nu_C \approx 10-15cm^{-1}$)), $\nu_{asym}(COO)$ vibration ($\Delta\nu_C \approx 35-40cm^{-1}$) and the $\nu_{sym}(COO)$ vibration (($\Delta\nu_C \approx 25-40cm^{-1}$)).

Whereas most cofactor spectra are very similar between PSII membranes of spinach and core complexes from cyanobacteria, certain differences in the S-state difference spectra do exist. [Remy et al., 2004] reported differences in the region between 1700 and 1750 cm^{-1} of the $S_1 \rightarrow S_2$ transition. Changes in the amide I and II regions were also reported by different groups, e.g. [Chu et al., 2001]. These were explained by the different sample preparations. Differences of bands at 1670 cm^{-1} and the size and shape around 1560 cm^{-1} reported in the same reference could be reproduced in cyanobacteria by the D1-N87A mutation ([Banerjee et al., 2018a], an alanine is present at this residue in spinach).

Besides their influence on the oxygen activity, the different extrinsic subunits mainly affect the amide modes of the S-states (as reviewed for different subunits and orsganisms in [Ifuku and Noguchi, 2016]). Only PsbO is required for the full carboxylate mode recovery after the depletion of all extrinsic proteins in cyanobacteria. Additionally each subunit may be present in a different isoform (D1,D2..). So far I have not found FTIR data on the characterization of these.

The shape of the amide bands is also strongly dependent on the sample preparation and water content ([Service et al., 2010]).

Interconversion of the high and low spin states in S_2 gave no measurable change of the S_2 minus S_1 difference spectrum [Onoda et al., 2000].

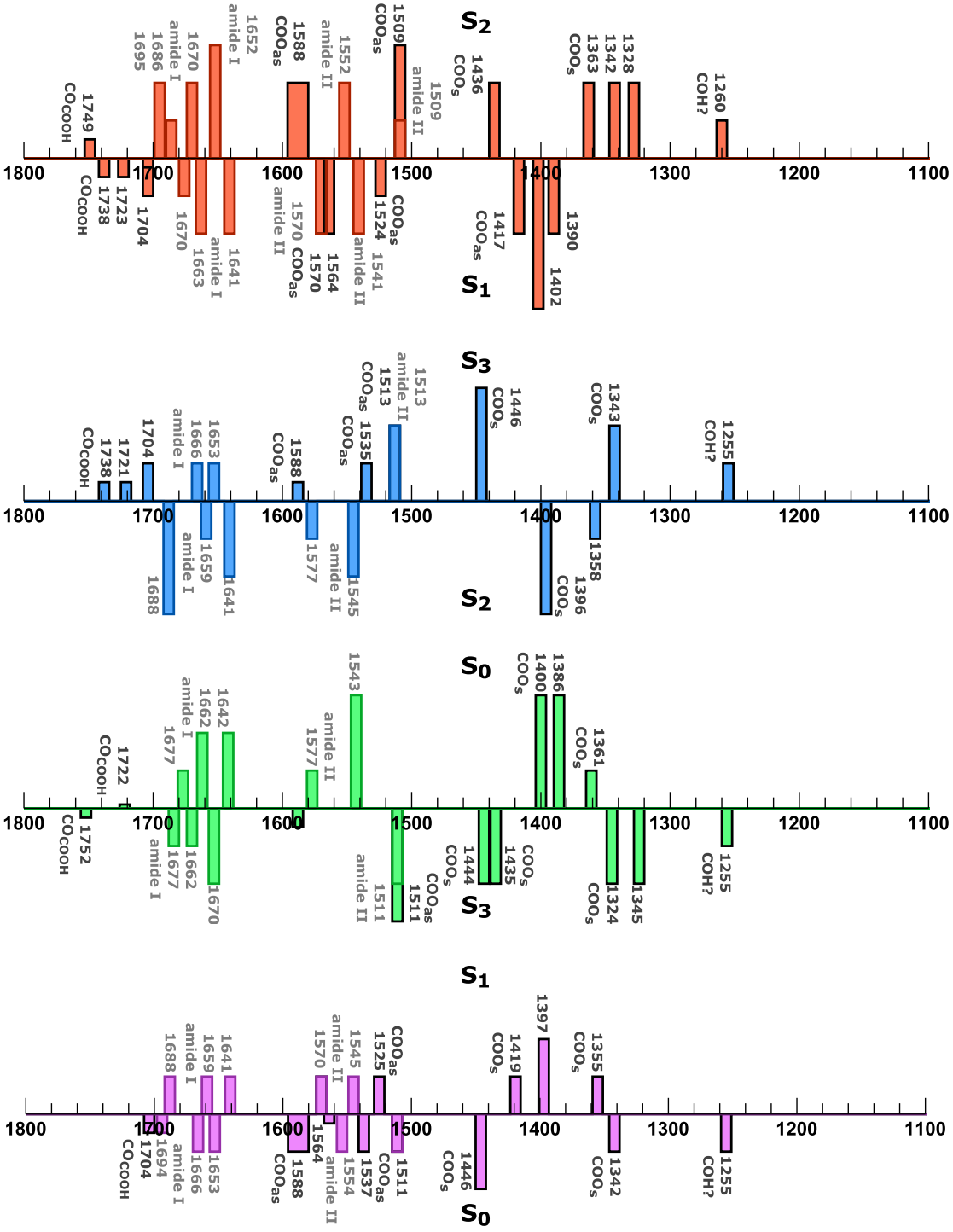

Figure 3.4: Band positions of the S-state transitions (*not deconvoluted*). In *red*: $S_1 \rightarrow S_2$,*blue*: $S_2 \rightarrow S_3$, *green*: $S_3 \rightarrow S_0$ and *magenta*: $S_0 \rightarrow S_1$. Darker contoured bands are assigned to carboxylate groups, brighter to the backbone changes reflected in the amide I and II modes. Only signals down to 1200 cm^{-1} have been discussed. Positions and assignments from [Noguchi and Sugiura, 2003].

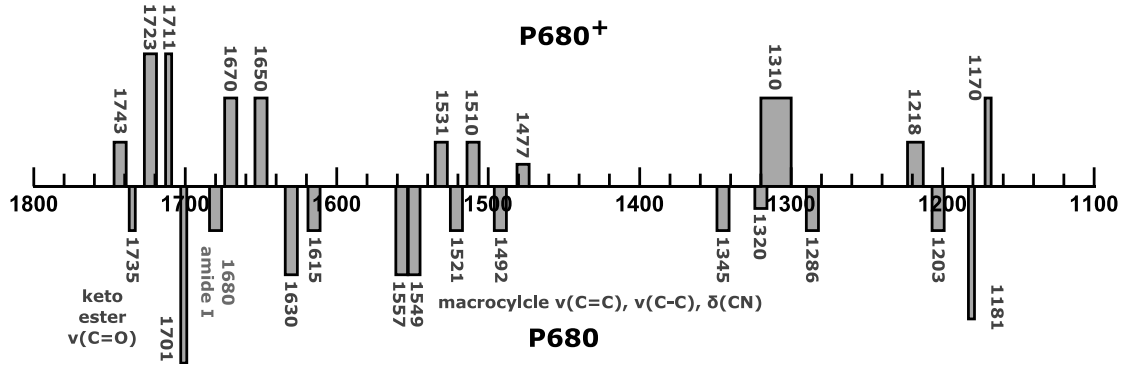

Figure 3.5: Band positions of P_{680}^{+}- P_{680} spectra recorded on Mn depleted samples with electron acceptor under continuus red illumination. Spectra of spinach and cyanobacterial samples look alike. Band positions and assignments are taken from [Okubo et al., 2007] and [Noguchi et al., 1998].

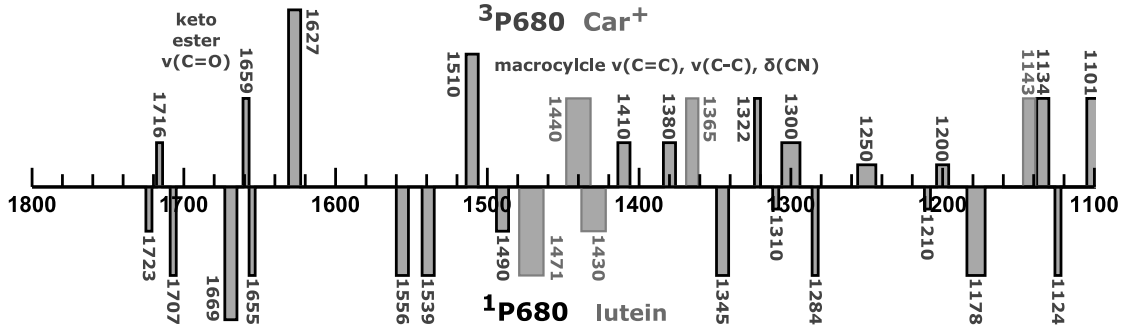

Figure 3.6: Band positions of the P_{680} triplet minus singlet (dark gray) and of the carotenoid cation (light gray +) and the singlet of the carotenoid lutein. Positition from [Christen et al., 1998] for P_{680} and [Noguchi et al., 1994] for the carotenoid cation and [A. Maxime, 2012] of the neutral lutin.

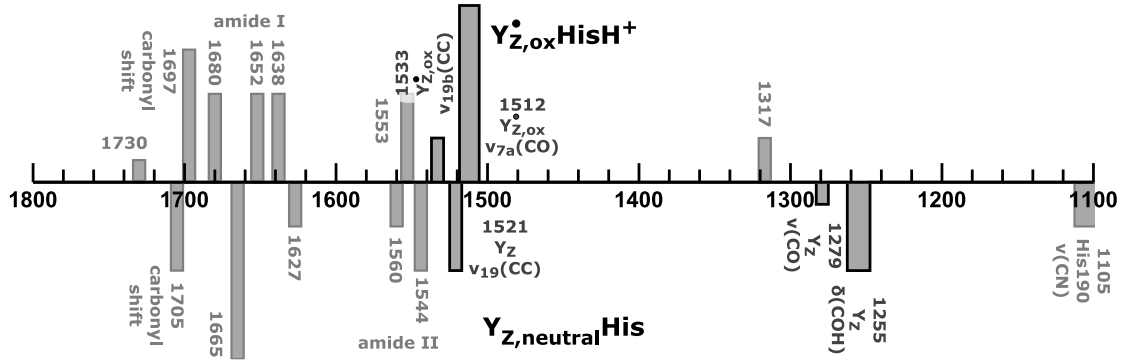

Figure 3.7: Band positions of $Y_Z^{\bullet ox}$- Y_Z spectra recorded on Mn depleted samples. Spectra recorded on spinach and cyanobacterial samples look quite alike. Band positions and assignments are taken from [Berthomieu et al., 1998], [Berthomieu and Hienerwadel, 2005] and [Nakamura et al., 2014].

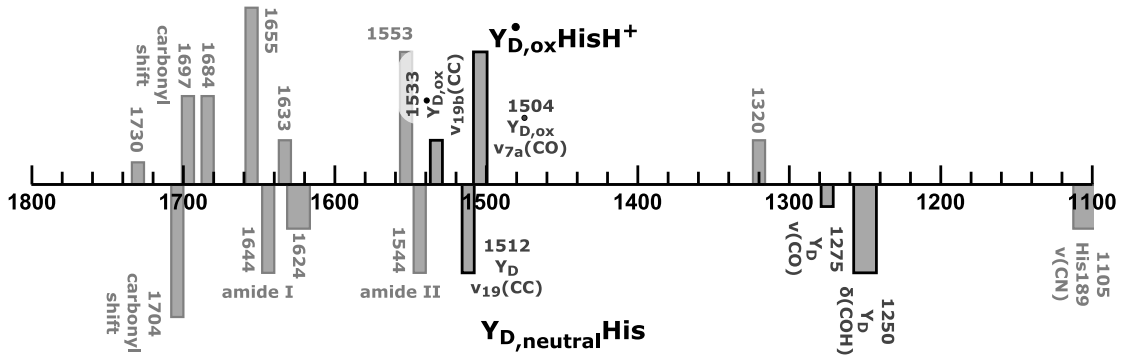

Figure 3.8: Band positions of $Y_D^{\bullet ox}$- Y_D spectra recorded on Mn depleted samples. Spectra recorded on spinach and cyanobacterial samples look alike. Band positions and assignments are taken from [Berthomieu et al., 1998], [Berthomieu and Hienerwadel, 2005] and [Nakamura et al., 2014].

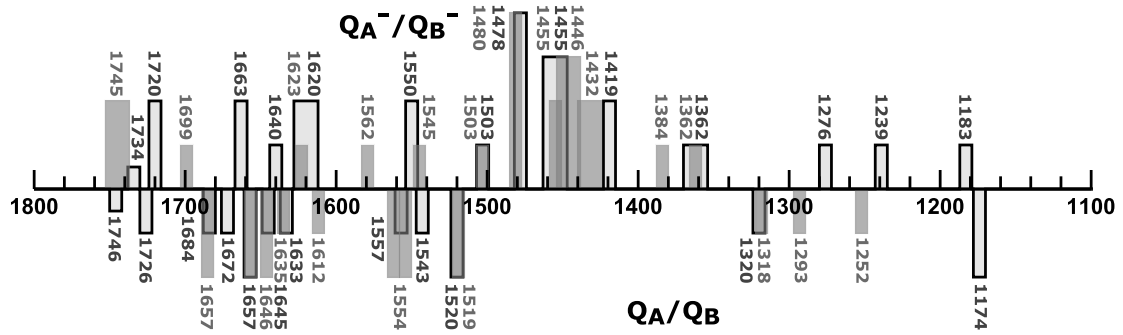

Figure 3.9: Band positions in Q_A^- minus Q_A (white bars) and Q_B^- minus Q_B (gray bars) spectrum. Band positions and assignments are taken from [Zhang et al., 1997], [Suzuki et al., 2005] and [Kato et al., 2016].

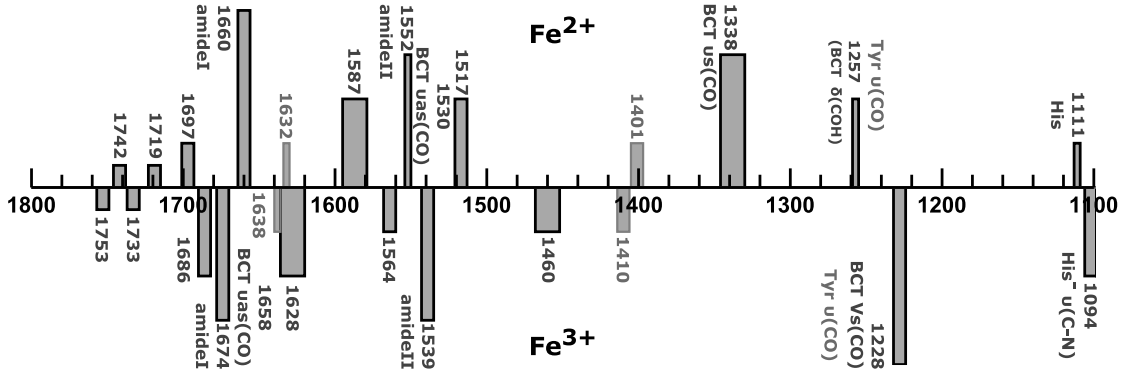

Figure 3.10: Band positions in Fe^{2+}/Fe^{3+} spectrum. Band positions and assignments are taken from [Berthomieu and Hienerwadel, 2001] and [Takahashi et al., 2009].

3.3 Steady State on different PSII fractions and cofactors

P680$^+$/P680

The difference spectra representing P_{680}^+ minus P_{680} are obtained of PSII membranes from spinach depleted of the quinones and Mn cluster. Mn depleted core complexes from cyanobacteria show identical spectra. To both samples SiMo and ferricyanide was added and continuous illumination with red light at 265 K applied ([Okubo et al., 2007]). With the negative charge present at the quinones possibly some bands might shift position as happens upon $Y_Z^{\bullet ox}$ formation (*see next section*).

Chlorophyll a in solution shows well defined bands in the whole spectral region from 1250 to 1750 cm^{-1} ([Nabedryk et al., 1990]). The spectrum of P_{680}^+ minus P_{680} is therefore feature-rich even if the protein contributes only weakly.

Figure 3.5 shows the diffence spectrum. The bands around 1715 cm^{-1} are assigned to the keto $\nu(CO)$ vibration. The wavenumber shift from the neutral P_{680} at 1700 to the oxidized state and the numbers of peaks and their amplitudes gives information of the degree of charge delocalization of the P_{680} unit ([Nabedryk et al., 1990]).

The chlorine macrocycle vibrations containing the $\nu(C=C)$, $\nu(C-C)$ and $\delta(CN)$ modes extend from 1100 to 1620 cm^{-1}. The $\nu(C=C)$ mode contains information about the coordination number of Mg, which is six for the neutral P_{680} judged from the bands at 1610 and 1515 cm^{-1} ([Noguchi et al., 1998]). The band at 1510 cm^{-1} in [Okubo et al., 2007] has a positive shoulder around 1505 cm^{-1}. The relative size of the bands at 1345 and 1320 cm^{-1} depends on the sample condition and the intensities are reversed compared to the ones in the figure when measured on reaction centers ([Okubo et al., 2007]).

P680 and carotenoid triplets

Although the signals of triplet states as well as the cation of the carotenoids are not of direct interest to study the forward electron transfer reactions in PSII, this species might appear as unwanted side products. Chlorophyll triplet states are always produced in low quantity by excitation and by some charge recombination pathway. The recombination of P_{680}^+ and Pheo$^-$ takes places within 30 ns at room temperature ([Diner and Rappaport, 2002]). In oxygen free solution these states might be long-living whereas in PSII oxygen is present and the carotenoids function as quenchers. Carotenoid cations might be produced by strong excitation with 532 nm as well.

While the neutral β-carotenoid is not IR active, its cation form absorbs with strong bands observed at 1440, 1365 and 1143 cm^{-1} ([Noguchi et al., 1994], figure 3.6). The only IR data I could find on triplet states of carotenoids is a side remark in an FTIR study of LHCIIs ([A. Maxime, 2012]). Here the negative bands at 1471 and 1430 cm^{-1} are assigned to modes of lutein - a carotenoid in LHCII that contains hydroxy groups on both rings. The triplet states have not been distinguishable from chlorophyll triplet states (positive bands appear at 1535 and 1515 cm^{-1}).

Carotenoid triplet decays were measured in LHCII with 3 µs[Christen et al., 1998] and 20 µs [A. Maxime, 2012]

The chlorophyll triplet was measured by [Noguchi et al., 1993]. It decays with a halftime of 0.5 ms in reaction centers at 160 K ([Takahashi et al., 1987]). The band assignment corresponds to the one of P_{680}^+.

The redox active tyrosines YZ and YD

Figures 3.7 and 3.8 show the position of bands in a difference spectrum $Y_Z^{\bullet ox}$ minus Y_Z and $Y_D^{\bullet ox}$ minus Y_D. The data is compiled from the sources mentioned in the captions. Spectra of Mn depleted PSII samples of different organisms were compared and it was shown that the peak positions did not vary significantly.

To obtain a tyrosine spectrum the samples needs to be depleted of Mn. A Y_D spectrum is usually obtained by measuring many flashes after one flash and subtracting these from the first in order to remove contributions from Y_Z or the non-heme iron.

Besides the $\nu_{19}(CC)$ vibration of the ring at 1521 and 1512 cm^{-1}, the protonated therefore neutral tyrosine shows a $\nu(CO)$ vibration, which absorbs at 1278 and 1275 cm^{-1} for Y_Z and Y_D, respectively ([Berthomieu and Hienerwadel, 2005]). [Nakamura et al., 2014] has observed overlapping of this mode with the $\delta(COH)$ in a broad feature around 1255 cm^{-1}.

The reduced form of tyrosine would absorb with a ring vibration around 1600 cm^{-1}, which is stronger compared to the neutral form, and an intense $\nu_{19}(CC)$ band would be found around 1500 cm^{-1} instead near 1520 cm^{-1} ([Venyaminov and Kalnin, 1990]).

When the tyrosine radical is formed in PSII and the shared proton moves towards the histidine, the $\nu(CO)$ shifts towards the frequencies of a double bond and absorbs around 1512 cm^{-1} as $Y_Z^{\bullet ox}$ ([Nakamura et al., 2014]). This vibration is strongly dependent on the environment and measurements in inert media showed a band even around 1480 cm^{-1}. The highest wavenumber in model compounds was observed at 1515 cm^{-1} ([Berthomieu and Hienerwadel, 2005]) although Noguchi recently suggested an upshift up to 1525 cm^{-1} in PSII ([Sakamoto et al., 2017]). Another band of the radical in solution – which is not visible in the spectra obtained from PSII – can be found around 1550 to 1585 cm^{-1} ([Berthomieu and Hienerwadel, 2005]).

The band shift from 1705 to 1697 cm^{-1} was assigned to the vibration of the keto group of P680 electrochromicaly shifting upon the radical formation [Nagao et al., 2017b].

The histidine $\nu(CN)$ vibration observable around 1100 cm^{-1} is very weak when the histidines are protonated. Therefore only a negative band is observed here. The doubly protonated species can be found in features around 2500 to 3000 cm^{-1} which lie on top of a broad band attributed to the highly polarizable proton shared by $Y_Z^{\bullet ox}$ and the histidine ([Nakamura et al., 2014]). Also a weak $\nu(CC)$ band of the doubly protonated histidine might be found around 1630 cm^{-1} ([Barth, 2000]).

It shall be mentioned again that the transient formed $Y_Z^{\bullet ox}$- Y_Z difference spectrum in oxygen evolving samples might appear slightly different. Both the protein backbone and the H-bond network might react quite differently.

Pheo

As the pheophytin gets reduced only transiently, it shall not be discussed in detail here. A spectrum of the reduced minus neutral pheophytin can be found in[Okubo and Noguchi, 2007].

QA, QB and BCT/Fe

Q_A is present in all of our samples and reduced rapidly. The electron is passed to Q_B if present or to an exogenous electron acceptor like PPBQ or FeCy – possibly via Q_B. The electron acceptors interact with the non-heme iron as well. When PPBQ is singly reduced, it can oxidize the iron. FeCy is known to oxidize the iron within 20 min (pH 8). For this

reason all signals of the difference spectra discussed here, might appear transiently in the time resolved data.

The Q_A^- minus Q_A spectrum of figure 3.9 (blank bars) shows bands and relative intensities mainly from [Zhang et al., 1997]. It is compared with the ones from [Suzuki et al., 2005] and [Kato et al., 2016] and band positions below 1320 cm^{-1} are added. In this region all spectra more very weak positive and negative bands.

The information of the Q_B^- minus Q_B spectrum of the same figure (gray bars) origin from [Suzuki et al., 2005] and are compared with the ones from [Zhang et al., 1998], which is poisoned with the S_2 minus S_1 spectrum. Both reports only show spectra down to 1200 cm^{-1} and in all spectra very weak positve and negative bands show up in the symmetric carboxylate region between 1250 and 1330 cm^{-1}.

The spectra and assignments of the quinone bands will be discussed in detail in section 7.

To measure a more or less pure Fe^{2+} minus Fe^{3+} spectrum the sample is depleted of Mn and ferricyanide added. The tyrosine signals will not be present as ferrocyanide will donate electorons to it.

Figure 3.10 shows the Fe^{2+}/Fe^{3+} spectrum. The dark contoured line are obtained by [Berthomieu and Hienerwadel, 2001] from PSII membranes extracted from spinach at pH 6. The pH has been chosen to avoid the contribution of a different rhombic iron signal appearing in EPR measurements above pH 7. On the other hand at a higher pH more Fe^{2+} is formed due to the higher midpoint potential of the iron couple (with $\tau_{1/2} \approx 20s$).

The marked bicarbonate $\nu(CO$ vibrations at 1530±10 cm^{-1} in the Fe^{2+} state and 1658±20 cm^{-1} in the Fe^{3+} state become only visible upon bicarbonate labeling. Upon iron oxidation a proton is reported to be released from the Q_B site. The band at 1094 cm^{-1} assigned to a deprotonated histidine might posses contributions from arginine or lysine $\nu(C-N)$ vibrations as well.

The brightly contoured bars are measured by [Takahashi et al., 2009] at pH 8 on core complexes from *T. elongatus*. Although bands around 1400 cm^{-1} are present in the aforementioned study, they are more pronounced in Nogouchi's data. He also labeled tyrosine globally. This caused unambiguous shifts of the 1257 cm^{-1} band as well as partially the 1229 cm^{-1}. Again it was found that proton movements accompany the redox transitions of the iron.

Non PSII bands

MES buffer

The pH dependent absorption of the buffer can be used to track protonation/deprotonation events during the reaction cycle, if no protonation takes place at the quinone site. This is the case when FeCy is added but not PPBQ. The difference spectrum of the MES buffer for pH 7.1 and pH 5 is shown in figure 3.11. An example how it is used in PSII can be found in [Noguchi, 2015].

Alternatively phosphate buffer can be used to detect proton release to the bulk at 1160 and 1090 cm^{-1} ([Berthomieu and Hienerwadel, 2001]).

Electron acceptor

The electron acceptor PPBQ absorbs in its neutral form with a strong band at 1670 cm^{-1} and weaker at 1590, 1330 and 1280 cm^{-1}. In its reduced and protonated form it absorbs with

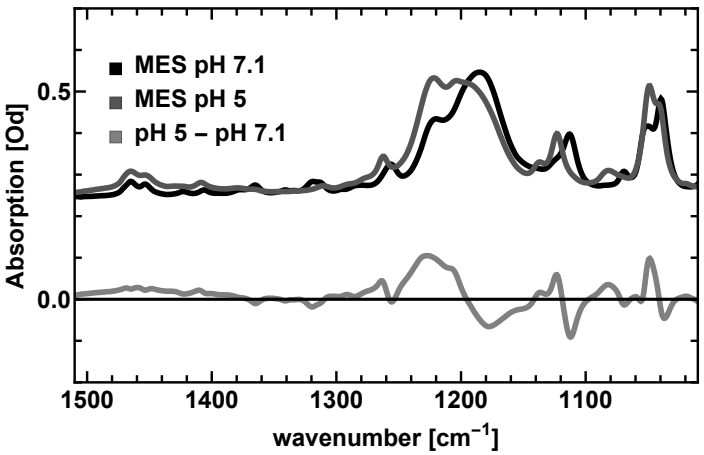

Figure 3.11: MES buffer pH difference spectrum measured at room temperature. The top traces show the absorption of a buffer solution only containing MES after a background subtraction of the water solvent and the CaF_2 windows. At the bottom the difference spectrum is shown. These peaks can be used to track the proton uptake and release of the solvent. The broad feature around 1450 cm^{-1} might stem from a not perfect water subtraction as the peak shape of the water bending modes is sensitive to the H-bond environment and spectrum of pure water has been subtracted.

strong bands at 1490 and 1170 cm^{-1} and weaker bands at 1330, 1290, 1230 and 1170 cm^{-1} (values from the NIST database for p-benzoquinone and 1,4-Benzenediol).

The electron acceptor/donor couple ferri- and ferrocyanide $\nu(CN)$ modes can be found at 2116 and 2038 cm^{-1} and used to track the reoxidation of the quinones as this band is well isolated [Noguchi, 2015].

Others

In the appendix (11.0.2) one can find the IR spectra of some buffer ingredients such as triton, β-dm, sucrose and betaine, well and water.

3.4 The difference spectra of altered amino acids close to the Mn cluster

The following tables of the changes of FTIR difference spectra of site directed mutation in PSII function as a guideline. One may find wavenumbers of interest for the own study, that are affected by the mutations. But the cause may be manyfold and I strongly suggest to double check the reported spectra and study the discussions in the respective publications. Underlined amino acids cause specific wavenumbers to disappear or alter and the authors assigned the bands to these residues.

Table 3.1: Overview of IR studies on PSII samples modified by site-directed mutagenesis close to the Mn cluster as in fig. 3.12. +,-: changes relative to WT. The oxygen activity [$\mu mol_{O_2}/mg_{Chl}h$] of WT samples of Debus is around 5000.

residue	inserted	activity, S-state cycling	position, bands [cm^{-1}]	reference
D1				
D61	A	20 % → S_3	fl1: 1747 -<-, 1664 ->>-, 1651 +>>+, 1634 0<<-, 1586 +>>0, 1543 -<-, 1509 >, →1513, 1364→1372, 1324-38 +>+ fl2: 1745 +>+, 1638 0>-, 1633 +>0, 1535, +>-, 1507 +>0, 1383 0>-, 1363 -<+, fl3: flat except 1514-, 1444-,1384+	(1)
D170	H	2800, full	ligates Mn4, Ca fl1: weak mod 1100-1200: His, 608 → 612 due to His; fl2-4: none	(2,3)
V185	N	→ S_3	fl1: 1746+,1677++,1629-,1587-,1416+, 1400+, 1364-, 1342-, 1260-, fl2: 1661-, 1549+, 1537-, 1509+, 1348+, 1325+, fl3,4: all weak	(5)
E189	Q, R (K)	3000-4000, cycles	ligates Mn1, backbone: H-bonded to breathing water; fl3: very weak mod 1340-1360, different for Q,R; R: 1509/44 mod	(6)
	D,N,H,G,S	0		(6)
	Q	70 %	fl1: 1678 -, 1506 -, upshift, 1435 → 1441, 1412 +, 1392 +, 623 +, 604 - (N shift?)	(7)
H332	*labeled*	full	ligates Mn1 fl1: 1113/1107; fl2: 1113/1103; fl4: part of 1109 *(see MES, 1099: His at Fe)*, 1180: Arg ?	(8)
E333	Q	1400, full	ligates Mn4, Mn3 fl1: $Y_Z^{\bullet ox}$ dominates: 1707 -,1697 +, 3663 gone fl2: weak mod 1510-1570, fl3,4: none	(9)
	ADNHCY	0		(9)
H337	*pol IR*	full	H-bond to O3, both Ns protonated through cycle, therefore no intensity at 1100, fl1 & 3: 2400-3000 minor peaks of His NH Fermi resonance coupled with overtones of imidazole	(10)
D342	N	1400-1800	ligates Mn1 & Mn2 fl1: 1730+, 1620+, 1587-, 1562+, 1530-, 1442→1434+, 1365-, 1220+; fl2: 1320-, 1254-, fl3: 1610-, 1522-, 1443→1437-, fl4: 1630+, 1605+	(11)
A344	G, S *labeled*	50 % 75%	ligates Mn2 and Ca S_1: 1356, S_2: 1339, 1320, restored in fl3	(12,13)
CP43				
E354	Q	20 % → S_3	ligates Mn2 & Mn3 fl1: 1525 0<+, 1502 +>+, 1431 +>+, 1394 ->-, influences A344 vibration & shifts 3588 water band, fl2: normal	(14)
E354	Q	20 % full	lacks CP43 extrinsic loop more differences to wt, fl1: 1754 0<+, 1665 -<+, 1528 0<+, 1466 0<+, 1394 ->-, fl2: 1397 ->-, fl3: 1542 +,-, 1412 +>-1383 +>0, 1346 0<+, fl4: very distinct	(15)
R357	*labeled*	full	vicinity of Mn4, protonated in S_1 & S_2 fl1 clear 1689+, 1682-, 1581 +, 1567-, others 1630-1675, none around 1180	(16)

From studies by (1) [Debus, 2014]; (2) [Chu et al., 2001]; (3) [Debus et al., 2005]; (5) [Kim et al., 2018]; (6) [Strickler et al., 2006]; (7) [Kimura et al., 2005a] ; (8) [Kimura et al., 2005b]; (9) [Service et al., 2013]; (10) [Nakamura and Noguchi, 2017]; (11) [Strickler et al., 2007]; (12) [Chu et al., 2004]; (13) [Strickler et al., 2005]; (14) [Shimada et al., 2009]; (15) [Service et al., 2011]; (16) [Shimada et al., 2011].

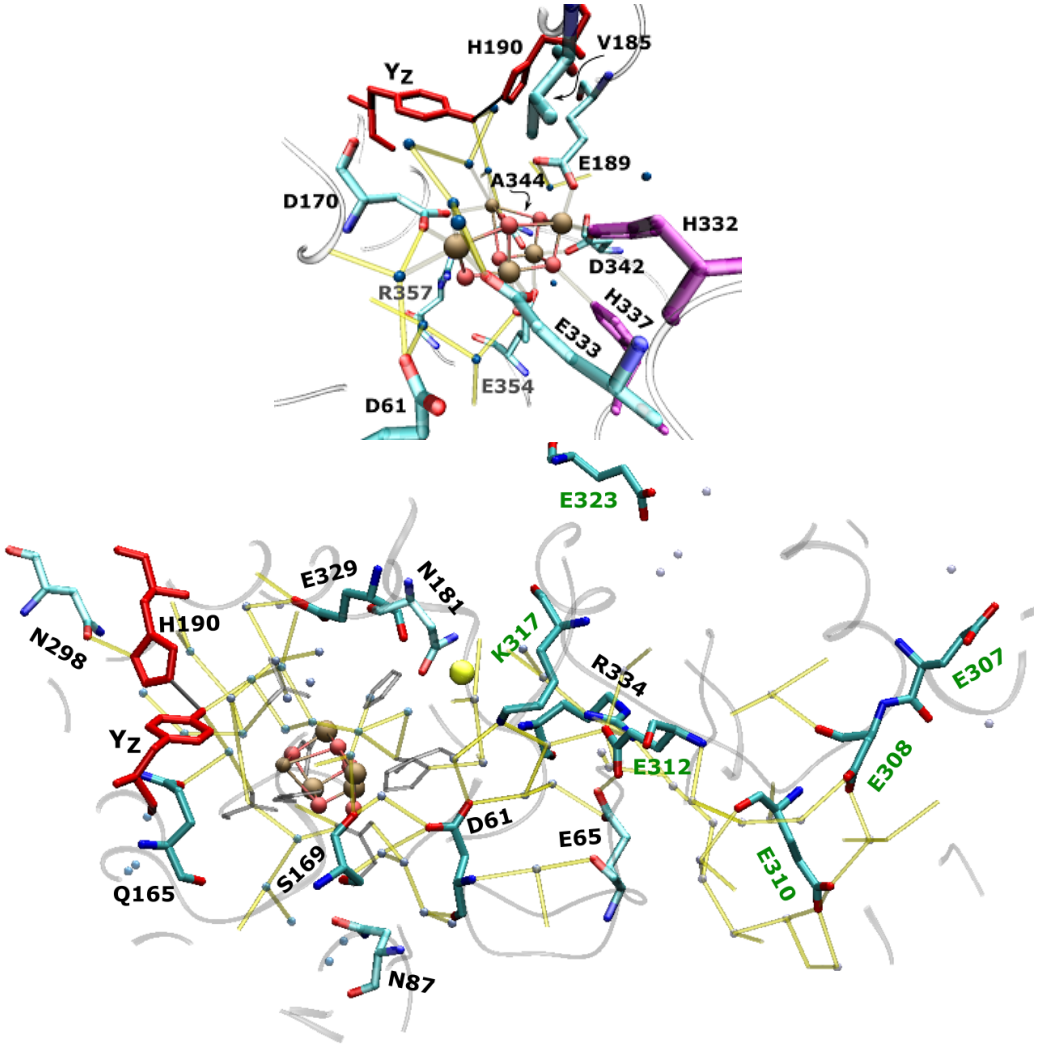

Figure 3.12: *top:* Amino acids altered close to the Mn cluster viewed from the close chloride position (tab. 3.1). *bottom:* Amino acids altered in the extended H-bonding region viewed from behind the close chloride position (tab. 3.2). Substituted amino acids are colored by element. The magenta histidines have been measured by polarization resolved and global His labeling. Y_Z and D1-His190 are only marked for orientation. Yellow bonds represent H-bonds to water molecules. Mn and Ca ligands are connected to the cluster by outlined bonds. Gray labeled amino acids belong to the CP43 protein. Green labeled amino acids belong to the D2 protein. *crystal 4UB6*

Table 3.2: Overview of IR studies on PSII samples modified by site-directed mutagenesis in the extended region around the Mn cluster as in fig. 3.12. Studied by: (1) [Service et al., 2010]; (2) [Banerjee et al., 2018b]; (3) [Nagao et al., 2017b]; 4) [Service et al., 2014a]; (5) [Pokhrel et al., 2015]; (6) [Nagao et al., 2017a]; (7) [Pokhrel et al., 2013]; (8) [Suzuki et al., 2013]. +,-: changes relative to WT. The oxygen activity of WT samples of Debus is around 5000 $\mu\text{mol}_{O_2}/\text{mg}_{Chl}\text{h}$.

residue	inserted	activity, S-state cycling	position, bands [cm^{-1}]	reference
D1				
E65	A	14 %	fl1: 1747 -<0, 1666+, 1625-, 1590+, 1552-, 1543+, 1462-, 1442-, 1399-, 1342-,1220-, fl2: 1745 0, 1697+, 1544+>-, 1506-<+, 1413+>-,1398-,1383 0,1342+, 1327+, fl3: 1747 0, 1695-<+, 1660+>-, 1588 0, 1565-, 1544-, 1509 0, 1447-<+, 1380-1420-, 1310-1350+	(1)
N87	D	850	narrow channel	(2)
		30% miss	fl1: 1670 +, 1684 +, strong on 1520-1590, weak COO^-_{sym} shift	
	A	2800 cycles	**as in spinach** 1670 ++, 1684 +, strong on 1520-1570, weak COO^-_{sym} shift, fl1: 1392 +	(2)
V157	H 72 %	P^+_{680} $Y^{\bullet ox}_Z$ $Y^{\bullet ox}_D$	close to P_{D_1} keto group reveals P_{D_2} 1699 cm^{-1} in P_{680} and 1708 cm^{-1} in P^+_{680}	(3)
Q165	E	35 %	fl1: 1689-, 1674++, 1629–, 1611-, 1566+, 1522+, 1493-, 1399→1394+, 1365-, 1340-, fl2: 1745+>0, 1706-, 1580-1650-, 1544-, 1344-, fl3: all weaker, 1530-1730-, fl4: 1720-1780+, 1608-1690- normal	(4)
S169	?			*unpub.*
N181	A (S)	35 %	fl1: 1706-, 1674+. 1586-, 1511+, 1416+, 1386+, 1322+, fl2: 1698+, amideI dif, 1543-, 1508+, 1362+, 1344-, 1257-, fl3: 1587+, 1544-, 1566+, 1529+, 1509+, 1443+, 1414-, 1320-1350+, fl4: amide I dif	(5)
N298	A	S_3- S_0 blocked	smaller 1544 and 1509	(6)
E329	Q	65 %	fl1: 1747 -<0, 1543+, 1342-, 1220-, fl2: 1745 +>0, 1696-, 1520-1560-, 1413-, fl3: 1747 0, amideI dif , fl4: 1745 0, amide I,II dif	(1)
R334	A	40 % → S_2	fl1: 1747 +, 1723-<+, 1716+, 1675+, 1610-<+, 1588-, 1543+, 1522-<+, 1509→1512, 1442+, 1399+,1365+>>+, fl2:1746 0, amideI,II dif, $\nu(COO)$weak	(4)
D2				
V156	H	80 % P^+_{680} & $Y^{\bullet ox}_Z$	close to P_{D_2} keto group reveals P_{D_1} 1703 cm^{-1} in P_{680} and 1726 cm^{-1} in P^+_{680}	(3)
E307	Q	80 %	minor changes: fl3: 1625-1650–, fl4: 1630-1670++	(4)
D308	N	60 %	minor change: fl2: 1670-1770+, 1500-1530+, 1327+, fl3: 1700-1750+, 1660-1690-, 1620-1660–, 1567-, 1509-, fl4: 1710+, 1649+	(4)
E310	Q	80 %	fl1: no dif, fl2: 170-1760+, 1633-, fl3: 1690-1760+, 1625-1665-, fl4: 1700-1760+, 1530-1670-	(4)
E312	A	27 %	fl1: 1747 -<0, 1729+, 1718+, amideI+, 1366-, 1342 0, 1260-, fl2: 1728+, 1706-, amideI dif, 1542-, 1510+, 1420-, 1383 0, 1363 0, 1310-1350+, fl3: v dif	(1)
K317	R	60 % full w Cl^-	less OEC assembled, fl1: 1362- high $Y^{\bullet ox}_Z$ signals fl2: 1575+, 1520-, 1399-¿1403, 1383+ fl3: 1631+ (R?)	(7)

	A,Q,E	60,30,30% full	A,Q,E:fl1 1586-, 1523+ also in Cl depletion, 1360- no signal after $S_1 \rightarrow S_2$ with 3 s spacing: S_3 instable because wo Cl^-, less OEC assembled	(7)
	R	100 %	fl1: 1699-, 1508-, 1399-¿1403, 1362-, fl2: 1575+ fl3: 1443+, very sensitive to hydration	(8)
E323	Q	50 %	fl1: 1690-1730+, 1588+, 1543-, 1509+, 1235-1305-, fl2: 1565-1760+, fl3: 1700-1760+, 1670-, 1655-, 1636-, 1607+, fl4: 1649-, 1544-, 1538-	(4)

4 PSII preparations and methods of fluorescence and infra red spectroscopy

4.1 PSII sample preparation

In this work I studied the quinone, P_{680}, Y_Z and Mn cluster dynamics of PSII membranes from spinach. PSII membranes are samples that exhibit a good oxygen evolving activity and high yield preparations with an intact environment including LHCs. The drawbacks are that they contain a certain amount of other proteins such as the Cyt b6f complex and even some PSI centers. Also some fraction of the PSII may be damaged by the detergent extraction. Because in literature thylakoid membranes are often assumed to be faster at the acceptor side I compared them with the PSII membranes.

Later I was able to compare the photocycle of the oxygen evolving complex of PSII membranes from spinach with the one of highly active, but less stable core complexes from the cyanobacterium *Synechocystis* sp. PCC6803. The fast growth rates, the ability to metabolize sugar (heterotroph with glucose) and easy genetic accessibility of these cyanobacteria allow the studies of point mutations. The one presented stems from the lab of Richard Debus from the University of California Riverside.

4.1.1 PSII membrane fragments and broken cloroplasts from spinach

PSII membrane particles and broken chloroplasts were extracted based on the protocol published in [Schiller and Dau, 2000], which in turn is a modification of the original work of **B**erthold, **B**abcock and **Y**ocum, giving this preparation the lab jargon BBY ([Berthold et al., 1981]). As the samples were prepared by myself (many together with Matthias Schönborn), a short summary shall be given below.

All buffers contain 15 mM NaCl, 5 (buffer B: 10) mM $MgCl_2$ and 5 mM $CaCl_2$ and are buffered with 25 mM MES at pH 6.2. Only buffer A is buffered with 25 mM HEPES at pH 7.5.

First the spinach needs to adapt to the dark on ice to allow tighter stacking of the grana regions ([Anderson et al., 2012]). After removing chloroplast poor regions of the leafs as stems, the leaves are ground in the presence of buffer A[1]. This buffer contains a high amount of the small protein bovine serum albumin (BSA) engaging the released proteases, also a high amount of ascorbate acting as an antioxidant and reducing agent, as well as a chelating agent and metallo protease inhibitor ethylenediaminetetraacetic acid (EDTA). The obtained particles are filtered trough a double layer of gauze bandage, followed by a filtration through a cheesecloth with a typical pore size of 22-25 μm^2. The filtrate is centrifuged for 10 minutes at 17000 g. The pellet is then resuspended in the osmotic buffer B containing 150 mM NaCl[3]

[1] 1 mM EDTA, 0.4 M saccharose and freshly added: 2g/l BSA and 1 g/l Na-ascorbate
[2] Miracloth, Merck
[3] buffer B contains no $CaCl_2$

in order to break the chloroplasts. The solution is centrifuged for 2 min at 1100 g and the obtained supernatant for 12 minutes at 50000 g.

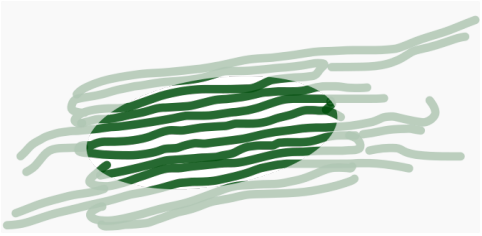

Figure 4.1: Illustration of a grana stack. These are interconnected on their outside via stroma lamellae, which mainly contain PSI and ATP synthase. Only the green area is not directly accessible by the detergent and will be part of the PSII membrane particles.

The obtained samples are called **broken chloroplasts** with the complete thylakoid membrane hosting all photosynthetic proteins of the light dependent reaction. Typically the stroma and lumen sides of the membrane are well separated allowing measurements with a pH gradient, but the membrane becomes leaky within hours.

To obtain **PSII membrane particles** the broken chloroplasts are dissolved in a mixture of buffer C and the detergent triton X-100. Detergents dissolve membranes and bind to proteins forming a detergent belt. When adding detergent to dark adapted thylakoid membranes of higher plants the easily accessible PSI and ATP synthase rich stroma lamellae will be attacked first leaving the the core of the grana stacks untouched (green rings of fig. 4.1). Thereby PSII and LHC rich PSII membranes with high protein to lipid ratios are obtained. The detergent to Chlorophyll ratio is set to 25 % (w/w)[4]. This solution is centrifuged for 2 minutes at 1100 g followed by about three washing steps in buffer D in order to remove remaining starch particles. The sample is stored at minus 80 °C in buffer D with 1 M betaine.

In this type of preparation on each monomer of PSII up to 100 Chlorophylls can be counted ([Wei et al., 2016]). Additionally some Cyt b_6f and a minor contribution of PSI of up to 25 % relative to PSII are present ([Danielsson et al., 2004]). The oxygen activity is in between 800 and 1200 $mmol_{O_2}/mg_{Chl}h$. An advantage of PSII membranes is their good activity, their high stability and the nearly natural lipid environment, a drawback that there is no defined stroma nor lumenal side, but one liquid phase. Measurements on proton motive forces, electric fields or pH effects separated for the donor and acceptor side are not possible. Also some PSII centers may be damaged by the detergent treatment.

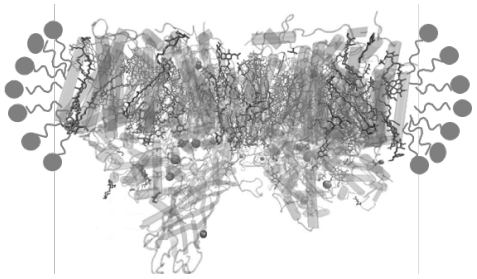

Figure 4.2: Simplified illustration of a PSII core complex in an detergent belt. The native lipid environment is dissolved, instead the detergent, here β-DM, forms a belt- like structure around the protein (crystal 4UB6).

4.1.2 Core-complexes from cyanobacteria

PSII core complexes (PSIIcc) are the pure dimeric photosystem II particles without any asociated antennas. Therefore they yield strong signals and very high oxygen avtivities. To purify samples a hexahistidine-tag (His-tag) consisting of six histidines is genetically attached to the C-terminus of the CP47 protein subunit. This allows

[4]Triton has a density of 1 g/ml, the molar mass of triton and chlorophyll are both in the order of 600-800 g/mol, expample: BBY378: $m_{Chl,thylakoid} = 400mg$, $m_{Trit} = 10g$,$m_{Chl,PSII} = 120mg$

a strong and highly selective binding to Nickel particles of an argarose gel. Most commonly PSIIcc are used as extracted in a detergent belt (here β-DM).

Single frequency IR measurements presented in this thesis have been done on PSIIcc extracted from *Synechocystis* sp. PCC 6803 supplied by Rick Debus of the University of California in Riverside. The preparation is described in [Chu et al., 2001]. The wild type (WT) samples had an oxygen activity of around 3000 $mmol_{O_2}/mg_{Chl}h$ and the D1-D61A mutants of only 500-700 $mmol_{O_2}/mg_{Chl}h$. This high activity (compared to PSII membranes) is payed off by lower stability and higher temperature sensitivity.

Growth of cyanobacteria in photobioreactors

In order to obtain PSIIcc that are also stable at room temperature and above, thermophilic cyanobacteria are cultivated. In our laboratory grows the species *Thermosynechoccocus elongatus*. These bacteria cannot metabolize sugar. Therefore, the introduction of point mutations that suppress oxygen evolution are not possible, yet.

To grow them and the many other types, four different scales of cultivation have been established. Starting from agarose plates, going over to small scale in flasks placed in illuminated shakers, over to medium size of 5 l up to the biggest commercial reactor of 35 l. The medium scale photobioreactors are home built devices. Matthias Schönborn and I designed and consttructed such a bioreactor based on similar ones in other laboratories (fig. 4.3).

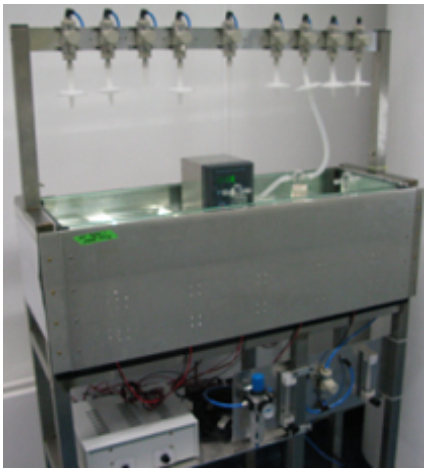

Figure 4.3: Photobioreactor as it has been constructed by Matthias Schönborn and myself. A thermostat placed centrally heats and steers the bath. The LED units are screwed onto an aluminium board at both sides. The board conducts the heat of the lights. The light controller can be seen at the lower left corner. Pressure, gas composition and flow rates can be controlled by the devices in the lower right corner. From there tubes go to the bat on top where the flow to each bottle is regulated by valves. Bottles are placed in a mule within the bath. The bottles and tubes are prepared in a clean bench and sealed with sterile filters.

The basic idea is to place conically ending flasks inside a temperate water bath. The culture is prevented from sedimentation by a gas flow to the the bottom of the flask. Two flow-meters set the desired mixture of air and CO_2. Dimmable LEDs illuminate the flasks from both sides (Matthias Schönborn). Cultures can grow very densely under well controlled conditions also allowing to compare the growth of different types of organisms at the same time. In order to harvest or measure the optical thickness of the culture, one needs to work on a clean bench. An improvement could be an extraction tube allowing to add or remove liquids in a sterile manner e. g. to determine the optical density of the culture or to do partial harvests.

4.2 Measurement buffers

PSII is embedded in the thylakoid membrane surrounding the thylakoid lumen. PSII, PSI and the cytochrome-b_6f create a pH gradient over the membrane. It is not a surprising observation that the donor and acceptor side evolved to perform best at the pH of the stroma (or for cyanobacteria: cytosol) and lumen, respectively. In PSII membranes and core complexes, the membrane is partially or fully dissolved and the pH of a buffer solution will be sensed at both sides of PSII. To measure a native-like behavior of the acceptor side, a pH of the buffer of about 7.5 should be set. Still one target of the acceptor side measurements is to extract the dynamics of the quinone reduction/oxidation kinetics at a pH of 6.2, which is used in measurements of the donor side. Water oxidation in intact membranes will take place in a more acidic pH range of 5.5 to 7 (pH values from [Antal et al., 2013]).

Typical chloroplast ion concentrations are: free Mg: 1-3 mM in the stroma (not chlorophyll Mg, [Portis, 1981]); Ca: 150 nM free, but 15 mM bound to the membrane in stroma, [Hochmal et al., 2015]), Na: 100-150 mM, K: 75-100 mM, Cl: 25-36 mM (dependent on the salinity of growth medium, [Demmig and Winter, 1986]).

Measurements on PSII particles are done in buffer D: 15 mM NaCl, 5 mM $MgCl_2$, 5 mM $CaCl_2$ and 25 mM MES buffer. The amount of IR absorbing betaine has been reduced from originally 1 M stepwise to 200 mM over 100 mM to 0 mM in order to decrease an excitation laser induced heat artefact, which is caused by a thermally induced shift of absorption bands (see section 5.3 and fig. 11.3 for details). The pH is set in most cases to 6.2. When set to an pH of 7.5 the MES was changed to 25 mM HEPES.

The measuring buffer of PSIIcc is $\text{buffer}_{\text{Debus}}$: 40 mM sucrose, 5 mM $CaCl_2$, 5 mM NaCl, 0.06 % (W/V) n-dodecyl β-D-maltoside and 10 mM MES buffer at pH 6.0. The buffer then has been filtered through 0.45 micron pores. The concentration of the salts are slightly lower than the PSII membrane buffer, because the original plan was to partially dry the sample, which would increase their concentration. In the presented measurements no water has been removed as a liquid sample was faster and easier to prepare and yielded good signals.

4.3 Electron acceptors

The natural electron acceptor in PSII is a plastoquinone molecule migrating in the membrane from PSII to the cytochrome-b_6f and back. Whereas in the intact chloroplasts and thylakoid membranes there are sufficient plastoquinones, in many preparations, such as the PSII membranes or especially PSII core complexes (no thylakoid membrane), the quinone pool size becomes limiting. In order to cycle the water oxidation reaction repeatedly by long flash sequences we need to add exogenous acceptors - which are often quinones as well.

PPBQ
If not otherwise noted, measurements on PSII membranes were done in the presence of **P**henyl-**p**-(1,4)-**b**enzo**q**uinone (PPBQ). PPBQ is dissolved in **dim**ethyl **s**ulf**o**xide[5] in a concentration of 700 mM. Per mg of chlorophyll 1 µl of the solution was added.

With an approximate molar mass of chlorophyll of 1000 g/ mol, we will have per mg_{Chl} one µmol of chlorophyll. There are 100-200 Chlorophylls per PSII (depending on the superstructure in the membrane), and thus about 5-10 nmol PSII per mg_{Chl}. For every mg_{Chl}, one µl of 700 mM PPBQ, i.e. 0.7 µmol, is added. This gives a ratio of PPBQ to PSII of about

[5] harmfull in high concentrations [Brünig, 2013]

70-140 to 1. One molecule of PPBQ can be reduced twice, just like the natural occurring plastoquinone. Therefore around 150 to 300 flashes can be given to each PSII.

In the single frequency setup a series of ten flashes is recorded (see 5.2.1). The amount of added electron acceptor **allows to record 15 up to 30 flash series**. To stay on the safe side and as other effects as drying or aging of the sample might lower the activity, typically only ten data sets were recorded on the same sample.

FERRICYANIDE

In PSIIcc the membrane has been dissolved and replaced with a detergent belt, thus quinones will most likely not be able to enter the PSII complex. Therefore hexacyanoferrate(III) or **fe**rri**cy**anide (FeCy), which does not need to bind to the Q_B site, was used.

The PSIIcc measurements of chapter 9.6 were prepared in the presence of 100 mM potassium FeCy dissolved in deionized water. On average about 2 µl of solution were added to 100 µg of chlorophyll. With only 35 chlorophylls per monomer of PSI,I we will have 30 nmol of PSII per mg_{Chl}. 100 μg_{Chl} results in 3 nmol PSII and we add around 200 nmol FeCy, resulting in 60 molecules FeCy per PSII. Each molecule of the electron acceptor can take up only one electron. This would allow for 60 flashes, not taking into account the possibility of electron donation from the reduced FeCy to higher S-states during dark adaption.

4.4 IR sample preparation

PSII MEMBRANES

Sample pellets are created by washing of the PSII membrane solution containing 1-2 mg/ml Chlorophyll in the described buffer and subsequent centrifugation with 50 000 g for 12 min. The obtained pellet was - when noted - mixed with exogenous electron acceptors and distributed between two CaF_2-windows covered with a peripheral ring of vacuum grease. The optical thickness in the FTIR experiments was adjusted to 1 Od at 1650 cm^{-1} by the use of a self-built, rotating step-motor controlled, compressed-air adjuster ([Süß, 2011]). The optical thickness around 1480 cm^{-1} is then about 0.25. The sample thickness in the single-frequency experiments were controlled by either 15 or 25 µm thick PTFE spacer-rings. One mg of chlorophyll was enough to load 2 or 1-1.5 sample plates, respectively. Their optical thickness at the measured wavenumber was compared with a neutral density filter of Od 1 and the subtraction of the absorption of the two windows. After the single frequency measurements IR-spectra were recorded on a spectrometer (see section 4.5).

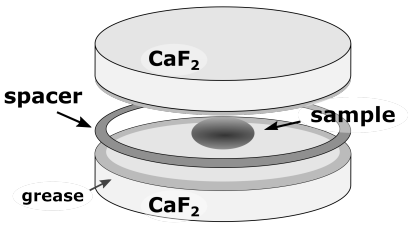

Figure 4.4: IR sample preparation. A PSII pellet or solution is sandwiched in between two CaF_2 windows greased at the periphery. A PTFE spacer of typically 15 or 25 µm thickness sets the distance between the windows.

CORE COMPLEXES

PSIIcc of the mesophilic *Synechocystis* sp. PCC 6803 are much more temperature sensitive than PSII membrane particles from spinach and therefore need to be cooled or on ice all the time.

The following protocol is based on the one used by Noguchi and was adapted by Richard Debus.

Care needs to be taken when modifying the buffer exchange protocol to a different method as this might induce changes in the FTIR difference spectrum. This has been shown by comparing samples exchanged by passage through a centrifugal gel filtration (method used *here*) and by repeated concentration-dilution cycles ([Strickler et al., 2006]).

Thawing the sample: Frozen samples should be aliquoted in correct volumes. The sample only needs some ten minutes to be ready to use. Richard Debus uses 100 µl of sample with a chlorophyll concentration of 1 mg/ml. This is sufficient for two CaF_2 disks and for the highly active wild type samples yielding amplitudes at 1478 cm^{-1} of around 0.5 mOd[6]. For the D1-D61A mutants, with only about one quarter of the activity, best results were obtained with 200 µl of sample.

Cleaning of the buffer exchange column: The two buffer exchange columns[7] are filled with a gel and buffer. After shaking the columns in order to resuspend the gel, the storage buffer is centrifuged out. The columns are then washed two times with 0.5 ml of water and five times with 0.5ml of the measurement buffer. Each centrifugation step is done at 800 rpm for 1 min (28 g)[8].

Buffer Exchange: Half of the sample amount is added per column. Richard Debus uses 50 µl for his experiments. One centrifugation step (1 min, 28 g) is done before 66 µl of buffer are added. This is repeated until no green traces are visible in the column anymore. For each step a fresh collection tube is used. The two greenest tubes are used in the next step. If three tubes are equally green the centrifugation speed needs to be adjusted in the next measurement, in order to reduce the volume for concentration.

Cleaning of the concentrator: The 0.5 ml concentrators[9] have a membrane retaining molekules larger than 100 kDa. This membrane needs to be wetted before use. Also some particles are on and need to be washed out by centrifuging 0.5 ml of water at 10 000 g for 10 min. After this step the concentrator needs to be inverted, as there is a minimum volume of around 15 µl always left, and centrifuged for 2 min.

Concentration: The sample of the two collection tubes (two times 132 µl) is added to one concentrator, counterbalanced and spinned at 14 000 g for 25 min in a cooled centrifuge (!, 4 °C).

Preparing and adding Electron acceptor: Meanwhile a fresh 100 mM ferricyanide water solution is mixed. Ten percent of the concentrated sample volume (if started at 100 μg_{Chl}) is added to the sample. Care needs to be taken that while adding no local high acceptor concentration is created temporally.

Sandwiching: In the original procedure for FTIR measurements the sample is pipetted onto a CaF_2 plate and dried under a stream of nitrogen gas. This reduces the water content and therefore the IR absorption, improving the signal to noise. In the single frequency measurements the power of the QCL is sufficient to pass through thicker samples. We decided to not dry the sample but just directly pipette 10-15 µl per CaF_2 plate with a 15 µm spacer enveloped in a thin ring of vacuum grease and seal it with a second plate. Care needs to be taken to avoid air bubbles trapped on the surface.

[6] oxygen activity $\approx 3000\, mmol/mg_{Chl}h$ During writing a sample with $\approx 3000\, mmol/mg_{Chl}h$ from Robert Burnaps lab measured by Sarah Mäusle yielded the same amplitude with half of the chlorophyll concentration

[7] Biorad P6 Tris buffer

[8] biorad states that 45° are suefficient, Richard Debus suggests to use 90° nonetheless

[9] Amicon Ultra 100k

4.5 UV/VIS and IR spectra of the samples

Visible absorption spectra

One important aspect of sample thickness is whether or not it is possible to excite the sample over the whole depth with saturating light. This is necessary to avoid desynchronization of the S-states.

In *figure 4.5* the absorption spectrum of visible light measured on a 25 µm thick sample is presented in black. The sample sandwich was placed directly in front of the detector to decrease the amount of scattering light. Otherwise no scattering background subtraction has been done to show the amount of light reaching the backside of the sample.

In the measurement the sample is excited at 532 nm in the so called green gap of the chlorophyll absorption spectrum. The absorption and scattering together give an absorption of roughly 0.5 Od, meaning only 30 % of the incoming light is reaching the backside of the sample. To excite the backside with saturating light, the front will receive three times the saturating intensity, thereby producing three times as much excitation laser induced heat as necessary (see section 5.3). Note, when for example red light was, where the optical thickness is about one, *10 times more* intensity would be necessary to saturate the back. A sample with 15 µm thickness has an absorption of around 0.3 Od – 50 % transmission – and will produce at the front only the double amount of the minimal heat signal.

It seems that we will have a trade-off of heat and photocycle signal. But we will see later that we can correct for the induced heat signals, and therefore a thick sample is desirable.

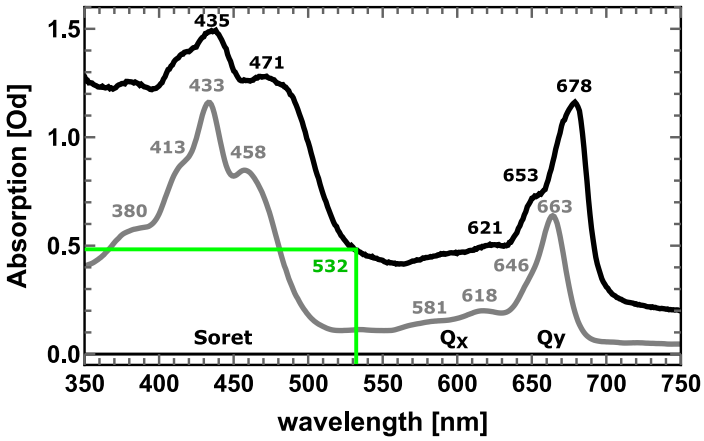

Figure 4.5: UV/VIS spectra of an IR sample created with a 25 µm spacer (*black*) and extracted chlorophyll in acetone-water (80/20 *gray*). The scattering background is not subtracted from the IR sample in order to show the amount of light reaching the backside of the sample. The peak shift between the samples is due to the solvent.

In the spectrum one can well identify the sorret band and the Q_X and Q_Y band of the chlorophyll molecules. PSII membranes contain PSII dimers and different light harvesting complexes. The pure PSII (usually) only contains chlorophyll a molecules whereas the LHCs contain both chlorophyll a and b in certain ratios. The exact ratio can be calculated when extracting them with aceton or methanol and using published extinction coefficients ([Wellburn, 1994], gray curve in fig. 4.5):

$$\begin{aligned} [Chl_A] = & \quad 12.21 * (Abs_{663} - 2.81 * Abs_{646}) * 0.25 \\ [Chl_B] = & \quad (20.12 * Abs_{646} - 5.03 * Abs_{663}) * 0.25 \end{aligned} \tag{4.1}$$

In our PSII membranes, usually a ratio of chlorophyll a to b of 2.5 is obtained. This agrees well with the value obtained for grana vesicles of 2.4 and much less with values reported for whole thylakoids around 3.1 ([Danielsson et al., 2004]).

Another abundant pigment species are the carotenoid molecules (11 β-carotenoids per PSII monomer [Umena et al., 2011], and 12 per LHCII-trimer [Wei et al., 2016]) absorbing up to 550-600 nm. As the amount of chlorophyll molecules outnumbers the carotenoids by far, the spectrum is dominated by chlorophyll absorption. The functions of carotenoids are light harvesting, excitation energy transfer and quenching of excess energy and of triplet states. To excite them as little as possible in the future, excitation should be tuned to a slightly elevated wavelength towards 560 nm.

Thickness series

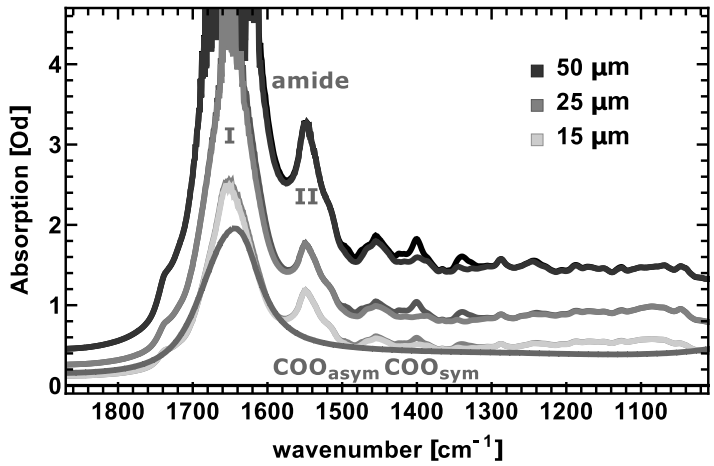

Figure 4.6: IR thickness series of concentrated PSII membrane pellets. The contribution to the absorption of the CaF_2 windows was subtracted. PTFE spacers of 15, 25 and 50 µm thickness set the distance of the windows. Betaine absorbs with strong bands at 1340 and 1400 cm^{-1}. This contribution can be subtracted. In darker colors 100 mM betaine are still present. For comparison a pure water spectrum is shown as well.

Figure 4.6 shows the infrared spectra of concentrated PSII membranes prepared with 15, 25 and 50 µm thick PTFE spacers as depicted in *figure 4.4*. In all traces the contribution of CaF_2, water vapor and CO_2 are removed. Plotted is the wavenumber region from 1000 to 1850 cm^{-1}. In this region the two main protein bands are the amide I around 1650 cm^{-1} overlapping with water vibration and the amide II peak around 1550 cm^{-1}. The strongest side chain vibrations include CO and COO^- symmetric and asymmetric stretching vibrations. Other weaker bands in this region are presented in *figure 3.2*.

For clarity, the slightly darker curves still contain the absorption of the 100 mM betaine. A zoom at the betaine absorption in PSII samples and the pure betaine spectrum extracted from buffer D with 1 M betaine is presented in the appendix (*fig. 11.6* and *11.5*).

When fitting the absorption thickness dependence at several wavenumbers, the simulated lines do not cross the coordinate origin but cross the absorption axis at a slightly higher value (*appendix fig. 11.7*). The crossing with the thickness axes happens in between -2 to -5 µm. These 2-5 µm are the slightly higher thickness of the samples due to the vacuum grease and not perfectly compressed sample. Besides this offset, the absorption increases linearly with the spacer thickness.

In the region from 1300 to 1650 cm^{-1} the absorption of the 50 µm sample stays above 1.5 Od. The 25 µm sample absorbs with an Od of 1 below 1500 cm^{-1} around 2 at 1550 cm^{-1} and around 4 at the amide I / water peak. The 15 µm sample absorbs with an Od of around 0.6 below 1500 cm^{-1}, around 1.2 at 1550 cm^{-1} and 2.5 at 1650 cm^{-1}.

A good measurement with the new setup can be achieved below an optical thickness of 2. This limit is given by the IR laser power close to the edges of the scanning range, e.g. at 1650 cm^{-1}. Below 1620 cm^{-1} the measurable maximal sample thickness is given by the combination of its absorption with the loss due to the optics in front of the detectors (*see section 5.1.1*). With a 15 or 25 µm spacer the optical thickness is in a good interval. Higher absorption will also increase the deposited heat by the IR beam. The presented measurements on PSII membranes therefore were done on samples prepared with a 15 or 25 µm spacer.

Even though the PSII membranes were concentrated by centrifugation, the relative protein absorption of the IR light is as low as 20, 50 and 15 % at 1650, 1550 and 1390 cm^{-1}.

IR spectra of cyanobacterial PSII core complexes, thylakoids and PSII membranes of spinach

In this small section I want to compare the absolute IR spectra of the three samples used in this thesis.

As the concentration of PSII and other proteins differs in all samples used, first the dominating water background needs to be subtracted. I have chosen to fit the pure liquid water spectrum to the protein solution in the region of the water association band around 2200 cm^{-1}. Here the proteins do not contribute. Because this band is a good marker band for the hydrogen bonding of the solution ([Giuffrida et al., 2017]), it needs to be clarified whether a fit of this band is a suitable approach.

The result of the subtraction for a solution of PSII membranes is compared with a vacuum dried sample of the same type (fig. 11.4). An example of the fit is presented in the appendix as well (fig. 11.8). The overall shape, intensity and position of bands is identical in both spectra including the ratio of amide I to II bands. A subtraction of the water band seems to deliver good results. However, the dried sample shows a broad residual absorption ranging from 1200 to 3000 cm^{-1} not following the water absorption. A possible explanation is a free proton or ion band involving protons or ions dissolved prior to drying and now weakly bound to amino acid residuals at the protein surface. Another possibility are water molecules bound tightly to the protein, which are not solvent accessible at all.

The spectra of PSII membranes and thylakoids from spinach as well as the core complexes from *Synechocystis* are presented in the upper part of figure 4.7. The traces represent the spectra in solution. Contributions of the CaF_2, water vapour, CO_2 gas, and buffer ingredients as betaine, triton, β-DM and sucrose have been removed (with the spectra presented in the

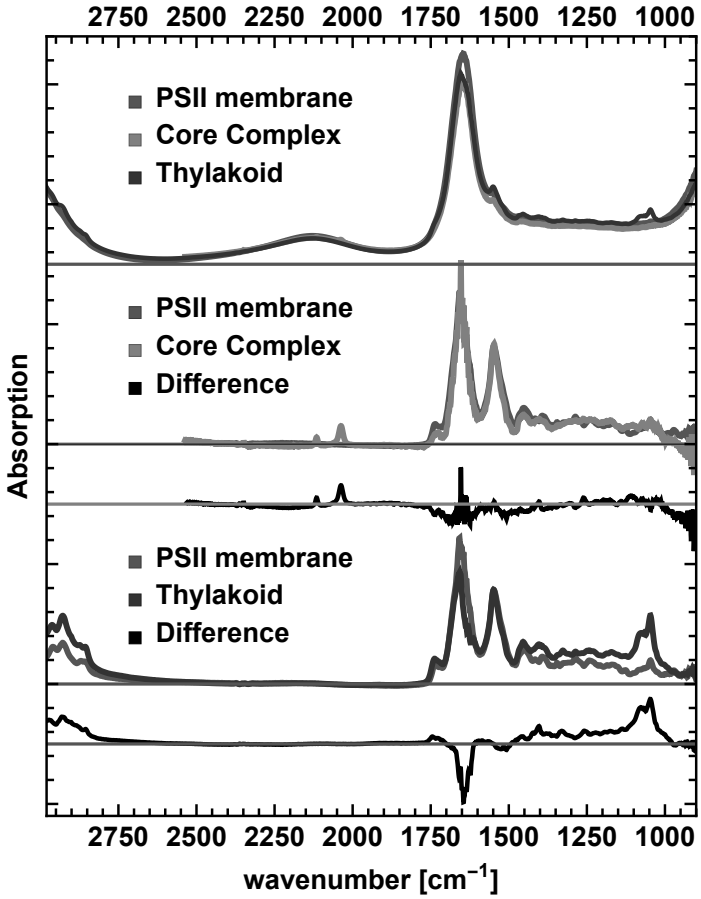

Figure 4.7: *top:* IR spectrum of PSII membranes compared with core complexes and thylakoid membranes. *center:* solvent subtracted PSII membranes compared to the core complex spectra no clear differences can be observed besides the ferri-/ferrocyanide absorption around 2116 and 2038 cm^{-1} in the core complex spectrum. *bottom:* the solvent subtracted thylakoid spectra differ strongly in the range where lipids absorb: at 2900 cm^{-1} the CH and around 1100 cm^{-1} the phosphor head group vibrations. Also the ratio of amide I to amide II absorption seems to differ indicating a different protein composition. However, this might stem as well from the water subtraction.

appendix). MES buffer has not been subtracted (25 mM in samples from spinach and 10 mM in core complexes). It absorbs strongest at 1200 cm^{-1}.

The spinach measurements were taken from aliquots containing $2\,mg_{Chl}/ml$ in buffer D (not concentrated – unlike fig. 4.6). The measurements of the core complexes were recorded after the measurements described in chapter 9 and contain $0.5\,mg_{Chl}/ml$. These were mixed with 2 µl of 100 mM FeCy solution. At these chlorophyll concentrations water vibrations dominate the entire range in the mid IR region. This explains directly why it is necessary to use concentrated or dried water-protein samples in order to use the complete dynamic range of an MCT-detector in an FTIR spectrometer.

The traces in the middle of figure 4.7 represent water solvent subtracted spectra of PSII membranes and core complexes scaled by a factor of 5.5 and 7.5, respectively. Below the

double difference is plotted. Within the error the spectra resemble one another, after the detergent and betain/sucrose is subtracted. Merely the ferri- and ferro-cyanide peaks at 2116 and 2038 cm^{-1} are present only in the core complex spectrum.

In the bottommost traces the PSII membranes and thylakoids are compared, scaled by a factor of 7.2 and 2.4, respectively. The main difference is the much higher intensity of the group of bands around 1100 and 3000 cm^{-1} in thylakoids. Both groups are also present in PSII membranes. The band position fits to phosphate groups at 1100 cm^{-1} and C-H stretches at high wavenumbers. Therefore, this difference seems to be due to the higher amount of phospholipids in thylakoids. The difference in the amide I / water region might be either due to an imperfect correction of the many substances or – and more likely – an inhomogeneous sample leading to non-linearities in the high absorption region at 1650 cm^{-1}. Still the band position in the symmetric carboxylate region differs to the PSII membranes. This favors the interpretation of a different protein composition (which is expected). Detailed analysis would be a thesis on its own and will not be undertaken here.

4.6 Variable chlorophyll a fluorescence

Variable chlorophyll is a standard tool in photosynthetic research. In this measurement, first a strong excitation flash is applied that initiates charge separation in all PSII. Then very weak probe flashes are given and their fluorescence measured. The fluorescence is high, but too fast to detect, when P_{680}^{+} is present. After a short time $Y_Z^{\bullet ox}$ and Q_A^- are formed, now the detected fluorescence stems is maximized (PSII closed). It will drop as soon as the electron is transferred to Q_B allowing another stable charge separation (PSII open).

Variable chlorophyll fluorescence were measured in 2 ml of buffer D solution with 10 µmol of chlorophyll at room temperature ($\approx 22°$). Measurements were conducted with a commercial fluorometer[10], but the 32 actinic flashes (1 Hz) were applied by a Nd:YAG laser[11] to avoid double excitation. Care has been taken that the measuring pulse-intensity of an orange LED is not influencing the observed dynamics by initiating charge separation.

The obtained curves (60 µs - 800 ms) were fitted by least square fits of a 3 exponential function including a constant. The rise of the signal was omitted by starting fitting at 110 µs. It reflects a combination of the rise-time of the set-up, and a quaternary amplitude dependence with a rise time for all flashes of about 30 µs. More details can be found in [Grabolle, 2005].

4.6.1 Non-linearity of Q_A^- oxidation due to inter-photosystem energy transfer

As closed PSII complexes can transfer the excitation energy to neighboring connected centers, the time dependent variable fluorescence F(t) is not linear anymore in the number of open states and thus of the amount of re-oxidized Q_A. Therefore,it needs to be corrected via (Paillotin 1976, Dau 1994, de Wijn and van Gorkom 2001):

$$[Q_A^-] = \frac{F(t) - F_0}{(1-p)(F_M - F_0) + p(F(t)(1 - F_0/F_M))}, \tag{4.2}$$

to obtain the amount of reduced quinones Q_A^-. F_0 is the fluorescence of dark-adapted samples, F_M the maximal fluorescence of each flash corresponding to all Q_A reduced, and p = 0.318 and

[10] PSI FL3000
[11] Continuum, Minilite I

0.7 the connectivity parameter for PSII and thylakoid membranes, respectively. The former has been obtained before by our group from a similar preparation and by measuring the DCMU fluorescence induction ([Grabolle, 2005]), the latter value has been assumed following [de Wijn and van Gorkom, 2001].

4.7 FTIR measurements

FTIR Steady-State measurements of the protein finger-print region (1050-1800 cm^{-1}) were recorded with a commercially available spectrometer[12] equipped with a home-built sample compartment ([Süß, 2011]). An xy-translation stage system automatically moves the samples alternately through the beam focus. In the measurements presented, 19 plates with a total of 620 spots in the desired optical thickness interval between 0.7 and 1.3 were averaged (chapter 7). A flash was applied about three hours before the measurement to synchronize the S-States of the Mn-cluster into the S_1-state. The long dark adaption time is needed to purge the sample compartment. Then a series of 12 flashes is conducted with 100 $\mu J/mm^2$. After each flash seven double sided interferograms are recorded with a bandwidth of 4 cm^{-1}, resulting in a flash-spacing of 900 ms. The Fourier transformation was performed with the use of a Norton-Beer window-function.

Measurements of this chapter were conducted on another commercially available spectrometer[13]. Also after each single frequency measurement I measured the thickness of the sample.

4.8 Data analysis

All data analysis was performed on Wolfram Mathematica. All visualizations of crystal structures were done with VMD. Schemes and drawings were made with Inkscape.

4.8.1 Deconvolution of the desynchronized photocycle signals

Not every absorbed photon advances the photocycle. The reasons for that are manifold and up to now not perfectly understood. A known fact is that the quantum efficiency is close to unity. This means that each photon in an open center does induce charge separation. Still per 100 charge separated events only about 90 will proceed to the next S-state (depending on pH etc.). One reason for these so called misses is the competing back reaction leading to recombination in form of fluorescence (delayed fluorescence), heat and partially damage - in conjunction with chlorophyll triplet state formation and reactive oxygen species ([Dau and Zaharieva, 2009]).

Therefore, if one wants to obtain the pure S-state transitions, one will need to deconvolve the measured data. In the scope of this thesis, a simple model was used assuming the same time-independent miss factor m in each S-state transition. This model will not be the most accurate one, but as only ten flash transitions are recorded per point in time, a more complicated model will have too many free parameters. The interested reader shall refer to [Pham and Messinger, 2016].

With the pre-flash and dark adaption protocol described in the next chapter, one will end up with all tyrosines Y_D in the oxidized state and an initial S-state distribution of

[12] Bruker, Vertex 70
[13] Bruker, Vertex 80V

$\mathbf{S}_{ini} = (1, 0, 0, 0)$ where the entries relate to S_1, S_2, S_3 and S_0. To obtain the population of states before the n^{th} flash, the transition matrix T needs to be operated $n-1$ times onto S_{ini}:

$$P_{n-1} = T^{n-1} \circ \mathbf{S}_{ini} \tag{4.3}$$

$$\text{with } T = \begin{pmatrix} m & 0 & 0 & 1-m \\ 1-m & m & 0 & 0 \\ 0 & 1-m & m & 0 \\ 0 & 0 & 1-m & m \end{pmatrix} \tag{4.4}$$

Table 4.1: Population of states in the dark and after up to ten flashes in the order: S_1, S_2, S_3 and S_0. A miss-factor of 10 % was used.

dark	flash 1	2	3	4	5	6	7	8	9	10
1	0.1	0.01	0.001	0.66	0.33	0.098	0.023	0.44	0.39	0.19
0	0.9	0.18	0.027	0.0036	0.59	0.35	0.12	0.033	0.39	0.39
0	0	0.81	0.24	0.049	0.0081	0.53	0.37	0.15	0.045	0.36
0	0	0	0.73	0.29	0.073	0.015	0.48	0.38	0.17	0.057

The resulting populations after each flash are listed in table 4.1 for a miss-factor $m = 10\,\%$. With the assumption that a signal is only contributing with $1-m$ i.e. the misses are silent (*see below: measurement matrix and time dependent misses*), the sum of signals after the n^{th} flash can be calculated by:

$$sim_{flash\,n} = M \circ P_{n-1} \circ \mathbf{t}. \tag{4.5}$$

Here, $\mathbf{t}$ is the transition vector containing the pure S-state transitions for each point in time: $t = (S_0 \rightarrow S_1, S_1 \rightarrow S_2, S_2 \rightarrow S_3, S_3 \rightarrow S_0)$ and M the measurement matrix:

$$M = \begin{pmatrix} 0 & 0 & 0 & 1-m \\ 1-m & 0 & 0 & 0 \\ 0 & 1-m & 0 & 0 \\ 0 & 0 & 1-m & 0 \end{pmatrix}. \tag{4.6}$$

The matrix M only scales up the pure signals. This is a valid description for the steady state signals, as not all centers proceed forward and give a signal. It is not possible to solve the problem with a simple matrix inversion. I therefore have minimized the following equation with respect to m, and the entries of $\mathbf{t}$:

$$\sum_{flash} (meas(t, flash) - sim_{flash\,n})^2, \tag{4.7}$$

where $meas(t, flash)$ is the recorded value for each flash at a certain point in time. The first flash data needs to be omitted. In this transition possibly Y_D and broken centers contribute (without a Mn cluster, with higher S-states blocked or no terminal electron acceptor).

The procedure was first applied to the steady state values and values averaged around 500 ns, 100 µs and 5 ms to obtain the different miss factors. This is necessary, because not all points in time especially in noisy data sets can be fitted well. Also data showing a weak flash dependent oscillation pattern can not be fitted. The obtained misses of a complete data set, consisting of several wavenumbers, were averaged excluding unrealistic values below 5 and above 15-20 %. With this average equation 4.7 was minimized for all points in time.

To judge whether or not a fit was working the transients of the $S_3 \rightarrow S_0$ and $S_0 \rightarrow S_1$ transition can be compared. Often the $S_3 \rightarrow S_0$ reverses changes occurring in the other transitions. So if the 1 to 5 ms kinetic component of this transition is removed from the $S_0 \rightarrow S_1$ transient the correction worked. Another hint gives the $S_1 \rightarrow S_2$, because the first flash has not been used. The pure signal should contain the main Mn oxidation characteristics also present in the first flash data.

The used model does not describe a full view onto the problem especially in time resolved spectroscopy. The method used in this thesis consists of some of the following shortages:

Initial population: Although two pre-flashes were applied to the sample, in between the measurements on one sample spot only dark adaption, and no synchronization flash, is performed. After ten flashes the S_0 population is as low as 6 % which can reduce $Y_D^{\bullet ox}$. This in turn will lead to higher misses than originally assumed.

Broken centers: PSIIs, that do not contain a functional Mn cluster, lack the terminal electron acceptor or centers in a stage of assembly or repair, are not considered in the model. Most of them likely create a charge separated state, which is stable until it recombines within ns, µs or ms, dependent on their nature. Transient states might become spectrally visible. These include states of the two quinones, pheophitin, the two redox active tyrosines, S-states and even here not at all considered states as the ones of cytochrome b559, which is is photoprotective during the assembly.

Measurement matrix: Whereas it is certain that in the steady state signals miss events will not contribute as signals (decay back to initial state – no signal), it is not sure how they manifest in time resolved measurements. One possibility is a recombination process resolvable within the time resolution of the experiment. The other option is that misses are silent. This is the case when either centers do not do charge separation or the recombination is faster than the time resolution. The measurement matrix M (equ. 4.6) assumes the latter.

Time dependent misses: Some miss events will be due to back reactions. This recombination will introduce higher misses only after certain steps, in which the forward and backward direction compete. Therefore, it is plausible that early points in time will show still a higher population of an advanced state then others. As an example let us consider that the rate limiting step in $S_3 \rightarrow S_0$ was the oxygen release from the cluster and most recombination would compete with this step. Then the transition to the S_4 state would happen in the centers populated in S_3 state. Then the miss matrix would only need to involve the $S_4 \rightarrow S_0$ transition.

Quinone state dependent misses: The population matrix obtained by the method above allows to fit a period of four flash dependent pattern. This also includes a period of two. With the pre-flash protocol (see sec. 5.2.1) only all S-states will be synchronized and we did not take into account the quinone states. 30-40 % of quinones Q_B were reported to be reduced in the dark under some conditions ([Pham and Messinger, 2016]). This will be described only inadequately with a population vector of 100/0/0/0 in the dark. To obtain the real quinone states a second transition matrix for the quinones needs to be implemented.

S-state dependent misses: In the model the 10 % of centers not proceeding forward in the reaction cycle are most likely not due to the just before mentioned impediments. They

rather will compete with the forward reactions in the most demanding steps. In models obtained before, a fit could be obtained with either S-state independent or dependent misses. The latter will materialize in high misses during the $S_2 \rightarrow S_3$ and $S_3 \rightarrow S_0$ transitions giving a slightly enhanced simulation quality.

Global simulations

All transients were fitted with a sum of multiple exponential functions and a constant:

$$f_{\bar{\nu}}(t) = \sum_i A(\bar{\nu})\, Exp[-t/\tau_i] + c. \tag{4.8}$$

The constant c gives the steady state value usually at 800 ms. The sum of all amplitudes and the constant yields the initial value at the start of the simulation. Whenever a different model was used, it is mentioned in the text.

To obtain shared decay constants for many wavenumbers, a global fit approach was used. The following equation was solved:

$$\mathbf{\Delta A}(t) = \begin{pmatrix} \Delta A_{\bar{\nu}1}(t) \\ \Delta A_{\bar{\nu}2}(t) \\ \vdots \end{pmatrix} = \begin{pmatrix} A(\bar{\nu}1,1) & A(\bar{\nu}1,2) & \dots \\ A(\bar{\nu}2,1) & A(\bar{\nu}2,2) & \dots \\ \vdots & \vdots & \ddots \end{pmatrix} \circ \begin{pmatrix} Exp[-t/\tau_1] \\ Exp[-t/\tau_2] \\ \vdots \end{pmatrix} + \begin{pmatrix} c_{\bar{\nu}1} \\ c_{\bar{\nu}2} \\ \vdots \end{pmatrix}. \tag{4.9}$$

This system of equation was implemented into the standard Mathematica fit routine by introducing an index for the wavenumber dimension n and writing the fit function $f_{\bar{\nu}}(t)$ as $f(n,t) = \delta(1-n) f_{\bar{\nu}n}(t)$.

All errors from the fit are the ones returned by Mathematica. These are usually small. Instead of a detailed statistical analysis of the fit quality, I will discuss the influence of one exponential more or less onto the residuals. Also influences of the measurement like the temperature stability, noise caused by the laser alignment[14], heat up of the sample and the excitation laser induced heat artefact will be discussed. These contributions outcompete the fit errors by far. Additionally I will rationalize my choice of the number of exponential functions by a comparison with reported dynamics from the literature.

Spectral simulations

In chapter 8.4 the time resolved spectrum is simulated with a sum of Lorenzian peaks:

$$L_i(\bar{\nu}) = \frac{A_i * b_i/2}{(\bar{\nu} - \bar{\nu}_i)^2 + (b_i/2)^2}. \tag{4.10}$$

A fit of gaussians yielded worse results. Each of the peaks was allowed to change in time with a number of amplitudes and exponential functions. The decay times were fixed with values obtained from the global simulations applied before. The number of exponential functions was chosen to their molecular origin. Two quinone peaks were allowed to change with kinetics mainly present at 1478 cm^{-1}. One peak was sufficient with the kinetics observed mainly at the clean 1398 cm^{-1} carboxylate band. A $Y_Z^{\bullet ox}$ peak was allowed to change with the same rates but without a fit constant, i.e. forced to decay or rise to zero. The remaining fast spectral changes were fitted with either one or two additional peaks only changing with the extracted P_{680}^+ kinetics.

[14] this noise is in some transients high enough that the best fit would follow it

5 Single Frequency IR setup

Matthias Schönborn has recorded time and flash resolved FTIR step scan difference spectra in the region from 1100 to 1800 cm^{-1} at 10 ° C and pH 6.2 of PSII membranes from spinach [Schönborn, 2017]. His decay associated spectra feature function related assignments of many transient bands. Unfortunately, such a measurement requires several months of continuous measurements and consumes more than 10 g of Chlorophyll. To allow efficient systematic studies of different organisms, modified Photosystems or environmental factors like pH or temperature on the IR bands an alternative approach is needed. . In the following chapter, a novel alternative experiment is described that employs a tunable continuous-wave Quantum-Cascade-Laser (QCL) for single-frequency IR (SFIR) detection of transients in the IR absorption of PSII induced by a series of visible nanosecond laser flashes (532 nm). The setups constituent components, along with the measurement protocol, data processing and some peculiarities are described. This is followed by the characterization and correction method of the rapidly produced excitation laser induced heat.

5.1 The setup

5.1.1 overview

Single frequency IR absorption transients have been recorded with a new self-built experiment schematically depicted in figure 5.1. The samples are placed in a 25 sample-holder fixed on a xy-translation-stage system and placed in a temperature controlled compartment (sec. 5.1.2). The motorized stage allows for automatic sample exchange. A ns-pulsed, frequency doubled Nd:YAG laser excites the samples (532 nm, sec. 5.1.3). Simultaneously, an energy meter (EM) records the pulse energy and a fast photodiode sets the zero time. An external cavity, cw quantum-cascade-laser (QCL) serves as the infrared probe (sec. 5.1.4). The tuning range of the two laser units inside the laser head ranges from 1300 to 1650 cm^{-1}. The whole setup is flushed with dry air[1].

The infrared signals are recorded by two electrically cooled MCT-detectors. The detectors are supplied with a built-in 10 MHz pre-amplifier. Their analog signal is transferred to a 4 channel A/D-converter. Signals are digitized with 65 M-samples/s at 16 bit resolution (sec. 5.1.6). In addition to the signal detector, QCL fluctuations are recorded with a reference detector for post processing (sec. 5.2.2).

Self written programs control the settings of the analog card, details of the measurements and the movement of the stages (sec. 11.0.1). The timing is controlled by a commercial pulse generator, that triggers the flash-lamps and Q-switch of the excitation laser as well as the start of the data recording ahead of the first flash (sec. 5.2.1).

Starting from the QCL the infrared beam first transits a wedged CaF_2 window *(1)*. The reflection is focused with a mirror *(2)* onto a gold coated diffuse reflector *(3)* placed just before the reference detector. The intensity of the reference beam is attenuated with the

[1] VSA2 from Puregas with up to 116 l/min at 6.9 bar. Equipped with: before 5 mum oil and 0.01μm water filters; and behind 1μm filter and pressure controller. Dewing point of -70 ° C equal to 0.003 g/m^3

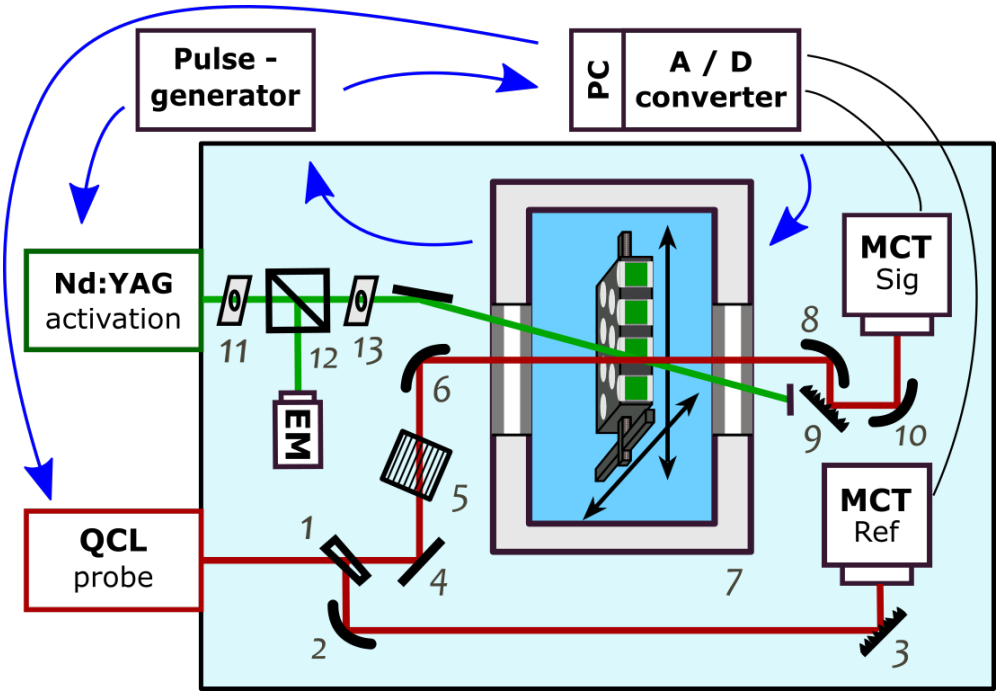

Figure 5.1: Setup of the single frequency experiment:
External cavity, **cw Quantum Cascade probe laser** (QCL).
1) Beam split by wedged CaF_2 window into reference and signal path.
Reference path: via 2) concave gold coated mirror (f=200mm), 3) gold coated polished diffusive reflector with 220 grit (50 µm) to
10 MHz MCT **reference detector** with LWP-filter (cut-on 4.5 µm).
Signal path: via 4), 5), 6) gold mirror, holographic wire grid polarization filter (attenuator, 150-300:1), off-axis parabolic gold mirror (f=200mm)
7) through tempered **sample compartment** equipped with an x/y translation stage of 150 mm travel with a sample board for 25 CaF_2 sandwiches attached,
8), 9), 10) focused by off-axis parabolic gold mirror (f=100mm) onto a gold coated polished diffusive reflector with 220 grit (50 µm), collected and refocused by two off-axis parabolic gold mirrors (2" and 1" f=50 mm) onto the
10 MHz MCT **signal detector** with LWP-filter (cut-on 4.5 µm).
A/D conversion card (16 bit, 65 MS/s) hosted in PC.
A **pulse generator** controls the timing of the measurement (trigger events depicted by arrows).
Frequency doubled, **ns-pulsed Nd:YAG excitation laser**:
11), 12), 13) Two irises and a 50/50 beam-splitter to cut out the desired area of the beam.
Pulse energies are recorded with an **energy-meter** (EM). A 15 ns rise-time photodiode measures t_0.

distance between detector and diffuse reflector. The transmitted beam (*4*) is attenuated with a rotatable wired grid polarization filter (*5*) and is focused (*6*) to a point just behind the samples to a beam width of approximately 0.3 mm (*7*). As with the reference path, the signal beam in focused onto a gold coated diffusive reflector (*8,9*). However, as the the detector can not be placed close enough to the reflector to collect enough light, the scattered light is collected with a 2" focusing mirror (*10*) and re-focused with a second mirror onto the signal detector.

This diffusing and re-focusing treatment results in high losses - attenuation by a factor of about 40. Nevertheless a spatial averaging is achieved, which is needed to correct for beam inhomogeneity, wavenumber dependent deflection and 2nd order reflections at the polarizing filter[2].

5.1.2 Sample compartment

Housing

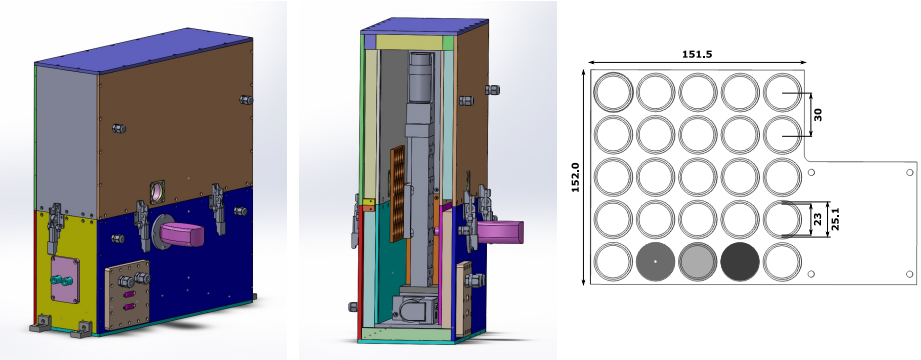

Figure 5.2: *left and middle:* Temperature controlled sample compartment. A double layer aluminum wall is filled with insulating material. In the center the two motorized translation stages are shown. Electric supply is provided through a flange (gray plate in the bottom left of the left figure). Optical access is located in the center of the lid. Peltier cooling elements are mounted on the front and back. The cooling tube fixation is visible on the yellow board in the left image. A thermo- and hygrometer is attached below the window. *(Images and final technical drawing made by Michael Kregielski of the institute's workshop.) right:* sketch of the sample board. Up to 25 windows can be loaded and fixed by a retaining ring. In the lower row an iris, a CaF_2 window and an Od1 filter are installed. *(Final technical drawing made by Andre Merli of the institute's workshop.)*

The housing of the sample compartment (fig. 5.2) consists of a double layer of anodized aluminum filled with heat and water vapor insulating material (armaflex: composition rubber). As with the complete setup the compartment is flushed with dry air. Air tubing and the electric supply enter via feedthroughs. Stage communication cables connect to two sub-D15 connectors fixed on a flange (gray square on blue wall). Inside, cables connect their counterpart to the stages with a flexible wire.

The dimensions of the box are optimized to reduce the total volume necessary to cool and dry, while the complete complete travel of the stages can be used. The top half of the

[2]due to back reflections a perpendicular alignment is harmful for the QCL without an optical insulator

compartment is removable allowing quick and easy exchange of the samples. Coupling of the laser beams is achieved via two ports enclosed by two 35 mm CaF_2 windows with about 3 cm of air in between. To keep the level of moisture constant this intermediate space is filled with silica gel.

Peltier-based Cooling

Two peltier elements are placed on the yellow wall in figure 5.2 on both sides of the compartment to cool the interior. The elements[3] have a maximal heat power of 31.4 W and electrical power consumption of 54 W (6.5A, 8.3 V) matching the maximal electrical power of the peltier controller[4] of 100 W. Two 20x20 mm^2 heat sinks are glued to the inside walls. The stream of dry air purging the compartment is directed directly onto them to foster heat exchange. Peltier elements are water cooled using an aquarium pump and external heat sinks.

The temperature inside the chamber can be measured with a combined thermo- and hygrometer placed just below the optical windows (pink in fig. 5.2). A PT100 giving feedback to the peltier controller is placed at the same height on the opposite wall. Both elements are like the samples thermally isolated from the outer walls. To test the cooling a third PT100 has been placed directly on the sample board. Relative to the air in the compartment the delay of the sample board reaching the set-point is around half an hour. In total the compartment can be cooled down to 5 °C and heated up to 35 °C, with the extremes reached in about four hours. Due to weak thermal contact the accuracy is approximately ±1 °C.

Linear Stages and sample holder

The sample holder is positioned using two 150mm travel linear stages.[5]. The DC motor driven stages have a maximum speed of 50 mm/s, with a step size of 0.25 and repeatability of 0.5. Limit switches hinder the stage from striking the housing and a reference detector in the center allows for calibration.

A **sample holder** (see fig. 5.2 *right*, samples in sec. 4.4) is screwed onto the stages allowing the fixation and compression of the samples by threaded rings. The thread is an M27 fine thread with a slope of 0.5 mm allowing a change of thickness by 125 µm per quarter of a turn. This allows to compress the PTFE-spacer and sample homogeneously and ensures a good seal with the vacuum grease.

In total there are 25 sample positions with a 25 mm diameter each. One of them is filled with a 0.5 mm pinhole, one with a CaF_2 window and one with a neutral density filter of OD1. Usual measurements require only 3 plates for strong signals and 12 plates for weak signals. Due to their limited stability PSIIcc have always been measured on two plates per day.

The diameter of the IR probe beam is around 0.3 mm at the sample. Because the entity of sample shall be excited, the diameter of the green excitation laser must be larger and is set to 1.2 mm. The **measurement spot** distance can be selected and is typically chosen between 2 and 2.5 mm. In total this gives around 30 points per sample-sandwich (only 20 mm in use).

[3] QC-71-1.4-6.0
[4] Peltron PRG-RS-H-100
[5] Physical Instruments: M-404-6PD and C-843 controller

5.1.3 Pulsed green excitation laser: Nd:YAG laser

We excite the samples with strong green laser light in the absorption gap of chlorophyll (see sec. 4.5). Therefore, saturating excitation light can penetrate through the whole sample and thus advance the photo cycle synchronously with a minimal heat artefact.

In this work, a frequency doubled Nd:YAG laser[6] functions as an excitation laser. The output of the fundamental at 1064 nm and the frequency doubled beam are internally separated. The flash-lamps of the laser need to be driven with 10 Hz for stable performance and smallest beam divergence [7]. In this mode the pulse energy has a stability of $\pm 10\,\%$ with a maximum pulse energy at 532 nm of 150 mJ and 5 to 7 ns pulse length. The short pulses ensure no double excitation of PSII. The energy can be controlled by either a built-in wave-plate and polarizer or by modulating the delay between the flash-lamps and the Q-switch trigger with the pulse-generator (see section 5.2.1).

Due to damage to the Nd:YAG rods laser, the quality of the beam profile has deteriorated over time. A 2 mm pinhole was installed to select a section of the beam unaffected by the damage.

The energy after a polarization independent 50/50 beam-splitter is measured with a pyro-electric sensor[8]. It has a resolution of 100 nJ and ranges from 10 µJ to 150 mJ. The damage threshold is given by 150 mJ/cm^2 for 1 µs pulses. With a diameter of 11 mm, a pulse duration of 10 ns and the approximation $E_{damage} = E_{spec} \cdot \sqrt{\tau_{pulse}/\tau_{spec}}$ this gives 14.3 mJ. A concave lens is placed in front of the sensor head to avoid the damage threshold. The beam area after the first pinhole is $3\,mm^2$ giving an intensity of $I = E_{pulse}[mJ]/3\,mm^2$. The intensity needed to record the laser induced heat signal is on the order of $1\,mJ/mm^2$ (see sec. 5.2.3).

5.1.4 IR probe laser: Quantum Cascade Laser

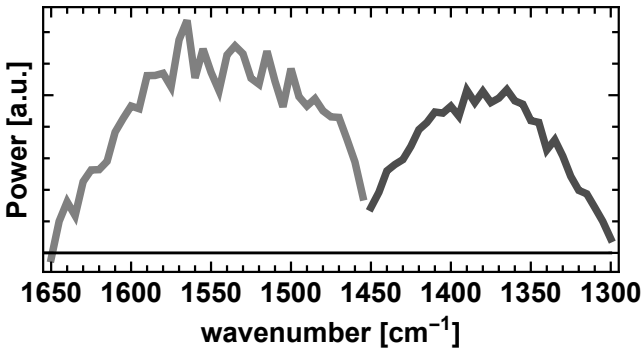

Figure 5.3: The spectrum of the two QCL diodes in CW operation. The maximal power value of the higher wavenumber laser is specified as 300 mW.

CW Quantum Cascade Lasers are still quite a new technology in science. The infrared active transition occurs within the conduction band of a layered semiconductor composition. There are a couple of suppliers for CW QCLs but most only offer very narrow spectral tuneability in sharp contrast to pulsed QCLs. We have decided to use a MIRcat external

[6] Inlite II from Continuum, now Amplitude Technologies
[7] This is a special setup for us - usually the factory setting is at 20 Hz.
[8] Thorlabs ES111C

Table 5.1: Specifications of the QCL MIRcat provided by Daylight Solutions

linewidth	$< 0.003\,cm^{-1}$
pointing stability	$< 1mrad$
beam profile	elliptical gaussian, non-astigmatic
divergency	$< 5\ mrad$
absolute accuracy	$\pm 0.5\,cm^{-1}$
tuning steps	$0.5\,cm^{-1}$
polarization	100:1, vertically

cavity QCL from Daylight Solutions, offering the possibility to host up to four laser diodes in one laser head, each of them tuneable over about 150 cm^{-1}.

The MIRcat QCL is tunable from 1300 to 1650 cm^{-1} (spectrum in fig. 5.3) with two distinct emission spectra stemming from the separate cavities. The overlapping sections default to the stronger of the two lasers. Cooling in the cw mode is done by a recirculating cooler[9]. The most important specifications given by the supplier are summarized in table 5.1.

The laser can be operated in four different modes:

1. Manual wavenumber selection
   Used in measurements without a wavenumber change.
2. Sweep Mode
   The sweep velocity can be set in cm^{-1}/s and the laser starts sweeping continuously.
3. Step and Measure
   In a specified spectral range the laser changes upon triggering the wavenumber by a specified step. *Used in the pre-measurements of the laser induced heat artefact spectra and the measurements of corroles.*
4. Multi-Spectral Mode
   The user can enter a list of desired wavenumbers, which tare selected upon triggering in ascending or descending order. *Used in most measurements with different wavenumbers on PSII.*

The laser electronics have been modified in order to improve the CW operation but making a stable pulsed operation impossible[10] Remaining sharp spikes (<14 ns, spaced with 800 kHz) are well suppressed by the use of the reference detector. On the order of seconds the laser is rather stable with only small drifts correctable by the reference detector signals as well. Rarely at some instable combinations of current and wavenumber it tends to show a sharp jump in the output power, possibly mode hops. Periodic oscillations are present of approximately 10 kHz. These are of opposite phase at different edges of the beam. The cause of these could not be identified in the optics of the setup so far, but are reduced by averaging spacially using the gold diffusive reflectors.

[9] Julabo F250

[10] The modulated temperature control current feedbacks into the laser current electronics. After revision by the company this is mostly gone.

5.1.5 Influence of laser polarization

Unlike the IR beam of an FTIR spectrometer the laser beam is polarized. Since the excitation laser is also polarized, one needs to consider possible polarization effects. There are *two different cases*:

First, if the pulse length of the probe is shorter than it takes for an excited molecule or its carrying protein to rotate, excitation and probing will couple (see [Linke et al., 2008]).

Unlike other photo-activated proteins, a PSII core complex contains about 35 chlorophylls, each capable of inducing photochemistry. Thereforee, the internal distribution of chlorophyll inside the protein complex is crucial. Because we are exciting on the red shoulder of the soret band(x and y absorption overlapping), only the distribution of the inner ring's normal vector is analyzed. These normal vectors are visualized in figure 5.4. Chlorophylls with normal vectors lying inside the membrane plane (mesh) are colored pink and green, and the ones perpendicular – with the ring inside the membrane plane – blue. The sum of all contributions is plotted in each direction as the length of the corresponding base. In the left picture the pink and green axes are of the same length. In the right picture one can see that the blue summation vector is shorter than the green one, meaning less chlorophyll rings are oriented parallel to the membrane plane (ratio of green:pink:blue 0.93:1:0.61). This near-homogeneous distribution of chlorophylls will render a polarization selective absorption negligible. However, this means that also photo-selective probing is not possible in PSII. Not taken into account is the distribution of the twelve carotenoids. On a first glance their orientation is also uniformly distributed..

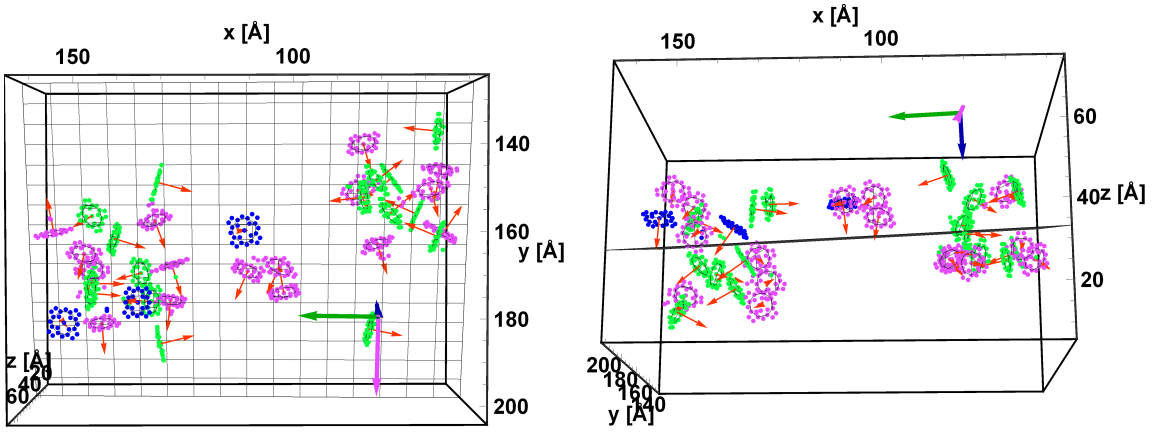

Figure 5.4: Chlorophyll orientation in a PSII monomer. *left:* yx plane *right:* xz plane. Chlorophyll molecules are colored in accordance to the orientation of the inner ring's normal vector. The length of the three base vectors represents the sum of all vectors. The ratio of green:pink:blue is 0.93:1:0.61. Coordinates from the room temperature crystal 5KAF.

Second, if the absorbing molecule is fixed in its position inside a repeating geometry, as it is the case for proteins inside aligned membrane layers, the polarized probe beam senses the alignment.

Because the membrane and detergent surfaces are hydrophilic, while the surface of the CaF_2 plates are hydrophobic, the alignment along the surface will be determined by the strength of membrane-membrane and membrane-detergent interactions. Upon partial dehydration PSII membranes are expected to form grana like stacking. When compressing

the samples, the membranes will most likely align parallel to the windows. The orientation of PSII inside the membrane is not well ordered, only differences outside the membrane plane can be visible. The QCL beam polarization is perpendicular to the window plane, lying parallel to the possible orientation of the membranes. Therefore, it might be possible that transition dipole moments perpendicular to the membrane are weakened. Because here concentrated pellets (not dehydrated) are used, in which the membrane orientation is less uniform relative to the IR polarization, only a small effect is expected.

However, this has been applied successfully by Noguchi to study partially dried PSII membranes in an ATR-setup ([Nakamura and Noguchi, 2017]). A strong polarization effect was found in the symmetric carboxylate region, when shining in light under 45°e.g. the band at 1400 cm^{-1} in $S_1 \rightarrow S_2$ decreased by a factor of three by rotating the polarization by 90°.

To summarize, assuming the above considerations are correct, no strong polarization effects should be present in our measurements. This is confirmed by the high similarity to the Step Scan data (compared in section 6). Still it might be possible that the PSII membranes are partially aligned in both experiments, then only the vibrations with a transition dipole moment perpendicular to the membrane may be weakened (in both experiments). So far no polarization resolved test measurements have been performed with this new setup. Nonetheless an experiment can and should be designed to exploit this accessible wealth of additional information.

5.1.6 Detection and analog to digital conversion

The two **detectors** in use are optically immersed photovoltaic **M**ercury-**C**admium-**T**elluride detectors[11]. A wedged BaF_2 window closes the detector. The detectors are optimized for a wavelength region from 3.5 to 8 µm, corresponding to 1250-2800 cm^{-1}. A four-stage peltier system cools the 1x1 mm detector element to 195 K (liquid nitrogen is obsolete). Although the unit itself has a rise-time of only 8 ns, a preamplifier module with a heatsink is built in limiting the frequencies from DC up to 10 MHz.

The damage threshold of the detector elements is 2.5 W/cm^2 whereas the QCL, without any focusing, can deliver around 6 W/cm^2 (300 mW, beam diameter of 2.5 mm). The output voltage scales linearly up to 1 V for 50 Ω or up to 2 V for higher impedance. The detectivity of the unit is $4.05 * 10^{10}\,cm\sqrt{Hz}/W$, the voltage responsitivity about 43 V/mW. At signals below 200 mV the noise of the detector can dominate.

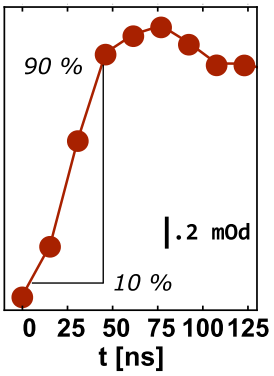

Figure 5.5: Rise of the signal at 1478 cm^{-1}. The 10 to 90 % rise time is approximately 40 ns given by the 10 MHz of the signal?s preamplifier.

An 16 bit, 4 channel **A/D card**[12] converts the analogue signal with a sampling rate of 65 MS/s and has an onboard memory of 2 GSamples. Possible input ranges can be set to ± 0.5, 1, 2.5 or 5 V, a choice made based on the reduction of intrinsic noise. It is protected against over voltage with 2 Vrms for settings of ≤ 1V or 5 Vrms otherwise. The relative input stage delay is specified as 0 ns. Data transfer to the PC is realized by a PCI express x8 generation 2 line, allowing a maximum transfer rate of 4 GByte/s. The card is used in the "FIFO" mode: Here the data is continuously recorded and transferred to the PC in chunks.

[11] VIGO: PVI-4TE-8-1x1 with MIPDC-10 preamplifier module
[12] Spectrum: M4i.44.11-exp

The **signal rise-time** is mainly limited by the preamplifiers of the detectors. The sampling of the rise by the A/D conversion is with a factor of 6.5 well oversampled concerning sampling theorem. In figure 5.5 a PSII signal at 1478 cm^{-1} recorded with 65 MS/s, corresponding to 15 ns spacing, is shown. The 10 to 90 % rise is reached within about 40 ns which is expected for 10 MHz (35 ns assuming a single exponential rise).

5.2 The measurements

Here only the general data recording and analysis procedure is presented. A more detailed look on the measurements presented in the results section will be given in each chapter.

5.2.1 Timing of the setup and pulse sequence protocol

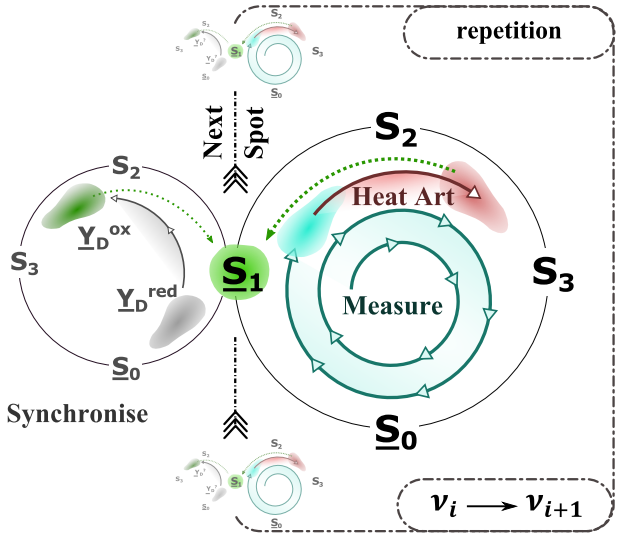

Figure 5.6: Measurement protocol scheme. Cloudy areas represent a distribution of states and underlined states are dark stable. Solid arrows represent flash induced advancement, dotted arrows recombination during dark adaption. *Left cycle:* The S-states of the Mn-cluster as well as the Y_D states are synchronized at each spot by two pre-flashes and a dark adaption time of at least 30 min to the S_1 state. *right cycle:* A series of nine flashes are applied to cycle twice through the photocycle (10 % misses) followed immediately by one flash of higher energy to enable the extraction of the excitation induced heat artefact. This process is repeated for every sample spot. Finally, the next repetition starts or the wavenumber is changed and the measurements repeats all over again.

In this section the pulse and trigger protocol used in the final measurements is described in detail. After the alignment and loading the samples, **two pre-flashes** with saturating intensities are applied to each sample spot (see figure 5.6 *left cycle*). This drives the Mn-cluster out of the dark stable S_0 and S_1 states, present in a ratio of about 1:3 (gray cloud in cycle). The final distribution of states is a mixture of the states S_1, S_2 and S_3 with either Y_D oxidized or reduced (green cloud in the left circle). These states will recombine

back to the dark stable S_1 state within about half an hour (depicted as a green arrow)[13]. The electron source can be either a reduced quinone or electron acceptor or the reduced Y_D forming eventually $Y_D^{\bullet ox}$ in all states. As PSIIcc particles are not stable, only two samples are measured at once to decrease the total duration of the measurements. This still results in a sufficient dark adaption time of 30 min.

In the **measurement** (*right cycle* of fig. 5.6) a series of 10 saturating flashes with a repetition rate of 1 Hz is recorded. These advance the S-state from S_1 to a mixture of 19 % of S_1, 39 % of S_2, 36 % of S_3 and 6 % of S_0 (assuming 10 % of miss events, see chapter 4.8.1). While all other spots are measured the higher S-states can decay back to the S_1 state (dotted green arrow). The S_0 state donates an electron to $Y_D^{\bullet ox}$. Before a new round of measurements is initiated the wavenumber can be changed (black dashed rectangular in figure). Per spot not more than ten flash series have been measured. Such a set of measurements takes about 8-30 hours depending on the amount of samples.

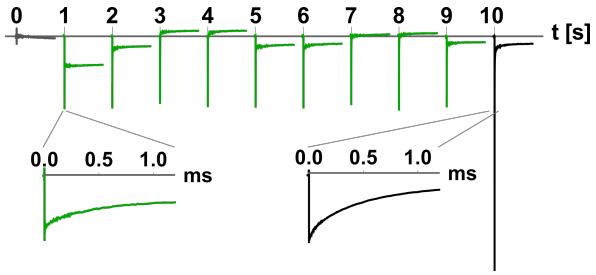

Figure 5.7: Flash series as measured at 1544 cm^{-1} with a flash spacing of 1 s and one dark measurement. The 10 ms before each flash are plotted at zero. The lower transients are a zoom into the first ms of the first and tenth flash. The latter measured at 5.25 times the energy of the former.

In order to record the excitation induced heat artefact under the same conditions as the measurements, 9 of the applied flashes were given with saturating intensities, while the 10th flash was recorded with a multiple of the excitation energy (3-5 x). Figure 5.7 shows how such a measurement looks like. The first transient is measured without excitation flash and serves as an noise estimate and identifies any slow drift. Initially, the signal to noise is low because no logarithmic averaging has been performed.

After the dark measurement the nine green transients represent the S-state transitions of the photocycle. The quaternary oscillation expected at this band is clearly visible in the transients. The tenth flash is plotted in black and shows a much larger initial amplitude. Zooming into the first ms of the first and tenth flash, one can see the similar early dynamics stemming mainly from heat deposited by the excitation laser. Details about its correction can be found in section (5.3).

A **pulse generator**[14] controls the timing of the measurement and the excitation laser. It has a resolution of 1 ns and an accuracy of 1 ns + 0.0001 x the setpoint. The RMS Jitter is given by < 250 ps. To control the complex flash sequence we make use of the multiplexing option, which allows for the programming of eight channels (a - g) individually

[13] the waiting time applied depends on the number of spots measured

[14] Quantum Composers: PG 9518 (also 9520). One of the devices did not keep the outputs silent every now and then. A solution to this was adapt the waiting time to a value of twice the flash sequence. This would yield two subsequent measurements at one spot but avoid crashing of the complex interactions of all programs and the pulse generator.

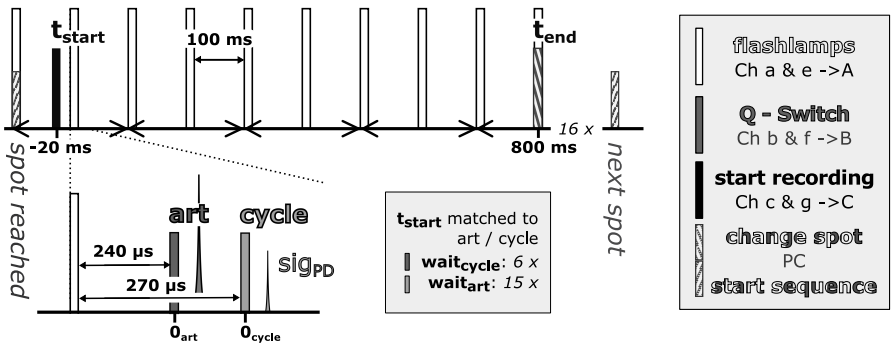

Figure 5.8: Trigger series of the pulse generator. The pulse generator controls the trigger of the flashlamps at 10 Hz, the Q-switch at 1 Hz and the start of the measurement at each flash relative to the Q-switch pulse. The Q-switch is silent for six rounds to allow the flash lamps to heat up and measure dark transients. Then, nine flashes to cycle the states of the PSII and a last flash with multiple energy is recorded. The pulse energy is varied by the delay between flashlamp and Q-switch. A complex multiplexing protocol (right) is used to control all events with four output ports.

on four ouput ports (A - D). The overall trigger pulse sequence is presented in *figure 5.8* excluding the pulse changing the QCL wavenumber sent by the PC.

In practice the pulsegenerator starts a puls-sequence every 200 ms *(intersections on time axes)*. From **port A** the outputs of channel *a* (at 0.1 ms) and channel *e* (0 ms) are sent to the flashlamps triggering them at 10 Hz *(empty bars)*. From **port B** the Q-switch is triggered by the signals of channel *b* and channel *f (gray bars)*. Both are four times silent while once active making a repetition rate of the excitation flashes of 1 Hz. To allow the heat-up of the flashlamps and the recording of dark transients (e.g. drift due to heat up by QCL) output B is waiting silently for 30 runs making 6 dark measurements. The output is then active to cycle nine times through the states with a delay of around 270 µs yielding saturating pulse intensities. Channel *f* is silent for 75 runs (6 + 9 transients), sending then a long trigger (covering the channel b signal) of a delay around 240 µs to fire the high energy heat-artefact pulse. At **port C** the output of channel *c* and *g* are multiplexed triggering the start of each flash transient's measurement 20 ms before the output of port B *(black bar)*. The silent waiting is the same as port B.

Because the clock of the pulsegenerator and the pc are slightly off (some ns in 10 ms) and because the electronics of the laser driving the Q-switch need some time as well, a photodiode signal (sig_{PD} is recorded at the third channel of the A/D conversion card giving the real time zero of the excitation flash.

5.2.2 Noise level, data treatment and numbers of measurements

In this section the data processing is described.

The following steps are executed:

1. Exclusion of data with too low or high signals
   If the voltage exceeds 1 V the detector might be out of its linear range and a too small amount of sample is present. If the voltage drops below 100-200 mV the noise of the detector becomes dominant. Only signals in the range of 100 mV to 1 V are passed

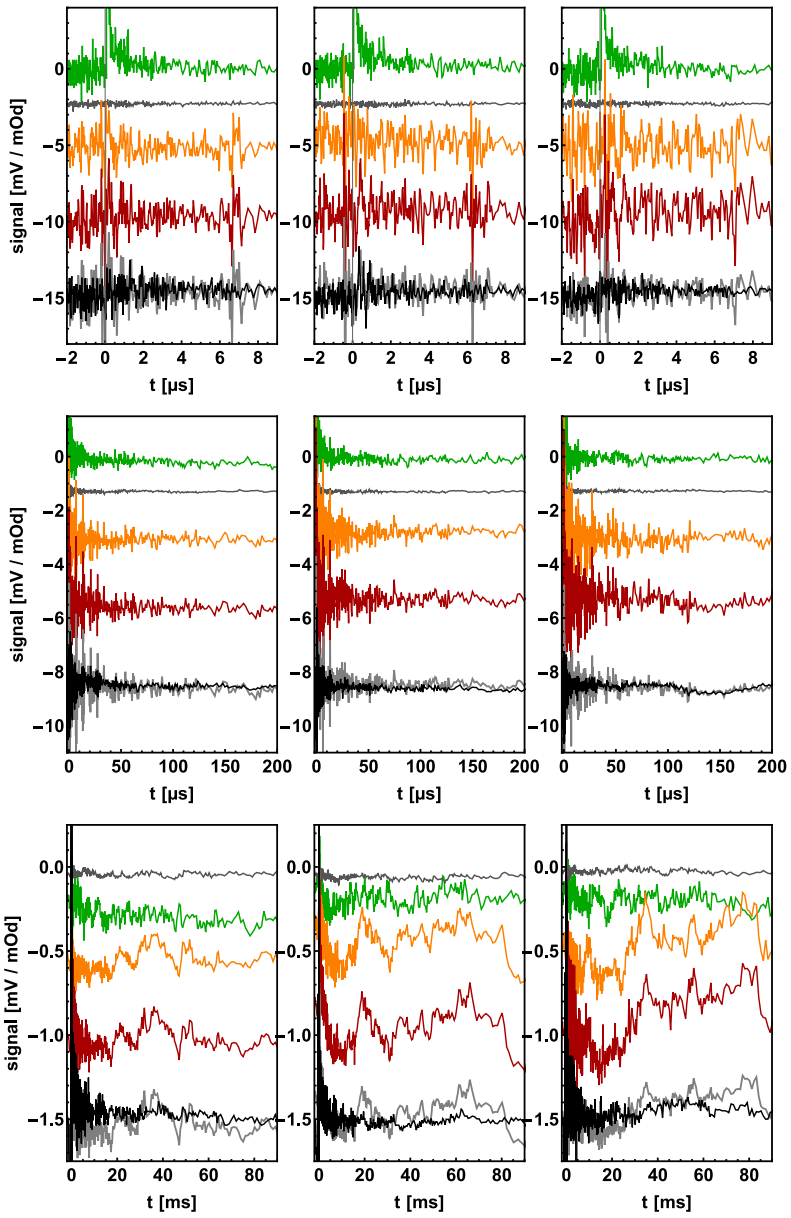

Figure 5.9: Effect of the reference detector correction on the signal quality. Shown are in *green* the signal of the photdiode channel, in *gray* the unused channel as a measure for the noise of the A/D card, in *orange* the reference channel and in *red* the signal channel (in mV). The lowest curve shows the calculated signal change in mOd when just using the signal channel (*gray*) or when correcting with the reference channel (*black*). From left to right the absolute voltage of the signal is increasing: 420 mV, 580 mV and 711 mV.
top row: the signals within 8 µs are dominated by the detector noise (decreasing with increasing signal in the reference corrected curve in black from left to right) and spikes caused by the electronics of the QCL (correctable). *middle row:* This time domain is mainly influenced by the alignment. A bad alignment will increase the 100 µs oscillation of the laser by an order of magnitude. Here it is weakly visible as a dip around 150 µs in the red curve of the right panel (not correctable). *bottom row:* Four sources of noise are present: variation and drifts of the QCL (correctable), sample heat up by IR radiation, fluctuations in the humidity in air and 50 Hz electric noise.

on. Therefore,during the alignment care needs to be taken to keep the signals around 700-800 mV.

2. Reference detector correction
   The strongest contribution of noise in the reference and signal channels is caused by the QCL laser. These can be corrected with the transient recorded at the reference detector. For this the pre-flash signals (20 ms) are averaged for both detector channels. The signal transient is divided by the reference transient after rescaling. Finally the signal is divided by the reference. The effect of this correction is summarized in figure 5.9. Over the whole dynamic range the use of the reference detector improves the signal quality by a factor of three to five. The biggest trouble is caused by the oscillations in the 10 kHz range as this phase is dependent on the alignment and might change only in the signal channel due to sample inhomogeneity. The trace in red of the right figure in the middle row shows this distortion only weakly. Because of these oscillations, many data sets were discarded completely. So far, the best alignment is achieved with the diffusing mirrors.

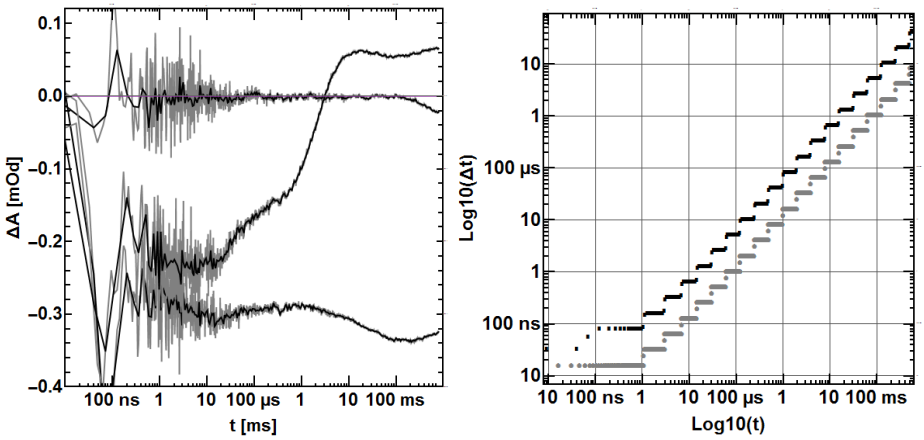

Figure 5.10: *left:* data as measured (gray) and binned (black), taken from a measuremtent at 1544 cm^{-1}. The zero line is a measurement in the dark, the constant negative the signal recorded after the first and the rising one after the third excitation flash. *right:* Quasi logarhithmic data binning as measured (gray, 1278 points after 0) and after data binning (black, 258 after 0, 42 points per decade).

3. Selection by steady state value, excitation energy and 100 µs dynamics
   The next step comprises the selection of good data per flash. If one of the criteria holds the complete set of ten flashes is removed. The criteria are slightly adapted to each data set. First transients with large drifts are filtered out by identifying those where the deviation is too high. Next, files are examined to see if the flashing cycle was correct. A pulse generator bug occasionally causes miss-timing and can be identified using the time stamps in the pulse energy file. The last selection criteria deal with the QCL oscillations in the 100 µs range. Here a first selection is based on the deviation of each measurement from an average of all transients - this time sampled from roughly 100 to 500 µs. Then a straight line is fit between 100-400 µs, large deviations from this line are taken as an indication of the kHz noise. About one third to half of the data recorded are filtered in each measurement.

4. Averaging and calculation of absorbance change
   Per transient about 150-600 measurements were averaged. Afterwards, when the noise in the 100 µs region is too high, the squared deviation of the linear fit (10 kHz filter) is used to weight the data. The decadic logarithm is calculated from the result.

5. Time shift and subtraction of laser induced heat artefact
   To correct the heat artefact, the signal of the tenth flash needs to be shifted in time (70 ns), because different delays between the flash lamp and the Q-switch are set and the clock of the pulse generator and the A/D card are not synchronous[15]. The details of the heat artefact correction are presented in section 5.3.4.

6. Data binning
   Finally the quasi logarithmic average in time is further binned to improve the appearance of the transients. Raw and binned data are shown in figure 5.10 in gray and black, respectively. Whereas the raw data has 1278 points after the 0, the sampled data only consists of 258 points after the 0. Per decade typically 25 to 45 points are left over for PSII membranes from spinach. In the measurements of PSIIcc form *Synechocystis* only 111 points remained starting at 1 µs with 21 points per decade.

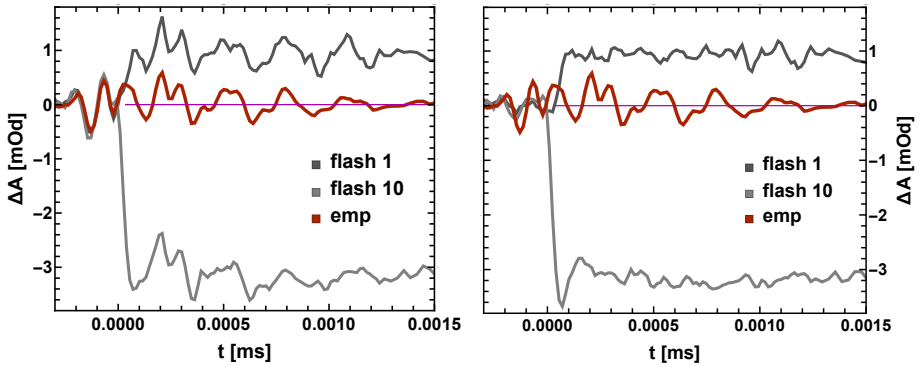

Figure 5.11: Correction of EMP (red, in both). The left figure shows the uncorrected, the right the corrected signals. This correction requires that the EMP is dominant over the actual signal as it is extracted by a fit procedure. When the correction is applied to a data set, it will be noted.

7. Emp correction (*if present*)
   In some measurements strong oscillations are present within the first µs. These do not shift in time with the excitation laser flash, meaning not with the Q-switch, possibly originate from the trigger pulses of the pulse generator or from the A/D card itself. If this signal was strong, it was extracted by simulating curves onto an all-flash-average transient. An example is shown in figure 5.11. In the left panel the uncorrected data after the first and tenth flash (artefact flash) is presented in gray. The emp is shown in red. The right panel shows the corrected data, again in gray and for comparison the emp in red. As can be seen, the real dynamics are only weakly affected but the transients are very clean. In the clean data of the tenth flash there became another feature visible at 100 ns. It appears in all measurements and looks like an overshoot disappearing within 300 ns (also present in fig. 5.10). It might be the effect of a pressure

[15] by the time writing this shift is implemented in the programming of the pulse-generator

wave upon rapidly produced heat. A fit approach is presented in the appendix (fig. 11.11). In general the first 300 ns need to be analyzed with care.

With the use of the reference detector, binning and a careful alignment single point transients can be obtained. In figure 5.12 a measurement of the two strongest bands in the accessible spectral region is presented. The noise level after binning to 1 µs of the first points is around 0.15 mOd.

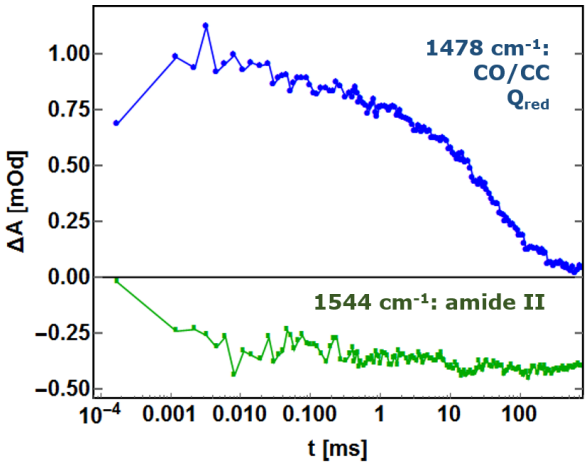

Figure 5.12: Noise level of a single flash measurement on one sample spot averaged temporally to 1 µs. The reference signal has been used to correct for IR laser noise. The transients are the two of the most prominent bands in the spectrum: at 1478 cm^{-1} the coupled CO/CC stretch vibration of the reduced quinone Q_A and the amide II band at 1544 cm^{-1}.

5.2.3 Saturation curve of PSII excitation energy

In order to obtain pure S-state signals one needs to excite all photosystems simultanously and proceed, synchronized, through the photocycle. A sample created with a 25 µm spacer transmits at 532 nm only 30 % of the light. When the back side of the sample is excited with saturating light, at the front three times that energy is absorbed. This means saturating light will create at the front of the sample three times more heat than at the back. A 15 µm spacer on the other hand absorbs 50 % of the light creating at the front surface only the double amount of heat (see section 4.5). In this section the optimal excitation condition for optimal cycling and minimal heat will be investigated. For this, a saturation curve of the photocycle signal is measured in two ways, one for the donor side of PSII and another for the acceptor.

The **first** option is to look in the full **time resolved** transients. The signal, related to photochemistry, will saturate as soon as all PSII have absorbed one photon. At higher intensities chlorophyll will continue to absorb more light and produce heat. This heat signal grows linear with the intensity. In figure 5.13 the components are shown for the reduced quinone's coupled CO/CC vibration at 1478 cm^{-1} *(with PPBQ, 20 °C, 200 mM betaine)*. The pure heat signal is calculated from the difference of the transients at 300 $\mu J/mm^2$ and the one at 130 $\mu J/mm^2$ and simulated by an exponential function (both in the saturated regime). The scaled heat simulation is then subtracted from the transients at 130 $\mu J/mm^2$ to get the

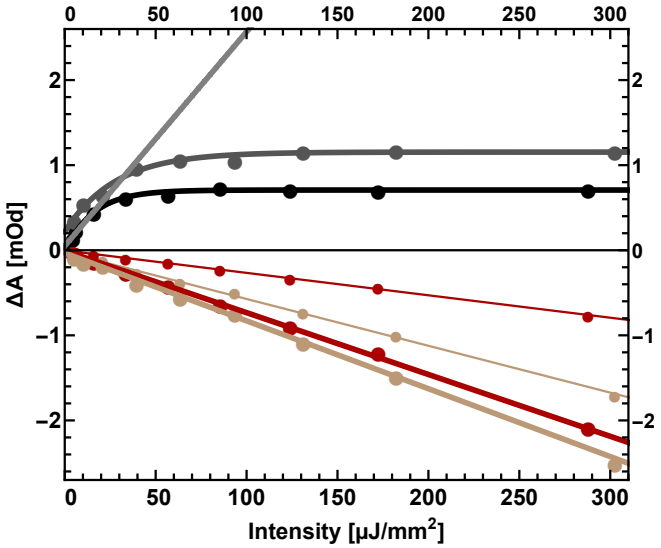

Figure 5.13: The kinetic components of signals measured at 1478 cm^{-1} decomposed into quinone and heat artefact signals. The amplitudes of each component at 1 µs is plotted. Measured on 15 µm (dark) and 25 µm (bright). *Gray:* saturation behavior of the quinone signals. A straight line is fitted through the first three points at 15 µm. *Red:* The intensity dependence of the linearly growing excitation laser induced heat signal. The thin red lines are the values at 300 µs.

pure quinone signal. Eventually, each transient is simulated with the sum of the two curves, multiplied by a prefactor. The simulations are presented in figure 11.12 of the appendix. In the figure 5.13 the amplitude at 1 µs of each component is plotted.

The gray curves represent the intensity dependent signals of the reduced quinones (dark: 15 µm, bright: 25 µm). The function $Sat_Q = a - (a-b)Exp[-x/I]$ simulates the saturation behavior well. The obtained 1/e values of the intensities are 16 ± 2 and $28 \pm 4\,\mu J/mm^2$. The ratio of the two is equal 1.75, whereas the ratio of the spacer thickness is 1.66. The saturated signals are .72 and 1.15 mOd giving a ratio of 1.6. Thus, the saturating behavior agrees with the predictions.

Judging from these results, **satisfactory excitation is achieved at 60 and 100** $\mu J/mm^2$, for each spacer size.

Interestingly the magnitude of the negative linear signal does not increase with the sample thickness. The slopes are simulated by -8.0 ± 0.1 and $-7.3 \pm 0.1\,\mu Od\,mm^2/\mu J$. The ratio gives about 1.1. Since the optical density scales with the sample thickness, the Od at 532 nm decreases from 0.5 to 0.3 (sec. 4.5) decreasing the amount of absorbed light from 70 to 50 %. Assuming that all absorbed light creates heat and the temperature of the buffer and PSII equilibrate faster than 1 µs, one obtains a ratio of heat per length of $(70\,\%/25\,\mu m)/(50\,\%/15\mu m)) = 1.2$. Adding additional 3 µm to the sample thickness (rationalized in sec. 4.5) a ratio of 1.1 is obtained, fitting well the observation.

When comparing the dynamics of the heat transients, the thinner the sample the faster it is in dispersing the heat signal. In figure 5.13 the thin red lines represent the values at 300 µs. The different kinetics are also visible in figure 11.12. Both data sets are recorded under the same conditions and the samples are prepared in the same way, excluding effects like the temperature or water content. The 1/e values are estimated to 300 µs and 1 ms

for the 15 and 25 µm sample, respectively. This implies that, after thermal equilibration of PSII and the surrounding buffer, the heat dispersion is mainly limited by the contact to the CaF_2 windows (refer to the next chapter for a detailed discussion of the cause, spectra and dynamics).

Overall the technique applied here to extract the heat signal works well. Therefore,in the measurements the **heat artefact is measured in the tenth flash with about 300** $\mu J/mm^2$, where it has an about three times higher amplitude than the quinone signals. This will give sufficiently clean heat transients used in the correction described in section 5.3.4. Details about the implementation into the measurement routine are presented in section 5.2.1. At the saturating intensities of 60 and 100 $\mu J/mm^2$ the quinone signal relative to the heat signal is .6/.6 = 1 and .7/1.1 = .64 for the two sample thicknesses respectively. Thus one can decrease the relative amount of the heat signal by using thinner samples (accompanied by a trade off of lower photochemical signals)[16]. This is especially interesting for the measurements on core complexes. Another way to decrease the created heat signals, is using samples with less possible quenching sites like LHC-trimers not bound to PSII.

The **second** way to obtain the saturating intensity, is to look at the **steady state** signal, when the heat has completely dissipated. These saturation curves are presented in *figure 5.14* for a symmetric COO^- vibration band at 1400 cm^{-1} sensing the changes **of the S-state transitions**. The left panel for a 15 µm PSII membrane sample of spinach, the right one for PSIIcc from *Synechocystis*. In these measurement it will become very clear why one needs to excite PSII under saturating conditions when the Mn photocycle is to be studied.

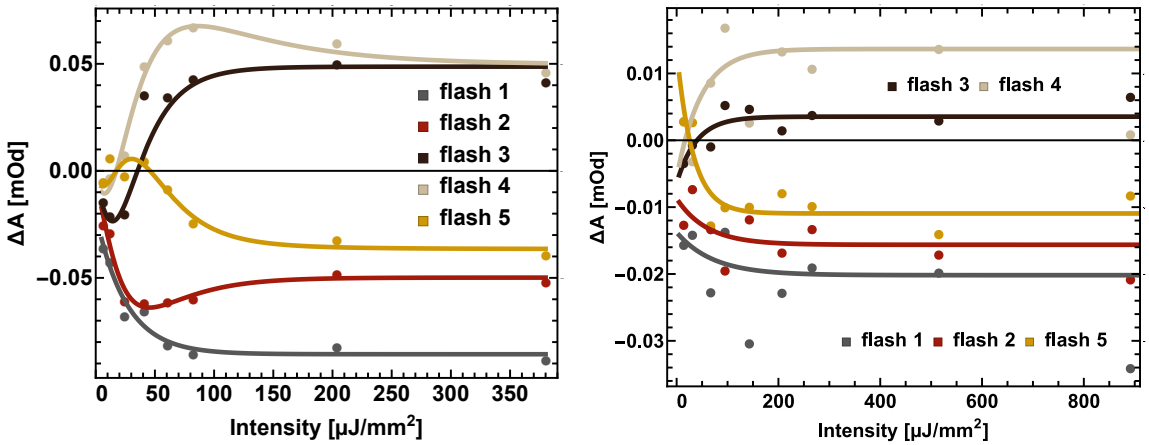

Figure 5.14: Saturation of the near-steady state donor side signal after flash transitions obtained at 1400 cm^{-1} for spinach PSII membranes (*left*, 20 °C, avg 100 to 800 ms) and core complexes of cyano bacteria (*right*, 5 °C, avg 8 to 100 ms). Both samples were created with a 15 µm spacer. The PSII membrane contained about 0.5 mg_{Chl}, the core complex 0.05 mg_{Chl}.

In the left figure measured on spinach the signals are averaged from 100 to 800 ms. The five traces represent the values after the first five flashes. To fit these data, first a miss factor m was defined by the value of the first flash at any intensity over its saturating value. This gives a good approximation of the first points. In later points however the intrinsic miss

[16]This could be used to measure with less heat in order to convince people, who do not trust our correction method

factor of about ten percent will dominate. Therefore, from each miss due to under-saturation another 0.1 are subtracted. The resulting misses start at 43 % and reach 10 % between 25 to 40 $\mu J/mm^2$. All flashes were then simulated with the following equation:

$$sat(fl, I) = \sum_{i=1}^{fl} m^{fl-i} * (1-m)^i * sat(i, I)$$

where only each flash's saturation $sat(fl, I) = a - (a - b)Exp[-x/I]$ curve was simulated and used for the fit of the next flashes fit. The intensities corresponding to the rise to 1/e were 25, 37, 15, 80 and 33 $\mu J/mm^2$. The rise of the third flash curve is too fast, trying to compensate for the initial negative values. This in turn makes the fourth flash too slow. Therefore, the average is calculated from flashes 1, 2 and 5 resulting in $32 \pm 5\,\mu J/mm^2$. Thus the 60 $\mu J/mm^2$ obtained from the acceptor side may not be sufficient anymore. A better value to advance the photocycle and **to allow a proper deconvolution** is **100** $\mu J/mm^2$ for a 15 µm spacer. This value allows slightly different sample thickness and 10 % fluctuations in the energy of the laser during operation.

The **core complex** data of the right panel in 5.14 is clearly more noisy. Due to the presence of slow drifts, the data was averaged from 8 to 100 ms. Here, no simulation based on misses was performed. The 1/e values of the saturating curves are: 70, 60, 40, 50 and 30 $\mu J/mm^2$ for flashes 1 to 5, giving an average of 50 $\pm 15 \mu J/mm^2$. The **intensities** used in the measurement were not below **150** $\mu J/mm^2$. The amount of chlorophyll of the PSII membranes is about ten times higher than in the sample of the core complexes. Per monomer there are about 100 molecules of chlorophyll in PSII membranes and 35 in core complexes. Together this makes a factor of about one third onto the expected signals and also a factor of three on the saturation intensities. Comparing figure 5.14 the signals do indeed scale by a factor of about four. The onset of the signal rise (flash 1 and 2) seems to be present much earlier as well. Still the saturation and the good cycling (see flash 4 and 5) need much higher energy. A cleaner measurement can possibly solve this discrepancy, and should be done in the future.

5.3 Excitation laser induced heat artefact

From the FTIR studies of Björn Süß, Mikaela Görlin and Matthias Schönborn is is known that there is an absorption change induced by excitation laser deposited heat. Why there is such a large production of heat in PSII and how this manifests spectrally, will be discussed in the following section. Furthermore, the method used to correct for this heat artefact will be discussed, as this was not satisfactorily solved in earlier FTIR studies.

5.3.1 The source of heat in PSII

Photosystem II has *not* evolved to a machinery solely transforming light energy into chemical energy as efficiently as possible, function reliably under different environmental conditions. As a compromise a fraction of the photochemical energy, as well as excess excitation energy, needs to dissipate harmlessly as heat. The photochemical energy loss prevents possibly harmful recombination events. Otherwise these would lead to the formation of chlorophyll triplet states, which can react with reactive oxygen species. Therefore, electrons need to be

conducted directional by a trade-off with energy. As described in ([Dau and Zaharieva, 2009]) about half of the excitation energy of P_{680}- that is $1/2 * 1.8$ eV (680 nm) - is lost[17].

In the measurements, the photosystems are excited with 532 nm. Assuming that only the energy of the first excited singlet state of P_{680} is used for energy conversion, the corresponding photon energy difference is 2.3 - 1.8 eV. In total per photon reaching the open reaction center 1.4 eV are transformed into heat ($\eta_{heat} = 60\%$). Additionally, when studying the multi-step photocycle of PSII all centers need to be synchronized (see section above). For this reason, we excite the sample with an intensity well above saturation. In photosynthetic antenna this excess energy can be quenched efficiently by carotenoids again in the form of heat. From the extrapolation of the rise in the beginning of the saturation curve the approximate amount of excess photons can be estimated (fig. 5.13, gray line): If all photons were used for photochemistry the signal would increase linearly with the intensity. Linear fitting of the first three points gives an absorption change of $2.6 \pm 0.4\, mOd$ at $100\, \mu J/mm^2$ but only 0.71 ± 0.01 are observed. Hence, from the absorbed $0.5 * 100\, \mu J/mm^2$ at least $72 \pm 4\,\%$ will released as heat, making $36 \pm 2 \mu J/mm^2$. When fitting only the first two points, one obtains $40 \pm 4\, \mu J/mm^2$. Only rest of the absorbed light, $10 \pm 4 \mu J/mm^2$ is used for photochemistry.

Thus in a 1.2 mm beam it might be possible that around

$$E_{heat} = (E_{excess} + E_{P680} * \eta_{heat}) * A = 40 + 10 * 0.6\, \mu J/mm^2 \approx 46 \pm 5\, \mu J/mm^2$$

of the excitation intensity are rapidly transformed into heat. Neglected here is all fluorescence, which has a really low quantum yield, and the amount of scattered light. Also the extrapolation should contain a higher error as the $4\, \mu J/mm^2$ calculated. At least a doubled error should be taken into account.

Now the increase in temperature caused by the excitation laser can be estimated for water and as the P_{680} is embedded in the hydrophobic part of the membrane for alkanes (approximating the membrane by a mixture of heptane, nonane and tridecane):

$$\Delta T_{H_2O} = \frac{E_{heat}}{c_{H_2O} d_{H_2O} V} \approx 0.06 \pm 0.01\, K$$
$$\Delta T_{Alkane} \approx 1.22 \pm 0.26\, K.$$

This is calculated with a sample thickness of around 18 µm and a 1.2 mm beam diameter giving the approximate volume of $V = 0.033\, mm^3$ and the beam area of $1.13\, mm^2$. The specific heat capacities are taken as: $c_{H_2O} = 4.184\, kJ/kgK$ and $c_{alkane} \approx 0.3\, kJ/kgK$; the densities $d_{H_2O} = 1\, g/cm^3$ and $d_{alkane} \approx 0.7\, g/cm^3$ (values from wikipedia).

The excitation induced temperature change is estimated to lie between 0.1 and 1 K.

Mikaela Görlin has compared the spectral changes seen after a high intensity laser flash in the FTIR setup with a temperature difference spectrum of 1 K ([Görlin, 2012]). The laser induced difference was about two thirds of the heights of the difference spectrum. However, the thermal contact between the Peltier elements in use and the sample was not really good. The actual sample temperate was found out to be closer to room temperature than assumed ([Schönborn, 2017]). The induced temperature change is therefore expected to be smaller as well. Overall a temperature change of similar magnitude as the estimate in water can be present in her measurement.

[17] To be correct at this point about half of this loss is instantaneously e.g. faster than 100 ns with Q_A^- formation, whereas the other half is lost during the analysed steps of the photocycle.

The group of Karin Hauser deposits the energy of pulsed NIR lasers into a sample to study protein folding dynamics ([Krejtschi et al., 2008]). With a 80 mJ pulse (1 mm diameter) they create a temperature jump of 10 °C. In this thesis, the pulse used is about 800 times weaker, making a temperature change of maximally 0.01 °C. Even if only one tenth of their light was absorbed this would still give less than one degree with our energies. They also state that at 1626 cm^{-1} in D_2O the absorbance changes by about $-0.5\,mOd/°C$. Comparing this to the heat induced change of 1 mOd at 1478 cm^{-1} and 100 $\mu J/mm^2$, a possible upper limit of around 2 °C can be found.

Therefore, we can safely assume that the deposited heat is accelerating the kinetics of the photocycle. The heat induced absorption change, however, will be discussed in the next section.

Heat deposited by the IR laser

The maximal power of the infrared laser is specified with 300 mW. The optical thickness of our samples is typically around one. With an attenuation of around 20-30 by the wired grid polarizer before the sample (not in the amide I region) about 10 mW of infrared light will be absorbed in the sample volume of $12^2\pi * 0.015\,mm^3$. This gives a mass of water of 5 mg. With a heat capacity of $4\,kJ/kgK$ a **heat up of the sample** of 0.5 °C per s can be calculated. This neglects any heat conduction to the CaF_2 windows. Indeed a slow drift can be observed in dark measurements before the first excitation pulse. From a four second extrapolation of six dark measurements at 1544 cm^{-1} in a spacing of 1 s to the time, when the new sample spot was reached, a possible heat-up of the sample was estimated about 4 times larger then the one of the excitation laser (compare sec. 5.3.1). This would result in a temperature change of 0.2 to 4 K. Luckily the drift is usually much smaller than in this measurement and a contribution from the absorption loss of water vapor by purging the sample compartment can not be excluded. Further investigation is needed.

5.3.2 The spectral manifestation of rapidly produced heat

Now that we have an approximation for the excitation laser induced temperature change, we want to take a look on the possible consequences on a transient absorption experiment. First our detector might sense the changed black body radiation, even with the longpass filter (cut-on 4.5 µm). In the setup the signal detector is separated from the sample by three focusing and collecting mirrors and a diffuser. Also the sample is not placed in the focus of the first mirror. This means, that a point source at the sample is not collected by the following optics. To test this, the sample was illuminated with an excitation laser, but with no IR probe, and no detectable effect was measured. Care is taken as well, that the excitation laser residue is not entering the detector chamber.

In [Andersen and Ogilby, 2002] two additional heat induced error sources are discussed. The first is the deflection of the IR beam by a thermal lens - the same effect exploited in our photothermal beam deflection setup ([Krivanek et al., 2008]). To investigate this, a series of heat induced signal changes with the QCL laser switched on was recorded. Meanwhile I slowly moved the position of the excitation laser. If there was a deflection signal, then this would alter the amplitude eventually switching sign. Again, there was not detectable difference.

The remaining alternatives are a spectral change due to the heat induced shifts of absorption bands and a drop of absorption due to lowering of the sample density. Shown in the left

of figure 5.3.2 are three different heat scans, all measured in steps of 5 cm^{-1} and obtained on PSII membranes. The **top scan** is from a pellet that contains no betaine. The artefact was measured with 250 $\mu J/mm^2$ and averaged over four flashes. At this intensity, the amplitude of the artefact is three times higher than the highest signal of the quinones at 1478 cm^{-1}. The data was recorded over two days with two samples - the higher frequencies with a thickness of 15 µm to allow the measurements of the amide I peak, the lower on 25 µm for cleaner signals. The sets merge at 1400 cm^{-1} and a rescaling of the high frequency set of 0.53 was applied. The black curve represents the average from 1 to 10 µs. At 1478 cm^{-1} a small peak is present due to the quinone signal. Possibly also some small donor side contributions are present. The spectrum shows positive absorption above 1600 cm^{-1} and negative absorption over the whole other spectral range. This spectrum represents the best the high power single-spot measurement of the Step-Scan experiment (p. 110, green, [Schönborn, 2017]), only that the absorption change is positive around 1540 cm^{-1}. The gray curve represents the early change and is the difference of the average from 300 ns to 1 µs minus the average from 1 to 10 µs. It is scaled by a factor of five. Here no quinone signal can be observed. Positive signals are present above 1575 cm^{-1} and as two features between 1495 and 1550 cm^{-1}. It seems to be kind of a shifted version of the black curve with different isosbestic points though. This spectrum rather reflects best the Step-Scan spectrum obtained by fitting the early absorption changes (p. 110, magenta, [Schönborn, 2017]).

The **middle scan** was measured on 25 µm thick samples containing 100 mM betaine. Because of the 25 µm thickness no signals could be extracted above 1605 cm^{-1}. The spectrum was recorded with 300 $\mu J/mm^2$. Five flashes were averaged, from these an average of four low energy flashes – recorded prior – were subtracted. Therefore, it is free of quinone contributions. The black curve is the average from 5 to 50 µs. Compared to the 0 betaine, this spectrum is a bit more noisy. There is only one isosbestic point at 1595 cm^{-1}. The large 1560 cm^{-1} feature is nearly gone. Two features appear at 1460 and 1400 cm^{-1}. The 1450 cm^{-1} feature might be hidden in the 0 betaine spectrum underneath a broad quinone peak. Starting at 1560 cm^{-1} the absorption change seems to decrease continuously with the wavenumber towards zero. The gray curve is the difference between 30 ns to 1 µs and 1 to 10 µs again scaled by a factor of five. Although more noisy it contains the features of the 0 betaine spectrum above 1450 cm^{-1}. There are changes higher than the noise level visible at 1350 and 1400 cm^{-1} not present in the 0 betaine spectrum.

The **bottom scan** is recorded on a vacuum dried sample with 200 $\mu J/mm^2$ and 100 mM of betaine. Only one flash was applied. It is averaged in time from 100 ns to 3 µs. Judging from its IR spectrum and the size of the water combination band at 2300 cm^{-1} it does not contain any free water. (see appendix fig. 11.4). The spectrum does also not contain any signals from quinones or the Mn photocycle. The maximum absorbance at 1555 cm^{-1} is as high as -5 mOd (similar to the other spectra). From 1300 to 1600 cm^{-1} this spectrum resembles very nicely the early spectral changes of the other scans (gray curves). Only in the amide I / water region is the the direction of change is inversed. When looking at the transients, the changes above 1620 cm^{-1} are about ten times higher than the noise level. Also the absolute voltage at 1630 cm^{-1} of the signal detector is with 2/3 of the value at 1400 cm^{-1}, which is high enough. Therefore,the negative absorbance change above 1600 cm^{-1} is not an artefact.

The deposited heat causes changes proportional to the derivative of the absolute absorption ([Andersen and Ogilby, 2002] and [Görlin, 2012]). The absolute spectrum of PSII membranes and its derivative are presented in the top traces of figure 5.15 (right panel, gray absolute, black derivative). The sample was in solution and the buffer and water contributions sub-

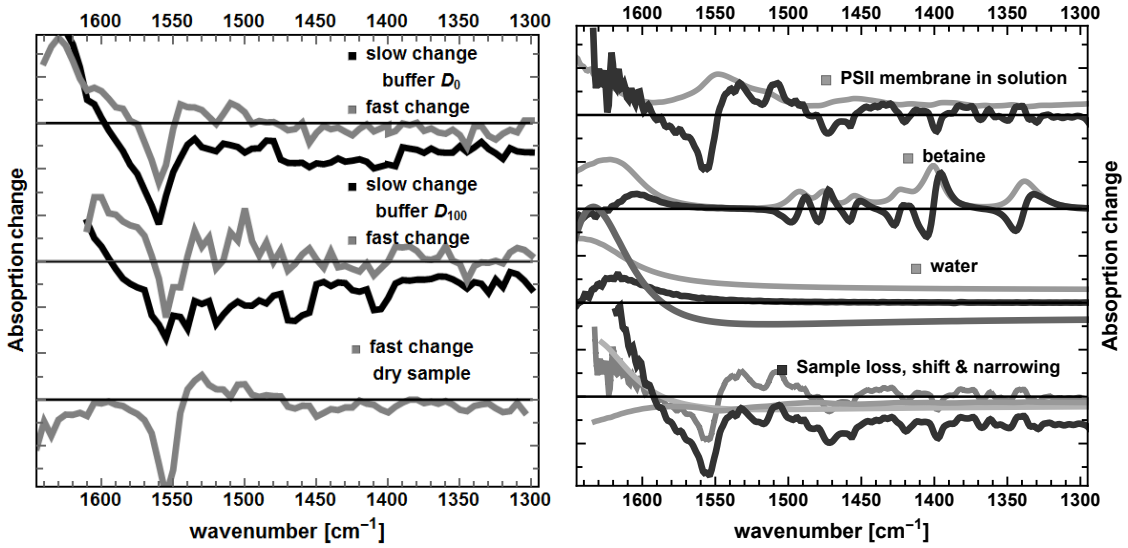

Figure 5.15: *left:* Heat spectra of a concentrated sample in 0 mM betaine buffer (top), 100 mM betaine buffer (middle). The gray curves are the difference from an average between 300 ns to 10 µs and 10 to 50 µs (*times 5*). The black spectra are the average around the maximal absorption change at 1 to 10 µs and 5 to 50 µs. At the bottom the average between 0.1 to 3 µs of a vacuum dried film is shown (bottom).
right: derivative (dark) of absolute absorption spectra (lighter gray) as indicated. The bottom curve is a combination of a shift and narrowing of the water absorption, the derivative of PSII and an small absorption loss of both. The single components are plotted in gray.

tracted. All three gray curves of the early laser induced changes posses the same shape and features as the derivative. Especially pronounced is the negative feature at 1555 cm^{-1} and the two positive ones at 1535 and 1509 cm^{-1}. Like the fast difference spectra the derivative of PSII remains around zero below 1480 cm^{-1}[18]. The derivative of the absorption above 1600 cm^{-1} is positive, similar to the heat difference spectra in solution. So far I do not have an explanation for the negative change of the dry sample. Possibly the protein lost some of the secondary structure while removing the water and formed an aggregate. Increasing the temperature, may break some H-bonds giving negative absorption changes at lower frequencies and positive at the higher ones - out of the QCL range. Overall the very **fast spectral changes within the first µs resembles the derivative of solely the PSII membrane absorption**.

As shown in the thesis of Schönborn, the ingredients of the buffer do contribute to the heat induced changes ([Schönborn, 2017]). Betaine contributions are the most prominent non-solvent bands[19]. With a concentration of 100 mM of betaine, strong features appear at 1330 and 1400 cm^{-1} (second plot right panel of fig. 5.15: gray absolute, black derivative). This is right in the vibrational region of the symmetric $\nu(COO)$, that we want to study. In order to decrease the excitation laser induced heat artefact the betaine content was decreased from 1 M first to 200 mM then to 100 mM and finally dropped, without observing a change

[18]The remaining features might be partially due to remaining buffer ingredients
[19]strong e. g. in Mikaela's heat data

in the activity of PSII. Bands of the derivative of betaine are weakly present at 1400 and 1350 cm^{-1} in the gray and black spectrum of the 100 mM scan in solution (middle trace, left pannel) and possibly as well in the dry sample.

The strongest contribution likely stems from water (third plot, right panel of fig. 5.15: gray absolute, black derivative). [Libnau et al., 1994] reports, that the $\delta(OH)$ band at 1640 cm^{-1} shifts with -.05 cm^{-1}/K and seemingly becomes sharper, with isosbestic points at 1655 and 1595 cm^{-1}. In between the absorption increases with temperature. Below 1595 cm^{-1} it quickly reaches a maximum of the absorption drop around 1560 cm^{-1}. From there the negative absorption change becomes less linear in wavenumber, vanishing around 1000 cm^{-1}. To reproduce these characteristics the water spectrum was simulated with two lorentzians and one exponetial decay for the broad low frequency shoulder, and the peak was shifted by 1 K and sharpened it from 45.69 to 45.65 cm^{-1}. From the shifted minus original difference spectrum 0.5 mOd of the absolute spectrum were subtracted, simulating the loss of absorption reported by Libnau. This is shown as the dark gray curve. One can already see the similar behavior of this curve and the black heat curves of PSII membranes in solution.

The last curve of the right figure in 5.15 represents the attempt to reproduce the heat artefact spectra of PSII membranes in a pellet. The black curve is the sum of a mixture of the above described components: the derivative of PSII membranes, the narrowing, shift and absorption loss of water, and the absorption loss of PSII membranes. The agreement between the black curve in the top left – measured on PSII membranes in solution without any betaine – and the synthesized spectrum is very large. We can therefore assume the following: **after a rapid (<10 µs) equilibration the heat is sensed equally by the sample and the buffer solution**. The absorption drop is not so strong in the FTIR measurements by Matthias Schönborn and Mikaela Görlin. In their heat spectra the trend follows rather the gray spectra of the fast differences or the dry sample bellow 1600 cm^{-1}. In both reports the absorption change was positive around 1510 and 1540 cm^{-1} and stayed around zero below. Judging from the new results, this can only be due to an overall dryer sample and is easily explained by the lack of a PTFE spacer and the fixation with a retaining ring, allowing the sample to dry faster. After a measurement, the samples in the new SFIR experiments are still moist whereas after an FTIR measurement they usually are very dry.

5.3.3 The dynamics of heat dissipation

Figure 5.16 shows the normalized dynamics of the transients from figure 5.15. The fast decaying transients are taken at 1600 (black) and 1595 cm^{-1} (light gray) for the 0 and 100 mM betaine spectra, respectively. At these wavenumbers the slow heat dissipation (black spectrum) does not contribute. They are compared with the strongest change of the dry sample at 1555 cm^{-1}. The decay constants and amplitudes can be found in table 5.2.

The kinetics are identical until 25 µs, with a decay constant of 5 to 7 µss present in all measurements. This is the dominant dissipation phase of the dry sample present at all other wavenumbers of this spectrum. In the concentrated PSII membranes this phase contributes with 60 %. A second phase with around 100 µs is the only other phase needed. These kinetics can be attributed to the relaxation of PSII with its environment, as these spectra reflect the derivative of the absolute absorption spectra of PSII membranes. A faster phase was not obvious but the data quality was also not sufficient to judge its absence. The rapidly produced heat stems from quenched excitation energy, this is located mainly in the membrane region, where the pigments bind. Because the amplitudes are so weak in the buffer containing

samples (5 times blown up in fig. 5.15) it is very likely that a faster temperature equilibration is not resolved.

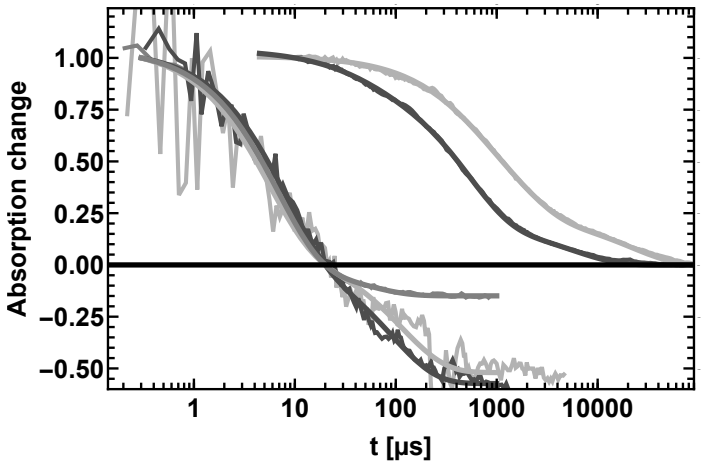

Figure 5.16: Heat transients: fast and slow phases of the samples with 100 mM betaine (light gray), 0mM betaine (drak gray) and the dried sample (gray). The fast decaying transients are taken at the zero crossing around 1600 cm^{-1} of the black spectra of fig. 5.3.2 and the slow decaying transients at 1540 and 1565 cm^{-1} at the zero crossing of the gray spectra. The transient of the dry sample is the one at 1555 cm^{-1}.

Table 5.2: Simulation results of the fast and slow heat dissipation curves. The transients are shown in figure 5.16. Values and errors are separated by a comma.

fast [cm^{-1}]		A_1 [%]	$\tau_1\,\mu s$	A_2 [%]	$\tau_2\,\mu s$		
1555	dry	87, 2	6.64, 0.12	13, 1	47, 5		
1600	0 mM	61, 2	7.5, 0.5	39, 2	92, 6		
1595	100 mM	64 4	5.3, 0.9	36, 3	114, 19		
slow [cm^{-1}]		A_1 [%]	$\tau_1\,\mu s$	A_2 [%]	$\tau_2\,\mu s$	A_3 [%]	$\tau_3\,[ms]$
1550	0 mM	2, 1	45.8, 3.5	78, 1	520, 10	21, 1	5.7, .3
1565	100 mM	25, 4	460, 40	51, 4	1600, 100	23, 1	22, 1

The slow phases of the 0 and 100 mM betaine samples (black spectra of figure 5.15) are taken from the 0 crossing of the gray spectrum - the 0 mM transient at 1550 cm^{-1} and the 100 mM one at 1565 cm^{-1}. They appear only shifted in time. Whereas the 0 mM sample shows a major fraction decaying with 500 µs, the 100 mM decays mainly with 1.6 ms. A similar trend was found for the heat artefact measured at 1478 cm^{-1} in the saturation measurement (see sec. 5.2.3). The only systematic difference between the fast and slow set was the spacer thicknesses. The slower kinetics (1-2 ms) were observed with a 25 µm spacer, while the faster kinetics (300-400 µs) with a 15 µm spacer. At the edges of the window is silicone gel and a PTFE spacer with very low thermal conductivity. The heat conduction parallel to the windows should not change with the spacer thickness, and is possibly responsible for the very slow phase of 5 to 20 ms. If the thermal contact between sample and windows was the

limiting factor, then the dry sample would be the slowest. Therefore, one interpretation can be a slow vertical heat conduction or a bad heat contact to the CaF_2 windows[20].

No effect on the heat artefact could be observed by varying the temperature of the sample. If this will be confirmed, then there is only a minor change of absorption due to lower densities of the medium at elevated temperatures. The shift of bands would rather reflect the weakening of bonds or H-bonds and the decrease in absorption the lowering of the transition dipole moment. If, on the other hand, a larger effect of the temperature of the medium can be found, then measurements at 4 °C, where the density of water is near constant, make sense.

To summarize: there is a 10 µs phase present following the derivative of the PSII membrane spectrum (without water) and interpreted as the PSII temperature equlibration with its solvent or in the thin dried sample directly with the window. Additionally there is a multi-phasic dissipation, which spectrally follows the change of water absorption and PSII membranes. The main decay component demonstrates a temporal shift with the spacer thickness.

Last remarks on the kinetics: Also Karin Hauser observed complex and slow heat dissipation kinetics. In one of her data sets, she found two fast phases: one assigned to peptide dynamics and one to "recooling of the solvent" with 14 µs. Until then only 10 % of the heat induced signal vanished. The remaining dissipated on the "multi-milisecond scale" and are not shown nor discussed (50 and 100 µm spacer). In the step scan experiment on PSII, the heat induced signal extracted decays by 77% within 37 µs, 18 % with 220 µs and only 6 % within 1.5 ms ([Schönborn, 2017]). The samples used were thinner by a factor of 2.5 (at 1650 cm^{-1}), i.e. approximately 10 µm. The main component should therefore be much faster than the 300-400 µs component observed here, possibly around 100 µs, This means the observed kinetics of both studies are in agreement with the observed thickness dependence found here.

A last remark on the two – spectrally distinct – phases: In the FTIR Step-Scan, the heat correction was tested with two different methods. None of them yielded perfect results. Matthias measured laser induced temperature spectra as well. When he normalized his temperature difference spectra he found small variations, present especially in the region from 1500 to 1580 cm^{-1} (p. 104, [Schönborn, 2017]). This region decayed stronger in between 9 µs to 1.3 ms than other regions. A possible explanation for this observation are the two distinct kinetics found here, leaving the correction approaches of the Step Scan even more demanding.

The dependence on the moisture of the sample[21] can be used to monitor the drying state of the samples. In the left plot of figure 5.17, ten normalized heat signals recorded over 48 hours and averaged over 8 samples each with 71 spots at 20 °C are shown. Obviously the dynamics of the heat dissipation do not change within the time of recording. The moisture checked by hand and eye before and after the 48 hours also seems to be unchanged. This is a precondition for recording a bigger data-set on different wavenumbers on the same PSII samples.

The fit results remain constant over the whole time and over all measurements (right panel).In this data set also the rise was fitted. The plot shows that all decay constants are equal. There is no 5 to 10 µs phase present, as in this spectral region the PSII membrane derivative is relatively silent.

[20] the thermal conductivity of CaF_2 is much higher than the one of water
[21] stronger or weaker water contributions will modify the spectrum

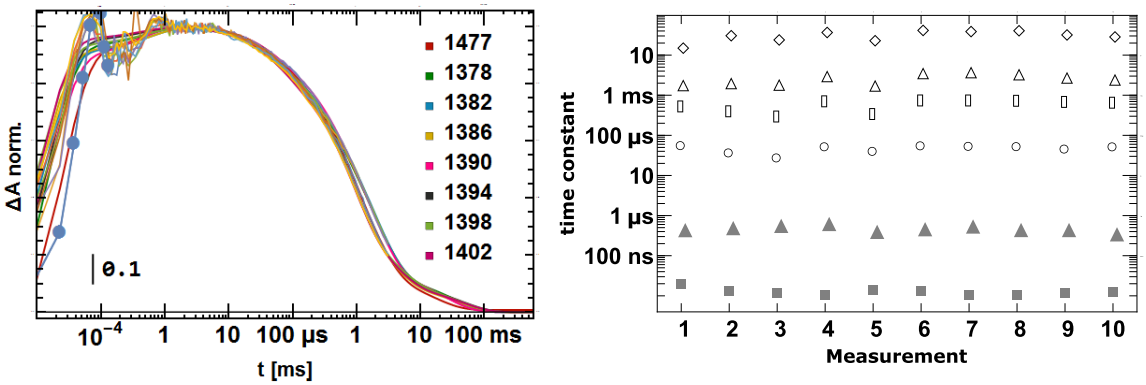

Figure 5.17: *left:* Normalized heat signal over 48 hours recorded at the indicated wavenumbers (in cm^{-1}). No kinetic difference is present meaning the heat artefact extraction is working and there was no significant drying. *right:* The decay times found in a simulation of the artefact traces. Empty symbols belong to the decay starting at 10 µs. Filled symbols represent the rise.

5.3.4 Correcting the laser induced heat signal

As seen in figure 5.16 the slow dynamics of the heat signal depend on the sample conditions. Therefore it is desirable to measure a higher heat signal directly at the end of a flash series under the same conditions on the same spot (sec. 5.2.1). A correction of the signal with this high energetic flash becomes possible as the heat signal scales linear with the excitation energy whereas the signals of the photocycle remains saturated. (*fig. 5.13*). The plot of figure 5.18 shows the pulse energy of two different data sets. The variation of intensity over the nine cycling flashes is small and no systematic increase due to laser heat up is detected. The tenth flash of these measurements is given with 4.5 times higher energy.

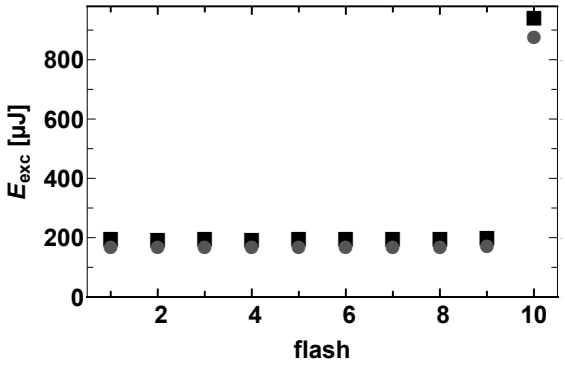

Figure 5.18: Excitation energy per flash used to scale down the artefact. This is an example with two data sets recorded at different wavenumbers on the same sample.

The S-state cycle follows a period of four patter, while the quinones a period of two. The pure artefact signal can be extracted as follows:

$$Art = dat_{hiI} - \sum_{flash=6}^{9} W_{Pop,flash} * dat_{flash} \qquad (5.1)$$

$$\text{with } W_{Pop} = \{0.656, 0.004, 0.049, 0.292\}$$

and dat_{hiI} the transient obtained at the high intensity flash - usually the tenth flash, $W_{Pop,flash}$ a weighting obtained from the population matrix of the tenth flash (*see sec. 4.8.1*), and dat_{flash} the transients of the last flashes.

We then can scale down the artefact to the individual signals. For that the flash intensities of each flash is averaged (*fig. 5.18*)[22]. The artefact is scaled by $E_{flash}/(E_{Art} - E_{fl6-9})$, where the energy of the last four flashes E_{fl6-9} is calculated with the same weighting as in equation 5.1.

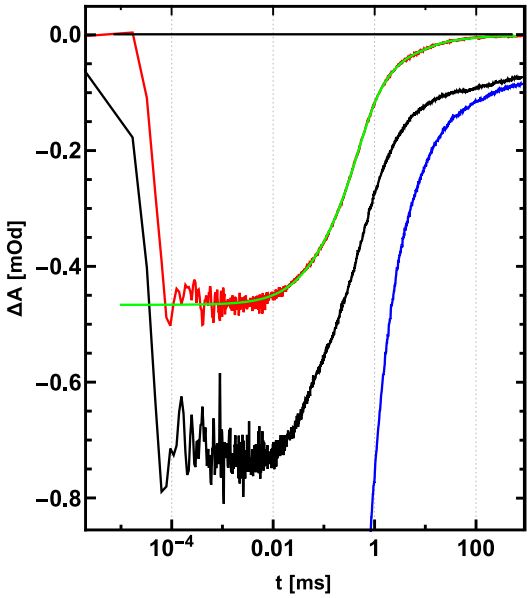

Figure 5.19: Extraction of the laser induced heat artefact at 1544 cm^{-1}. The signal in black represents the population weighted average of the last four flashes measured with 140 $\mu J/mm^2$. The blue line is the high energy flash transition decaying from a maximum of 2.5 mOd. It was measured with 700 $\mu J/mm^2$, 5 times the intensity of the measurement flashes. The red curve is the scaled difference of the two former. The green line is a five exponential fit used to correct the data.

An example of the extraction is shown in figure 5.19. The five times stronger high intensity flash is not shown completely (*starting in blue*). The weighted average of the last four flashes is plotted in black. Subtraction and scaling onto the measurement energy gives the red trace, the extracted heat artefact. This curve is simulated with three to five exponents and used for the correction.

The photocycle signal is in general smaller than the heat artefact. Two of the strongest signals accesible by the QCL laser are the reduced quinone signal at 1478 cm^{-1} (see fig. 5.13) and the amide II band at 1544 cm^{-1} (compare red and black curve in fig. 5.19). To get a feeling of how delicate the problem is, figure 5.20 compares the transients of both vibrations before and after the correction. The quinone signal (left) is already recognizable without the correction but afterwards the dynamics differ dramatically. The amide II signal (right) shows strong dynamics prior to the correction. Afterwards it becomes visible that the absorption change of the first flash is formed rapidly and remains, while the third flash transient only rises with Mn oxidation.

[22]The differentiation of the single flashes is needed due to the heat up of the laser possibly present in some measurements.

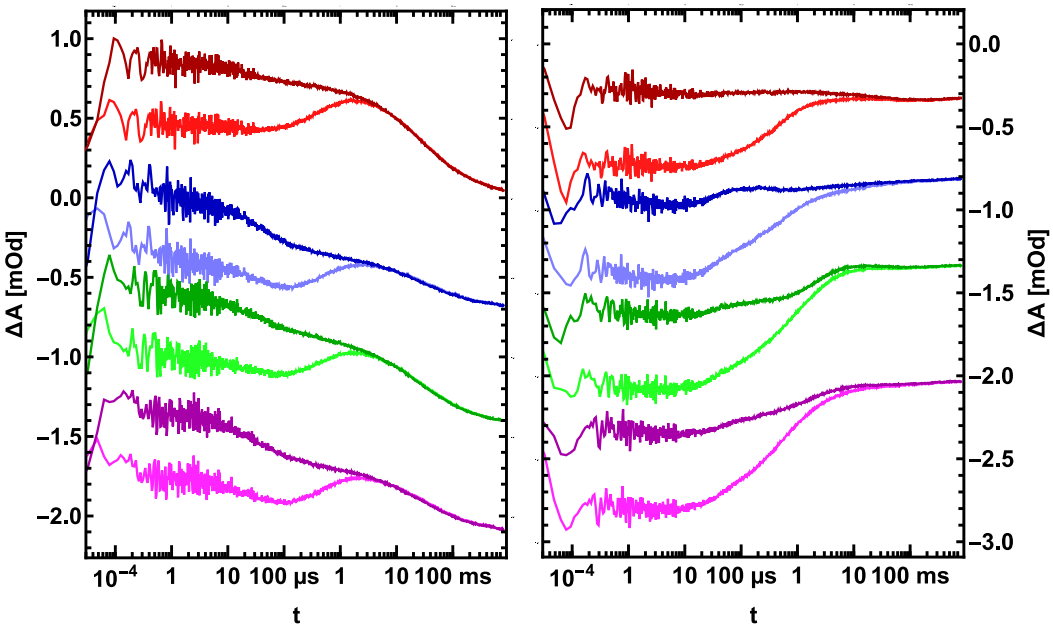

Figure 5.20: Heat correction on the example of the first four flashes at 1478 cm^{-1} (*left*) and 1544 cm^{-1} (*rigth*). The darker curves are corrected. In both cases the excitation laser induced heat signal causes negative absorption changes. Flash 1: red, 2: blue, 3: green, 4 magenta.

5.4 Suggestions for future improvements

Sample

In this thesis, I present the first time resolved IR measurements on mutated PSII core complexes. The signal quality in the wild type sample is really good. To improve the signal of the less active and less efficient mutant sample, one should use **higher concentrated samples**. When doing so some **light drying** procedure should be applied as well: this will decrease the necessary IR light in-turn decreasing the heat deposited by the QCL. With twice the amount of sample the signal would be doubled, this in-turn would decrease the numbers of measurements by a factor of four, ultimatelively halving the amount of samples.

The **salt concentration** in the PSIIcc buffer is adapted to partial drying. If no drying is applied, the salt concentration should be increased to a similar value as in PSII membranes.

Of course a nice next step is record time resolved transients first on complete thylakoid membranes and then on full cells or even leafs (thylakoid see [Nagao et al., 2018]). A possibility target of the latter to measure was suggested by David M. Kramer: the leaves of the red alga genus *Porphyra* are only one to two cell layers thick and thus ideal candidates to study[23].

Aquarium V2

The medium scale bioreactor constructed by Matthias Schönborn and myself, does need some improvement to allow sterile on-bench partial harvests, sample extraction and refilling. For this, a new type of lid needs to be found, that has at least three ports, one for air supply

[23] I am not sure he meant that one, but I remembered the connection to Sushi

and bubbling, one for air release and one multi porpoise port. The ideal flask is conical at the bottom to prevent sedimentation and wide at the middle part, to allow for homogenous illumination and large sample volumes (double to triple possible).

Deconvolution

In section 4.8.1 the lag of the current method and possible expansions are described in detail. In short, assuming 100 % S_1 occupancy, no transition dependent miss events and only one source of misses may not be enough. The reader may refer to [Pham and Messinger, 2016] and forthcoming publications.

Noise control

In some measurements **electric noise** starts about half a µs before the flash and enters the data up to 700 ns. The issue might be grounding or shielding of the cables. So far I could not identify the source, but I envy the one doing so. A possible source is the IR detector, whose connection is not well shielded. Another source might be the A/D card, the pulse generator or the excitation laser.

The main issue of the setup is the noise of the infrared beam. One can align the setup well on one wavenumber, but when changing it, one often needs to realign. Right now this is only possible, when opening the sample compartment to access the mirrors. This is always accompanied by a change of humidity. To fully automatize the measurement one **motorized mirror** and a control algorithm is sufficient. The other option is the use of a gold covered **integrating sphere**. The signal loss is really high (up to 1000, currently with the diffuser 40), but the advantage as well.

Optics

A solution to the problem of the QCL instability can also be a good **focus on the detector elements**. Then the noise at both elements should be always identical. Right now however the power of the laser is too high. We only use one wired grid polarizer to reduce the power in the signal beam (up to 300x). A second one placed before the beam splitting window and careful focusing might solve this. In the group of Joachim Heberle a slightly tilted iris does this job[24] The current polarizer is not wedged, but ideally both are wedged[25]. When realizing the new alignment, keep in mind, that you do not collect the changing black body radiation from the excited sample.

In the FTIR experiment Matthias Schönborn implemented a **photodiode for ideal alignment** of the excitation laser.

Another suggestion is to measure the **reference signal through** the same **sample** and record it in the same compartment as the signal beam. By this, one can measure the heat-up by the IR beam or possible humidity changes and correct for them.

In order to measure on samples thicker than 25 µm (partially dried), possibly one needs to **excite from both sides**. The intensity of the laser is high enough and the signal increase would be tremendous.

[24] the provider of the QCL advised to use special irises that do not reflect ration back to the laser.

[25] a broad band optical polarizer will allow to align the QCL beam perpendicular to the optics, solving the wedge-issue

Programming

At the moment, there are separate programs controlling the data recording, the translation stages and the wavenumber change, and the recording of the excitation energy. The timing of the pulse generator and the temperature control are handled manually. **All** these features should be **merged into one program**.

Currently the data is recorded in equally spaced packages. At the end of one package the spacing is increased in logarithmic steps. Ideally this method is adapted to the new needs.

Temperature

A measurement at $T = 4°C$ will minimize the heat induced density change of the sample.

I recommend to measure the heat increase caused by the IR radiation at different laser powers. If it was more than a degree a good infrared camera could detect it[26]. A photothermal beam deflection method could do so as well.

Modified laser systems

We are right now limited to the spectral range between 1300 and 1650 cm^{-1}. New laser modules can **access other vibrations** including the complementary region of the CO stretch of protonated caroxylates, the neutral tyrosines (Y_Z, Y_D and the two next to the BCT), the histidines around 1100 cm^{-1}, OH stretch vibrations or even the vibrations of the Mn cluster itself. For the latter a new set of windows and detectors would be needed.

The main contribtuion to the laser induced heat artefact was found to stem from excess energy. One might reduce this slightly, by **tuning the excitation** out of the carotenoid absorption ranging up to 550 nm and **towards** the Qx band of chlorophyll around **570-600 nm**. Because we would then excite slightly more specifically the chlorophyll less excitation energy might be needed[27].

I discussed whether the **polarization of the lasers** disturbs our measurements. Now I want to state we should use the additional information already accessible. For this the PSII needs to embedded in membranes and these need to be aligned.

[26] contact AG Nordmeier

[27] carotenoids function as quencher but also as antenna pigments.

6 Overview of the transients in the accessible spectral region

This small chapter shows an overview of the bands accessible by the QCL. No analysis nor simulation has been performed, but the most prominent bands will be introduced and the reader will find the chapters, in which some of the bands are discussed.

Figure 6.1 shows the transients plotted on top of each other for each S-state transition. Figure 6.2 shows the transition dependent amplitudes at various time averages.

The data is measured at 10 °C and pH 6.2 on 15 µm thick PSII membrane samples. The data was recorded in two sets and the band at 1544 cm^{-1} measured in both showed that no scaling was necessary (see figure in appendix 11.34). To show more information the measurement at 1344 cm^{-1} from section 8.3 obtained under the same conditions and the measurement at 1382 cm^{-1} from section 9.4.3 obtained at 20 °C are added.

Albeit not all accessible bands were measured, the overview shall serve as a catalog for further studies. The wavenumbers presented were chosen due to the following reasons (information from chapter 3):

- 1310 cm^{-1}: a band reflecting P_{680}^{+} reduction and the P_{680} triplet (sec. 8.3)
- 1344 cm^{-1}: a band possibly sensing P_{680}, $\nu_S(COO)$ and the bicarbonate (sec. 8.3)
- 1364 cm^{-1}: a band sensing $\nu_S(COO)$ and the quinones (sec. 7.3 and 9.4.3)
- 1382 cm^{-1}: a band sensing $\nu_S(COO)$ and weakly Q_B^- (sec. 9.4.3)
- 1400 cm^{-1}: a $\nu_S(COO)$ band sensing events of the Mn photocycle (sec. 9.4.3)
- 1478 cm^{-1}: a band of the reduced quinones (sec. 7)
- 1514 cm^{-1}: proposed to sense $Y_Z^{\bullet ox}$, (sec. 8.4, also Q_A and Q_B and Fe^{2+})
- 1544 cm^{-1}: amide II band sensing all charge transfer events (sec. 9.5)
- 1552 cm^{-1}: amide II sensing all charge transfer events, contribution of Q_B^- higher than Q_A^-
- 1564 cm^{-1}: a $\nu_{AS}(COO)$ band also sensing Fe^{3+} and Q_B^-
- 1575 cm^{-1}: amide II: possibly showing pronounced fast proton release phases [Schönborn, 2017]
- 1587 cm^{-1}: a $\nu_{AS}(COO)$ band and sensing Fe^{2+}
- 1623 cm^{-1}: a band in a crowded area, sensing Q_A^- (Q_B^-), differing strongly in D1-D61A ([Debus, 2015])
- 1633 cm^{-1}: a band in a crowded area, sensing P_{680} and neutral quinones, differing strongly in D1-D61A ([Debus, 2015])

Because the whole accessible spectrum is covered by this data set, it will next be compared with the FTIR step scan data of [Schönborn, 2017].

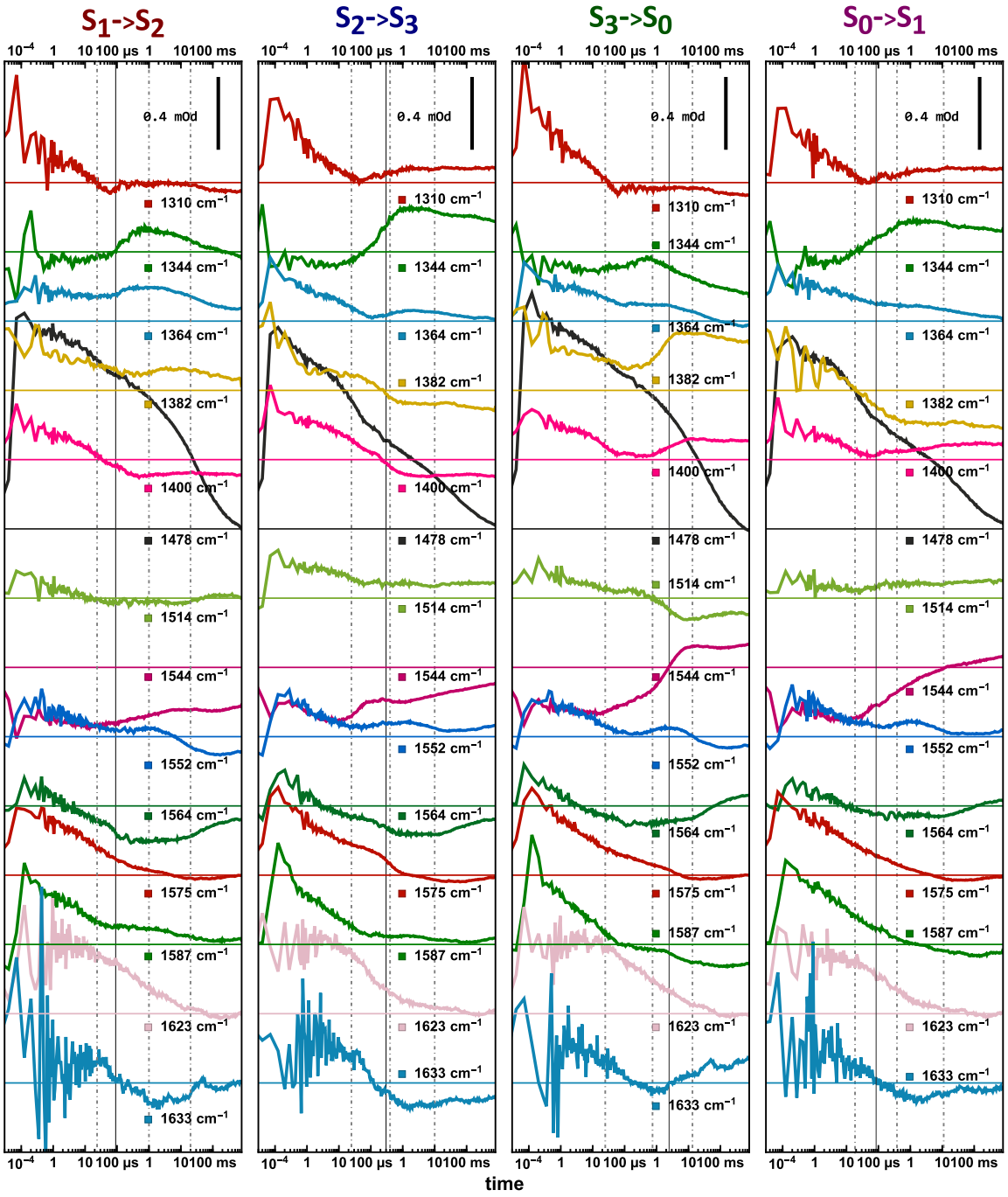

Figure 6.1: Overview of prominent, deconvoluted bands in the tuning range of the IR-QCL laser. Measurements taken at 10 °C and pH 6.2 on 15 µm thick PSII membrane samples. Also shown is the measurement at 1344 cm^{-1} from figure 8.5 taken at the same conditions, and at 1384 cm^{-1} from figure 9.6 obtained at 20 °C. Vertical lines indicate the found kinetics of the Mn oxidation (black) and of the quinone reaction (dashed).

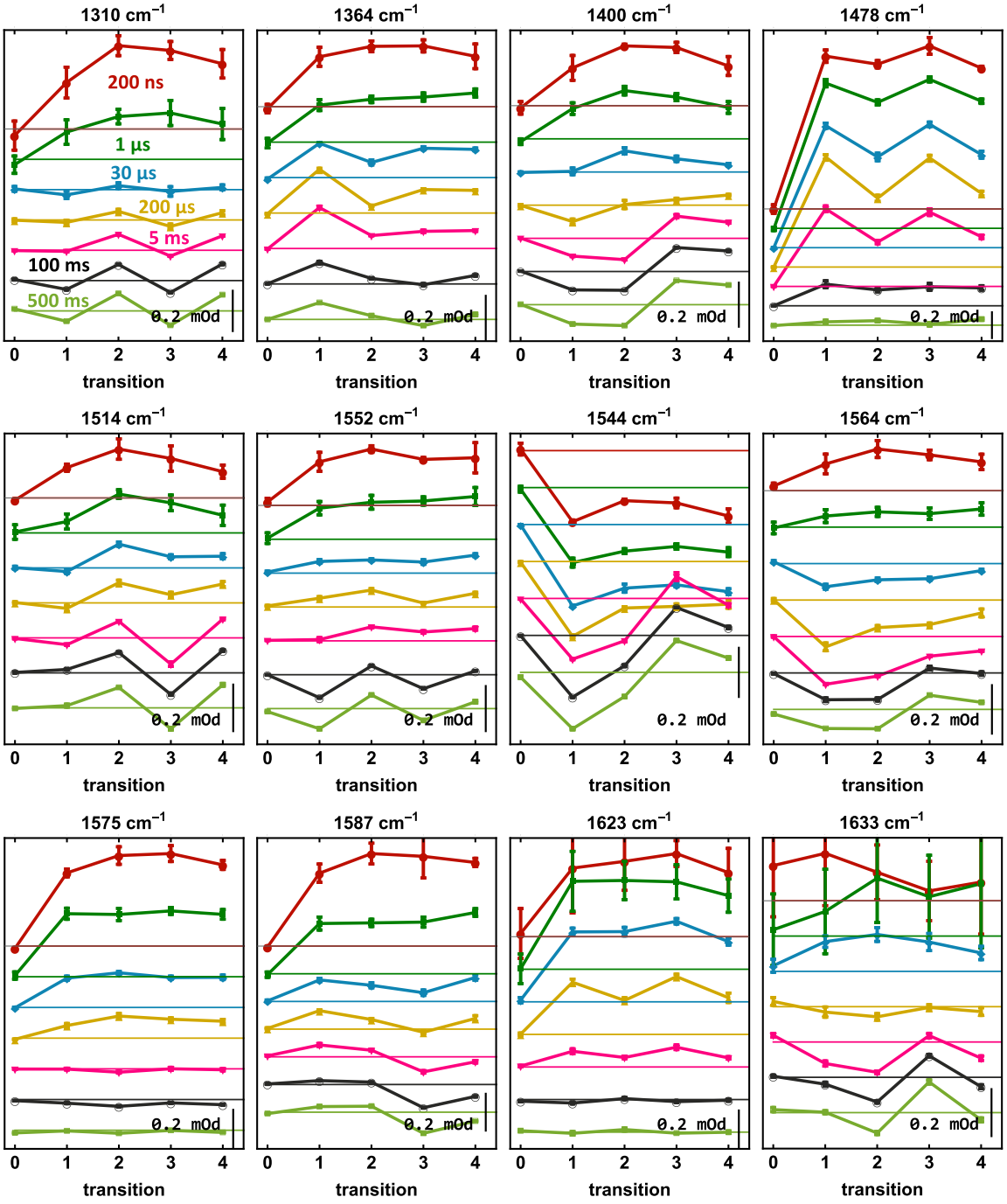

Figure 6.2: Transition pattern of prominent bands in the tuning range of the IR-QCL laser. Measurements taken at 10 °C and pH 6.2 on 15 µm thick PSII membrane samples. Also shown is the measurement at 1344 cm^{-1} from figure 8.5 taken at the same conditions, and at 1384 cm^{-1} from figure 9.6 obtained at 20 °C. Averages in time were calculated between 3/4 to 3/2 of the following times: **200 ns** (*red*), **1 µs** (*darker green*), **30 µs** (*blue*), **200 µs** (*yellow*), **5 ms** (*pink*), **100 ms** (*black*) and **500 ms** (*lighter green*).

6.1 Comparison with FTIR Step-Scan from Matthias Schönborn

[Schönborn, 2017] recorded a very rich data set between 1100 and 1800 cm^{-1}. It is a catalog containing all the Mn oxidation transitions[1]. In principal the setup used had a time resolution of below 10 µs and a spectral resolution of 10 cm^{-1}. Only the data quality is not sufficient for the 10 µs and the heat artefact correction is not as simple as with the new single-frequency-QCL setup. The date set used for comparison is the version improved by Paul Greife[2].

The transients at 1310 cm^{-1} are nearly identical. Merely the $S_1 \rightarrow S_2$ curve is more negative in the step-scan data and is more sensitive to the quinone rise.

At 1344 cm^{-1} all transients of the step-scan show initial absorption drops. From 100 µs onward the data sets merge. The quinone shoulder, a rise and decay with 1 ms and 30-100 ms, however, are much more prominent in the QCL-data. In the Step-Scan data the $S_1 \rightarrow S_2$ transient stays below zero.

The 1364 cm^{-1} band is identical with only the quinone shoulder again more pronounced in the QCL data. Also the transients at 1382, 1400 and 1478 cm^{-1} are identical.

The transient at 1514 cm^{-1} differs only in $S_1 \rightarrow S_2$. In the step scan it shows a rise within the first 300 µs. This might be caused by the limited spectral resolution as in the neighboring lower wavenumbers a rise and positive transients, in the higher a decay and negative transients are present.

The amide II band at 1544 cm^{-1} is identical.

Ignoring the first 100 µs where the Step-Scan data shows a strong rise, the data at 1552 cm^{-1} is similar when taking the limited bandwidth into account.

Except for the first 100 µs, the transients at 1564 and 1575 cm^{-1} are the same.

At 1588 cm^{-1} the $S_2 \rightarrow S_3$ transition differs. The QCl data is positive, staying nearly constant. The step-scan data is negative and rises for 2 ms, also in neighboring bands.

Only after the first ms the 1623 cm^{-1} transients compare well.

Except for the first flash the signals at 1633 cm^{-1} compare well when looking at the 1636 cm^{-1} transients of the Step-Scan.

Despite the spectral resolution, **the data sets are very similar**. **Only in the heat artefact sensitive region the first 100 µs differ**. As the heat in the Step-Scan dissipated within 100 µs but the one in the QCL setup within 0.5-1 ms, I think the heat correction used in the step scan is not ideal. The biggest struggles are in the in the region from 1550 to 1700 cm^{-1}. In this region another method introduced by Matthias Schönborn yields better results. He fitted the heat transient, obtained from the interferogramm, onto the data.

The band at 1623 cm^{-1}, on the other hand might be imperfectly corrected by myself. But comparing this band with the one at 1478 cm^{-1}, it shows the same behavior in even and odd flashes (compare the flash pattern in fig. 6.2). Only it decays within about 1 ms, which matches again the vanishing of Q_A^- nicely (dashed vertical bars in fig. 6.1). Keeping in mind that it is assigned mainly to Q_A^-, the data does not appear wrong. Then only the crowding of the amide I region together with an averaging over 10 cm^{-1} might cause the difference of the two data sets at 1623 cm^{-1}.

[1] excluding $S_0 \rightarrow S_1$

[2] "New_H2O_Spec_corrected_Deconvoluted.py" from 21.06.2018

7 Quinone reduction dynamics following Q_A^- formation

In this chapter I will present the results on the various events following the rapid Q_A^- formation. The main focus lies on the electron transfer to the second native quinone Q_B. Here I will compare the results with the ones obtained from the variable chlorophyll fluorescence. The latter is not directly proportional to the amount of reduced Q_A^- but needs to be corrected for inter-PSII excitation energy exchange. This model never was directly verified by other methods.

The following smaller section explores the dynamics of the electron transfer from Q_A^- to the exogenous electron acceptors p-phenyl-benzoquinone (PPBQ, in PSII membranes) and ferricyanide (FeCy, in PSIIcc). The knowledge of these dynamics is a prerequisite, when one wants to separate these kinetics from the ones observed around the Mn cluster.

7.1 Native PSII without addition of exogenous acceptors

7.1.1 Introduction

The two quinones are bound in a highly symmetric environment centered around a non-heme iron (Fe^{2+}), which is 6-fold coordinated by two oxygens of a bicarbonate and four nitrogens of histidines located on four helices of the D1 and D2 protein subunit ([Chernev et al., 2011], [Chernev et al., 2013]). The overall structure is presented in figure 7.1. The role of the iron and its ligands in the inter-quinone electron transfer (depicted by red arrows) is not completely clarified, but indications are given that the bicarbonate and its surrounding tyrosines (D1-Tyr246 and D2-Tyr244) reorient and the redox potential of the iron complex changes depending on the redox states of the two quinones ([Ishikita et al., 2007], [Saito et al., 2013]). It was shown, that when adding redox-active compounds like ferricyanide as an electron acceptor the iron will be reducible ([Petrouleas and Diner, 1987]) and thus be directly involved in the electron transfer.

In photosystem II similar electron and proton transfer motives are present as in the extensively studied bacterial reaction center (brc) and reviewed well by [Muh et al., 2012]. Detailed calculations were done by Saito et al. ([Saito et al., 2013]). Some essential findings are summarized in the following: When Q_A becomes reduced rapidly by the pheophytin it is suggested that this induces the uptake of a proton from the stromal side as in the brc. Afterwards the electron can be transferred towards Q_B. It is stated that the dynamics of the electron transfer from Q_A to Q_B vary depending on the species and the kind of protein preparation. If Q_B is bound characteristic transfer times of 200 µs - 1.2 ms and 2 to 5 ms were reported under physiological conditions (see also ([Mathis and Haveman, 1977], [Haumann and Junge, 1994b], [Putrenko et al., 1999], [de Wijn and van Gorkom, 2001], [Petrouleas and Crofts, 2005]). Measurements indicate that the electron transfer is coupled to a proton transfer probably to the vicinity of Q_B^-. With the transfer of a second electron, Q_B takes up both protons and is replaced. Whether the intermediate between both electron

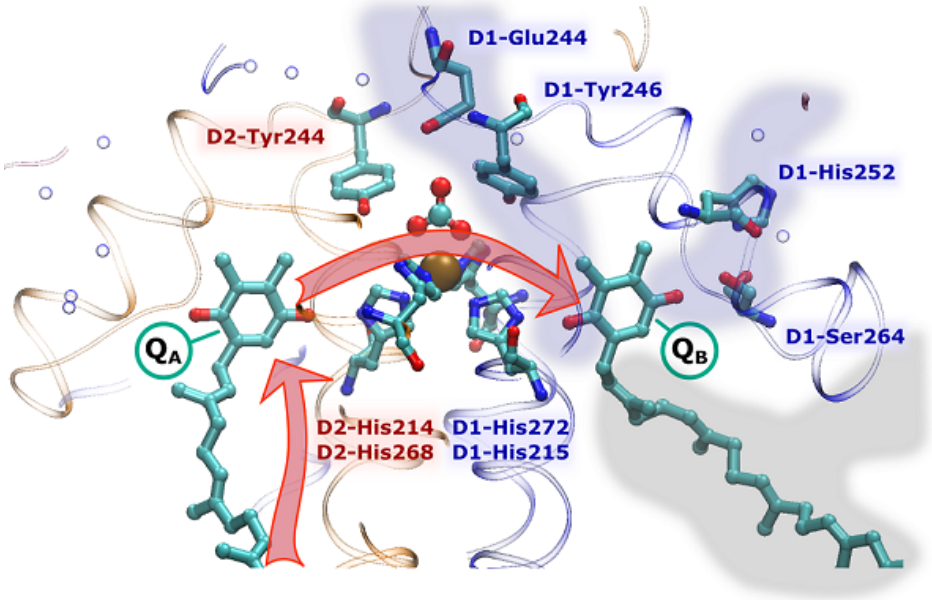

Figure 7.1: The environment of Q_A and Q_B in PSII of *T. vulcanus*. Red arrows indicate electron transfer (ET) steps. The first ET steps towards Q_A proceeds within less than 1 ns after laser-flash excitation. The ET transfer step from Q_A^- to Q_B or Q_B^- will be explored in this work. The blue and red helices are part of the D1 and D2 protein, respectively. Relevant amino acid residues are shown in more detail. The Fe^{2+} atom in the center is ligated by four histidine residues and a bicarbonate (HCO_3^-: BCT). The hydrogen of the BCT is located away from the iron. Waters within 10 Å of the quinones are shown as empty balls. Along the blue shaded area, proton transfer pathways are suggested. The grey area depicts possible access channels for Q_B and Q_BH_2. (Figure prepared from the crystal structure 4UB6 (Umena 2014))

transfers is Q_B^- or $Q_BH^\bullet$ is not clarified, yet. Calculations and comparison with the brc results suggest that a first proton could be delivered via the D1-His252 and D1-Ser264, and a second taken up by a proton antenna at the stroma-interface not far from the iron and transferred via the bicarbonate towards Q_B ([Saito et al., 2013]). Both paths are highlighted in blue in figure 7.1.

When Q_B has become doubly reduced and taken up two protons it needs to be replaced by a plastoquinone from the pool inside the thylakoid membrane. In the 2.9 Å structure two possible channels from the Q_B side have been identified ([Guskov et al., 2009], see fig. 2.1). The approximate direction of the two possible channels are depicted as a gray area in the figure. Lately a 50 ns molecular dynamic simulation (MD) hinted towards plastoquinol exiting through channel II ([Zobnina et al., 2017]), whereas another 0.5 ms course grain MD suggests a third channel and that all channels are used ([Van Eerden et al., 2017]).

Even after decades of intensive PSII research by far not all questions related to the quinone redox reactions have been solved. Most experimental studies made use of indirect measurements of the quinone redox state like the very popular variable chlorophyll a fluorescence (see e.g. [Dau, 1994]) and fluorescence induction (Lazar 1999) or a bit more directly by the EPR signal of the $Fe^{2+}Q^-$ (see review by [Miller and Brudvig, 1991]). These measure-

ments are usually not straight-forward to interpret. Absorption measurements in the visible spectral range were conducted as well, e.g. by Mathis in 1977 measuring at 320 nm ([Mathis and Haveman, 1977]) or measuring the electrochromic induced changes at 532 nm ([Haumann and Junge, 1994b]). The problem in the visible range is that absorption bands are very broad and thus a strong overlap of different signals is expected. In contrast, vibrational bands in the infrared are narrow making assignments of the bands in a difference spectrum feasible ([Barth, 2007]).

As the photosystem II is a large and complex system, the difference spectra are also very rich. Attempts were made to separate contributions from different sides by adding specific chemicals like inhibitors, by depletion treatments or by local and global isotope labeling ([Hienerwadel and Berthomieu, 1995], [Zhang et al., 1997], [Zhang et al., 1998], [Kimura et al., 2003], [Noguchi and Sugiura, 2003]). Some of these technique might directly affect the redox potentials of relevant cofactors and therefore mask the band positions (e.g. Mn-depletion, [Kato and Noguchi, 2016]). In addition, many point mutations were analyzed with FTIR measurements mainly targeting at water oxidation ([Service et al., 2014a]). Still up to now, only a few bands have been clearly assigned to one residue. Concerning the quinones many vibrational bands of the neutral and the semiquinone anion form as well as related changes in the backbones and close by amino-acid residues were identified and discussed ([Berthomieu et al., 1990], [Zhang et al., 1997], [Zhang et al., 1998], [Razeghifard et al., 1999], [Kato and Noguchi, 2016]). To our knowledge, no studies of the quinol vibrations in photosystem II were published so far (in contrast to the brc or cytochrome protein complexes ([Hellwig et al., 1999], [Zhang et al., 2002], [Mezzetti et al., 2003], [Mezzetti and Leibl, 2005], [Mezzetti et al., 2011])).

In this section we present combined FTIR rapid scan, time resolved single frequency IR (SF-IR) and variable chlorophyll measurements on the quinone reduction and re-oxidation in PSII-enriched membrane fragments extracted from spinach. The interquinone electron transfer is tracked with the SF-IR experiment from 100 ns to 850 ms after the excitation flash. We probe several wavenumbers around the strongest bands originating from the reduced quinone species, i.e. around 1478 cm^{-1}. The dynamics are compared with the Q_A^- reoxidation dynamics observed with the variable chlorophyll fluorescence. This technique is extensively used in the past decades of photosynthetic research ([Putrenko et al., 1999], [de Wijn and van Gorkom, 2001]). We can verify and extend the assignments of the variable fluorescence measurements leaving out the S-state dependent variation of signals. Finally, as one can sometimes read ([Zhang et al., 1998]) that the sample type influences the electron transfer kinetics, a short comparison of the kinetics of PSII enriched membranes and broken chloroplast will be given.

Measurements of this section

In this section PSII membranes from spinach were measured at 20 °C, pH 6.2 and with a betaine concentration of 200 mM. Variable chlorophyll fluorescence was measured and corrected as described in section 4.6 and FTIR spectra recorded as described in section 4.7. The thylakoid and PSII membrane samples, that I compare, were prepared freshly on the same day and differ from the PSII membranes used to compare with the SFIR data in the size of plastoquinone pool. The SFIR samples were prepared with a 25 µm spacer. On each sample only one series of 10 flashes was recorded. Between 150 and 600 measurements were averaged per wavenumber.

The simulation of the miss parameter in figure 7.10 was done similarly as explained in sec. 4.8.1. Only a 2x2 transition matrix was used. The population of Q_B^- in the dark and the absorption of the same was left variable. No contribution of Q_BH_2 was allowed. The fit quality was not altered by the population or the absorption of Q_B^-.

7.1.2 Dark state and plastoquinone pool depletion

Table 7.1: Quinone and S-state populations in the dark and after the first flashes in PSII membranes without preflashes. Dark S-state distribution are assumed. Q_A^- reduced after the first flash and upper limit of Q_B^- found here.

	Dark	**Flash 1**	**Flash2**	**Flash10**
Q_A	Neutral	30 % Reduced 70 % neutral	30 % Reduced 70 % neutral	Reduced
H_2PQ	???	dark	dark +1	dark + 4-5
Q_B	$>65\%$ oxidized	mainly reduced	dark -1	dark - 4-5
Binding Pocket	partially filled	Filled Q_B^-	partially filled	mainly empty
S- States	25 % S_0	3 % S_0 30 % S_1 68 % S_2	6 % S_1 34 % S_2 60 % S_3	all states mixed

Table 7.1 describes the distribution of states in dark adapted PSII membranes and after several flashes. All quinones Q_A are in their neutral state. 30 % of stable Q_A^- in higher flashes are obtained in this section. However, some fraction of the quinone Q_B may be reduced. Here we found 65 % present already in the dark, [Pham and Messinger, 2016] found up to 20 % of Q_B^- without applying a preflash. The amount of S_0 was assumed.

The left panel of figure 7.2 shows the normalized variable chlorophyll fluorescence over 32 flashes compared for PSII membranes and thylakoids. A rise of the fluorescence represents the reduction of the plastoquinone pool (see [Krivanek et al., 2007]). Dynamics slower than 100 ms are usually assigned to recombination events involving of Q_A^- in PSII, that can not take up fresh Q_B. In bright colors a measurement of the thylakoid particles is shown. Up to eight flashes can be applied without a significant rise and without a strong damping of the quaternary pattern of the early fluorescence. This means for each PSII at least four quinones are available. After a rise and about 14 flashes a plateau is reached. Here the amount of freshly formed Q_BH_2 by PSII, the amount of recombining Q_A^- in empty Q_B-PSII and the reduction by Cytochrome b6f is in equilibrium. The latter has a turnover-half-time of 1.5-15 ms ([Antal et al., 2013]). The darker data in figure 7.2 is measured on PSII membranes. Already after the first flash less Q_A^- becomes oxidized by Q_B (higher fluorescence before the second flash). This means, that not every PSII can take up a quinone, either due to insufficiently numbered quinones in the membrane pool or due to more damaged centers at

the acceptor side (e.g. by detergent treatment). The onset of the rise starts already after the second flash. The slow down of the kinetics rather after the fourth flash. This indicates, that this preparation contains less quinones (2nd flash) and less cytochrome (earlier rise). After about 12 flashes the rise saturates. Opposed to the thylakoid preparation more than half of the oxidation occurs with slow recombination kinetics. If no cytochrome at all was present and all quinones were oxidized in the beginning, about 6 plastoquinones per PSII are found.

The right part of figure 7.2 compares the SFIR data at 1478 cm^{-1} (black) with the raw variable fluorescence (gray) of PSII membranes (different sample). At 1478 cm^{-1} the maximum at the first flash represents the reduction of all Q_A and the maximum of the second the sum of Q_A^- and Q_B^-, in created by the first flash in some centers. The variable fluorescence is projected onto the first flash. In both data sets the rise starts after the fourth flash. As we are going to compare this data in detail, we can be sure that the first 3-4 flashes will sense the same reactions.

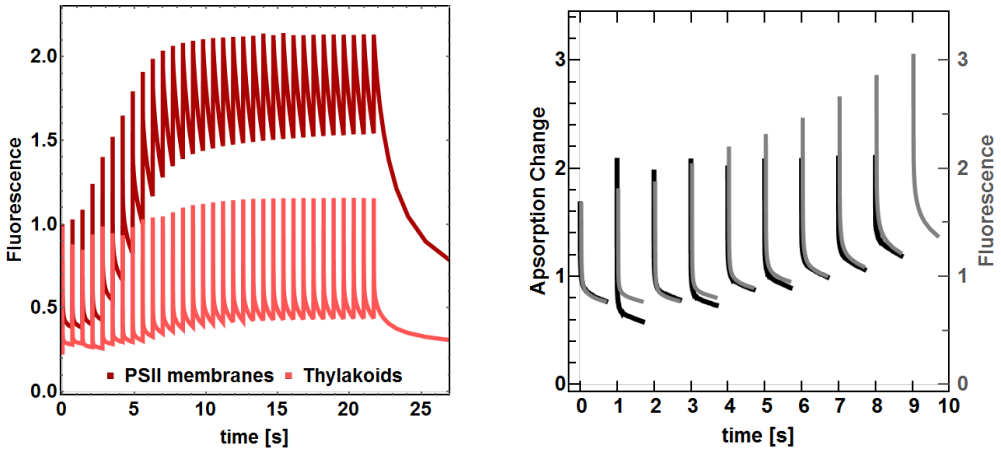

Figure 7.2: Pool depletion in PSII membranes and thylakoids at room temperature and pH 6.2: *left*: 32 flashes of PSII membranes and thylakoids from spinach. Raw variable fluorescence – normalized at the first flash. *right*: absorption change tracked at 1478 cm^{-1} (black) vs raw variable fluorescence (gray) of PSII membranes. Both in arbitrary units normalized at the first flash.

7.1.3 Steady state difference spectra of accumulating species

In figure 7.3 a difference spectra of the first transition (S_1 & $Q_A \rightarrow S_2$ & Q_B^- & (Q_A^-)) is compared to a difference spectrum obtained by subtracting the dark state from the state obtained after the 10th flash (top, S_1 & $Q_A \rightarrow S_{mix}$ & Q_BH_2 & Q_A^-). Below the double difference spectrum is presented showing the S_2 & Q_B^- & (Q_A^-) $\rightarrow S_{mix}$ & Q_BH_2 & Q_A^- transition. In the top of panel B the relating state is the one obtained after the first flash. In black the transition towards S_3 & Q_BH_2 is shown. In blue below again the double difference.

The spectrum of the first flash transition does not significantly differ from the $S_2\ Q_B^-/S_1\ Q_B$ measured by Zhang et al. ([Zhang et al., 1998]) and shall therefore not be described in detail. It must be noted that the amount of reduced Q_A^- seems to be higher in our measurement judging from the ratios of the 1718 and 1747 cm^{-1} peaks ([Kato et al., 2016]). The recording time in [Zhang et al., 1998] was 4.44 s measured 4.44 s after excitation. This is time enough for the remaining Q_A^- to recombine. The difference spectrum of the tenth flash minus dark

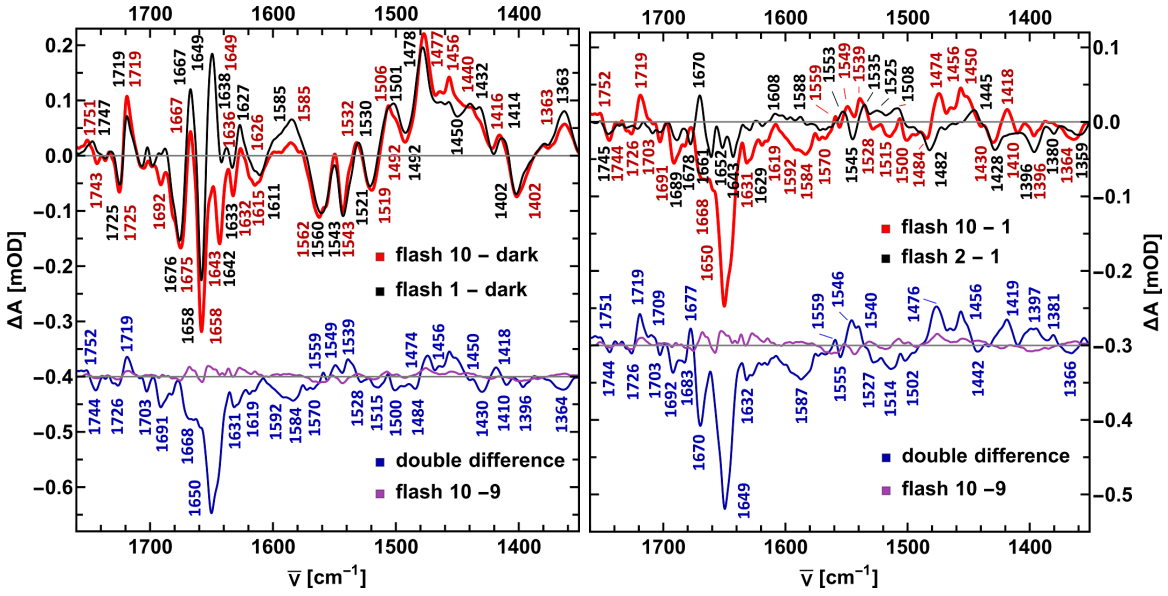

Figure 7.3: *left:* Steady-State difference spectra for the 1st flash transition (black) and the data after flash 10 minus dark (red). Below the double difference spectrum (blue) and for comparison the 10th flash transition (purple). *right:* Steady-State difference spectra of the 2nd flash transition (black) and the data obtained by subtracting the 1st flash data from the 10th (red). Below the double difference spectrum (blue) and for comparison again the 10th flash transition (purple) Averaged has been from 600 to 840 ms after the flash, the purple trace over the first 360 ms.

(*left*: red) is obviously dominated by the changes induced by the first flash (*left*: black). When comparing it to the second flash transition (*right*: black) all changes are by a factor of 3-4 smaller. Nonetheless, in the right panel it is visible, that there are bands accumulating over 10 flashes clearly above the noise level.

To have an idea which band originates in accumulated species and which are canceled during the photocycle the tenth minus ninth flash difference spectrum is also shown in the bottom in purple. As one can see in the last flash nearly no additional changes occur indicative for an already depleted quinone-pool and a high S-state mixing.

Amplitudes of other bands strongly increase relative to the dark state with every flash. The most pronounced growing negative bands are at 1649 and 1670 cm^{-1} (*blue spectra*). It needs to be mentioned that within the first flashes the signal is overlapping with (positive) amide vibrations and other contributions not related to the quinone side. In our measurements the pattern exhibit both contributions of binary and quaternary sources. We assign the accumulating part of the band at 1649 cm^{-1} mainly to the C=O antisymmetric stretching of the neutral plastoquinones (in solvents: [Berthomieu et al., 1990], simulatin, solvent, in PSII: [Razeghifard et al., 1999], simulation:[Ashizawa and Noguchi, 2014]). These may overlap with the vanishing bending vibrations of the two water, oxidized during the two complete catalytic cycles. The band at 1670 cm^{-1} may be the same vibration caused by an asymmetric H-bonding of the oxygens ([Ashizawa and Noguchi, 2014]).

Positive bands from 1400 to 1480 cm^{-1} in the spectra are assignable to the reduced quinone and quinol species. They all show a clear binary pattern up to the sixth flash. The reduced quinones were also identified by theoretical calculations as well as present in UV generated

radicals of model compounds in solution ([Razeghifard et al., 1999], [Burie et al., 1995]). The common interpretation is that the lower wavenumbers refer to methyl group vibrations (neutral and reduced quinones), the intermediate to coupled C=O/ring CC (sym and asym) and the peak around 1478 cm^{-1} to the C=O groups of the reduced quinones. The discussion of individual peaks will be done in the next section.

The positive band at 1719 cm^{-1} is commonly assigned as a marker band of the Q_A^-/Q_A spectrum. It was shown, that this band does not shift upon H_2O/D_2O exchange ([Berthomieu et al., 1990]). The tentative interpretation, that it is caused by a protonation event of a carboxylate induced by the Q_A reduction was therefore ruled out. [Suzuki et al., 2005] interpreted it as a vibration of a C=O group of the pheophytin next to Q_A. A feature at 1747 cm^{-1} is positive in our first flash data and negative in the second flash. Also it exhibits a binary flash pattern. Interestingly in both double difference spectra it is close to zero. Therefore it matches well the interpretation as a Q_B^- marker band, also not shifting upon deuteration. [Suzuki et al., 2005] assign it to the corresponding pheophytin at the D1-side.

This all indicates that the shown double difference spectra mainly reflect negative contributions from the reduction of the neutral Q_A in all photosystems, and positive features a mixture of reduced quinones Q_A^- and formed Q_BH_2. The bands of neutral quinones are of higher intensity than the reduced form and of much higher intensity than the accumulated plastoquinol Q_BH_2.

Miss factor

A proof that the PSII membrane particles are active and the OEC is undergoing photocycling, can best be seen by a damped quaternary pattern present at specific bands. For example a band, attributed to the symmetric stretching of so far not identified carboxylate groups around 1400 cm^{-1} ([Nakamura and Noguchi, 2016],[Debus, 2016]), shows a strong quaternary pattern around the baseline (fig. 7.4, *top*). Another good example is the amide II band at 1544 cm^{-1} (fig. 7.4, *bottom*).

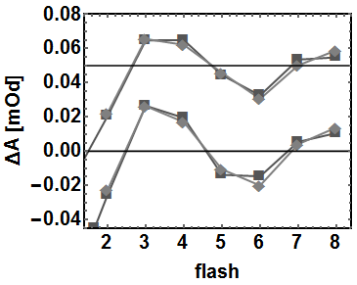

Figure 7.4: Cycling of the donor side in the FTIR: data in black, simulation in gray, assuming 25 % S_0 and 75 % S_1. *top:* 1400 cm^{-1} with 12 ± 3 misses; *bottom:* 1545 cm^{-1} with 14 ± 3 misses

As we have not applied a preflash in the SFIR experiment to synchronize the S-states of the Mn-cluster, a distribution of states in the dark will have a stoichiometry of about 1:3 for S_0 to S_1 (see tab. 7.1). A simulation of the flash number dependent amplitude pattern at both wavenumbers when neglecting the first flash and assuming the mentioned S-state distribution, results in misses of 12 ± 3 and 14 ± 3 % (simulation in gray of fig. 7.4). The fit quality decreases from the 6th flash onward. This result is only slightly worse than what we obtain with added electron acceptor (typically 8-10 %, see following chapters).

7.1.4 Time resolved spectra of reduced quinones and frequency selection for high time resolution

Figure 7.5 shows the spectral region symmetrically around the main $\nu(CO)$ peak of the reduced quinone species at 1478 cm^{-1} for the first six flash induced transitions measured at pH 6.2 and room temperature. Black lines represent the FTIR difference spectra averaged

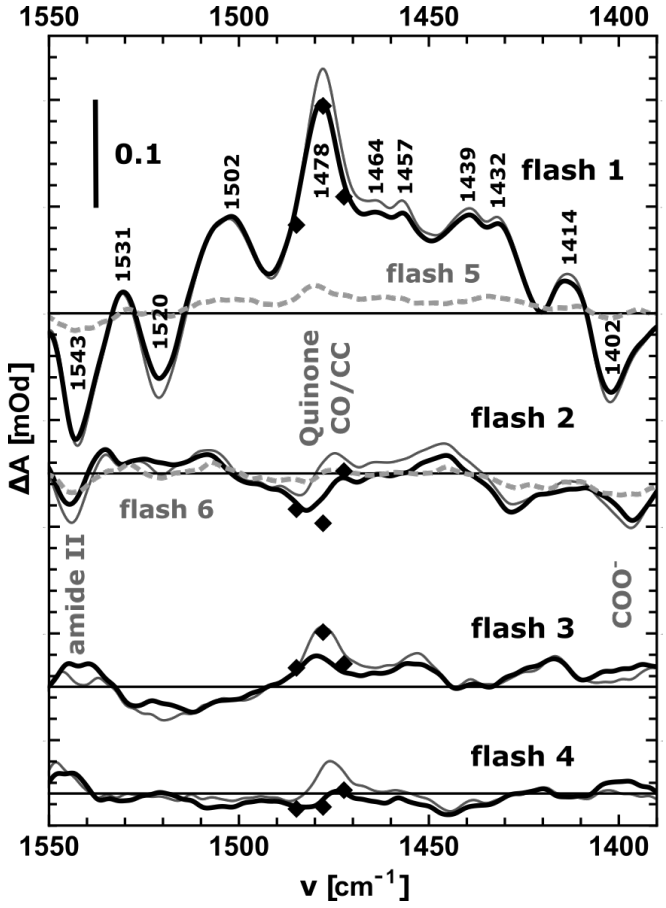

Figure 7.5: FTIR rapid scan difference spectra on PSII membranes at pH 6.2 without PPBQ and data points of the three sf-transients (x 0.25,1472.5, 1478 and 1485 cm^{-1}) after the indicated flashes (1 s spacing). The lighter curves are averaged over 120 ms, the dark curves and the sf data points from 360 to 840 ms, dotted curves are spectra of the subsequent photocycle obtained four flashes later. Marked are the strongest peaks belonging to the $\nu(CO)$ stretch of the reduced quinone species around 1478 cm^{-1} cycling with a period of two, and two bands cycling with a period of four assigned to amide II vibrations at 1545 cm^{-1} and a $\nu_{sym}(COO)$ vibration around 1400 cm^{-1} indicating the integrity of the cycling PSII.

from 360 to 840 ms (dashed for flash 5 and 6), light grey curves show the average over the first 120 ms. The single frequency transients at 1475, 1478 and 1485 cm^{-1} are shown as points (360-840 ms). The amplitudes of these transients are scaled by a factor of 0.25 as the absolute optical density is about four times higher (see sec. 4).

Positive bands in the first and third flash transition from 1450 to 1490 cm^{-1} are well assignable to the coupled CO/CC stretching vibrations of reduced quinone and quinol species. The vibrations were identified by theoretical calculations as well as present in model compounds in solution, or in PSII, when removing OEC contributions ([Burie et al., 1995], [Razeghifard et al., 1999], [Ashizawa and Noguchi, 2014]). They all show a clear binary pattern up to the sixth flash. The broad shoulder at lower wavenumbers is assigned to coupled vibrations of methyl group bending (neutral and reduced quinones), H-bonding partners as

the histidine 252 near Q_B, and coupled CO/ring CC. The peak around 1478 cm^{-1} origins mainly from the CO stretch of the reduced quinones.

The changes of the quinones in the first flash signal are about four times higher in amplitude than in the third flash. In the first flash transition a fraction of Q_A^- stays reduced in inactive centers, as the marker band at 1719 cm^{-1} and a side peak at 1455 cm^{-1} are very pronounced ([Berthomieu et al., 1990], [Kato et al., 2016]). In intact centers mainly Q_B^- is present after the first flash. Therefore,the negative signal at 1482 cm^{-1} reflects the vanishing of these reduced Q_B by the formation of Q_BH_2. From this, the pure Q_B^- CO vibration can be determined at 1482 cm^{-1} (compare [Nagao et al., 2018]). The positive or close to zero signal in the second and fourth flash from 1450-1475 cm^{-1} (not 1444 cm^{-1}: period of 4) indicates quinol contributions as observed for ubiquinol-10 at 1470 cm^{-1} in photosynthetic membranes of the purple bacteria Rhodobacter sphaeroides ([Mezzetti et al., 2003]).

In the figure also bands sensing the events of the Mn cluster undergoing the photocycle can be seen by a damped quaternary pattern present at specific bands: 1390-1408 cm^{-1} ($\nu_S(COO)$), 1495-1510 cm^{-1} ($\nu_{AS}(COO)$ and amide II) and 1530-1548 cm^{-1} (amide II), assignments from ([Noguchi and Sugiura, 2003]).

7.1.5 Time resolved single frequency transients of the reduced quinones

The single frequency transients induced by flash one to four and corrected for an excitation laser induced heat artefact are presented in figure 7.6. Wavenumbers are indicated next to each trace. All curves show an initial instant rise resulting from the rise time of the 10 MHz preamplifier. A sharp maximum is observed around 80 ns. This sharp feature decays in all flashes within 100 ns and is temporally not fully resolved. Especially in flashes two to four decay kinetics faster than 50 µs can be observed (sec. 7.1.10). Around 100 µs the noise of some transients increases, as here the infrared laser is less stable. At 100 µs after the first flash the amplitude is by about 30 % higher as in later flashes. This difference reflects well the differences between flash one and three presented in figure 7.5 (black traces). It indicates, that a fraction of 30 % of PSII do not cycle.

The µs decay is followed by a major decay within the first ms. In the first and third flash the biggest changes are observable at 1472 and 1478 cm^{-1}. Whereas the decay faster than 10 ms is less pronounced at 1485 cm^{-1}. The fast and strong decay at the lower wavenumber side of the peak and a weaker at 1485 cm^{-1}, results in a decay concerted with a line-shift. The rise at 1485 cm^{-1} and the decay at 1472 and 1478 cm^{-1} within 10-50 ms will result merely in a shift toward 1485 cm^{-1}. As the main band of Q_B^- was identified in PSII membranes around 1480 cm^{-1} and the Q_A^- band around 1477 cm^{-1} we assign both decays (1-2 ms and 10-20 ms) mainly to the electron transfer from Q_A^- to Q_B. The faster phase seems to be mixed (no 1485 cm^{-1} rise) with the similar fast process of the even flashes where all curves show a strong decay and no shift can be identified. This process is therefore assigned to the electron transfer to Q_B^-, which forms after binding of two protons Q_BH_2, meaning a stronger decay due to the loss of both reduced quinone species. A small fraction of the signal decays in all transitions over hundreds of ms and is related to recombination events.

A strong damping of a binary oscillation can be observed, when comparing the final value of each wavenumber after the different flashes (see also appendix, fig. 11.15). In odd flashes Q_B^- is formed in most of the centers and contributes to the absorption. In even flash-numbers the remaining amplitude is very close to (1472.5 cm^{-1}) or below zero (1478/1485 cm^{-1}). At 1485 cm^{-1} the negative amplitude in the second flash is of a similar order as in the third flash. Here the reduction of Q_B and its oxidation are observable and Q_BH_2 seemingly does

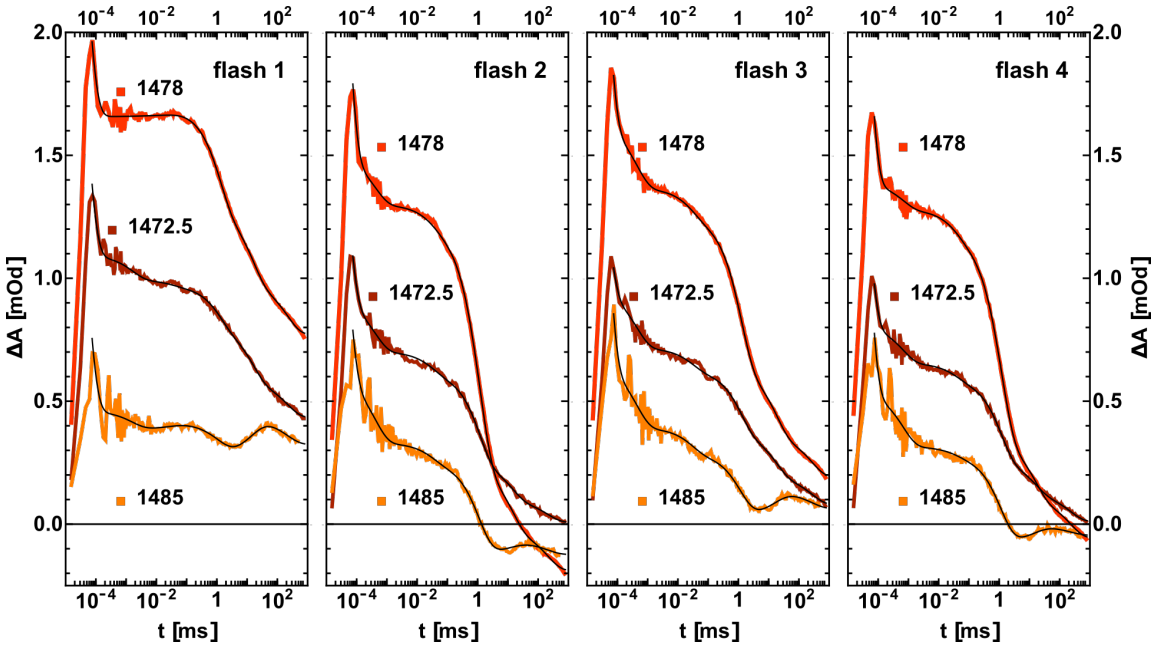

Figure 7.6: Single frequency IR transients of wavenumbers around the $\nu(CO/CC)$ vibration of the reduced quinones Q_A^- and Q_B^- after the first four flashes (1 s spacing) measured on PSII membranes at pH 6.2 and room temperature. Wavenumbers given in cm^{-1}. Six exponential least-square fits with shared decay times for each flash are shown as black lines. A small fraction of a signal sensing the $P680^+$ reduction decaying within 50 µs contributes as well. Main absorption changes by the re-oxidation of Q_A^- is visible in all curves starting around 30 µs with a fraction of Q_A^- not being re-oxidized after its formation by the first excitation. The values at 800 ms show a period of two pattern indicating the stable Q_B^- with positive amplitudes and its second reduction/formation of Q_BH_2 as negative amplitudes.

not contribute. At 1472.5 cm^{-1} the steady state values are in all flashes positive reflecting contributions of Q_B^- in odd and of plastoquinol in even flashes. The formation of the latter causes stronger changes than the vanishing of the Q_B^- absorption.

To extract the rate constants and the corresponding amplitudes a global fit approach with six exponentials and shared decay times was applied. The fit ranges from 80 ns to 800 ms as presented in figure 4 (black lines).

7.1.6 Global fit results of the single frequency data in comparison with variable chlorophyll fluorescence

In the SFIR data (figure 7.6) the only flash number dependent amplitudes, cycling with a period of four, are present at times below 50 µs, where no binary contributions are observed. All later amplitude patterns are purely binary except for the small slow 200 ms phase, which has no flash number dependency. Therefore,the increase in absorption from zero to the value at around 50 µs is interpreted as the creation of Q_A^-. Based on the assumption that the dynamics of the connectivity-corrected variable chlorophyll fluorescence later than 200 µs reflect solely the reoxidation of Q_A^-, we compare the dynamics of the maximum of the IR

band of the reduced quinones at 1478 cm^{-1} with the (supposed) Q_A^- concentration, $[Q_A^-](t)$, extracted from the fluorescence via equation 4.2.

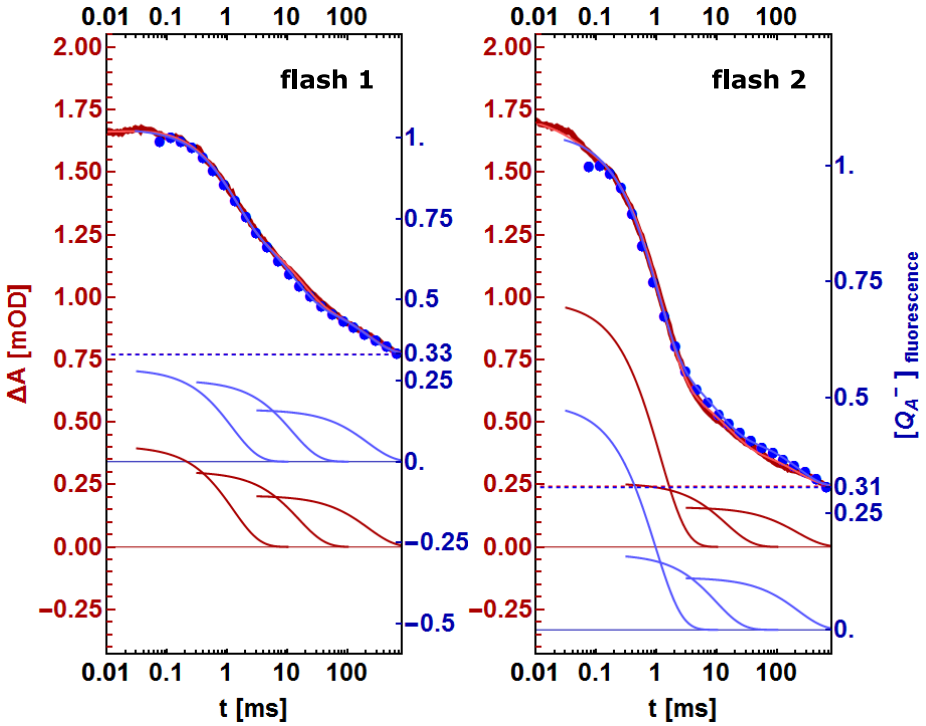

Figure 7.7: Dynamics of the SFIR transients at 1478 cm^{-1} (red) and the amount of reduced Q_A estimated from the variable fluorescence (blue) for the 1st and 2nd flash both for PSII membranes at pH 6.2 and room temperature. I added to the 2nd flash of the SFIR the absorption corresponding to 33 % Q_A^-. The total decay of the fluorescence data was normalized to the one of the SFIR data. The components of the multi exponential fits (6 exponential global fit for the single frequency data, 3 exponential fit for fluorescence) with the same normalization are shown in the corresponding color. The dashed lines are the fit constants. (result of four exponential function shown in fig. 11.17)

Dynamics

The $[Q_A^-](t)$ was fitted with a three exponential function starting at 100 µs. The time resolution of the experiment is not high enough to resolve the rise observable earlier. The decay of the $[Q_A^-](t)$ (blue) was projected onto the decay of the SFIR transient (red), shown for flash 1 and 2 in figure 7.7. The fit components of both data sets are shown below. Both decays show the same behavior and the fit-components differ only slightly. As the two data sets match very well, one can directly verify the Q_A-redox-state dependent interpretation of the fluorescence and the assignment of the reduced quinone vibration tracked in the infra-red.

The final value of the $[Q_A^-](t)$ fluorescence tells us that about 30 % of Q_A do not become oxidized. This level stays constant after the first four flashes as expected for a sufficiently sized plastoquinone pool[1]. In figure 7.7 we added the amplitude change at 1478 cm^{-1}, corresponding to the remaining 33 % of Q_A^- of the first flash, to the IR data of later flashes.

[1] this shows a weak quaternary period, see e.g. [Putrenko et al., 1999]

Now the initial amplitude of each flash stays about constant up to the fifth flash as expected, because initially 100 % of Q_A are reduced. After later flashes (5-9) the fraction of the initial Q_A^- decreases as the quinone pool starts to deplete and more closed centers remain after 800 ms.

The fit results of the fluorescence and the line at 1478 cm^{-1} (global fit) are presented in figure 7.8. The total amplitude of the decay (with decay times of ms) was used to normalize the components, yielding a *relative* decay. This is necessary, because the magnitude of decay in the IR depends on, whether Q_B or Q_B^- take up an electron. The decay constants of the global IR and the fluorescence fit roughly were in the order of a ms, 10-15 ms and about 200 ms (fig. 7.8, A). The results of the simulation are summarized as well in the scheme shown in figure 7.9.

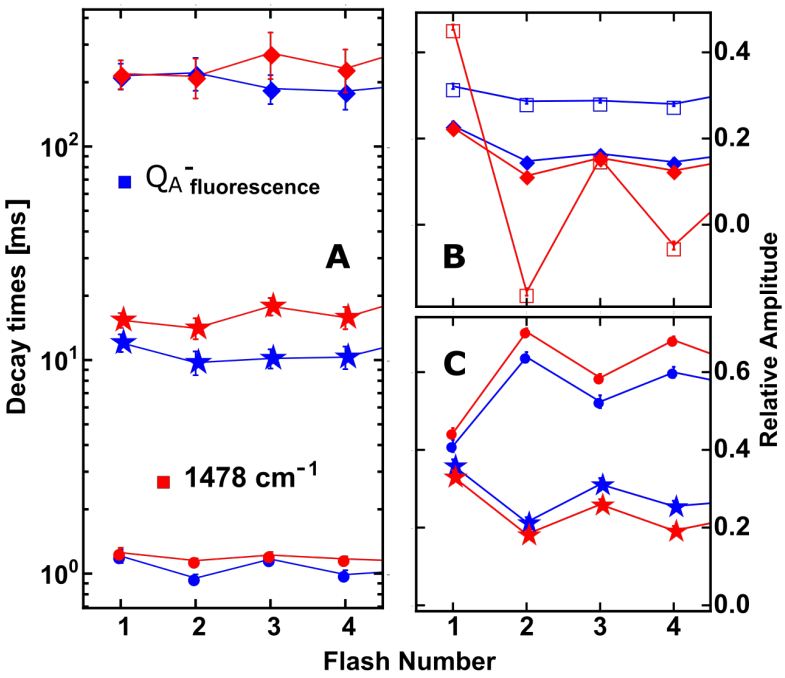

Figure 7.8: Simulation parameters for transients of variable PSII fluorescence (blue) and infrared absorption at 1478 cm^{-1} (red) detected for PSII membranes excited with a sequence of saturating flashes of green laser light (532 nm, flash duration of ca. 5 ns, flash spacing of 1 s). (A) Time constants of the multi-exponential decay function; (B, C) corresponding amplitudes divided by the total quinone related decay (filled symbols) and absolute constant term (empty squares). The simulation parameters were obtained by least-square curve-fitting of the transients initiated by the 1st, 2nd, 3rd, and 4th laser flash applied to the dark-adapted PSII particles (at pH 6.2 and room temperature, result of four exponential function shown in fig. 11.17).

The fastest decay, characterized by a binary flash-number dependence (circles, fig. 7.8 A), has a decay time of 1.2 and 1.1 ms for odd and even flashes in the infrared. It is interpreted as the forward electron transfer from Q_A^- to an occupied Q_B-site meaning in odd flashes mainly to a neutral Q_B and in even flashes mainly to Q_B^-. In the fluorescence data the decay times are found by 1.2 and 1.0 ms. The amplitudes are smaller in odd flashes at all three

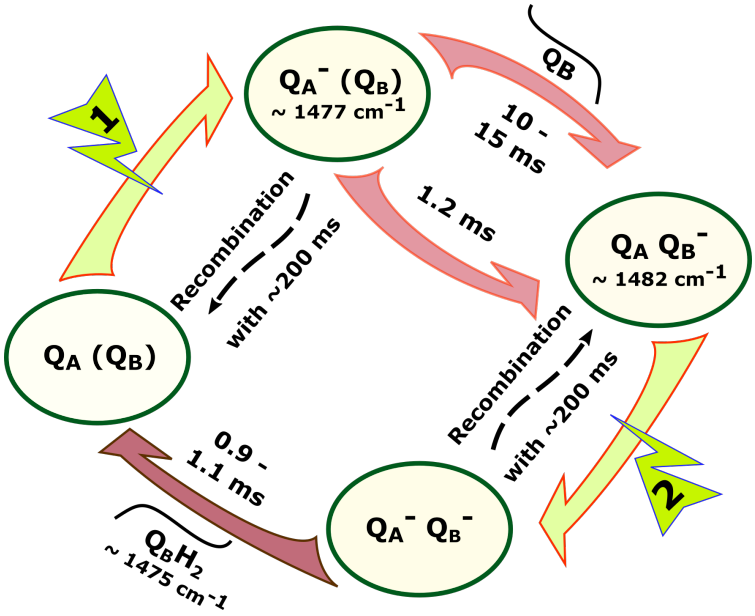

Figure 7.9: Reaction cycle of inter quinone electron transfer. Kinetics at pH 6.2 taken from the fit results presented in figure 7.8. Absorption of Q_A^- from flash 10 minus dark, Q_B^- from the negative absorption in flash 2, Q_BH_2 from flash 10 minus flash 1 and flash pattern of transient at 1472.5 cm^{-1}. Note, that in our samples in the dark some Q_B^- is bound which will increases the uncertainty of the kinetics.

wavenumbers and in the fluorescence data. In these flashes the majority of centers does either have a neutral Q_B bound or an empty Q_B binding site, therefore the amplitude change is split into at least two kinetically distinct processes (see fig. 7.9). In contrast the Q_B^- is tightly bound, thus the transients decay strongly within the first ms in even flashes.

In odd flashes the amplitude of the 10-20 ms decay phase is higher than in even flashes (stars, fig. 7.8). We can assign this decay to the uptake and subsequent reduction of quinones by the centers with an empty Q_B side. Comparing the amplitude after the 1st and 2nd flash, a fraction of Q_B^- bound in the dark of 35 % is obtained. In contrast to the other decay processes the 1485 cm^{-1} transient shows a rise with this phase (fig. 7.6). The absorption of Q_B^- seems to dominate at this wavenumber. In the 1st flash the faster (1ms) phase does not manifest in a rise as the reduction of 35 % of Q_B^- (absorption loss of Q_A^- and Q_B^-) is overlapping with the fraction of bound Q_B (loss of Q_A^-, gain by Q_B^-).

The dynamics observed here are located in between the ones obtained by [de Wijn and van Gorkom, 2001] at pH 5.5 and 6.2. They found a faster uptake in their thylakoid sample, but also only fitted up to 10 ms. The results compare very well to the ones obtained on PSII membranes at pH 6.5 by [Putrenko et al., 1999].

Both fast ms amplitudes add up to 80 - 90 % of the decaying part of the [Q_A^-] and the 1478 cm^{-1} signal. The remaining part decays with 200 ms (rhomb, fig. 7.8 A and B). We observe that the amplitudes of both the ms and the 10 ms phase start to decrease from the sixth flash onward, in contrast the 200 ms amplitude and the fit constant both increase because of the quinone pool depletion. This phase therefore needs to be a recombination process and its spectrum is discussed in section 7.1.9. Decay times of the recombination recorded below one second were attributed to a recombination between $Y_Z^{\bullet ox}$ and Q_A^- ([Metz et al., 1989], [Zhang et al., 1997]) or electron transfer from Q_A^- to Cyt b559 with 100 ms. Recombinations

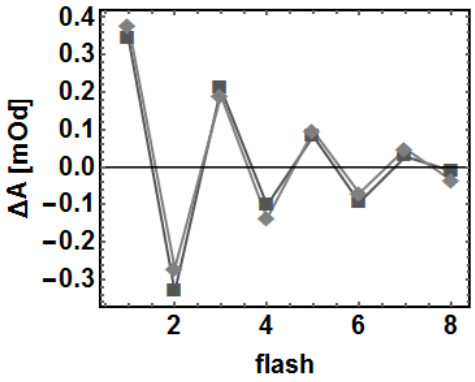

Figure 7.10: Absorption difference of the transient at 1478 cm^{-1} only of Q_B reduction and re-oxidation of PSII membranes. The IR amplitude of the first flash corresponding to the fraction of non-cycling PSII is taken from the value of the variable PSII fluorescence at 800 ms. This non-cycling fraction is subtracted from the absorption at 800 ms. For later flashes only the absorption at 800 ms is taken (dark squares). A simulation with a missfactor of 14 ± 2 % is shown in gray colors. The correspondence of fit and data especially for the first flash suggests a good estimation of 33 % of non-cycling centers. As this value is increasing with higher connectivity parameters, p=0.3 is a good value for the correction in PSII membranes.

of higher S-states with Q_A^- are reported to be slower with the fastest phase of around 1 s ([Zhang et al., 1998], [Rappaport et al., 2005], [Rantamäki and Tyystjärvi, 2011]). The kinetics point to a recombination process either involving Q_A^- with Q_B un-fill able and $Y_Z^{\bullet ox}$ or Q_A^- and Cyt b559.

SFIR steady state values corrected with the variable chlorophyll fluorescence

We can look again at the steady state values at 1478 cm^{-1}. Only half of the initial signal decays after the first flash. The remaining signal can be split into two parts: (I) contribution from Q_A^- of inactive centers. The amount of remaining Q_A^- is described by the $[Q_A^-](t)$ fit constant giving 33 % of Q_A^- after the first flash (indicated on the axes in fig. 7.7). What remains in the IR, is (II) the absorption of Q_B^- yielding about 20 % of the initial Q_A^- absorption. To understand the low fraction of remaining Q_B^- absorption we have to keep in mind that in the dark also a fraction of the occupied Q_B-side can be reduced. This results upon Q_BH_2 formation in a strong negative absorption after the first flash as both Q_A^- and Q_B^- vanish, and cancels some of the absorption of the newly formed Q_B^-.

In figure 7.10 only the final absorption of cycling centers at 1478 cm^{-1} is plotted (black points). For the first flash the absorption corresponding to 30 % of non-cycling PSII was subtracted from the value at 800 ms. For later flashes the absorption at 800 ms is shown. This flash pattern shows a very symmetric behavior around zero. A simulation (grey points) of the pattern gives a miss factor of 14 ± 2 % comparing well to the mean of 13 ± 2 % of the FTIR-donor side pattern at 1398 and 1545 cm^{-1} (fig. 7.4). The simulation also states that 32 ± 2 % of pre-reduced Q_B are bond in the dark and that the absorption at 1478 cm^{-1} of Q_B^- is 1.2 mOd which is about 90 % of the absorption of Q_A^- in cycling centers. These value for the absorption and pre-reduced Q_B^- are coupled in the simulation and do not influence

the fit quality – only the errors of both values are minimized. These 32 ± 2 % match well the estimate of 35 % obtained from the Q_B uptake pattern.

Because when applying equation 4.2, the amount of non-cycling PSII depends on the connectivity (see 11.19), one result from the pattern presented in figure 7.10 is that the first flash is well corrected by the amount of closed centers at p=0.3.

7.1.7 Electron transfer to Q_B at pH 7.5

The motivation to measure the quinone electron transfer in elevated pH, is the observation by [de Wijn et al., 2001] that their electron transfer phase to bound Q_B is faster than ours. They measured at a pH of 5.5, where the electron transfer was slowed down by a factor of two to three compared to pH 6.5. At a pH of 7.5 the transfer to Q_B and Q_B^- was found with 0.32-0.35 and 0.73-0.83 ms and the uptake by 2.6-3.3 ms. I want to reproduce this in order to test the experiment and verify the results discussed above, In *figure 7.11* the two measurements are compared. The left panel shows the transients normalized to the value at 10 µs (pH 7.5 in dark, pH 6.2 in bright).

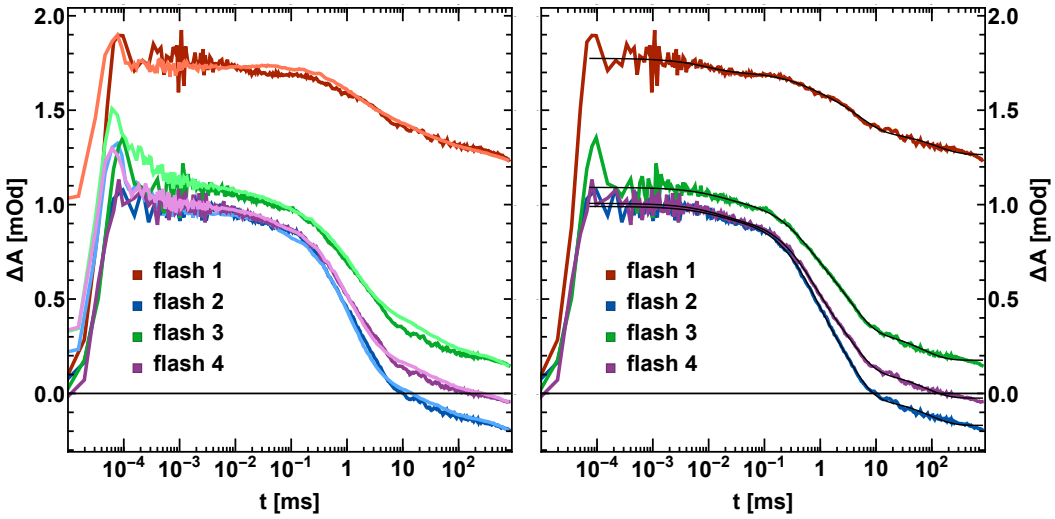

Figure 7.11: *left:* Quinone dynamics at pH 7.5 (dark, 15 µm) and pH 6.2 (light, 25 µm) measured at 1478 cm^{-1} and normalized at 10 µs. *right:* a four exponential fit of the pH 7.5 data. Results presented in table 7.2.

The first observation is the absence of the decay phases faster than 10 µs in the pH 7.5 data set, most pronounced in flash two and three. I will discuss this observation in *chapter 9.4.4* and focus here on the quinone reactions. The second observation is the much higher signal in the first flash compared to the third flash (compare with fig. 7.6). From this we can estimate the amount of cycling centers by dividing the amplitudes in the third and first flash at 100 µs, that is $1.06/1.7 = 62\%$ at pH 7.5. At pH 6.2 we obtained about 70 %.

And finally we can see that the quinone dynamics do not differ dramatically, but the absence of the fast features will allow a clearer analyses of the Q_A^- reoxidation dynamic. A four exponential fit is presented as black lines in the *right* part of figure 7.11. In table 7.2 the results are presented.

The fastest phase found is decay with 10 µs. Its amplitude is very small and may be a residuum of the two fast phases of the pH 6.2 transients. The next decay is slightly faster in

odd flashes with 460 ± 70 µs, when more Q_B is bound, and a bit slower in odd flashes with 574 ± 50 µs to Q_B^-. The amplitude is higher in odd flashes. The slow phase found is now with 3.3-3.6 ms relatively fast (pH 6.2 10-15 ms). The amplitude is more or less constant except in the first flash. The slowest phase is found to be between 70 and 120 ms. This compares very well with the results obtained by [de Wijn et al., 2001] mentioned in the beginning. Again our fastest phase seems to be a mixture of the 0.32-0.35 ms and 0.73-0.83 ms found for Q_B and Q_B^-, respectively.

Table 7.2: Fit results of the pH 7.5 transient just at 1478 cm^{-1}: all times in ms and amplitudes in mOd. Fitted interval: 150 ns - 800 ms

	c	a_1	t_1	a_2	$\mathbf{t_2}$	a_3	$\mathbf{t_3}$	a_4	t_4
flash 1	**1.27**	0.07	0.010	**0.08**	**0.515**	**0.24**	**4.83**	0.12	119.
%		14		**16**		**47**		24	
σ	**0.01**	0.01	0.003	**0.02**	**0.200**	**0.02**	**0.71**	0.01	23.
flash 2	**-0.17**	0.06	0.013	**0.41**	**0.574**	**0.55**	**3.35**	0.15	90
%		5		**35**		**47**		13	
σ	**0.004**	0.01	0.003	**0.029**	**0.050**	**0.03**	**0.23**	0.01	11
flash 3	**0.18**	0.06	0.015	**0.25**	**0.462**	**0.45**	**3.40**	0.16	68
%		7		**27**		**49**		17	
σ	**0.004**	0.01	0.004	**0.02**	**0.068**	**0.02**	**0.30**	0.01	9
flash 4	**-0.025**	0.07	0.013	**0.37**	**0.574**	**0.45**	**3.59**	0.15	77
%		7		**36**		**43**		14	
σ	**0.004**	0.01	0.003	**0.03**	**0.052**	**0.03**	**0.30**	0.01	10

7.1.8 Dynamics of broken chloroplasts and PSII membrane fragments

As we just have seen, the kinetics of Q_A^- reoxidation depend strongly on the pH. In measurements of thylakoids at pH 6.5 and room temperature a decay time of 0.28 & 2.3 ms and 0.68 ms for the transition from S_1 Q_B and from S_2 Q_B^- were found([de Wijn and van Gorkom, 2001]). Fits were done up to 10 ms, resulting in a faster second phase compared to 700 ms (compare in table 7.13). For PSII membrane fragments at pH 6.3 half times of the phases in the transition from S_1 Q_B^- of 0.52 and 6.4 ms were reported ([Vass et al., 1992]) translating into decay times of 0.69 and 9.2 ms. Therefore the question was often raised whether the dynamics of thylakoids and PSII membrane fragments differ.

We measured both freshly prepared sample types at pH 6.2 and room temperature with the variable chlorophyll fluorescence setup. The left part of figure 7.12 shows the normalized raw data of flash 2 and 3 (flash 1 and 4 shown in 11.23). We can see that Thylakoids appear slightly faster in the second flash transition and much faster in flash 3. The corrected transients are shown in the left figure. Now the second flash looks nearly identical. The third flash data is still slower ins PSII membranes.

In table 7.13 the results of our simulations are presented (different sample than in other chapters). Without any correction for the connectivity of the PSII units the sample types differ drastically especially in flashes of odd number, in which Q_B is mainly in its neutral state (first four rows). Both forward electron transfer times (τ_1 and τ_2) differ by a factor of two to three, whereas the corresponding amplitudes are of similar order.

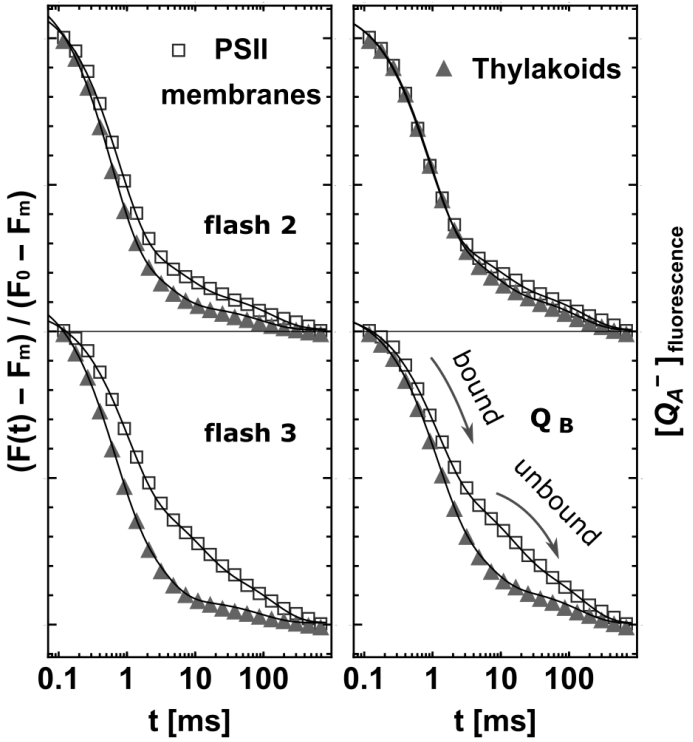

Figure 7.12: Normalized fluorescence transients of the second and third flash data for PSII membranes (empty squares) and thylakoid membranes (triangles) at pH 6.2 and room temperature. Left: no correction in Q_A^- nonlinearity has been applied (p=0). Right: connectivity parameter of p=.3 and p= .7 for PSII membranes and thylakoids respectively and equation 4.2 has been used. Shown is also a three exponential fit. The second flash transients match well after correction. The third flash transients do not match as good. The decay times and amplitudes of the simulation match after correction and only the ratio between fast and slow decay changes with less forward electron transfer to Q_B bound.

When correcting both measurements with equation 4.2 and p = 0.7 for thylakoids and p = 0.3 for PSII membranes the agreement in even flash numbers is perfect. Just the fraction of closed centers is in favor for the forward electron transfer in thylakoids slightly lower (5-15 %). Except for the first flash odd numbered flashes exhibit the very same fast dynamics as well. The Q_B uptake kinetics appear slower in PSII membranes. The main difference is the amplitude of the fast decay, which is by 0.2 units higher in thylakoids again in trade for the same amount of non-cycling centers in the PSII membrane. These 10 to 20 % more inactive units might be due to the harsh triton X-100 treatment (see e.g. ([Montoya et al., 1994], [Ruan et al., 2002])), as the measurements were conducted on samples of the same age and otherwise the same measurement conditions. In conclusion we can state that the apparent difference of thylakoid membranes and PSII fragments stems solely from a higher fraction of photosystems that can not take up plastoquinones. Otherwise the observed dynamics of both preparations are the same.

It is known that there is also a dependency of the minimal and maximal values of the fluorescence transient on the S-states of the Mn-cluster ([Putrenko et al., 1999]). It remains

partially after the connectivity correction in the fit amount of closed centers at the end of the measurement time, but only for thylakoids. This effect seems to be much smaller than the differences discussed.

Figure 7.13: Fit results of the variable chlorophyll fluorescence at pH 6.2 and 20 °C measured on PSII membranes and thylakoids from spinach. The normalized fluorescence is simulated in the first four rows. Then the results on connectivity connected samples is presented (with p=0.3 for PSII membranes and p=0.7 for thylakoids, see equation 4.2). Finally the simulation only ranged to 10 ms like in [de Wijn and van Gorkom, 2001].

	τ_1 [ms]		A_1		τ_2 [ms]		A_2		τ_3 [ms]		A_3		const	
	Thyl	PSII	Thyl	PSII	Thyl	PSII	Thyl	PSII	Thyl	PSII	Thyl	PSII	Thyl	PSII
Flash 1 $(F(t) - F_0) /(F_M - F_0)$	0.37	0.93	0.69	0.40	2.13	10.9	0.30	0.28	62	125	0.07	0.17	0.08	0.21
Flash 2	0.60	0.72	0.79	0.67	4.4	6.7	0.16	0.14	104	134	0.07	0.11	0.10	0.20
Flash 3	0.56	0.97	0.65	0.51	2.9	10.9	0.30	0.20	93	135	0.07	0.16	0.07	0.21
Flash 4	0.53	0.70	0.80	0.62	3.3	6.0	0.21	0.15	84	137	0.06	0.13	0.06	0.20
Flash 1 $[Q_A^-](t)$	0.70	1.0	0.58	0.34	4.9	12.9	0.23	0.28	118	146	0.10	0.17	0.16	0.25
Flash 2	0.93	0.85	0.63	0.61	8.1	9.6	0.14	0.13	144	165	0.10	0.11	0.19	0.24
Flash 3	1.07	1.10	0.60	0.44	5.8	13.2	0.21	0.19	142	154	0.11	0.17	0.14	0.25
Flash 4	0.92	0.83	0.69	0.56	7.4	8.9	0.19	0.13	162	165	0.09	0.14	0.10	0.25
Flash 5	0.92	0.95	0.58	0.44	8.2	15.1	0.2	0.11	154	225	0.11	0.17	0.16	0.33
10ms-fit														
Flash 1	0.60	0.84	0.50	0.29	3.0	7.2	0.30	0.30	-	-	-	-	0.27	0.46
Flash 2	0.90	0.76	0.62	0.56	6.9	4.3	0.17	0.17	-	-	-	-	0.28	0.37

7.1.9 Recombination spectrum

In the data acquired more than 120 ms after the excitation flash, the electron transfer between the quinones definitely finished ([Putrenko et al., 1999]). Thus, at this time only Q_B^-, Q_BH_2 and Q_A^- (in centers without an intact Q_B-side) are present and spectral changes occur mainly due to recombination events. Over time the peak of the band around 1477 cm^{-1} (Q_A^-) after the first and third flash shifts towards 1480 cm^{-1} (Q_B^-, fig. 7.5, gray – 30-120 ms – vs black lines – 360-840 ms). In figure 7.14 a difference spectrum in time (first 360 ms minus the average from 360 to 840 ms) averaged over all flashes is shown with bands at 1477 and 1719 cm^{-1} indicative for Q_A^- decay.

Typical features of the $S_1 \rightarrow S_2$ transition such as a strong positive band around 1585 cm^{-1} or a negative band at 1402 cm^{-1} (*shifted*) are not present, neither are the marker bands for the Y_Z radical at 1514 cm^{-1} and a band-shift at 1705(-)/1697(+), which is a marker for both the Y_Z and Y_D radical. Overall, the spectrum in figure 7.14 resembles closely the one recorded by ([Zhang et al., 1997]) of Tris-washed PSII membranes with added DCMU. Still some bands differ especially the negative bands at 1398 and 1560 cm^{-1} and the amide I region.

Very recently another supposed $Y_Z^{\bullet ox}$ Q_A^- recombination spectrum was published ([Guo et al., 2018]). They first trapped the S_2 state at 190 K and created then a $Y_Z^{\bullet ox}$ Q_A^- spectrum. Except for the amide I bands at 1640-1650 cm^{-1} and a weaker, but present

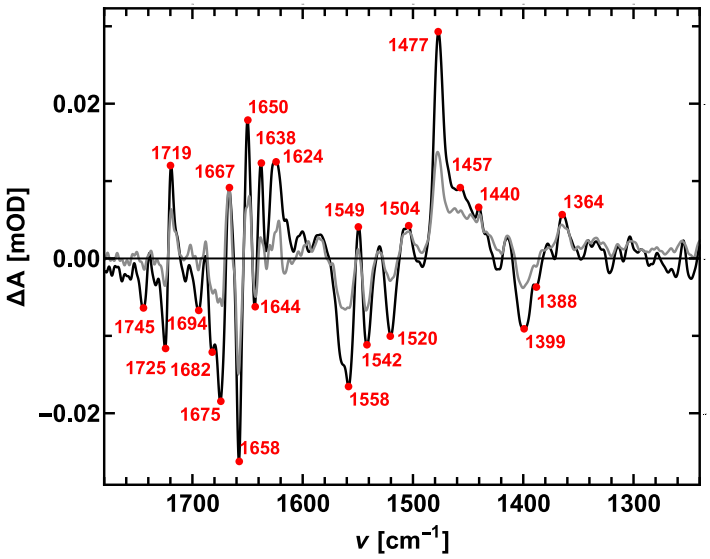

Figure 7.14: Difference spectrum reflecting the recombination: in *black* the difference of the average between 360 to 860 ms and the one of 1-120 ms. In *gray* the difference between 360 to 840 minus 120 to 360 ms is shown. The spectra of flashes one two twelve have been averaged. The black spectrum reflects well the spectrum obtained by Joachim Buchta on Mn-depleted PSII membranes. It has contributions from Q_A^- with marker bands at 1456, 1477 and 1719 cm^{-1}, as well as bands of the oxidized tyrosine, with marker bands at 1520 and 1504 cm^{-1}. As the Y_Z has bands rather at 1514 cm^{-1} a better assignment is the Y_D.

band at 1719 and 1399 cm^{-1}[2] the spectra are identical. They discuss their spectra under the assumption that the H-bonding properties of $Y_Z^{\bullet ox}$ are unaltered with S_2 present, but blocked. However, we will see in a later chapter that this is not the case, because we will find the $Y_Z^{\bullet ox}$ vibration at 1512.5-1515 cm^{-1} as in Mn depleted samples (sec. 8.4). They also interpret the bands at 1658 and 1675 cm^{-1} as amide I bands. As discussed above, I would prefer the perfectly matching band positions to the splitting of the neutral Q_A CO stretches ([Razeghifard et al., 1999], same group).

We suggest therefore that the recombination takes place in centers with an empty Q_B site – i.e. Q_A^-– and, tentatively, with a not fully intact Mn-cluster. The latter assignment is mainly based on the kinetics (discussed in sec. 7.1.6) and on the lack of clear Y_Z signals and the band at 1399 cm^{-1}, that only shows up in S-state difference spectra (see sec. 3.2 in $S_2 \rightarrow S_3$). Possibly the CO vibration of $Y_Z^{\bullet ox}$ is then shifted from 1513 cm^{-1} towards the Q_A^- signal, meaning that it changed its H-bond to His190 ([Berthomieu and Hienerwadel, 2005]). We can at the moment not exclude other options as the cytochrome b559.

7.1.10 A P_{680}^+ not a $Y_Z^{\bullet ox}$ signal overlapping at the quinone band

Because I wanted to compare the SFIR transients with the variable chlorophyll fluorescence, I did not mention the decay faster than 100 µs in the last sections. I want to present this now. The temporally not well resolved sharp feature at 80 ns does not show a clear flash number dependent amplitude pattern (*not shown*) possibly due to a flash number dependence

[2] and a baseline drift in theirs

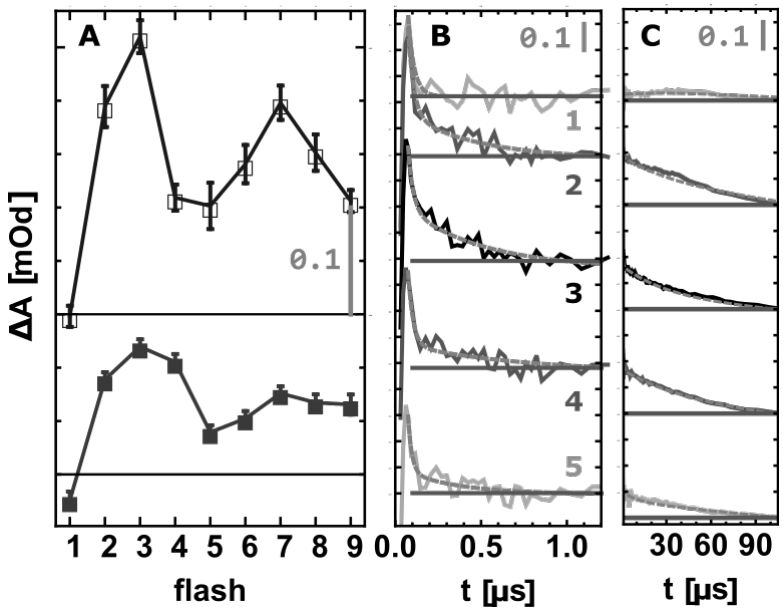

Figure 7.15: Fast decay of the transient recorded at 1478 cm^{-1} in PSII membranes at pH 6.2 and 20°C. A: Simulation amplitudes obtained from the six exponential global fit presented in fig. 7.6 for each flash. *Top*: 400 ns phase with clear maxima after the second and third flash when the Mn-cluster is positively charged. *Bottom*: amplitudes of the 35 µs phase with minima at the first and fifth flash in which no proton is released from the OEC. *B and C*: Zoom into the transients at 1478 cm^{-1} for the first five flashes. The time courses of B correspond to the 400 ns phase, the one of C to the 35 µs phase. The fit is presented as dashed lines.

of the decay time (fig. 7.6). The six exponential global fit results of the two fastest decay components at 1478 cm^{-1} are presented in figure 7.15 .

The right panels (B and C) show a zoom into the transient and the left (A) the amplitudes of the exponential functions after the first nine flashes. The averaged decay time of the upper panel is about 450 ± 50 ns. The quaternary pattern has a maximum at the 2nd and 3rd flash when the Mn-cluster is overall positively charged and minima at the 1st, 4th, 5th and 9th flash when it is neutral. The 35 ± 5 µs phase is minimized only at the 1st and 5th flash.

The ratio $S_0 \rightarrow S_1/S_1 \rightarrow S_2/S_2 \rightarrow S_3$ /$S_3 \rightarrow S_0$ of state-transitions in the third flash would be 0/6/31/49 %, in the fourth 42/1/10/34 % and in the fifth flash 35/37/2/12 % (see tab. 7.1). This means that either the amplitude of the 35 µs decay is high in all transitions except from S_1 to S_2 or only high in the transition from $S_2 \rightarrow S_3$ and $S_3 \rightarrow S_0$. The former is unlikely as the first flash signal shows nearly no decay, ruling out a contribution from $S_0 \rightarrow S_1$.

In both the S_2 and S_3 state the Mn-cluster is overall positively charged, thus slowing down P_{680}^+ reduction by Y_Z. A similar decay constant was reported for a rise in the fluorescence ([Schlodder et al., 1985]) as well as for the absorption change at 830 nm indicative for the P_{680}^+ reduction-kinetics ([Christen et al., 1998]). The absorption experiment was performed on PSII membrane fragments as well but at 4 °C and at pH 6.5. The origin of a 35 µs phase and the very identical amplitude flash pattern was assigned to a slow phase of the P_{680}^+ reduction in samples with an intact WOC, with a marked kinetic H/D isotope exchange effect, thus involving proton movement. Time resolved IR experiments can help to address

the nature of this proton. The 400 ns decay is also sensing P_{680}^{+} reduction but without an H/D kinetic effect (as reported before in ([Klauss et al., 2012b]). The possible observed vibration around 1480 cm^{-1} are carboxylate residues of amino acids sensing the positive charge at Y_Z and a change of a hydrogen bond network (H/D-effect) or a broad but weak absorption of the P_{680}^{+}, as has been reported for the P^{+} state of the bacterial chlorophyll in the bRC ([Remy and Gerwert, 2003]) but excluded so far in PSII ([Hienerwadel et al., 1996]) or directly the vibration of Q_A^{-}, as fast recombination with P_{680}^{+} needs to depend as well on the Y_Z oxidation state. Still further experiments are needed for a clear assignment and understanding of the processes.

7.2 Conclusion and outlook

In this section I merged for the first time two very commonly used methods with time resolved IR measurements into one complete picture of the quinone reaction. By this I could explain directly the strong residual absorption after the first flash of the reduced quinones – which most likely is the cause, why no one dared to publish the weak second flash FTIR data, where Q_BH_2 is formed.

P_{680}^{+} reduction is observable at 1478 cm^{-1}, but only at pH 6.2. Three phases are present and the two slower ones clearly resolved: a stronger with 400 ns and a weaker with 35 µs. Both phases were observed before: We previously assigned the faster phase to a specific structural change, with a higher volume change in the $S_2 \rightarrow S_3$ and a smaller in the $S_3 \rightarrow S_0$ transition ([Klauss et al., 2012b]). In the here presented data, both transitions contribute rather equally. However, we did not synchronize the S-states before the measurements, which might cause a mixing of up to 25 % (compare sec. 8.3). The 35 µs phase was attributed to deprotonation, possibly a proton release to the bulk and fully stabilizing $Y_Z^{\bullet ox}$ ([Renger, 2004]). The flash number dependent amplitude pattern follows well the change of absorption at 830 nm ([Eckert and Renger, 1988]).

To our knowledge, for the first time I could obtain the neutral quinone vibrations at 1650 and 1670 cm^{-1} in functional PSII at room temperature ([Razeghifard et al., 1999] at 80 K with P_{680}^{+} contributions). In PSII research there are no reports on the vibration of Q_BH_2. Here I could obtain the first tentative assignment of bands located at 1474 cm^{-1}.

The kinetics of the connectivity corrected variable chlorophyll fluorescence represent Q_A^{-} re-oxidation. This was shown by projection of the fluorescence decay onto the SFIR transient at 1478 cm^{-1}. That band senses all electron transfer events, because the absorption of the reduced quinone Q_B is slightly upshifted towards 1482 cm^{-1}. The dependence of the number of closed centers after each flash to the S-states of the Mn cluster is not discussed.

The three exponential decay exhibits at pH 6.2 and room temperature the following phases: the fastest phase, 1.2 and 1.0 ms, is assigned to the electron transfer from Q_A^{-} to bound Q_B and Q_B^{-}. The middle phase with 10-15 ms to the up-take of Q_B from the membrane plastoquinone pool and the 200 ms phase to recombination of Q_A^{-} and tentatively $Y_Z^{\bullet ox}$ in a modified environment. For comparison a four exponential simulation yields for the fastest phase 700 to 900 µs and a new 2-5 ms phase (details can be found in the appendix).

As we have not preoxidized the plastoquinone pool, I found some of the Q_B s are reduced already in the dark. Because the amplitude change in the IR are stronger, when two reduced quinone species vanish, the pure Q_B reduction kinetics can be masked. We therefore want to stretch that the results published earlier by e.g. de Wijn and van Gorkom are valid and match our data ([de Wijn and van Gorkom, 2001]). These are rates of 0.24-0.9, 2.8-10 and

0.8-1.8 ms for the transfer to Q_B– bound, Q_B– uptake and Q_B^- in the pH range of 6.5-5.5 at 10 °C.

With a correction due to energy transfer to connected centers the fluorescence of PSII membranes and thylakoids decay with the same kinetics (p=0.3 and 0.7 respectively). Together with the great agreement of the SFIR data and the variable chlorophyll fluorescence, this proves for the first time clearly the necessity to correct for the non linearity of closed centers. Still some difference between the two sample types was observed: in PSII membranes a smaller fraction of centers does forward electron transfer to bound Q_B and 20 % more centers are completely blocked most likely due a modification of the QB binding pocket by the detergent or due to the smaller plastoquinone pool.

Outlook: Some further questions are still open: I could not address the quinone exchange pathways. Here site directed mutations might alter the Q_B binding dynamics.

Although I could show, that Q_B^- is stable and Q_BH_2 is formed upon double reduction, the proton pathways are not clear, yet. This may be addressable with the SFIR setup. Both pathways involve histidines (see introduction). Measuring with a new QCL module time resolved the histidine vibrations might assist in clarifying the protonation events.

Also it is known, that the cytochrom b6f complex can oxidize Q_BH_2 in 1.5-15 ms ([Antal et al., 2013]). To exclude any contribution of it to the slow 10-15 ms phase, we could make another measurement with DNP-INT, which blocks the cytochrome's function (see [Haumann and Junge, 1994a]).

7.3 Electron transfer to exogenous electron acceptor

We studied in the last sections, how the electron is transferred from Q_A^- to the mobile electron accepting quinone Q_B. We found that about 30 % of all PSII can not fulfill this transfer and that after 10 flashes a significant amount of additional Q_A^- accumulates. When one wants to measure the reaction cycle of the Mn-cluster repetitively on the same sample and with low misses, one needs to add exogenous electron acceptors. Various of these are in use (see [Kurreck et al., 1995] or [Shevela and Messinger, 2012]).

In the measurements on PSII membranes from spinach we add 2-Phenyl-1,4-benzoquinone (PPBQ, details see 4.3). PPBQ is a quinone head with a phenyl ring attached. It was tested in the FTIR experiments by our group before and yielded the best results. [Görlin, 2012] found that the singly reduced PPBQ was able to extract a second electron from the non-heme iron.

In order to understand and possibly separate the kinetics from the acceptor and donor side of PSII, I measured in every measurement at least once the CO stretch of the reduced quinones at 1478 cm^{-1}. Figure 7.16 shows exemplary the measurement at 10 °C, pH 6.2 and on a 15 µm thick sample of section 6. In the left panel the first four flash transitions are drawn. After each flash the signal jumps to a maximal value of 1.05-1.15 mOd, representing mainly the reduction of Q_A. It decays back to almost zero within 800 ms. This means all quinones are reoxidized and ready for the next excitation.

The middle and the right panel show the results of the simulation. The constant (empty circles) is highest after the first flash and lowest after the third flash. When looking at all nine flashes, this repeats with a maximum after the fifth and ninth flash. Some contribution from the donor side seem to be lying underneath. The fastest phase varies between 300 and 500 ns. It was fixed at 450 ns in the first flash. The pattern is clearly the one already found

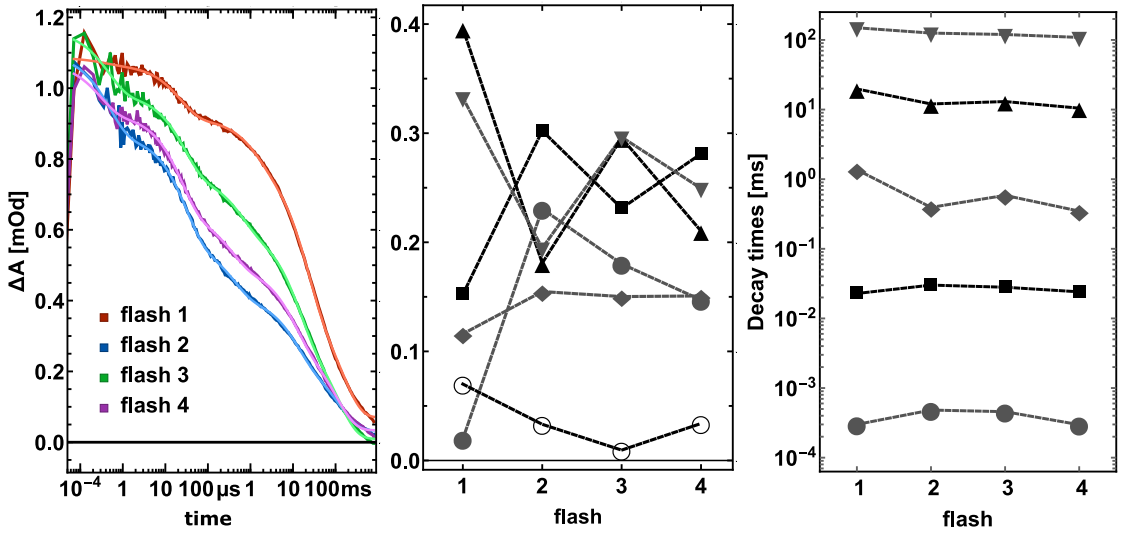

Figure 7.16: *left:* transients of the of the electron transfer from Q_A^- to PPBQ obtained after the first four flashes at 1478 cm^{-1} at pH 6.2 and 10 °C. *center:* simulation results: amplitudes of the five phases, empty circles represent the fit constant; *right:* decay times found.

without any acceptor with a maximum after the second flash (sec. 7.1.10). It shows that some $Y_Z^{\bullet ox}$ stabilization phase is present.

The first binary pattern is found in a 22-30 µs phase. This decay time is the same as the one found for the oxidation of the non-heme iron by Q_A^- in time resolved X-ray spectroscopy (15 ± 3 µs at 18 °C, [Chernev et al., 2011]). The amplitude ratio of odd to even flashes gives 2 to 3. Because only the reduced PPBQ can reduce the non-heme iron and the only stable electron donor is Q_B, about 40 ± 10 % of the quinones Q_B are reduced in the dark. This matches well our estimate found without the addition of PPBQ (35 %, sec. 7.1.6).

The next phase does not show a pronounced amplitude pattern but an oscillating time. It is with $1.4 \pm .2$ ms slowest after the first flash and shows as well the lowest amplitude. With 390 ± 30 and 350 ± 30 µs it is fastest and strongest after the second and fourth flash. An intermediate value is found for the third flash: 590 ± 50 µs. The next two phases show both a strong binary pattern with higher values after odd flashes. The decay times are between 10-15 ms and 110-125 ms.

The amplitude pattern of the slow phases correlate very well with the one of the iron phase and are different to the ones without PPBQ. When much iron was present (even fl) the slow decay is around 0.2 mOd, when there was little iron present (odd) around 0.3 mOd. Because it correlates that nicely with the iron signal, this seems to be the electron transfer from Q_A^- or Q_B^- to PPBQ. Indeed [Schönborn, 2017] found that in the decay associated spectra of a 30 ms phase typical iron features appear. He only had a data set until 130 ms, which is the reason, why he only found one phase. To find more evidence about what is happening, the darker traces in figure 7.17 show other bands sensing the transfer. The left one is measured at 1364 cm^{-1} and is supposed to sense Q_A^- and Q_B^-. The rise starting at 100 µs might stem from quinone signals, but it does not show a binary, rather a quaternary pattern. The decay can only arise from the quinones. Here, the signal seems to decay with 10 and 100 ms and stronger in odd flashes like the band at 1478 cm^{-1}. The central figure is measured at an amide II band at 1552 cm^{-1}. It senses nearly all electron transfer events. It shows a rise within

1 ms in all flashes, decays within 10-15 ms and does not change with 100 ms. It indicates that the two slow phases refer to different processes. The right figure shows a band at 1564 cm^{-1} sensing the Fe^{3+} state, asymmetric carboxylate stretches and weakly Q_B^-. After the initial decay it stays silent up to 10 ms and rises with about 100 ms. It indicates that Fe^{3+} is formed with the slow phase. To summarize, the bands sensing Q_A^- and Q_B^- (1478 and 1364 cm^{-1}) decay until the end. The bands sensing stronger Q_B^- rise and decay within 10 ms. The band that senses the oxidized non-heme iron rises with 100 ms.

The phases in my data set then can be explained in two ways: the constant small phase of 400 µs to 1.2 ms represents the electron transfer to Q_B already bound to its binding pocket. The amplitude appears small because Q_B^- contributes to 1478 cm^{-1} as well. We added quite some PPBQ which even when slower in exchange is present in most centers. But if a Q_B is already bound, it is unlikely that the at the more bulky PPBQ will squeeze it out of the binding pocket. Because we do not see a strong binary oscillation or a decrease in the amplitude of this phase, it might be, that PPBQ is extracting an electron from Q_B^-. With the middle phase some signals disappear that were formed with the last phase. This means it is the electron transfer either from Q_A^- or Q_B^- to PPBQ

The 100 ms is present in bands sensing Q_A^- and Fe^{3+}. Therefore,one explanation is the direct electron transfer to PPBQ. The size of Q_A^- decaying with this phase is the very same of Q_A^- decaying in the next flash upon electron transfer to the non-heme iron. It might be so slow because PPBQ does not have the lipophilic tail of a plastoquinone, for which the quinone channels of PSII are specialized. Its replacement would then compare to the plastoquinone exchange with 110-125 ms by a factor of about 5 slower. Because a singly reduced PPBQ will have similar bands as a singly reduced plastoquinone, another explanation is, that the vanishing of the quinone signal corresponds to the uptake of the second electron from iron by the singly reduced PPBQ, and that neither Q_B^- or Q_A^- are involved. This will explain the strong correlation with this amplitude pattern and the one of the 10 ms phase.

The dependency of oxygen release on the repetition rate of excitation was found to decrease in spinach PSII with PPBQ present only slightly up to 50 Hz ([Shevela and Messinger, 2012]). This means that after 20 ms all Q_A^- need to be gone. Together with the observations stated before the 300 to 600 µs phase belongs to Q_A^- to Q_B or Q_B^-, the 10 ms phase to Q_A^- (or Q_B^-) to PPBQ and the 100 ms phase to Fe^{2+} to $PPBQ^-$.

In all measurements of PSII core complexes from *Synechocystis* sp. PCC 6803 we added hexacyanoferrate(III) (ferricyanide, FeCy). We do not add quinones because there is no membrane but a detergent belt enclosing the protein. I measured on WT and the D1-D61A modified version. I averaged all quinone transients at 1478 cm^{-1} of each, obtained from about five different days. The results of the first four flashes are shown from 1 µs to 800 ms in figure 7.18. The left figure shows the WT and the right the D61A.

Both measurements look very identical: after each flash the signal reaches the same amplitude and decays to zero. The first flash (red) is faster than later ones. When comparing figures 7.16 and 7.18, one can notice immediately the difference in the amplitude after the flash: the spinach amplitude is with 1.0 mOd about two times higher as the one in the WT of 0.45 mOd. We can estimate which factor we would expect. The activity per chlorophyll of this type of spinach samples is around five times smaller, but we concentrate the sample in terms chlorophyll about ten times more (0.5 mg vs 0.05 mg per sandwich), this gives a factor of two on the signal of spinach.

All decays are well fitable with a three exponential function. The decay of the fast phase is biggest in the first flash. In all other flashes including the fifth the decay is similar. In average about 25 % of the Q_A^- formed, decay with 15-25 µs and again it reflects the electron

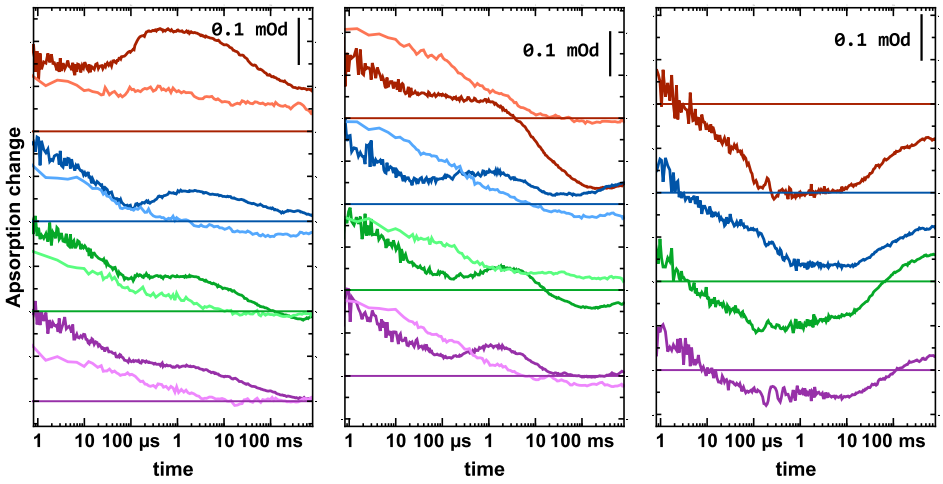

Figure 7.17: Transiently observed quinone dynamics measured at 1364 (left), 1552 (center) and 1564 (right) cm^{-1}. The darker traces correspond to PSII membranes with PPBQ as in fig. 7.16. The brighter ones to PSIIcc of the WT with FeCy from fig. 7.18. From top to bottom the S-state transitions 1-4 are plotted.

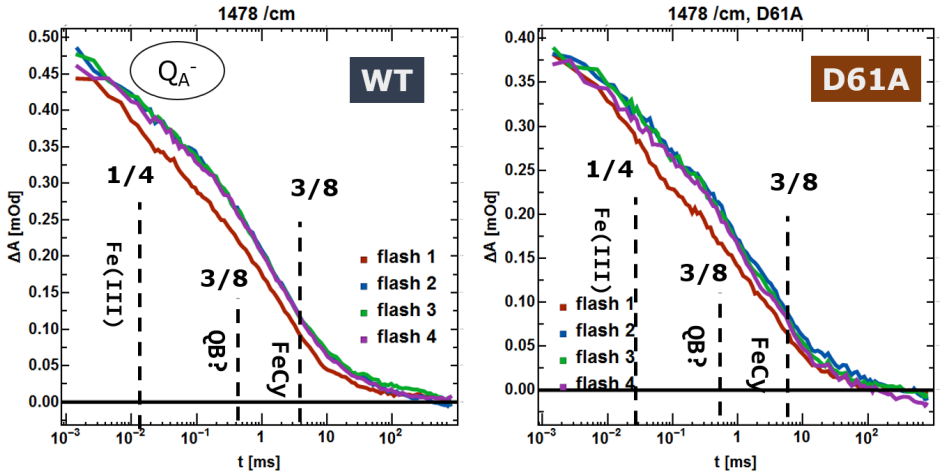

Figure 7.18: Dynamics of the electron transfer to FeCy in PSIIcc. *left:* WT, *right:* D1-D61A. Both sets measured at 6-9 °C and pH 6.0. The decay times of a three exponential fit can be found via the dashed lines. The relative amplitude is indicated.

transfer to the reduced iron. The iron reduction by FeCy in the dark thus needs to be slow, so that only the first flash shows an increased value. About 75% - the majority - of Q_A^- decay in equal parts with around 400-600 μs and 4-5 ms. The first phase matches the reduction of Q_B and the second is likely the direct transfer from Q_A^- (or Q_B^-) to FeCy. This, compared to PPBQ in PSII membranes fast transfer, unfortunately lies in the dynamic region of interest.

Figure 7.17 compares the transients of some bands discussed above for PSII membranes (dark) with PSIIcc (bright, left: 1364 cm^{-1}, right: 1552 cm^{-1}). We can see that the PSIIcc measurements are much less affected by the quinone reactions at later times and that the rise due to an electron transfer to Q_B^- is not found. There may be again two explanations for that, either the assignment of the transfer to Q_B is wrong or both the carboxylate and the amide II band in PSII membranes react on a proton uptake and transport towards Q_B^-.

It may for example be that FeCy binds somewhere at the proton uptake site (D1-H252) and hinders this. Exactly this was found to be the case with Zn in brc, and how the proton uptake path could be identified ([Utschig and Thurnauer, 2004]).

[Noguchi et al., 2012] measured the 1480 cm^{-1} band with $\Delta\nu = 16cm^{-1}$ in PSIIcc from *Thermosynechoccocus elongatus* at 10 °C. He found a phase of 300-500 µs and assigned it to the electron transfer to Q_B as well (30 % of decay). The slow phase (70 %), however, was slower than 20 ms. His time resolution was not high enough to track the iron reaction. It is known that in *Thermosynechoccocus elongatus* Q_B is bound ([Krivanek et al., 2007]). In *Synechocystis* it was a surprise to find this phase as well [3]. We can not explain the discrepancy of the rate of the slow phase. Possibly the binding site for FeCy differs between the organisms or the thermophilic one is too rigid for optimal binding.

[3] private discussion with Richard Debus

8 The slow phases of P_{680}^{+} reduction and Y_Z oxidation

Why is it necessary to search for a $Y_Z^{\bullet ox}$ signal with time resolved infrared spectroscopy and the new QCL setup after many decades of PSII research?

First, the kinetics and energetics of the multiphasic Y_Z oxidation are known, but no clear and accepted reaction mechanism exists. Changes involving H-bond networks, includung water movements and volume changes are thought to occur during an ill understood slow kinetic component.

Second, as $Y_Z^{\bullet ox}$ is only formed transiently most measurements caractericing this state have been measured on Mn or Ca depleted preparations, however, it has been shown that the removal of one of these makes the region more flexible and modifies the H-bonding properties of Y_Z and His190 (see e.g. [Haumann and Junge, 1999]). Furthermore, samples illuminated with NIR light or at cryo temperatures might not proceed trough the full stabilizing events.

Third, measurements on intact PSII samples in which Y_Z is supposed to be oxidized only transiently have been performed with indirect measurements of the electrochromic shift of chl absorption, Mn absorption changes monitored in the UV/VIS absorption, reduction of P_{680}^{+} tracked by absorption changes at 830 nm or very indirect, as delayed chlorophyll fluorescence or volume changes.

The only direct measurements of $Y_Z^{\bullet ox}$ in intact PSII were done with the EPR and the UV absorption of tyrosine ([Boussac et al., 2012] [Haumann et al., 1999]). Still the UV absorption is strongly mixed with contributions from Mn oxidation and partially with the quinones and P_{680}. This mixing makes it difficult to assign the measured signal to a certain species. On the contrary the EPR signal of the neutral tyrosine radical is purer but a time resolution of 500 µs made it only possible to track $Y_Z^{\bullet ox}$ after illumination in the S_3 state ([Boussac et al., 2012]).

To probe the Y_Z^{ox} induced changes and to get insights in the mechanism other experimental approaches must be considered. IR spectroscopy is a promising candidate as molecular vibrations are sensitive to redox states in the environment. Although several characteristic bands have been suggested for the $Y_Z^{\bullet ox}$, their assignment is still under intense debate ([Sakamoto et al., 2017], [Guo et al., 2018]).

8.1 Introduction to known processes and kinetics

Environment of Y_Z as seen in XFEL crystal structures

The *environment* of the Y_Z-H190 unit as seen in the XFEL crystal structure is shown in figure 8.1. It is located half way in between the Mn cluster and P680 consisting of four chlorophyll molecules (fig. 8.1). Only parts of the two central chlorophyll are visible in green. Both H190 and Y_Z are located at the lumenal part of two transmembrane helices. Their strong H-bond interactions may be crucial in stabilizing the transmembrane helices. Three prolines at positions 162, 173 and 196 fold the two helices into one membrane parallel

part, on which important amino acids as E189, S167, S169 or E170 are located, which span the Mn cluster's binding pocket.

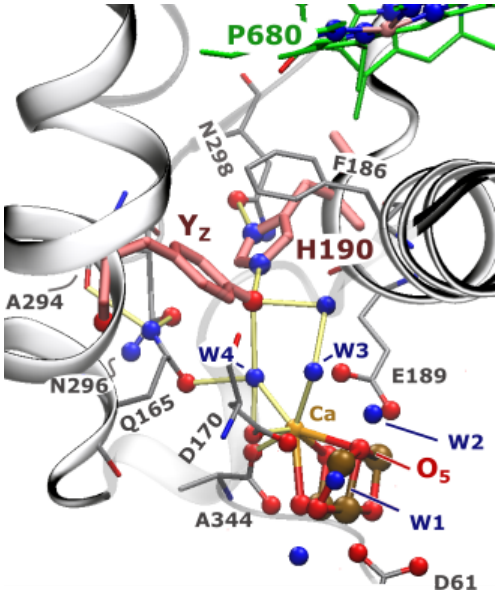

Figure 8.1: Y_Z environment in the crystal structure from *thermosynechococcus vulcanus*. H bonds are shown as yellow connections. Only the directely involved waters and amino acids of D1 are shown. Parts of two chlorophyll molecules of P_{680} are visible in the top. Y_Z is H-bonded to H190 and within H-bonding distance to two waters connecting it to the Ca atom of the Mn cluster. *crystal: 4ub6*

Most waters within four Å of the Mn cluster and the Y_Z-His190 unit are shown in figure 8.1. In between P_{680} and Y_Z there are no waters and the environment is hydrophobic. Just above the histidine there is a hydrophobic phenylalanine present, possibly blocking the entry for water and aiding in stabilizing the H190-Y_Z position through π stacking[1]. The distance between all three rings is about 3.5 Å. At this side H190 is H-bonded via its second N to the O of N298.

The distance between the ring of Y_Z and the Ca of the Mn-cluster is 5.5 Å and allows for the electronic and magnetic interactions of these redox cofactors[2]. An H- bond network serves to bond Y_Z to Ca via one water and W3 as well as W4. W4 inturn lies within an H-bonding distance of 3 Å to D170 and Q165. W3 and the other water lie within 3.1 and 3.4 Å to E189. This broad H-bonding network exceeds towards the other side of the Mn cluster as well [Service et al., 2014b].

When the Y_Z-H190 unit is transiently oxidized conformational rearrangements were observed ([Kern et al., 2018]). In the following text, accepted and suggested processes will be discussed.

Kinetics of P_{680}^{+} reduction and Y_Z oxidation

The Y_Z in its **neutral form** is often depicted as a neutral phenyl side chain with a strong H-bond to His 190 (see fig. 8.2 I or [Retegan et al., 2014], [Narzi et al., 2014]). Comparison of its UV absorption with model compounds, the strong H-bond character suggested a slightly more negative side chain with the proton rather shifted towards H190 (H-bonded tyrosinate, [Haumann et al., 1999]).

After the ps charge separation P_{680}^{+} oxidizes Y_Z in a multi phasic reaction. In the current consensus there are three kinetic components depending on the S-state of the Mn cluster (compare with fig. 8.2):

I) **20-50 ns: $Y_Z^{\bullet ox}$ formation, main component**
A low activation energy of 10 kJ/mol within 248-295 K suggests that both $Y_Z^{\bullet ox}$ and P_{680}^{+} are in an equilibrium ([Renger, 2004], [Klauss et al., 2012b]). This non-adiabatic Markus-electron-transfer phase is not proton limited, as measurements at

[1] e.g. as found for the distal position of Q_B in bRC [Muh et al., 2012]
[2] ENDOR S-state fine splitting on EPR $Y_Z^{\bullet ox}$ radical signal and dipole reorientation very weak magnetic coupling [Retegan et al., 2014]

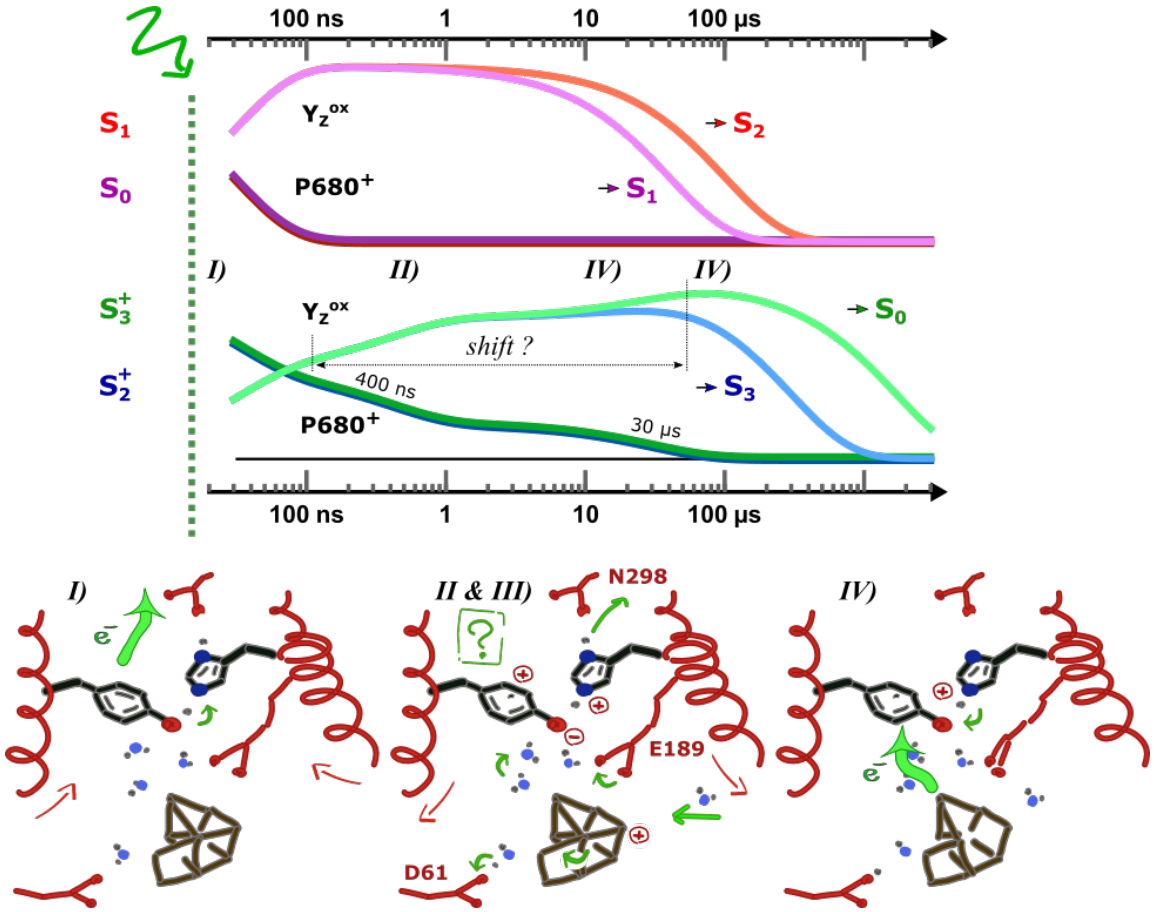

Figure 8.2: *top:* expected $Y_Z^{\bullet ox}$ and P_{680}^+ signals starting in an S state indicated on the left. Four phases are marked (*I-IV*). *bottom:* suggestions on the mechanism from literature: *I)* Y_Z oxidation and H^+ shift to H190. *II & III)* - in S_2 and S_3- $Y_Z^{\bullet ox}$ relaxation coupled to water or H^+ movement, amino acid rearrangement and cluster conformation change. *IV)* Mn oxidation and H^+ shifts back.

different pHs and H/D exchange suggests. Still, as only $Y_Z^{\bullet ox}$ is EPR active it is assigned to a neutral tyrosine radical meaning that the shared proton shifted rapidly towards H190. The state can be described as a neutral tyrosyl H-bonded to an imidazolium cation [Retegan et al., 2014], [Narzi et al., 2014]. The inactivity at low pH and pH induced changes lower than 7 in Mn depleted samples suggests that only with H190 bound as a base, $Y_Z^{\bullet ox}$ formation can be achieved with its high redox potential ([Christen et al., 1999]). The charge separated state at P_{680}^+ or $Y_Z^{\bullet ox}$ formation causes a contraction of around 15 Å^3 due to the movement of polarized groups in the vicinity of the charges possibly coupled to a small large scale conformational change (this phase is not resolved in [Klauss et al., 2012b]).
This phase is large in the S_0 and S_1 state, when the cluster is neutral, and only contributes to around half of the P_{680}^+ decay in the S_2 and S_3 states when the cluster is positively charged.
The single frequency IR setup can not resolve this phase. Signals from P_{680}^+ after

the first and fourth flash might not be visible and first signals of $Y_Z^{\bullet ox}$ will be seen instantaneously.

II) **300-500 ns;** 1^{st} $Y_Z^{\bullet ox}$ **stabilizing phase in** S_2 **and** S_3
With an activation energy of 25-30 kJ/mol this phase shifts in S_2 and S_3 the redox equilibrium towards $Y_Z^{\bullet ox}$ ([Christen and Renger, 1999]). The relative fraction of the P_{680}^{+} decay is estimated to about 30 % (in S_2 higher than in S_3). The process is accompanied by a protein extension of 40 and 10 $Å^3$ in S_2 and S_3, respectiveley. Our group suggested a "specific chemical or structural change" with no pronounced H/D exchange effect, but a strong pH dependence has been observed [3].

III) **30-50 µs:** 2^{nd} **stablilzing phase involving protons**
The relative amplitude starting from the S_2 and S_3 state is approximately 15 to 20 %. Because a strong H/D exchange effect characterizes the amplitude pattern of this phase, it is interpreted as a protonic stabilization within an H-bond network ([Christen et al., 1998]). A movement of hydrogen, protons or waters might as well be a cause [Schilstra et al., 1998]. During this phase PSII expands slightly by 5 $Å^3$ ([Klauss et al., 2012a]).
Whether this change of the H-bond network also comprises a proton release to the bulk ([Klauss et al., 2012a]) is under debate but the strong pH dependence of the decay time and a (*unusually*) high H/D kinetic effect suggest this.

Bands sensitive to P_{680}^{+} and $Y_Z^{\bullet ox}$ should share the kinetics as those presented in figure 8.2. It is however possible, that the $Y_Z^{\bullet ox}$ bands shift with some protonic rearrangement. Other groups involved may only sense the 300 ns or the 30 µphase. Mn oxidation occurs with 100 µs in $S_1 \rightarrow S_2$, 300 µs for $S_2 \rightarrow S_3$, 1.6 ms in $S_3 \rightarrow S_0$ and 40 µs in $S_0 \rightarrow S_1$ ([Klauss et al., 2015], discussed in detail in chapter 9).

The detailed orchestration of events is not known after the shared proton shifts towards H190. Some suggestions are summarized in the schemes on the lower part of figure 8.2. Only the vague involvement of protons, possible rearrangements of the H-bonding network and volume changes give us experimental indications for the stabilizing processes. It is not even completely clear whether it is the same proton that moves back and forth in between Y_Z and H190 or if it is always replaced by one from the cluster ([Styring et al., 2012]).

Some suggestions to the origin have been made through simulations. [Retegan et al., 2014] suggest that upon Y_Z oxidation in S_2 the dipole of the Mn cluster reorients but no deprotonation of nearby amino acids takes place. The direction of the dipole might suggest the subsequent deprotonation of W1. [Narzi et al., 2014] found that upon $Y_Z^{\bullet ox}$ formation in S_2 only one of the two Mn cluster confornmation can proceed. This interconversion might cause the µs stabilization. Then Mn is oxidized while D1-D61 accepts a proton from W1 and rotates by 120°. Siegbahn[4], on the other hand, suggests the first process happening after $Y_Z^{\bullet ox}$ formation is the binding of a new water molecule to Mn4 which directly deprotonates and leaves the OEC via D61 ([Siegbahn, 2008]). Also for the first step in $S_2 \rightarrow S_3$ the positive charge at $Y_Z^{\bullet ox}$ leads to proton expulsion of the meanwhile reprotonated water next to D1-D61 ([Siegbahn, 2012]). In his mechanism both proton releases are exogenic. A proton release within 30 µs was also observed experimentally using pH sensitive dyes (electrostatic, [Junge et al., 2002]).

[3] decreasing amplitudes of both ns phases below pH 6.5 [Christen et al., 1999]

[4] he proposed in this paper already a complete reaction scheme which only got weakly modified up to date and matches most experiments and also the latest flash resolved XFEL data

Charge recombination and chlorophyll or carotenoid triplets

When researching the above mentioned processes one needs to keep in mind which alternatives to the forward charge transfer processes are possible. Also undesired reactions may occur on the same time scale, which can be enhanced by the experimental conditions.

Especially relevant for studies of the early µs phases is the creation of triplet states. Triplets of chlorophyll decay in the higher µs to ms time domain. Noguchi found a decay phase of even 1.5 ms at pH 7.5 in PSII reaction centers ([Noguchi et al., 2001]). This is accelerated down to the ns, depending on the amount of quenchers present. Efficient candidates are oxygen and in PSII carotenoids, which is next to light harvesting their main function.

During chlorophyll quenching and also excited directly **carotenoid triplet** states are formed. These decay with about **3 µs** in light harvesting complex II [Christen et al., 1998] and, therefore, might also be present in PSII. Usually the amount of formed triplet is low, but in the here described experiments we are exciting at 532 nm, right in the absorption range of carotenoids.

The recombination processes involving P_{680}^+ and $Pheo^-$ or Q_A^- might cause other signals in the same time domain. [Christen and Renger, 1999] reported a half time of P_{680}^+ and Q_A^- recombination of 150 µs. It has been proposed that this pathway is the main contribution to miss events during the S-state cycle ([Renger, 2004]).

Fast quinone electron transfer

see section 7.3

8.2 Experimental details of the measurements presented

In this chapter two sets of measurements are described.

The first is a scan around a prominent band of P_{680}^+ at 1310 cm^{-1}. The measurements are taken at 10 °C and pH 6.2. The thickness of the sample was 15 µm. PPBQ was added. No EMP correction was necessary. A deconvolution was done with a miss parameter of 9 ± 2 %. The data was averaged over the following points: 1305 cm^{-1}: 372, 1308 cm^{-1}: 166, 1310 cm^{-1}: 284, 1315 cm^{-1}: 207, 1320 cm^{-1}: 183, 1344 cm^{-1}: 96, 1400 cm^{-1}: 135 and 1478 cm^{-1}: 142.

The second measurement is a scan around the potential $Y_Z^{\bullet ox}$ band at 1514 cm^{-1}. The measurements were conducted at 10 °C. To reach the high pH 2 ml of sample ($2mg_{Chl}$/ml) was washed in 40 ml buffer of pH 7.5 buffered with 25 mM of HEPES. The single wavenumber transients are averaged over: 1398 cm^{-1}: 121, 1478 cm^{-1}: 109, 1495 cm^{-1}: 101, 1497.5 cm^{-1}: 127, 1500 cm^{-1}: 134, 1502.5 cm^{-1}: 110, 1505 cm^{-1}: 41, 1507.5 cm^{-1}: 62, 1510 cm^{-1}: 138, 1512.5 cm^{-1}: 130, 1515 cm^{-1}: 105, 1517.5 cm^{-1}: 107, 1520 cm^{-1}: 41, 1544 cm^{-1}: 52 and 45 points.

8.3 Wavenumbers around 1310 cm^{-1} for the observation of P_{680}^+ reduction

To track the kinetics of P_{680}^+ reduction the region around a band at 1310 cm^{-1} was chosen. The coupling of $\nu(CC)$, $\nu(CN)$ and $\delta(CH)$ of the chlorin ring contribute mainly to the vibrations observed. The advantage of this wavenumber is that no strong bands are expected from the

steady state spectra of the cluster's S-state cycle. Also the neutral quinones contributes only weakly around 1320 cm^{-1}. However, contributions of the P_{680} triplet and neutral state may contribute at 1310 and 1344 respectively ([Okubo et al., 2007]).

Remark on data quality

This data set showed at all wavenumbers 50 and 400 µs noise stemming from the QCL. When subtracting the average of all flash transients from the single transients, only smooth curves remained. These smooth curves showed only the difference signals with kinetics expected for the quinones, the cluster and P_{680}^{+}. Because of this observation, the all flash average was fitted with a six exponential function to obtain a good residuum. The fit result is meaningless, but the residuum is used to extract most of the noise. In the appendix (fig. 11.24) some examples are given. The reader will see that no artefacts (as changed kinetics) have been created that would interfere with the following discussion. After the correction a rise with quinone dynamics especially at 1520 cm^{-1} became apparent.

8.3.1 Decay up to 30 µs and the transient around 1310 cm^{-1}

The S-state resolved data up to 35 µs is presented as **decaying spectra** in figure 8.3. For easier reading error bars are omitted. The early signal rise around 60 and 200 ns (circles) is highest in the $S_2 \rightarrow S_3$ (blue) and $S_3 \rightarrow S_0$ (green) transition. Here, half of the signal decays approximately until 500 ns, the other half in the next 35 µs. Although the measurement stops at 1305 cm^{-1} we can see a maximum of the 200 ns spectrum at 1310 cm^{-1}. This fits very well the assignments of [Okubo et al., 2007]. The 60 ns spectrum may reach further towards 1300 cm^{-1}. This could indicate some P_{680} triplet contributions In $S_1 \rightarrow S_2$ (red) and $S_0 \rightarrow S_1$ almost all of the signal decays within 1-2 µs. The dynamics are very different at 1344 cm^{-1}. At 60 ns this transient is very noisy and varies around zero. At 200 ns the initial signals are negative in all transitions remaining constant until the 10 µs rise.

What is not shown is the rise of all transients starting between 10 and 100 µs (fig. 11.24). This trend is most prominent at 1320 cm^{-1}, where it begins at 10 mus from negative values. The fact that it is negative matches the assignment to a neutral quinone related band (see sec. 3.3). Some contribution of rising signals in $S_2 \rightarrow S_3$ and decaying ones in $S_3 \rightarrow S_0$ are present as well but much slower (rise of 300 µs and decay with 2 ms). These signals may interfere with the fast kinetics we are interested in.

The average of the deconvoluted **transients from 1305 to 1315** cm^{-1} are shown in figure 8.4. In all flashes a very sharp feature is formed within 60 ns - the rise time of the setup, however, it completely vanishes by 100ns. This feature displays period of two behavior, and is stronger in the $S_1 \rightarrow S_2$ and $S_3 \rightarrow S_0$ transition. From 100 ns to 1.5 µs the initial amplitude, which is higher $S_2 \rightarrow S_3$ and $S_3 \rightarrow S_0$, decays strongest in $S_2 \rightarrow S_3$. In the central panel the transients up to 80 µs are shown. In $S_1 \rightarrow S_2$ the signals decay only weakly. One can already spot the rise of the signal at late times. The main decay is present in $S_3 \rightarrow S_0$. It is about 2-3 as large as in the first and fourth transition. A larger decay is also visible in $S_2 \rightarrow S_3$.

8.3.2 Global fit results

To extract the kinetics of these decays a joint simulation of each transition is preformed utilizing all wavenumbers presented in figure 8.3 and additionally the symmetric stretch at 1400 cm^{-1} of reactions at the Mn cluster and the CO/CC stretch of the reduced quinones at

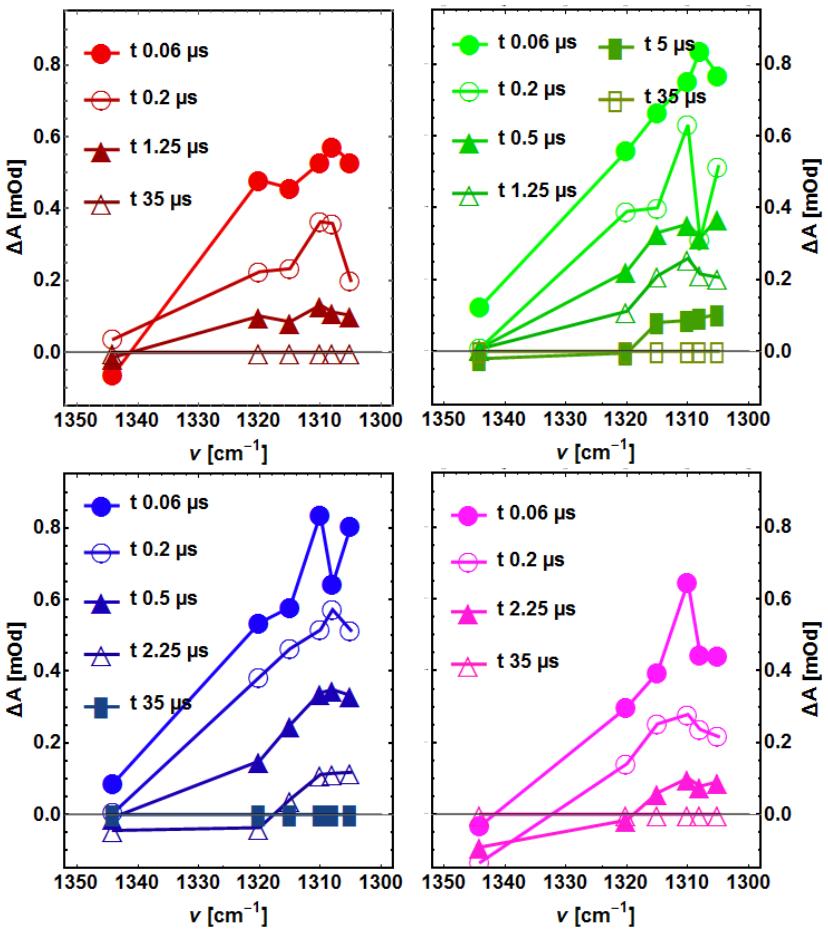

Figure 8.3: Fast spectral changes of the deconvoluted $P680^{+}$ bands around 1310 cm^{-1}. Measurement at pH 6.2 and 10 °C on PSII membranes from spinach. The colors red, green, blue and magenta correspond to the $S_1 \rightarrow S_2$, $S_2 \rightarrow S_3$, $S_3 \rightarrow S_0$ and $S_0 \rightarrow S_1$ transition, respectively. The data was averaged around the indicated time. Error bars were omitted for readability. The value at 200 ns (empty circles) clearly shows a dependency on the S-state transition.

1478 cm^{-1}. These phases where included to help characterize weak binary and quaternary oscillations present around 1310 cm^{-1}. The clear kinetics of these two wavenumbers assisted in judging about the amount of exponential functions necessary. Good results were obtained with seven components. The $S_1 \rightarrow S_2$ was better fitted with six exponentials, however, to allow better comparison it was fitted with seven with the fast phase fixed at 30 ns and the slow to 25 µs. Both represent the phases found in the other transitions. The fits are presented for the averaged transients in figure 8.4.

All results of the fit except for the fastest[5] 20-30 ns phase are shown in figure 8.5. The fastest phase is not shown. For the averaged 1310 cm^{-1} transients the value of this 20-30 ns phase is calculated at 60 ns (yellow, right panel of fig. 8.4). During the transition they clearly follow a binary pattern even when taking the big error into account.

[5]Faster than the time resolution of the setup. Thus the amplitudes are enormous.

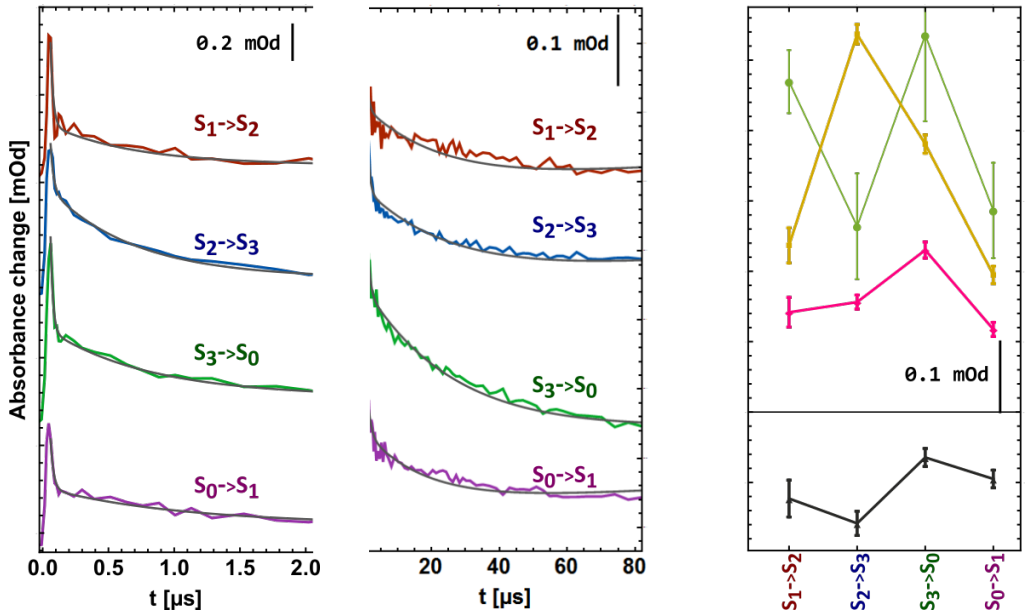

Figure 8.4: P_{680}^{+} reduction by Y_Z followed around 1310 cm^{-1} and at pH 6.2 and 10 °C. *left and middle:* Decay of the transient averaged from 1305 to 1315 cm^{-1}. Within 2 µs a much stronger decay is observed in the $S_2 \rightarrow S_3$ and $S_3 \rightarrow S_0$ transition. This is also visible in the yellow pattern on the *right* corresponding to the 600 ns fit component. The decay with 30 µs has a maximum in the $S_3 \rightarrow S_0$ transition, the $S_1 \rightarrow S_2$ transition is not fitted well as the decay time was fixed. The magenta pattern in the right panel belongs to this phase. The green pattern is the contribution at 60 ns of a 30 ns phase and shows a binary repetition. The yellow and magenta pattern represent very well the flash number dependence reported by [Eckert and Renger, 1988] - except for the first transition in magenta. Also shown is the contribution of the 200 µs rise in black.

The next phase is found with 600-900 ns. The pattern around 1310 cm^{-1} shows a very strong quaternary structure (yellow) with a maximum in $S_2 \rightarrow S_3$ and higher amplitude in $S_3 \rightarrow S_0$. The next phase was fixed in $S_1 \rightarrow S_2$ and is found to be 20-30 µs in the other transitions (magenta). In has a strong maximum in $S_3 \rightarrow S_0$. The amplitude in $S_2 \rightarrow S_3$ is larger as in $S_0 \rightarrow S_1$. In the first transition the error is larger and the fit quality bad. To have an idea how it will look like without the fixation one can find a fit only at 1310 cm^{-1} of the *flash resolved* data in the appendix (11.25. In this figure it is obvious that there is no 30 µs phase in flash one and only a small one in flash 5.

When looking at the amplitudes of the two phases at 1320 cm^{-1} one can find a zero or negative contribution for the 30 µs. This reflects contributions of the quinones to this band which also show a high contribution due to the non-heme iron reduction (see sec. 7.3). The 1345 cm^{-1} band is rather silent in these phases.

In the global fit several more phases were encountered. The first one is a 150 to 200 µs phase which is mainly contributing to the wavenumbers at 13105-1320 and 1345 cm^{-1}. All transients rise strongly within this phase without a clear spectral discrimination. Only in $S_1 \rightarrow S_2$ and $S_2 \rightarrow S_3$ the 1400 cm^{-1} band decays with this phase. Because the 1400 cm^{-1} band senses Mn oxidation, thee 100 and 300 µs kinetics of the reaction cycle will alter the fit

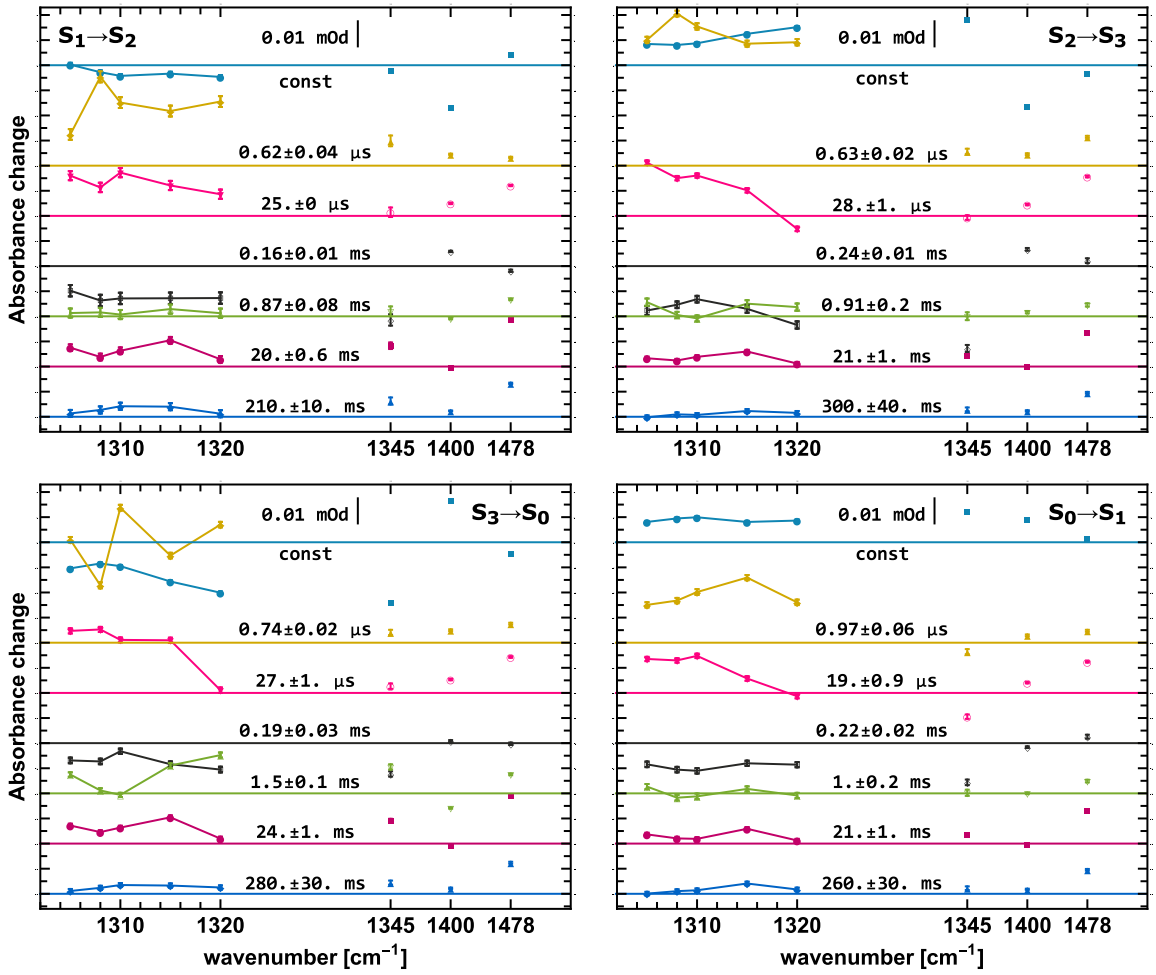

Figure 8.5: Decay associated spectra of a global fit of the deconvoluted transients around 1310 cm^{-1}. Included are also the wavenumbers 1345 cm^{-1}: P_{680}, 1400: cm^{-1} carboxylates around the Mn cluster and 1478 cm^{-1}: reduced quinones. The transitions are marked in the top corners. All measurements at pH 6.2 and 10 °C on PSII membranes. The amplitudes of the decays at 1400 and 1478 cm^{-1} have been scaled by 1/3. Compared to the quinones and carboxylates high 600 ns and 25-30 µs amplitudes contribute around 1310 cm^{-1}, approving the assignment to P_{680}^{+}.

result of this phase (see sec. 9.4.3). The origin of this otherwise feature-less phase is unclear but it is also present in the FTIR data recorded by [Schönborn, 2017].

The next phase found is with 1 ms a quinone phase. While it is silent around 1310 cm^{-1} (compared to the 600 ns or 30 µs phase), it contributes to 1478 cm^{-1}. Only in $S_3 \rightarrow S_0$ it is mixing with the Mn oxidation /O-O bond formation. In this transition a band at 1315-1320 and also the 1345 cm^{-1} band contribute by a strong decay. A counterpart to this decay seems to be the rise with 240 µs in $S_2 \rightarrow S_3$ (stronger in this transition than in others). The two remaining slow phases are present at 1478 cm^{-1} but not at 1400 cm^{-1}. A band can be found at 1520 and also 1345 cm^{-1} but mainly for the 20 ms phase - distinguishing the two as distinct, quinone related processes.

The constant (blue, top) shows around 1310 cm^{-1} a binary pattern with some additional contributions in $S_2 \rightarrow S_3$ and $S_3 \rightarrow S_0$ at 1515-1520 cm^{-1} (see 240 µs and 1.5 ms phase).

8.3.3 Discussion

Like stated in the introduction to this chapter, the main component of P_{680}^+ reduction by Y_Z takes place within 20-50 ns. To find such a large binary pattern of the 30 ns phase (at $t = 60\,ns$) was a surprise, because no quinone related phase with these kinetics is known. In $S_1 \rightarrow S_2$ and $S_3 \rightarrow S_0$ related quinone transitions, the relative amount of non-heme iron reduction is smaller by 2:3 compared to the other transitions. The pattern found for the 20-30 ns phase shows – within the error range – similar behavior, with an amplitude ratio of 5:3. Thus a possibility might be, that some fast change occurs related to the iron state. A very broad band of the bicarbonate was found at 1338 cm^{-1} reaching down to 1300 cm^{-1} ([Berthomieu and Hienerwadel, 2001]), but the transient at 1345 cm^{-1} is silent, however, the signal to noise of this band is rather poor.

As predicted in Klauss, early kinetics as 600 ns and 25-30 µs are clearly present in this data ([Klauss et al., 2012b]). Only the fast phase in this measurement is slower than the 300-400 ns reported. In a later chapter the very same kinetics are found (sec. 9.4.2 at 20 °C and 9.4.4 at 10 °C). Then the questions arises why it is slower in this section. Analysing the decay associated spectra of this phase we find no clear maximum of the band, which is expected around 1310 cm^{-1} for P_{680}^+ ([Noguchi et al., 1994]). In the spectra contribution also towards 1320 cm^{-1} are present and this phase – although weaker – is found also in $S_1 \rightarrow S_2$ and $S_0 \rightarrow S_1$. A straightforward explanation is, that this phase is mixed with the P_{680} triplet state. It is expected to contribute at 1320 and weakly at 1300 cm^{-1} ([Noguchi et al., 1993]). The decay of a triplet of the chlorophyll quanching carotenoid in LHCII was reported to be within 3 µs ([Christen et al., 1998]). Both the decay associated spectra and the kinetics suggest a mixture of the 300 ns and 3 µs phase.

The flash pattern of the 600 ns phase matches very well the one of the absorption change of P_{680}^+ monitored at 830 nm ([Christen and Renger, 1999]). Only in my pattern a maximum is found in $S_2 \rightarrow S_3$. The apparent flash dependent amplitude discrepancy between the $S_2 \rightarrow S_3$ transitions is due to a deconvolution approach applied to data in this work. Before deconvolution the pattern showed similar amplitudes in $S_2 \rightarrow S_3$ and $S_3 \rightarrow S_0$ (fig. 11.25). The flash pattern of the 30 µs phase compares very well with the one reported in [Eckert and Renger, 1988]. Again, discrepancies are attributed to the deconvolution, see appendix for raw flash dependent amplitude patterns. This is also an observation not reported before: in $S_3 \rightarrow S_0$ the fraction of P_{680}^+ reduction with the 30 µs phase is higher than in $S_2 \rightarrow S_3$, with the sum of both being constant. Before each transition the Mn cluster and its environment posses a positive charge, therefore the altered response must reflect more than just electrostatics.

The pattern of the 200 µs phase, shown in black of figure 8.4, states that it rises stronger in $S_2 \rightarrow S_3$ and weaker in $S_3 \rightarrow S_0$, at the same time not showing a pronounced binary pattern. If the heat artefact correction was a problem the rise would continue until 1 ms and not show up in the FTIR Step-Scan data. A possibility is a recombination pathway including P_{680}^+ and Q_A^- which is reported to decay within 130 to 200 µs ([Christen and Renger, 1999]) matching the observed kinetics. But such a pathway should lead to a decay of the P_{680}^+ band at 1310 cm^{-1}– a rise is present, a rise of the neutral Q_A at 1320 cm^{-1}– present, and a decay of the reduced quinone band at 1478 cm^{-1}– not present. Hence, from the current assignment of bands this explanation is not working and further research is needed.

Overall the 1310 cm^{-1} band is good marker for tracking the reaction kinetics of the P_{680} Y_Z reaction in functional PSII.

8.4 The quest for the bands reflecting Y_Z oxidation

An overview of possible bands visible in $Y_Z^{\bullet ox}$-Y_Z spectrum was presented in section 3.3. The big problem is that most of these spectra albeit recently published or discussed ([Berthomieu and Hienerwadel, 2005], [Nakamura et al., 2014]) are measured on Mn-depleted PSII at pH 6. This pH is lower than the pK_a of a close-by base (His190), which will affect the H-bonding properties of the tyrosine-histidine unit as well as the environment. Therefore the position of certain bands especially the bands sensing the slow, proton movement related relaxation processes may be altered [Zhang et al., 2017] [Haumann and Junge, 1999].

There are three very recent works utilizing infrared spectroscopy on fully functional PSII. All three come to completely different conclusions concerning the position of the $\nu(C=O)$ band of $Y_Z^{\bullet ox}$. Therefore,I want to introduce the reader to them:

[Guo et al., 2018][6]: In this interesting publication steady state difference spectra in calcium depleted and resubstituted (Ca, Sr, Ba) spinach PSII membranes were measured at 190 K, where the S_2 $Y_Z^{\bullet ox}$ Q_A^- is frozen after two flash illumination. A $Y_Z^{\bullet ox}$ band at **1503** cm^{-1} in Ca resubstituted samples varies with the element and is assigned as the $\nu(C=O)$ of $Y_Z^{\bullet ox}$. A neutral Y_Z band is found at **1245** cm^{-1} and assigned to a strongly H-bonded, protonated tyrosine.

[Sakamoto et al., 2017]: The second time resolved IR study on oxygen evolution of Noguchi examined the $S_2 \rightarrow S_3$ transition of *Thermosynechoccocus elongatus* core complexes ($\Delta\nu \approx$ 16 cm^{-1}). The band of $Y_Z^{\bullet ox}$ in Mn depleted samples at **1514** cm^{-1} showed in $S_1 \rightarrow S_2$ on top of an instantaneous signal a rise with around 100 µs. In $S_2 \rightarrow S_3$ an instantaneous signal decayed with around 100 µs followed by a slow rise around 600 µs. This is not matching the expected $Y_Z^{\bullet ox}$ kinetics of fig. 8.2. No data is presented for the $S_3 \rightarrow S_0$ transition. They also made a scan in steps of 10 cm^{-1} around the 1514 cm^{-1} band. After a global fit with a consecutive reaction model, they found a shift from around 1510 to around **1525** cm^{-1} with 100 µs. They interpret this - based on other wavenumbers as well - as an H-bond rearrangement or water movement possibly associated with an open to closed cubane transition of the Mn cluster. Unfortunately they do not discuss a quinone contribution at this wavenumber, which is present at 1520 cm^{-1} (see sec. 3.3 or below). Their kinetic analysis of the band at 1478 cm^{-1} gave a decay of 300-500 µs ([Noguchi et al., 2012]), strongly interfering with the band shift observation and their fit model. Furthermore, back reaction processes visible in the P_{680}^+ kinetics are not discussed (sec. 3.1 and 8.1). On the other hand, the band of Y_Z at **1256** cm^{-1} seems to reflect the expected kinetics, i.e. instantaneous negative amplitude followed by a rise with 100 µs in $S_1 \rightarrow S_2$ and in $S_2 \rightarrow S_3$ a slower builtt-up of a negative amplitude followed by a 400-500 µs rise.

[Schönborn, 2017]: in parallel to the results of this work, Matthias Schönborn has performed an FTIR step-scan experiment at pH 6.2 and 10 ° C on oxygen evolving PSII membranes. In a target fit with fixed time constants[7] several bands related to 20 and 50 µs kinetics were found, with some sensitive to Mn oxidation. The ones sensing both are: I) a

[6] with this publication it's research group made a step away from their previous 1478 cm^{-1} assignment as a band from $Y_Z^{\bullet ox}$ contrary to about four research groups (others e.g. in [Berthomieu and Hienerwadel, 2005]). This band is only discussed as a 2^{nd} $Y_Z^{\bullet ox}$ conformation not sensing Ca depletion albeit in all $Y_Z^{\bullet ox}$ Q_A^-- Y_Z Q_A spectra present.

[7] Multi exponential funciton fitted globally with sophisticated chosen decay constants

band shift, that has been found from 1710 to 1700 cm^{-1} fitting very well the expected kinetics presented in fig. 8.2. A **1705(-)/1997(+)** feature can be found in the Mn depleted $Y_Z^{\bullet ox}$ difference spectra (see sec. 3.3). II) changes in the amide I and II region at 1665, 1575 and 1560 cm^{-1} mainly sensing charge built up and compensation. Around 1500 cm^{-1} no band fitting the $Y_Z^{\bullet ox}$ kinetics was found. A band around 1250 cm^{-1} is not found or discussed. That **no band** is found **around 1500** cm^{-1} would contradict the model of the formation of the deprotonated Y_Z radical as $Y_Z^{\bullet ox}$, it might therefore be likely that the poor bandwidth of 10 cm^{-1} was not suefficient to separate the narrow $Y_Z^{\bullet ox}$ signal.

Non of the above mentioned studies was able to locate well the vibrational frequencies of $Y_Z^{\bullet ox}$ in functional centers and during the slow relaxation processes not even mentioning the present molecular mechanism.

8.4.1 A scan around the proposed location of the $Y_Z^{\bullet ox}$ CO stretch

To locate the position of the oxizidized tyrosyl radical, a scan in steps of 2.5 cm^{-1} were performed ranging from 1495 to 1520 cm^{-1}. The measurement were done at 10 °C and an pH of 7.5 on PSII membranes from spinach. The high pH was chosen as at this pH also a fraction of PSII centers might conduct electrons from the reduced Y_D to the Mn cluster in the S_2 or S_3 state or the other way around in S_1 possibly allowing the observation of both tyrosines in active PSII. Also at pH 7.5 the spectra of Mn depleted and oxygen evolving PSII are expected to be more similar as the pK_a of around 7 of D1-H190 is not crossed.

The deconvoluted data is presented in figure 8.6 as 3d plots with negative difference bands colored in blue and positive ones in red. Examples of the miss factor extraction from patterns at 3-10 ms are shown in figure 8.7. The averaged miss factor of 8.3 % was used to deconvolute all points in time. First when looking at the amplitude flash pattern around 10 ms, binary **contribution** steming **from quinone bands** are present at **1520** cm^{-1} with contributions ranging down to 1515 cm^{-1}. The value in odd flashes is negative (blue) whereas it is close to zero (white) in even flashes. Minor contributions of the quinones seem to be present as well at **1495** cm^{-1} manifesting in a slightly elevated 10 ms amplitude after the first and third flash. At 1500 cm^{-1} this contribution is already small. The quinone decay is shown in figure 7.11. The steady state spectra of the reduced minus neutral quinones shows a negative band at 1520 cm^{-1} in both Q_A^- and Q_B^- and a small positive at 1505 cm^{-1}, with the main band at 1478 cm^{-1}.

Strong bands showing **late quaternary behaviour** (compare fig. 8.7) have maxima in $S_1 \rightarrow S_2$: a broad feature around **1500** cm^{-1} with an instant and a crowing (100 µs - 1ms) part and a weak narrow one at **1510** cm^{-1}; in $S_2 \rightarrow S_3$: only an early weak band around 1510 cm^{-1} crowing with 100 µs to one ms; in $S_3 \rightarrow S_0$: a negative feature at 1510 cm^{-1} and possibly a negative band at 1497.5 cm^{-1} masked by the quinone band both developing with one to 10 ms; in $S_0 \rightarrow S_1$: two positive features appear at 1500 and 1510-1512.5 cm^{-1} and seem to stay over the time course. The bands at 1509-1511 cm^{-1} in *Thermosynechoccocus elongatus* were assigned to a mixture of amide II and $\nu_{AS}(COO)$ ([Noguchi and Sugiura, 2003]).

Instantanously formed signals can be observed at **1500**, at **1505** cm^{-1} and and weaker at 1512.5-1515 cm^{-1}. These first two are especially strong in $S_2 \rightarrow S_3$ and $S_3 \rightarrow S_0$. Figure 8.8 shows the amplitudes averaged from 100 to 400 ns for each transition (left). The right panel shows the difference between 2-8 µs and 100-400 ns. Note the different scale. Half of the strong bands at 1500 and 1505 cm^{-1} decay nearly completely within this time. These bands are located on top of a broad decaying feature. They decay further within 100 µs. This behaviour is indicative of groups sensing the presence of P_{680}^{+} (compare fig. 8.2). The Mn

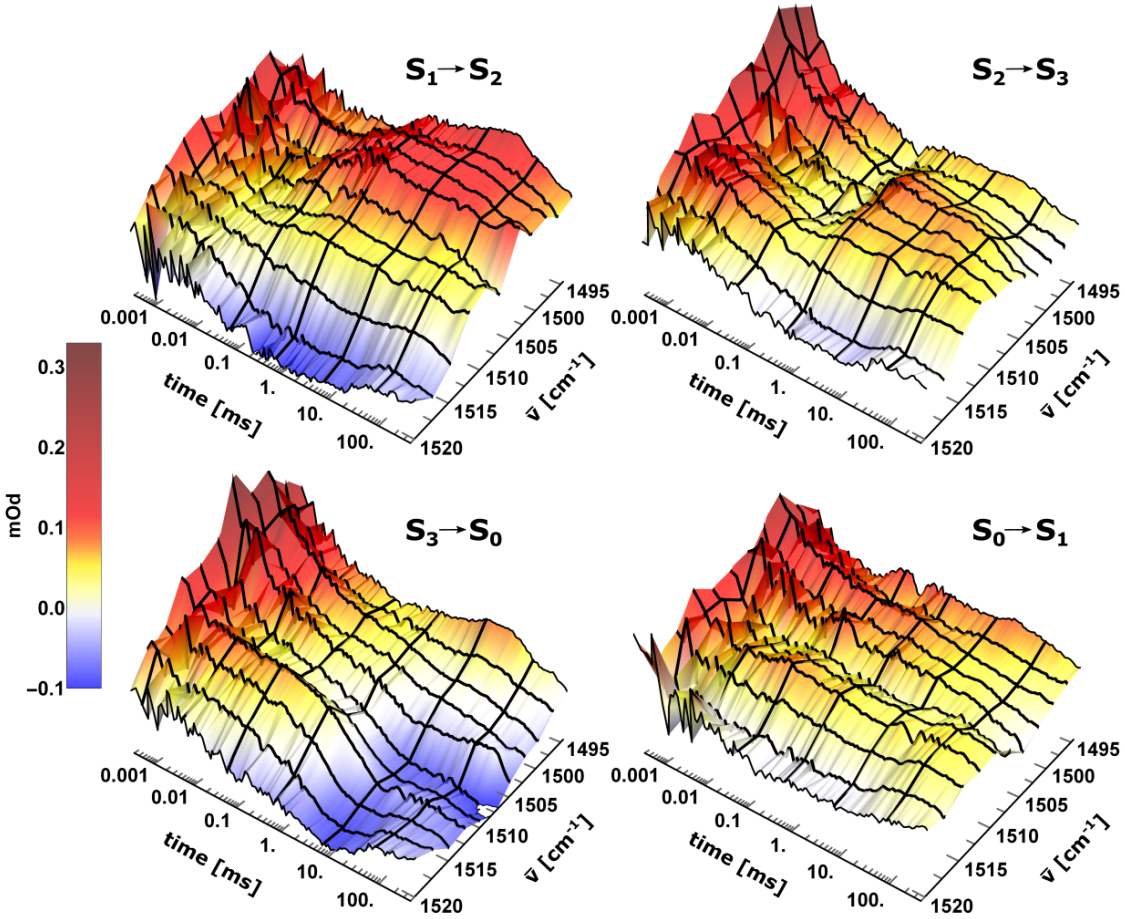

Figure 8.6: Scan in steps of 2.5 cm^{-1} around the expected position of the CO stretch of $Y_Z^{\bullet ox}$. Black lines represent the wavenumbers or decadic time intervals. In $S_2 \rightarrow S_3$ and $S_3 \rightarrow S_0$ a candidate band is visible at 1512.5 to 1515 cm^{-1}. In these transition a $\nu_{AS}(COO)$ band is located around 1507.5-1510 cm^{-1} (+,-). In the $S_1 \rightarrow S_2$ and $S_0 \rightarrow S_1$ the two bands seem to overlap. The dark red early amplitudes represent unidentified chemical groups which sense P_{680}^+. (PSII membranes from spinach, pH 7.5, 10 °, with PPBQ.)

cluster band at 1398 cm^{-1}, does not decay with this fast kinetics. In the right panel in gray the remaining signals at 2-8 µs are shown. In these spectra there is a clear discrimination of different features. In all except maybe for $S_1 \rightarrow S_2$ **a distinct band located** at the same position **between 1510 and 1515** cm^{-1} remains.

Bands showing the expected $Y_Z^{\bullet ox}$ kinetics, are not easily visible in the flash transitions. In $S_2 \rightarrow S_3$ **and** $S_3 \rightarrow S_0$, the bands present around 5 µs and 1510-1515 cm^{-1} decay with the approximate Mn cluster oxidation. In the former transition it is overlapping with a rising band at 1510 cm^{-1}. In both transitions they do not seem to sense the 400 ns and 30 µs rise or shift. In the $S_1 \rightarrow S_2$ transition around 1515 cm^{-1}, might be a band formed rapidly but is then dominated by the rise of the 1510 cm^{-1} band. At its high wavenumber shoulder, a decay with around 100 µs is visible. In $S_0 \rightarrow S_1$ only one positive band is present over the whole

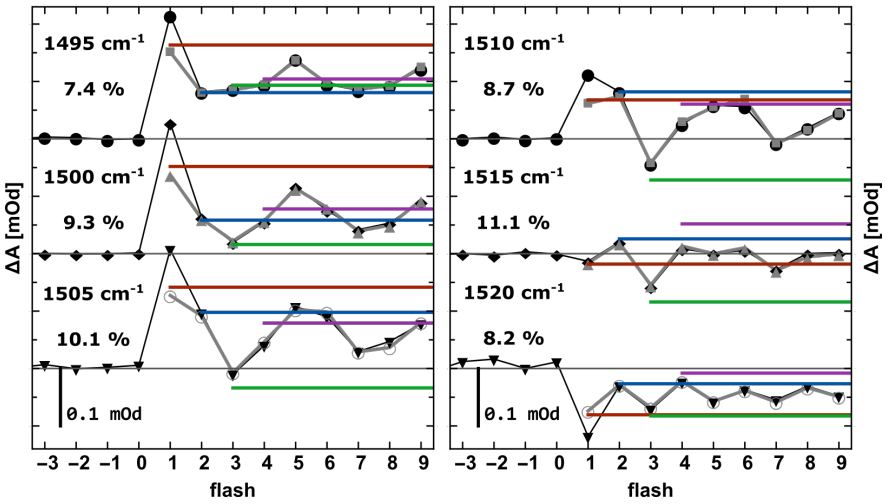

Figure 8.7: 10 ms flash pattern of bands around 1510 cm^{-1}. Measurement at **pH 7.5** and 10 °C. Miss factors are indicated assuming 100 % S_1 in the dark, excluding the first flash data. Beginning with $S_1 \rightarrow S_2$ the four deconvoluted amplitude are presented in red blue, blue, green and magenta. A contribution of the quinones in both 1495 and 1520 cm^{-1} is visible in the mixture of the quaternary pattern of the neighboring wavenumbers and a binary one.

time course starting between 1510 and 1515 cm^{-1}. Whether there are two bands involved cannot be judged at this point.

A clearer view of the **differences** in each spectrum occuring **with the known Mn oxidation times** is presented in figure 8.9 (left panel). Here the difference spectra in time for $S_1 \rightarrow S_2$: 400 µs minus 40 µs; $S_2 \rightarrow S_3$: 1 ms minus 100 µs, $S_3 \rightarrow S_0$: 10 ms minus

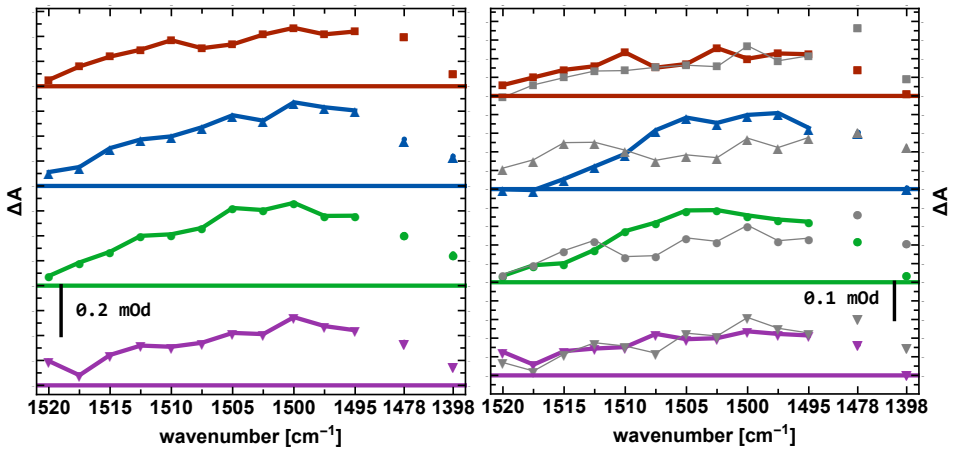

Figure 8.8: *left:* Averaged spectra from 100-400 ns recorded at pH 7.5 and 10 °. From top to bottom: $S_1 \rightarrow S_2$, $S_2 \rightarrow S_3$, $S_3 \rightarrow S_0$ and $S_0 \rightarrow S_1$. The quinone band at 1478 cm^{-1} is scaled by 0.2. *right:* decay calculated between 2-8 µs minus 100-400 ns. The quinone band is unscaled. In *gray* the averaged spectrum at 2-8 µs is shown, here the quinone band is scaled by 0.2. Note the different scales in the two figures.

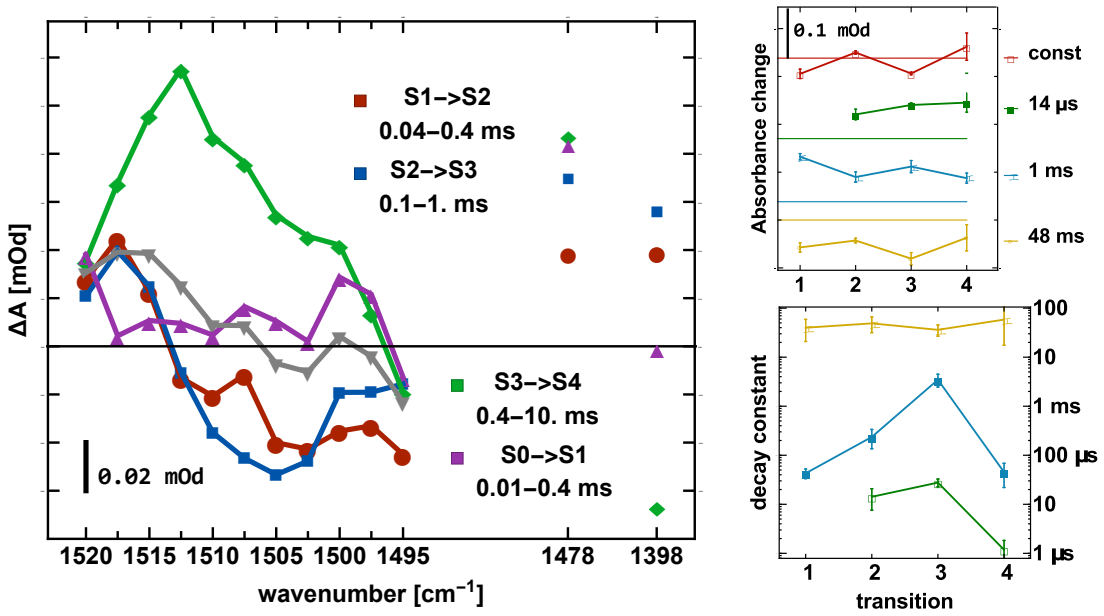

Figure 8.9: *left:* Spectral change associated with Mn oxidation around the suggested $Y_Z^{\bullet ox}$ band at 1514 cm^{-1}. The spectral differences of the times indicated are plotted (.5 to 2x $t_{indicated}$). In gray the average of all changes is plotted with a strong non-zero band around 1515 cm^{-1}. Measurements at pH 7.5 and 10 °C. The bands at 1478 cm^{-1} and 1398 cm^{-1} are scaled by x .3 and x .5; *right:* results of the curve simulation at 1520 cm^{-1}. No constraints have been given. The number of exponentials is chosen as the highest from where further increments do not provide better fit residuals or too high fit errors. The blue components reflect well the known Mn oxiadation times with a similar amplitude in all flashes (top).

400 µs and $S_0 \rightarrow S_1$: 100 µs minus 10 µs are plotted. In both $S_1 \rightarrow S_2$ and $S_2 \rightarrow S_3$ a band a 1517.5 cm^{-1} decays, whereas one or two bands at 1505 to 1512.5 cm^{-1} rise. In the 3d plots we can see, that this is rather not a band shift but two separate bands. We can therefore judge that in both transition a $Y_Z^{\bullet ox}$ candidate band is present, but masked by another band. In $S_3 \rightarrow S_0$ a broad and strong band with several shoulders at lower wavenumbers decays from 1495.5 to 1520 cm^{-1}. The changes in $S_0 \rightarrow S_1$ are small. The change at 1495 cm^{-1} in $S_1 \rightarrow S_2$ might stem from the electron transfer from Q_A^- to Fe^{III} or Q_B. But at 1478 cm^{-1} the changes are smallest in $S_1 \rightarrow S_2$ and of similar size in the other transitions. That behavior is not visible at 1495 cm^{-1} and thus the dynamics observed in $S_0 \rightarrow S_1$ might be a small contribution of the Y_Z band.

The carboxylate/amide II bands at 1510 and 1502.5 cm^{-1} behave similarly upon Mn oxidation (fig. 8.9). In $S_1 \rightarrow S_2$ the amplitude change at 1505 cm^{-1} seems higher than at 1510 cm^{-1}. In $S_2 \rightarrow S_3$ the bands overlap due to an apparent downshift of the 1510 cm^{-1} band. The big broad decaying feature in $S_3 \rightarrow S_0$ is reverting the changes of the two earlier transition at 1510 and 1502.5 cm^{-1}. All changes of these two bands are inverted at 1398 cm^{-1}, a band assigned to the $\nu COO^-_{\ sym}$ groups, sensing Mn oxidation and the 30 µs phase (see se. 9.4.3).

Keeping in mind that all changes occurring during the S-state cycle need to be reversed (visible at 1398 cm^{-1}) and that quinone kinetics are observed in this time range as well (to various amounts, 1478 cm^{-1}), the average of all changes are compared. This spectrum

represents the **non-reversed change per flash** and is plotted in gray triangles in figure 8.9. There is a prominent band appearing from 1510 to 1520 cm^{-1}, matching perfectly our expectations of the position of $Y_Z^{\bullet ox}$ vibrations. A contribution from quinones can be ruled out, because the measurement at 1478 cm^{-1} shows smallest changes in $S_1 \rightarrow S_2$, whereas even the shoulder at 1520 cm^{-1} changes equally in all transitions.

8.4.2 Global analysis around 1510 cm^{-1}

To further decompose this spectrum and find the exact peak positions, a global fit analysis has been done in three steps. Included are the 11 wavenumbers of the scan from 1495 to 1520 cm^{-1} in steps of 2.5 cm^{-1}, two measurements of the amide II band at 1544 cm^{-1}, the symmetric COO^- stretch band at 1398 cm^{-1} and the coupled CO/CC quinone vibration at 1478 cm^{-1}. *First*, independent simulation of every wavenumber were performed. To degrees the number of free parameters in a *second* step, a fit with common decay constants for all wavenumbers is done. The number of free parameters is then:

$$nb_{\bar{\nu}} \cdot (1_{const} + nb_{exp,Amp}) + nb_{exp,\tau}$$

For a six exponential fit with 15 wavenumbers this yields **111 parameters**. To reduce these vast amount it was tried, *third*, to couple neighboring points by fitting decaying and rising lorenz peaks into the scan(omitting peak shifts). Also the decay constants were fixed by the values obtained in step 2. In a test run the scan from 1495 to 1520 cm^{-1} could well be fitted with five peaks (with only ten spectra in time). The number of free parameters was:

$$nb_{peaks} \cdot \left(lorentz(width, \bar{\nu}) + nb_{exp,Amp} + 1_{const}\right) + nb_{exp,\tau}$$

For six exponentials and five peaks this yields 51 parameters. With fixed decay times only **45 parameters** will be left free. As only the spectral scan can be used, the number of data will reduce from 15 wavenumbers times 130 points in time to 11 wavenumbers. Still the improvement of the fit due to the reduction of free parameters is more significant (ratio points per free parameters: 17.5 improved to 31).

I) Single $\bar{\nu}$ fits

To select the right amount of time constants, simulations of every wavenumber at every transition were performed individually. The number of exponential functions was chosen until the residual plot was not improving, while keeping the errors small. All decay times obtained for the four transitions are shown in figure 8.10. The variety is very high but some gathering is present as well.

The decay times resulting from the simulations of the quinone band at 1478 cm^{-1} are highlighted in black. One can see that the **quinone dynamics require time constants across the whole dynamic range**, namely: 400 ns, 10 µs, 200 µs, 1ms, 10 ms and 100 ms[8].

The COO^- band at 1398 cm^{-1} and the band at 1520 cm^{-1} both sense Mn oxidation. 1520 cm^{-1} is located at the edge of the possible $Y_Z^{\bullet ox}$ band where no asymmetric carboxylates are contributing. The results of the simulation at 1520 cm^{-1} are presented in figure 8.9. The amplitudes of the Mn oxidation kinetics are within the error identical in each flash. Only in $S_1 \rightarrow S_2$ some quinone kinetics might contribute. The results mark this wavenumber as

[8] the detailed results see 11.22

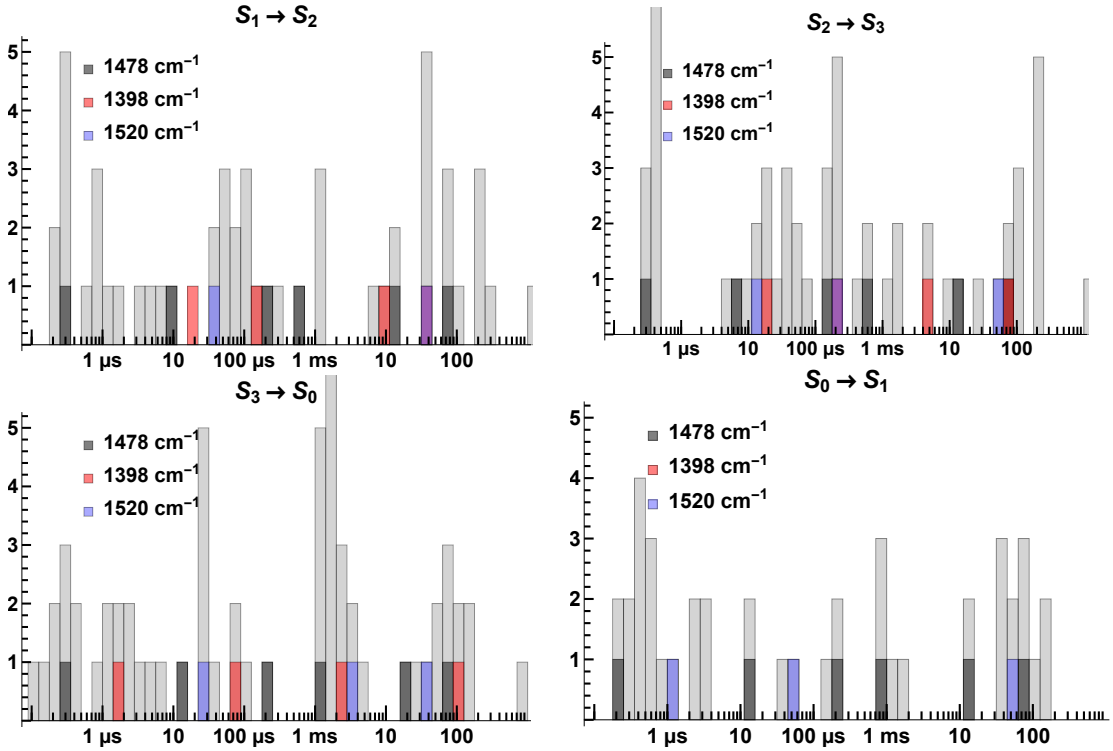

Figure 8.10: Histogram of the decay times obtained from individual wavenumber simulations (1398, 1478, and 1495-1520 cm^{-1}). Highlighted are the ones obtaines of the *reduced quinone band* at 1478 cm^{-1} (gray), a band of contributions from *symmetric* COO^- *vibration* sensing the Mn oxidation at 1398 cm^{-1} (red) and the results of the shoulder of the *putative* $Y_Z^{\bullet ox}$ band at 1520 cm^{-1} (blue) from figure 8.9 sensing the Mn oxidation always by a decay.

a good candidate to study the behavior of the tyrosine. The decay constants found at 1398 and 1520 cm^{-1} are in: $S_1 \rightarrow S_2$ 140 ± 50 and 43 ± 9 µs, in $S_2 \rightarrow S_3$ 245 ± 20 and 235 ± 100 µs and in $S_3 \rightarrow S_0$ $2.4 \pm .2$ and 3.5 ± 1 ms. In $S_0 \rightarrow S_1$ only the 1520 band decays with 45 ± 2 µs, the 1398 cm^{-1} band does stay constant. Both bands show contributions of the 20-100 µs phase in $S_2 \rightarrow S_3$ and $S_3 \rightarrow S_0$ as well.

All other bands contributing to the gray bars in the histogram of figure 8.10 group around the following decay times (transition): 400 ns (all), 1-5 µs (all but $S_2 \rightarrow S_3$), 20 and 50 µs ($S_2 \rightarrow S_3$) and 30 µs ($S_3 \rightarrow S_0$), 100 µs ($S_1 \rightarrow S_2$, $S_3 \rightarrow S_0$) 200 µs ($S_2 \rightarrow S_3$, $S_0 \rightarrow S_1$), 1 ms (all) and 100 ms (all). As shown in the introducton PSII reactions do include all those kinetics.

II) Global fit

The results of the single wavenumber fits where, next, used for a global simulation. The result is presented in figure 8.11. All transitions contain a 20 ms and 100 ms phase of the quinones (green and magenta).

The fastest phase found decays in $S_1 \rightarrow S_2$ and $S_3 \rightarrow S_0$ with 150-170 ns and in $S_2 \rightarrow S_3$ with 330-360 ns and in $S_0 \rightarrow S_1$ with 550-650 ns. The former are close to a sharp feature sometimes present at 100 ns and possibly caused by electric disturbances. In $S_2 \rightarrow S_3$ two

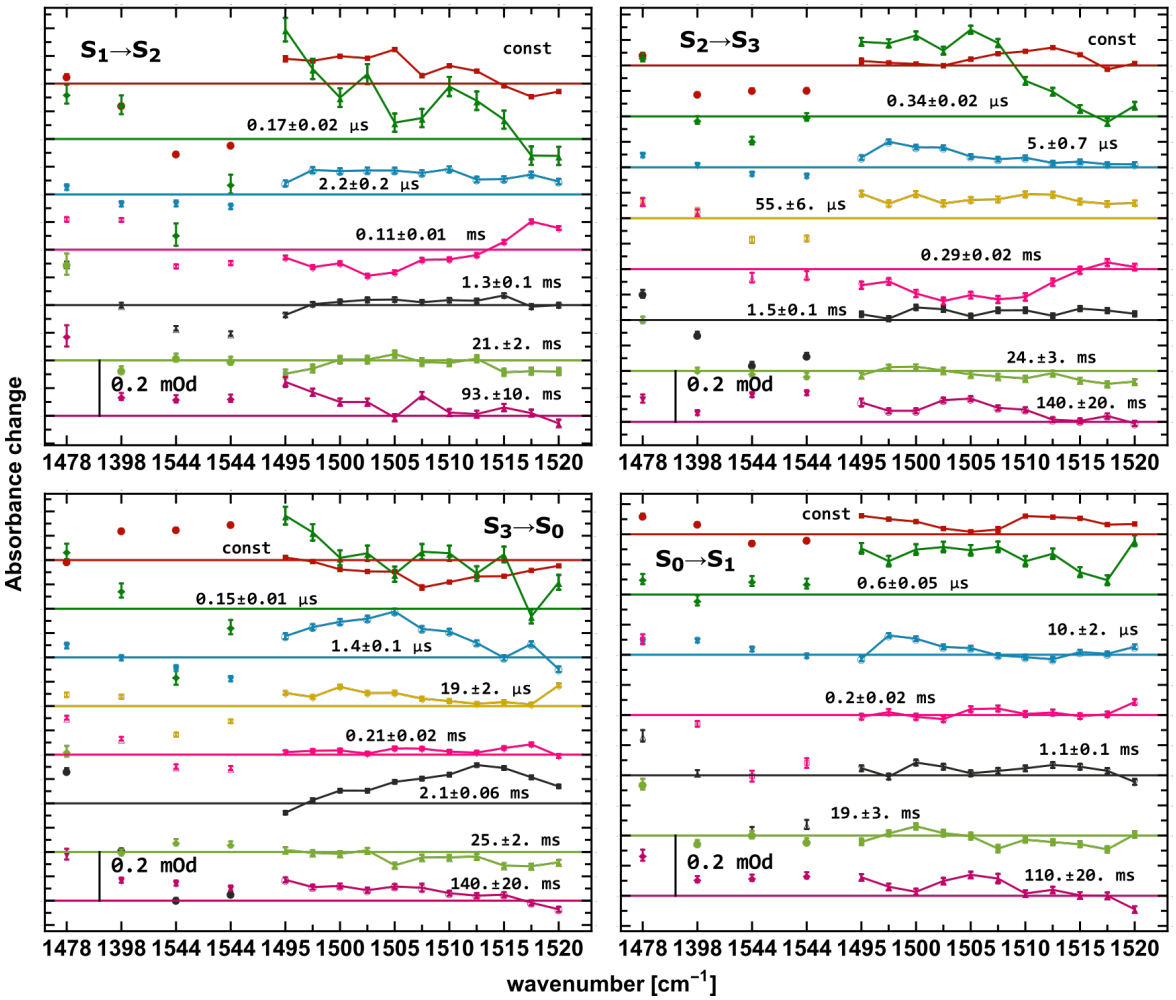

Figure 8.11: Decay associated spectra of a global fit obtained for the single transitions: *top left*: $S_1 \rightarrow S_2$, *top right*: $S_2 \rightarrow S_3$, *bottom left*: $S_3 \rightarrow S_0$ and *bottom right*: $S_0 \rightarrow S_1$. The band at 1478 cm^{-1} reflects quinone dynamics, 1398 cm^{-1} reflects carboxylates sensing the Mn photocycle and the amide II bands at 1544 cm^{-1} were included in the simulation (100 ns - 400 ms). The data is obtained on PSII membranes from spinach at 10 °C and **pH 7.5**. A decay is present around 1515 cm^{-1} with the Mn oxidation times (120 µs, 300 µs, 1.8 ms. Only in the $S_0 \rightarrow S_1$ transition no clear indications of the Mn oxidation is found.

bands at 1497.5 and 1505 cm^{-1} contribute (similar to fig. 8.8). The broad band centered at 1505 cm^{-1} $S_3 \rightarrow S_0$ seems to split into several components decaying either with 150 ns or 1.4 µs. The slow component is also centered at 1505 cm^{-1}. Such a slow component of 2-10 µs was found in all transitions (blue). On average, it is higher between 1497.5 and 1505 cm^{-1}, as in $S_2 \rightarrow S_3$ and $S_0 \rightarrow S_1$, and may be related to the decay of P_{680} triplet states. A similar shape is found in $S_3 \rightarrow S_0$ in the spectrum of the 19 µs component. This again might indicate the mixing of several phases. A 55 ± 6 µs component was only found in $S_2 \rightarrow S_3$. It is rather featureless but might contain a band at 1510 cm^{-1}.

The **100 to 300 µs component**, plotted in magenta, is silent in $S_3 \rightarrow S_0$ and $S_0 \rightarrow S_1$. In $S_1 \rightarrow S_2$ it is with 110 ± 10 µs relatively fast and matching Mn oxidation kinetics (see sec. 9). From 1495 to 1510 cm^{-1} the transients rise while from 1515 to 1520 cm^{-1} they decay. The decay associated spectrum does *not* follow a typical derivative like shape of a band shift. When comparing it with the fit constant (red), a big fraction is a mirror of it but leaving some contribution around 1515-1520 cm^{-1}. In $S_2 \rightarrow S_3$ a 290 ± 20 µs phase is found. Two bands, or one broad band, rise at 1505 to 1510 cm^{-1}. The bands are not well reflected in the fit constant. However when we look at the data in figure 8.6 we see an onset of probably a drift at 100 ms. Indeed when we add the 140 ms phase to the constant, the 300 µs rise is well presented up to 1512.5 cm^{-1}. However, above at 1515-1520 cm^{-1}, where there is even some weak decay found, the fit constant is still positive or zero. This means a small band might be present at these wavenumbers.

The **1-2 ms** phase (black) is mainly active in $S_3 \rightarrow S_0$ and shows the Mn oxidation with some quinone reaction contributing. The spectrum consists of a broad positive band centered at 1512.5 cm^{-1}. Comparing this with the steady state value in red, it mainly is mirrored up to 1510 cm^{-1}. From there the decay is stronger than what will remain. Some instantaneously formed signal decaying with the Mn oxidation needs to be present.

textbfIn summary, the time constants needed for the next step are found. The early phases are noisy but in $S_2 \rightarrow S_3$ and $S_3 \rightarrow S_0$ one or two distinct bands were found. In S_1 to S_0, there are indications for a signal formed early on around 1510-1517.5 cm^{-1}, that decays with Mn oxidation kinetics. The $S_0 \rightarrow S_1$ transition seems to be silent. Because its steady state spectrum shows a band in the very same region, a decay and a rise might overlap.

III) Global spectral fit in between 1495 and 1520 cm^{-1}

So far not all available information has been used. The spectral information is valuable as changes will always appear as difference bands. These may take on the form of a derivative like shape for band shifts, or independent rising and decaying bands. Given that the only negative feature in the region between 1495 and 1515 cm^{-1} are present in S_3 or the binary pattern of the quinone influenced band at 1520 cm^{-1}, only band appearance and decays are considered. The line shape used is a lorentzian (see sec. 4.8). The number of peaks was kept as low as possible and good results were obtained with two quinone peaks, one amideII/carboxylate band changing with the Mn oxidation and proton release kinetics and one very fast peak changing with the P_{680} Y_Z kinetics. This simulations will not yield perfect results for the complex behavior of PSII, but will yield peak positions of the missing signal around 1515 cm^{-1}. The quality of the fit is presented in figure 11.26

The single components are plotted in figure 8.12. Horizontal lines indicate all rise and decay times the peak may use. These times were obtained with the global fit before. The location of the low wavenumber quinone peak was kept between 1475 and 1500 cm^{-1}. All other peaks were only fixed between 1490 and 1525 cm^{-1}. The width was limited between 4

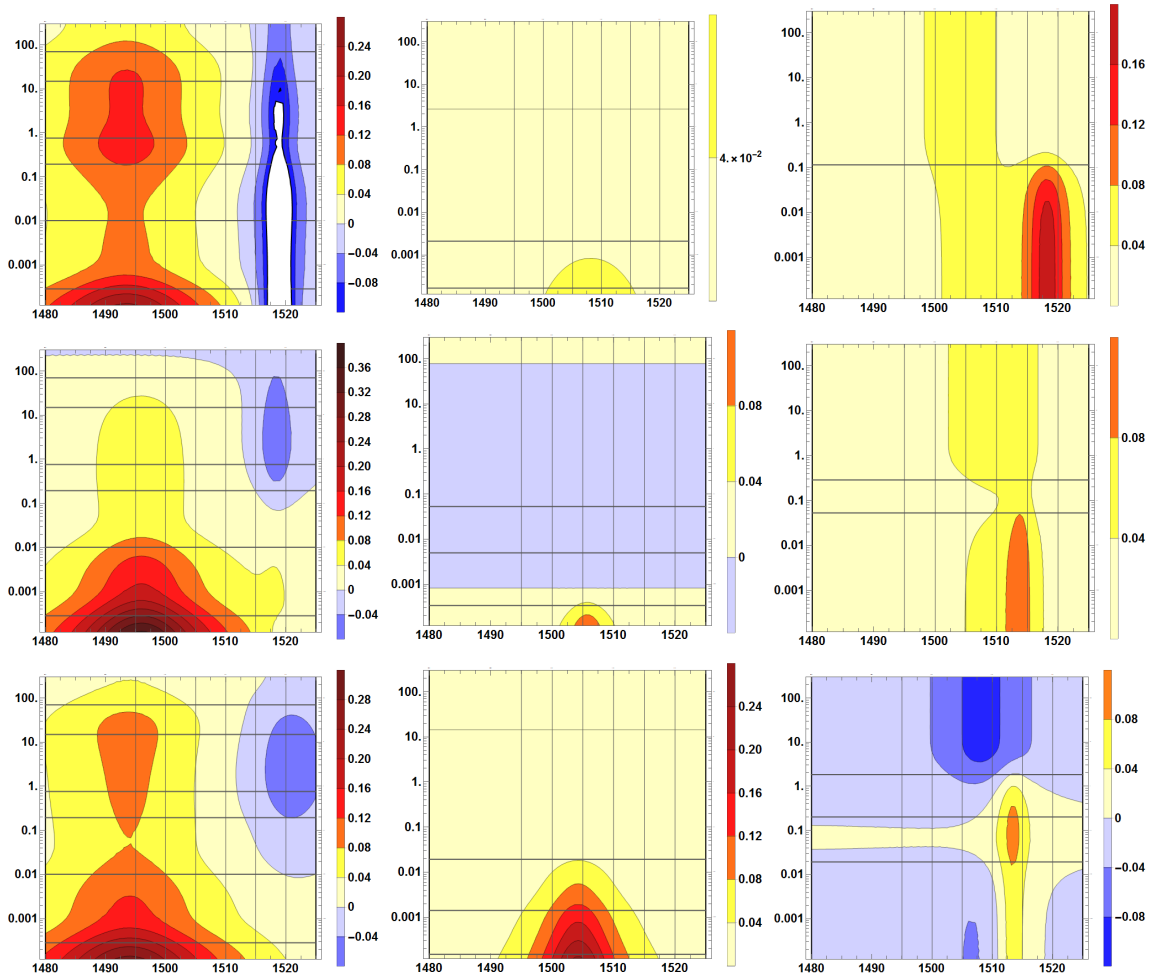

Figure 8.12: Lorenzian peaks with fixed position and width fitted to the S-state transitions (top to bottom: $S_1 \rightarrow S_0$). They may change their amplitude with the time constants obtained from the global fit (marked as horizontal lines). *left*: Two peaks are sufficient to describe the quinone behavior. $S_1 \rightarrow S_2$ (top): The fit of the 1520 cm^{-1} band differs from the other two fits presented due to the strong overlap with the $Y_Z^{\bullet ox}$ band. $S_2 \rightarrow S_3$ (center) and $S_3 \rightarrow S_0$ (bottom): similar fit results for the two peaks. *center*: the fast peaks decaying mainly with 300 ns or 1-2 µs: In $S_1 \rightarrow S_2$, weak, at 1508 cm^{-1}, in $S_2 \rightarrow S_3$ at 1506 cm^{-1} and in $S_3 \rightarrow S_0$ at 1504 cm^{-1}, partially compensated by the carboxylate peak on the right. *right*: $S_1 \rightarrow S_2$ (top): at 1504 cm^{-1} and a band assignable to $Y_Z^{\bullet ox}$ at 1518 cm^{-1} are fitted with one decay constant of 120 µs. $S_2 \rightarrow S_3$ (center): one carboxylate/amideII peak at 1509 cm^{-1} and a band assignable to $Y_Z^{\bullet ox}$ at 1514 cm^{-1} are fitted with two decay constants of 53 and 290 µs. The 1509 cm^{-1} band starts positive, decays with 0.4 mOd and rises again with .6 mOd. The $Y_Z^{\bullet ox}$ band decays slightly with 50 µs (0.04 mOd) before it decays completely with 0.12 mOd. $S_3 \rightarrow S_0$ (bottom): one carboxylate/amideII peak at 1508 cm^{-1} and a band assignable to $Y_Z^{\bullet ox}$ at 1513 cm^{-1} are fitted with three decay constants of 19 and 200 µs and 1.8 ms. The $Y_Z^{\bullet ox}$ band is slightly rising with 200 µs and 1/4 of the 1.8 ms decay amplitude. The carboxylate band starts negative, rises with 19 µs and decays with both later phases (0.1 and 0.6 mOD). The fit ranged from 120 ns to 200 ms.

and 25 cm^{-1}. The starting values were crucial for the fit results. In the plots a rise or decay within one color can best be seen by the broadening or narrowing of the peak.

The *left column* shows the two quinone peaks. The peak located at 1492-1497 cm^{-1} shows some binary behavior like the data. A Q_B^- peak rises with 200 µs and 1 ms to decay with 20 ms. This fits the observation of the quinone behavior, where less non heme iron is oxidized in odd flashes and, therefore, more electron transfer takes place towards Q_B or PPBQ (see sec. 7.3). The position of a Q_B^- peak is rather expected to contribute at 1480-1485 cm^{-1}- out of the scanning range. The high wavenumber peak matches the assignment of a neutral quinone (sec. 3.3). In $S_1 \rightarrow S_2$ clearly a too strong contribution was fitted[9].

The *middle column* represents the additional fast peak. Mainly in $S_2 \rightarrow S_3$ and $S_3 \rightarrow S_0$ there is some stronger peak located between 1502.5 and 1506 cm^{-1}. The one is $S_2 \rightarrow S_3$ decays with 300 ns very rapidly, the one in $S_3 \rightarrow S_0$ mainly with 2 µs. The intensity of the latter is higher as it is partially compensated from the neighboring band. Both, positions and decay speed, match the decay associated spectra. At 1503 cm^{-1} small contribution of the reduced quinones may be present or at 1510 cm^{-1} P_{680}^+ and its triplet.

The *right column* shows the overlap of the two remaining bands. Both are allowed to vary with the indicated times in heights and one is forced to decay completely. In $S_1 \rightarrow S_2$, the result is not very meaningful. Here the strong band decaying at 1518 cm^{-1} is almost completely canceled by the quinone band at 1519 cm^{-1}. In the sum of all bands, this will result in a decay of a band located between 1512 and 1515 cm^{-1} (fig. 8.13). In $S_2 \rightarrow S_3$, a band is found at 1514 cm^{-1}. Underneath, a small contribution of a band at 1509 cm^{-1} first decays with 30 µs but then strongly rises with 300 µs. In $S_3 \rightarrow S_0$, the fit found a band at 1513 cm^{-1} and one at 1508 cm^{-1}. The latter starts with negative absorption but only to compensate the strong band at 1504 cm^{-1}.

The $S_0 \rightarrow S_1$ is not shown because here the result was a cancellation of the $Y_Z^{\bullet ox}$ peak (forced to go to zero). Still a decay of the band at 1512.5 cm^{-1} is present and together with the fits of the other transitions indicates a contribution of $Y_Z^{\bullet ox}$ in this transition as well (fig. 11.27).

In figure 8.13 the sum of all contributions is shown. This fit result is not unique and especially the peak in $S_0 \rightarrow S_1$ (bottom right) is questionably (comp. fig. 11.26). Nonetheless, the data in the other transitions is well represented and a clear band even in $S_0 \rightarrow S_1$ can be spotted.

8.4.3 Discussion

In this section I found at least one band decaying with the fast phase of P_{680}^+ reduction kinetics was found at 1505 cm^{-1}. Some broad equally fast band seems to contribute around 1495-1500 cm^{-1}. Around 1510 cm^{-1} a band of the triplet and the oxidized form of P_{680} is expected (see see 3.3). This may be split into two features in the reported spectra ([Okubo et al., 2007]), possibly matching my observations .

With Mn oxidation kinetics, another band appears at 1504 (+) in $S_1 \rightarrow S_2$, 1509 (+) in $S_2 \rightarrow S_3$ and a broader one at 1508 (-) cm^{-1} in $S_3 \rightarrow S_0$. In $S_0 \rightarrow S_1$ it is located at 1510 to 1515 cm^{-1} but no kinetics could be extracted. The band in $S_1 \rightarrow S_2$ is shifted compared to the one at 1509 cm^{-1} in PSIIcc of cyanobacteria (comp. fig. 3.3 and 3.4). This shifted band also explains the kinetic differences of this study and the one in [Sakamoto et al., 2017].

[9] The white color means it is out of scale

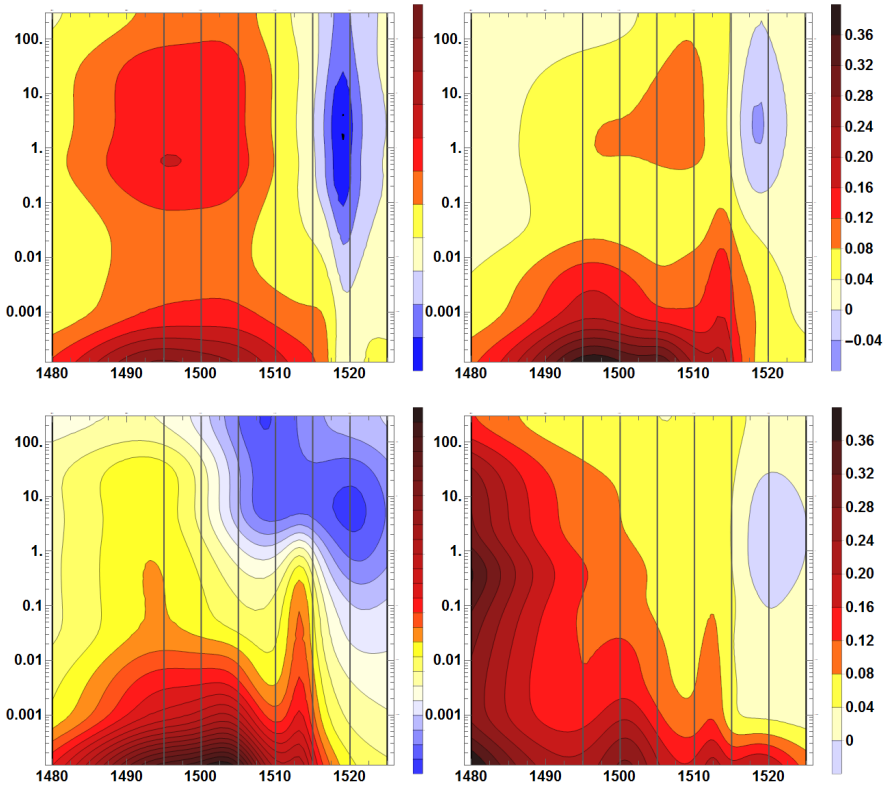

Figure 8.13: Contour plot of the simulation results with all five lorenzian peaks at pH 7.5 and 10°C. Top left: $S_1 \rightarrow S_2$, top right: $S_2 \rightarrow S_3$, bottom left: $S_3 \rightarrow S_0$, bottom right: $S_0 \rightarrow S_1$. The quality of the fit is presented in figure 11.26. The results presented here are (possibly) not unique.

They observe the zero crossing of the transients at 1504 cm^{-1}, whereas it was observed here at 1517.5 cm^{-1}.

The contribution of a $Y_Z^{\bullet ox}$ vibration was extracted by three different methods in the region between 1495 and 1520 cm^{-1} in completely functional PSII. First, by looking at the raw data and calculating the differences before and after Mn oxidation (fig. 8.9). In $S_1 \rightarrow S_2$ and $S_2 \rightarrow S_3$, a band was present but only when extracting the averaged non-cyclic contributions a clear band appeared between 1510 and 1520 cm^{-1}. Next, the scanned region and some marker bands were simulated globally. The decay associated spectra of Mn oxidation match the one of the fit constant (and a slow drift), but not around 1515 cm^{-1}. Again not including $S_0 \rightarrow S_1$. In a last approach five lorentzian peaks with fixed width and position were fitted into the data. Two of which were varying with quinone kinetics, one with fast P^{+}_{680} and two with the Mn photocycle kinetics. By this a band was located at 1514 and 1513 cm^{-1} in $S_2 \rightarrow S_3$ and $S_3 \rightarrow S_0$, respectively. In $S_1 \rightarrow S_2$ and $S_0 \rightarrow S_1$, the approach did not resolve the single bands, but the sum showed also some band contributing around this position.

In total strong indications of the band of $Y_Z^{\bullet ox}$ **located at 1512-1515** cm^{-1} were found. Within the limited quality of band separation, it did not alter with the 300-800 ns or 30 µs of P^{+}_{680} decay. Although masked by an amideII/$\nu_{AS}(COO)$ band rising, the band at 1512-1515 cm^{-1} decays with the times found for Mn oxidation. Only in $S_0 \rightarrow S_1$ no changes in time

could be observed. The evidence for this band being a $Y_Z^{\bullet ox}$ signal is much stronger than the one presented in the literature:

In [Guo et al., 2018] the approach to track the vibration of the tyrosine radical was to first deplete the sample of Ca, resubstitute it with various divalent cations (oxygen evolving samples) and then track the recombination reaction with Q_A^- in a trapped state at 190 K. Their spectra looks very much like my recombination spectrum with a peak at 1504 and 1478 cm^{-1} (reported in 7.1.3). Also the marker band for Q_A^- at 1418-1419 cm^{-1} is present in both. Therefore,their band at 1478 cm^{-1} assigned to the $\nu(CO)$ mode of $Y_Z^{\bullet ox}$ is rather some quinone contribution. Also the band at 1504 cm^{-1} is present in all reported quinone studies. The band at 1504 cm^{-1} assigned by them to the $\nu_{7a}(CO)$ stretch might be shifted due to the lack of rearrangements when trapped at 190 K with the S_2 state present (transition to S_3 blocked). In the recombination spectrum of this work. either the cluster was not intact or $Y_Z^{\bullet ox}$ was trapped in a 190 K state.

In [Sakamoto et al., 2017] the spectral resolution was very limited ($\delta\nu \approx 16\, cm^{-1}$). They report the instant formation of a $Y_Z^{\bullet ox}$ signal at 1514 cm^{-1} in $S_2 \rightarrow S_3$. As most of the cofactor spectra of mentioned in the introduction are reported by this group, it is unfortunate, that they do not discuss quinone vibrations in their scan from 1494 to 1534 cm^{-1}. In their own data one can find a Q_A^- band at 1531 and a Q_A^- band at 1521 cm^{-1} ([Okubo and Noguchi, 2006]). Their Q_A^- decays also with a 300-500 µs channel (PSIIcc + FeCy [Noguchi et al., 2012]). However, they discuss a shift due to a strengthening of the H-bonding of $Y_Z^{\bullet ox}$ with 100 µs to 1520 to 1530 cm^{-1} (the only kinetics visible in the transients). They explain the missing decay with a rise of the carboxylate band covering the weak decay (broad, centered at 1513 cm^{-1}). Their explanation is possible, but other signals, including the quinones or instantaneous signals formed by P_{680}^+ or its triplet, might play a role in this rich spectral range as well. Additionally, when looking at the $S_2 \rightarrow S_3$ 3d-spectrum fin figure 8.6, measurements with 10-16 cm^{-1} spectral resolution will hardly see a peak decaying, because the amideII/$\nu_{AS}(COO)$ band is weaker but broader. This might be even stronger in cyanobacteria, where the band reported at 1513 cm^{-1} absorbs up to 1535 cm^{-1} ([Noguchi and Sugiura, 2003]).

The position of the $\nu_{7a}(CO)$ vibration of $Y_Z^{\bullet ox}$ at pH 7.5 at 1512-1515 cm^{-1} is very similar to the one in Mn depleted PSII at 1514 cm^{-1} ([Suzuki et al., 2005]). This supports the simulation results on Mn depleted PSII by [Nakamura et al., 2014] and many studies before. Note, that there is no data obtained on the neutral Y_Z before excitation. But it can be clearly stated that $Y_Z^{\bullet ox}$ becomes deprotonated in a concerted proton-coupled electron transfer and keeps a strong H-bond to D1-His190 at least in $S_2 \rightarrow S_3$ and $S_3 \rightarrow S_0$[10]. Because the band does not decay before Mn oxidation, the results of this section disagree on the upshift of the $Y_Z^{\bullet ox}$ band and therefore no H-bond strengthening of $Y_Z^{\bullet ox}$ during 100 µs ([Sakamoto et al., 2017]).

Neither a rise with P_{680}^+ reduction kinetics was observed. This is somehow surprising, but might be due to the severe overlap with the P_{680}^+ signal expected at 1510 cm^{-1}, that was found to decay at 1505 cm^{-1} in $S_2 \rightarrow S_3$ and $S_3 \rightarrow S_0$. If the real center of the band was slightly upshifted, then the rise and decay around 1512.5-1515 cm^{-1} of $Y_Z^{\bullet ox}$ would be masked. Indeed, in the simulation of the peaks (fig. 8.12, there are indications for this in $S_3 \rightarrow S_0$. Only the rise was simulated as part of the $\nu_{AS}(COO)$ vibration. A time resolved study on PSII with isotope labeled tyrosine may shed light on this.

[10] a deprotonated Y_Z would contribute in the investigated spectral region.

9 Proton coupled electron transfer events of the oxygen evolving complex

After many decades of PSII research, the general process within PSII, its organization in the thylakoid membrane and also many feedback loops with other metabolic functions are known. Still up to now we are lacking a detailed atomic model of the water oxidation mechanism. On a more positive note, the knowledge is – due to the very confined environment of the oxygen evolving complex – much more advanced than in synthetic metallo oxide catalysts, where the nature of the active sites is not identified, yet.

This confined environment of the active site, the Mn_4Ca-μ-oxo cluster and its ligands, is known from X-ray absorption spectroscopy (giving among others an average bond length and coordination number, [Grundmeier and Dau, 2012]) and high resolution X-ray free electron laser studies of up to about 2 Å (e.g. [Young et al., 2016]). These yield the in principal time-resolved positions of all static atoms including water molecules without introducing any radiation damage. The X-ray radiation scatters on electrons making protons invisible. This is unfortunate, because the location and movement of protons is most important when studying the reaction mechanism of water splitting: When specific Mn atoms become transiently oxidized, in order to accumulate a sufficiently high redox potential to drive O-O bond formation, the coordinating water and hydroxo groups eventually release a proton. One might see the process as governed by nature's law: the weakest player and hardest to study - hydrogen - can not keep its electron and, in order to keep the accumulated charge low, becomes released[1].

Thus getting access to the location of protonation and deprotonation events around the Mn cluster as well as the routes proton need to follow to the lumen, will assist in identifying the underlying mechanism experimentally. A theoretical model including every single step of the reaction within a limited environment of the cluster was already proposed by Siegbahn some years ago ([Siegbahn, 2013]). Although satisfying most experimental constraints it might not be the ultimate answer and needs to be verified.

An experimental technique allowing to study the proton movements and bond changes everywhere in the protein is infrared spectroscopy. In the accesible spectral region of the setup one can follow, among others, the changes of deprotonated carboxylates and the protein backbone. The carboxylates represent an important group, as all except for one amino acid ligands of the Mn-cluster are aspartates, glutamates or the C-terminus of the D1-protein or the carboxylate group of the D1-C-terminus. They are also part of an extended H-bond network connecting the cluster with the bulk ([Debus, 2015]). Our progress on the time-resolved single frequency IR study on the photocycle the Mn cluster shall be highlighted here.

First, measurements in the symmetric carboxylate stretch region will be presented. Optimal wavenumbers shall be identified, that allow to follow the individual S-state transitions. Next, an overview of several other wavenumbers in the accessible region will be given. These

[1] Still all released hydrogens function as the working power driving ATP synthase. Again as in real life the unified force of the weakest powers the existence of the strongest.

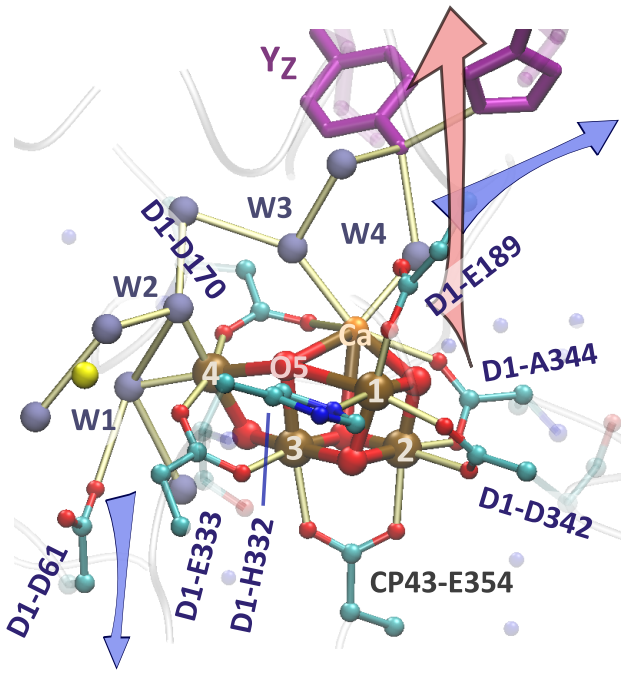

Figure 9.1: First sphere ligands of the Mn_4Ca-µ-oxo cluster including water. The electron is transferred via the redox active tyrosine Y_Z-H190 unit (magenta) towards P_{680}. Carboxylates, water and the histidine ligate the manganes atoms. In the S_1-state Mn1 is coordinated by two µ-oxos, two carboxylate oxygens and one nitrogen. In the S_2 and S_3 states there are conformations, in which O5 is bount to Mn1. In S_2 and S_3 conformations exist where O5 is bound at Mn1. Four water (W1-W4) only bind to Mn4 and Ca. The proposed site for O-O bond formation is O5. All of the carboxylates and waters are part of an extended H-bond network ranging to the lumenal bulk. Blue arrows indicate proposed proton release paths (compare 9.2). *crystal: 4UB6*

are the first discussions of well heat artefact corrected transients in this especially crowded region of amide II and asymmetric carboxylate vibrations with a time resolution down to hundreds of ns. Finally measurements of spinach PSII membranes and core complexes from *Synechocystis* sp. 6803 are compared. The chapter ends with first results on a genetically modified PSII at the D1-D61A site. This residuum binds to water W1, which in turn is bound to Mn4. Also it resides on the entrance of a proposed proton egress channel.

9.1 Water oxidation

At the moment there are mainly two possible mechanisms in debate for the O-O bond formation: nucleophilic attack and the radical coupling.

In a nucleophilic attack, a water attacks an oxyl or oxo group bound to Mn. A calculation showed that the product (OOH or OOH_2) is very high in energy. Therefore, this mechanism was ruled out ([Siegbahn, 2017]).

In the radical coupling mechanism, the O-O bond forms between an oxo-oxyl pair, which then is strongly bound to the cluster. Many experimental and theoretical results point to the location of O-O bond formation to be between Mn1, Mn4 and Ca.

9.1.1 The structure of the cluster, proton egress pathways and substrate water

The structure of the Mn cluster including the first sphere amino acid and water ligands is shown in figure 9.1. It is a radiation damage free S_1 state but might possess some S_0 contribution due to the long dark adaption ([Suga et al., 2015],[Askerka et al., 2017]). The oxygen O5 is bound to Mn4, leaving all Mn atoms except Mn1 six coordinated. Most ligands are carboxylates. Mn1 has one nitrogen ligand provided by D1-His332. Mn4 and Ca are each coordinated by two water molecules: W1 to W4. These waters and the carboxylates span an extensive H-bonding network including Y_Z, the cluster and D1-D61 and ranging to the lumenal bulk.

The four protons released during one catalytic cycle are transported away from the cluster via channels formed by these H-bonding networks of waters and carboxylates. Several variations of these were found by different techniques and even in a simulation, where one carboxylate of the network was removed, it stayed intact, which renders them, to some extend, flexible ([Guerra et al., 2018]). Three of them are shown in figure 9.2[2]. The “Back” channel involves Y_Z and passes by His190 and D1-N298 to PsbV. Channels ”Broad“ and ”III“ lead via D1-D61 and D1-E65 either to an exit at the D2 - CP47 interface or closer to PsbO, respectively. A review is given by [Ho, 2012] (see also [Umena et al., 2011]). So far it is not clear which of the channels is used in which transition. Noguchi tentatively suggested the back channel in the $S_2 \rightarrow S_3$ transition [Sakamoto et al., 2017]. At the entrance of the other two shown channels the D1-D61 residuum is located. Studies of mutated versions presented here might help identifying the channels in use.

At the moment most experimental and theoretical results converge and locate O-O bond formation between Mn1, Mn4 and Ca. Possible substrates include O5, W2 and W3 in all combinations ([Nilsson et al., 2014]). In $S_3 \rightarrow S_0$ one of the substrates needs to bind, thereby releasing oxygen. The other one most likely binds in $S_2 \rightarrow S_3$ at its final position. The delivery of substrates to the active site in $S_2 \rightarrow S_3$, is commonly thought of in two models: the carousel and the pivot mechanisms. In the carousel mechanism, water W2 binds between Mn4 and O5 (see fig. 9.1) and is replaced by a water previously H-bonded to the µ-oxo of Mn3 and Mn4. In the pivot mechanism the Ca-bound water W3 binds to Mn1 ([Askerka et al., 2017]).

In the S_2 state, there are two different types of cluster conformations with different spins and therefore different EPR activity. In the open state, O5 is bound to Mn4, whereas it is bound to Mn1 in the closed state. Because there is no evidence that the two conformations are differently IR active ([Onoda et al., 2000]), they are not further discussed here.

9.2 The photocycle of the Oxygen Evolving Complex

The photocycle of the Mn-cluster is presented in figure 2.2. The dark stable states S_0 and S_1 are underlined. After the preflashes followed by dark adaption, all PSII centers will be in the S_1 state. After a flash, the excitation energy of any antenna chlorophyll is transferred to the special chlorophyll unit P_{680} and initiates charge separation. The created positive charge

[2] this picture is lacking the “narrow channel”

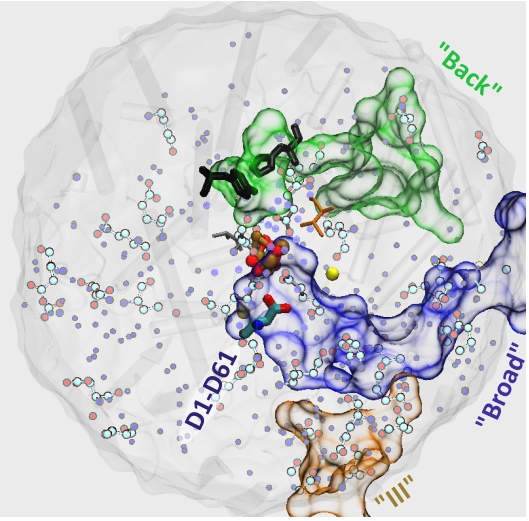

Figure 9.2: A protein sphere of 24 Å in diameter with the Mn-cluster in the center. The blue, red and green H-bonding networks represent suggested proton egress pathways (complete side-chains and close waters are included). Naming as reviewed in [Ho, 2012]. The D1-D61 residue is located at the entrance of two of these channels[3]. All other dots shown are either water (light blue) or side-chains containing carboxylate groups (C - white, O - red). Especially in the blue and orange channel these cluster strongly. Not shown is the 'narrow' channel. It includes the water chain to the left of D1-D61.

is transferred to the redox active tyrosine Y_Z. The kinetics depend on the S-state and are multiphasic when a positive charge is located on the catalytic site, namely in S_2 and S_3 (see chapter 8).

In the S_1 state, two Mn are in the oxidation state *III* and two in *IV*. In $S_1 \rightarrow S_2$ most likely Mn4 becomes oxidized without a change in its coordination number. The kinetics of around 100 µs are not very sensitive to deuterium exchange (KIE of 1.2) and proton release was not detected with proton sensitive dyes ([Junge et al., 2002]). This means that the positive charge stays in the vicinity of the cluster.

The $S_2 \rightarrow S_3$ transition is much more complicated. Because the cluster and its vicinity possess a positive excess charge, $Y_Z^{\bullet ox}$ formation is much slower with components of 300 ns and 30 µs. Within 30 µs, a proton release was observed using pH sensitive dyes (electrostatic, [Junge et al., 2002]). Therefore, the last phase of $Y_Z^{\bullet ox}$ stabilization and the proton release depicted in the scheme somewhere close to the Mn cluster are concerted or the same event. After the neutral S_2 state is formed, it may be oxidized within 300-400 µs. The most probable oxidized manganese Mn1 also changes its coordination number from five to six ([Zaharieva et al., 2016]). With a factor of 1.7, the KIE for this transition is very high and proton and/or water movements will occur. It was suggested that a water might bind to manganese turning into a hydroxide by deprotonation. The proton in turn might fill up the vacant site created within 30 µs[4]. [Siegbahn, 2013] for example proposed W1 to deprotonate first and the proton from the Mn1 site to travel to W1 via a network of three other water molecules, including one coordinating a chloride anion. In the scheme of the photocycle,

[4]It was also detected as a release into the bulk, discriminating between a chemical and an electrostatic proton [Junge et al., 2002].

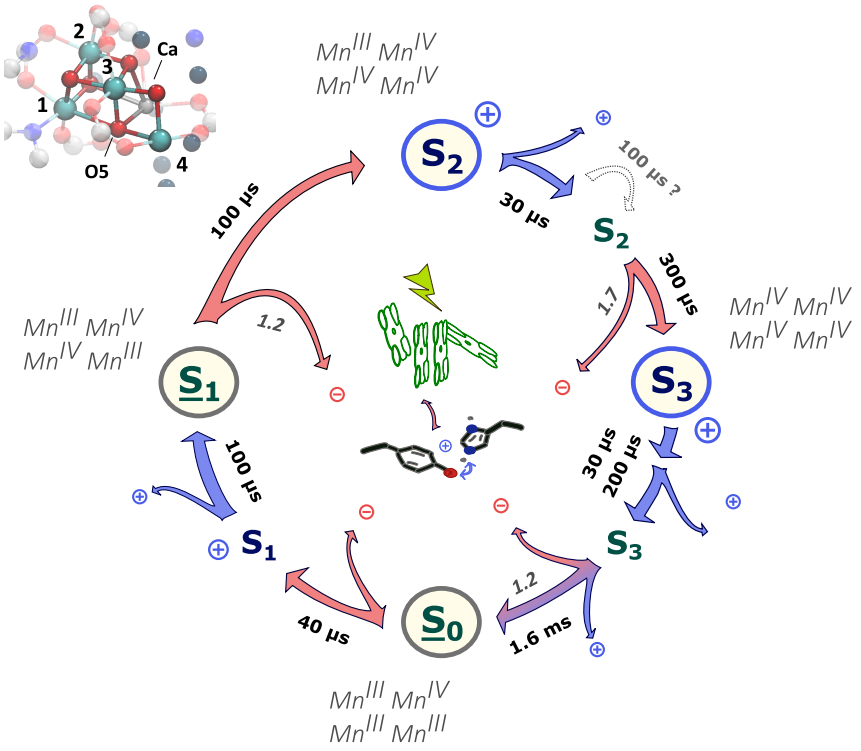

Figure 9.3: Photocycle of the Mn cluster including the Mn oxidation states. The inset in the top left shows the XFEL structure of the S_1 state (*crystal: 5GTH*). Red arrows represent electron transfer events to $Y_Z^{\bullet ox}$; the slow down upon deuteration is indicated. Blue arrows represent pure proton transfer events. The fast ones in $S_2 \rightarrow S_3$ and $S_3 \rightarrow S_0$ are induced by the positive charge at $Y_Z^{\bullet ox}$. In the $S_2 \rightarrow S_3$ a third phase was observed by some groups (see text). In the $S_3 \rightarrow S_0$, a third phase is definitely present. Indicated Mn oxidation states stem from [Zaharieva et al., 2016], time constants from [Klauss et al., 2015] and the kinetic isotope effects of the Mn oxidation steps from [Gerencser and Dau, 2010].

a third arrow of a 100 µs phase is drawn. It is based on time resolved IR observations of tyrosine (Y_Z and $Y_Z^{\bullet ox}$) and the strongly H-bonding region by [Sakamoto et al., 2017] and interpreted as a change of the H-bonding network between tyrosine and the cluster, possibly related to the movement of water W3 to the Mn binding site[5].

The dynamics of the $S_3 \rightarrow S_0$ transient can be described again by the two $Y_Z^{\bullet ox}$ stabilization phases, associated with a fast proton release (electrostatic in nature, [Junge et al., 2002]). This is followed by a poorly understood 200 µs phase – often referred to as a "lag phase", because experiments tracking solely the subsequent Mn oxidation or the oxygen release show no signal until the termination of this phase. It is often ascribed to movements of protons, as it has an KIE of around 1.4 and a strong pH dependency ([Gerencser and Dau, 2010]). Because the 30 µs proton release is electrostatic in nature and may get reversed in the ms time range, the actual proton release might be as slow as this phase and seen in measurements of

[5]There are some problems in the assignment to his $Y_Z^{\bullet ox}$ and the decay associated spectra around 1514 cm^{-1}. this will was discussed in 8

e.g. electrochromic shifts ([Nilsson et al., 2014][6]). All the remaining changes at the cluster, including Mn oxidation, O-O bond formation, water replacing the bound oxygen as well as further proton rearrangements and release into the bulk, were so far only found as one single step with about 1.6 ms (proton release: [Junge et al., 2002] and [Nilsson et al., 2014]). As in the S_3 state all manganese ions are already oxidized and coordinated six-fold the electron might directly origin from water. Afterwards, in S_1, all manganese except Mn2 are in the oxidation state *III*. The KIE is as low as 1.2 and it shows only weak pH dependence. Thus it can be assumed that either the Mn oxidation or the oxygen replacement by water are rate limiting.

The last step described is the $S_0 \rightarrow S_1$ transition. This is because it is the last step in experiments. While dark adapting, higher S-states may decay back to S_1 increasing its relative occupancy. Thus, until reaching the $S_0 \rightarrow S_1$ transition the S-states of the Mn cluster are already mixed, making it difficult to observe it. Additionally, the changes of this transition relative to the $S_3 \rightarrow S_0$ are weak. This is the reason for the varying reports on its kinetics. In our group, the consensus is that first Mn becomes oxidized (Mn3) within 40 µs and later a proton is released in about 100 µs. However, the separation of both phases was not straightforward.

To give an example of possible deprotonation events, Siegbahn's point of view on the $S_2 \rightarrow S_3$ transition shall be summarized briefly ([Siegbahn, 2013]): Upon $Y_Z^{\bullet ox}$ formation W1 bound to D1-D61 and Mn4 deprotonates (exergonic). This allows Mn1 to oxidize endogenically. It is more or less concerted with the binding of a previously inserted water coming from behind W2 and W3. Upon binding, the water needs to deprotonate (strongly exergonic). In his simulation the proton is transferred step-wise[7] via the water network to the vacant site at W1 (exergonic). Although this model does not necessarily display the full truth, it helps to understand the events we are targeting for. It also directly explains the high KIE effects observed in some Mn oxidation steps.

Although this summary shows that the kinetics are well understood, the detailed mechanism is not. It is the task of the future and on-going research to identify the exact atomic location and sequence of events. Time resolved infrared studies on mutated PSII have the potential to do so. With the following sections, the basis for this shall be given.

9.3 Measurements of this chapter

Scan from 1358 to 1410 cm^{-1}
2 sets of measurements, PSII membranes from spinach with PPBQ, 25 µm spacer, 20 °C, pH 6.2, 100 mM betaine, EMP correction via residuum of simulation of an all-flash-average, cycling intensity: 80/60 $\mu J/mm^2$, artefact intensity: 450/350 $\mu J/mm^2$, average of 300-600 sample spots (after selection).

Bands presented in the overview of fig. 6.1
1344 cm^{-1} from sec. 8.3 (10 °C), 1382 cm^{-1} from scan described just before (20 °C); others: 2 sets of measurements, PSII membranes from spinach with PPBQ, 15 µm spacer, 10 °C, pH 6.2, 0 mM betaine, cycling intensity: 40-60 $\mu J/mm^2$, artefact intensity: $210 - 240\,\mu J/mm^2$, average of 150-300 sample spots (after selection)

Measurement at pH 7.5
Taken from chapter 8.4: pH 7.5 at 10 °C

[6] Mentioned as a side remark in the SI.
[7] with individual transition barriers

Core complex from Synechocystis sp. 6803
prepared as described in sec. 4.4 with FeCy and a 15 µm spacer. Measurements at 5-10 °C and pH 6.0. Cycling intensity: 100-150 $\mu J/mm^2$, artefact intensity: $300 - 330\,\mu J/mm^2$.

Numbers of independent measurements (numbers of spots after selection):

WT: 1364: 2 (66,67); 1384: 2 (48,60); 1398: 3 (139,63,56); 1400: 2 (143,39); 1478: 4 (159,81,78,35); 1514: 1 (52); 1544: 3 (128,77,55); 1552: 1 (43).

D1-D61A: 1383: 2 (30,63), 1398: 2 (41,32), 1401: 1 (67), 1412: 1 (56), 1444: 1 (73), 1478: 3 (70,22,61), 1509: 1 (35), 1514: 3 (45,52,60), 1544: 4 (34,31,33,49), 1564: 1 (59), 1569: 1 (27), 1586: 1 (53), 1633: 1 (34).

9.4 The symmetric carboxylate stretching region from 1360 to 1410 cm^{-1}

In his three papers on time resolved IR spectroscopy of oxygen evolving PSII, Takumi Noguchi uses the band at 1400 cm^{-1} ($\Delta\bar{\nu} = 16\,cm^{-1}$, time resolution of 2.5 µs) as a viable tool to track the changes of the H-bonding network around the cluster upon Mn oxidation ([Noguchi et al., 2012], [Sakamoto et al., 2017], [Shimizu et al., 2018]). An assignment of bands to single amino acids so far is excluded by the mutation studies of Richard Debus (see 3.4). Only the C terminal alanine 344 was found to contribute at 1356 cm^{-1} in S_1 and 1339 and 1320 cm^{-1} in S_2. Mutation of other residues did either not alter the steady state spectra or various alterations modified the same bands. As a reference, all carboxylates within 24 Å of the cluster are presented in figure 9.2 and the first sphere ligands in figure 9.1.

In chapter 8.3 we found that the 1344 cm^{-1} band contains relatively strong quinone contributions. Also above 1410 cm^{-1} measurements showed that the spectra are dominated by the ones of quinones (see 7.1.3). The data presented here therefore ranges from 1358 to 141 cm^{-1} in steps of 4 cm^{-1}.

9.4.1 Decaying spectra of the first four flashes

The measurements of the scan in the symmetric COO^- stretching region is recorded in two data sets. The first ranges from 1358-1378 cm^{-1}, the second from 1378 tp 1410 cm^{-1}. The time resolved spectra of the complete scan in steps of 4 cm^{-1} is presented in figure 9.4 (pH 6.2, 20 °C, PSII membranes from spinach). The four plots represent the different S-state transitions. The two data sets were not scaled and match pretty well in $S_1 \rightarrow S_2$ (1) but much worse in later transitions.

Because of this I want to first discuss the quality of the measurements. Overall the spectra averaged around 530 ms show a clear transition number dependent signal only in the higher wavenumber data set. The lower wavenumber set shows nearly no remaining signal at 530 ms except in $S_1 \rightarrow S_2$ and a small negative one in $S_3 \rightarrow S_0$. Around 3.5 ms, it shows a clear binary pattern. At a first glance one might think the sample was damaged. However, a repetition at 1364 cm^{-1} showed the same trend, while at other wavenumbers of the repetition clean S-state transitions could be observed (10 °C, shown in fig. 6.1). In the repetition, the amplitude change within 10 µs is only half the size of the measurement here (app. fig. 11.30). The same smaller early amplitude change is observed at 1378 cm^{-1} in the high wavenumber set. Therefore, the strong early change at wavenumbers below 1378 cm^{-1} might stem either from damaged centers or from a systematic error in this measurement. At the point of overlap,

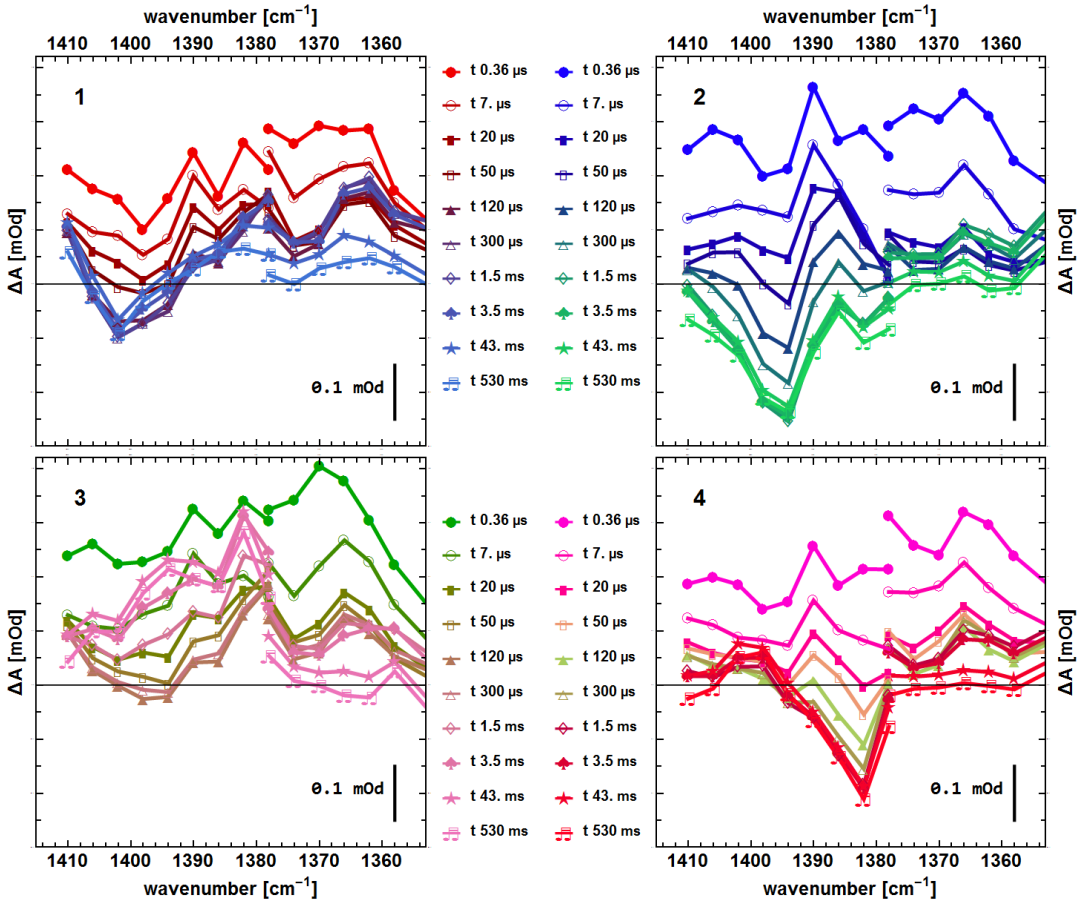

Figure 9.4: Changes in the symmetric COO^- region recorded on PSII membranes from spinach. Measurement carried out at pH 6.2 and 20 °C. Panels 1 to 4 represent the data of the $S_1 \rightarrow S_2$, $S_2 \rightarrow S_3$, $S_3 \rightarrow S_0$ and $S_0 \rightarrow S_1$ transition. The deconvoluted data is measured in two data sets: One ranging from 1358 to 1378 cm^{-1} and one from 1378 to 1410 cm^{-1}, both in steps of 4 cm^{-1}. The two sets were not scaled to the respective value (*arguments see text*). One can see that slow changes (> ms), attributable to quinone electron transfer events, are present only below 1386 and above 1406 cm^{-1}.

the transition dependence of the signals is stronger in the higher wavenumber set. They also match the spectra of the FTIR step-scan better ([Schönborn, 2017]). As the 1364 cm^{-1} data still represents a good measurement, also in comparison to the step-scan, and higher wavenumbers in each set were measured after longer time, the sample might got damaged or dried (after $\approx 40 - 48h$). At the connection of the two sets, the higher wavenumber set is therefore more trustworthy.

In panel of figure 9.4 the $\mathbf{S_1} \rightarrow \mathbf{S_2}$ transition is presented with early times in red and later times in blue. At all wavenumbers, initially a positive amplitude change is observed. The prominent negative peak around *1400* cm^{-1} forms until around 120 µs and only between 1394 and 1398 cm^{-1} is rises weakly with ms kinetics. This band therefore mainly reflects changes at the donor side. From *1378 to 1386* cm^{-1} very fast changes up to 20 µs are present, indicative for an earlier decay channel. Afterward, this region starts to decay at

3.5 ms. The spectra of the low wavenumber data set from *1364 to 1378* cm^{-1} decay slowly, mainly within 40 ms – a strong indication for quinone contributions.

The higher wavenumber set in the $\mathbf{S_2} \rightarrow \mathbf{S_3}$ (panel 2) shows initially a higher absorption change than in $S_1 \rightarrow S_2$. The decay of the spectra within 7 µs is clearly stronger at 1382 to 1386 and 1402 to 1406 cm^{-1}. After 7 µs the remaining signal vanishes within 50 µs above 1390 cm^{-1}. Also in the lower wavenumbers the initial amplitude is slightly higher than in the last transition. Between 50 µs and 1 ms the higher wavenumbers show a strong decay in two bands, the lower ones rise a bit. Slow decays are not present from 1386 to 1402 cm^{-1}.

The $\mathbf{S_3} \rightarrow \mathbf{S_0}$ transition is shown in panel 3. From 1378 to 1410 cm^{-1}, the initial positive absorption change is about as high as in $S_2 \rightarrow S_3$ but higher than in $S_1 \rightarrow S_2$. Around 1382 and 1406 cm^{-1}, the decay within 7 µs is strongest. Between 1386 and 1402 the spectra decays up to about 120 µs and rises until about 3.5 ms. The lower wavenumbers again stay quite constant up to 1.5 ms and show slow decays onward.

The $\mathbf{S_0} \rightarrow \mathbf{S_1}$ in panel 4 possesses slightly smaller initial amplitude changes than the two transitions before. The band at 1400 cm^{-1} shows only a very weak rise within 1 ms. A strong negative band develops between 1378 and 1394 cm^{-1} within 300 µs. The low wavenumber region only decays within 50 ms.

To *summarize* the bands at 1390-1406 cm^{-1} do not sense the quinone dynamics. In the first three transitions, they change with known Mn kinetics. The bands at 1378 to 1382 and 1402 to 1406 cm^{-1} show a very strong decay faster than 7 µs. At 1382 cm^{-1} the strong changes in the $S_3 \rightarrow S_0$ are not reversed in the $S_1 \rightarrow S_2$ and $S_2 \rightarrow S_3$, but the band developing at 1382 cm^{-1} in $S_0 \rightarrow S_1$ does so and needs to stem from the donor side. Thus this spectral interval is well suited for a joint fit approach.

Judging from the steady state values, the band at 1364 cm^{-1} should mainly contribute in the $S_1 \rightarrow S_2$. Here it seems to rise weakly, but as it also senses the quinones, the real magnitude of the rise might be hidden. Indeed, when we compared the data from spinach at 1364 cm^{-1} with the one from PSIIcc of *Synechocystis* (section 7.3), we found that all slow changes disappear with FeCy present. The band then stays constant throughout the time course. But because it decays in all later transitions, most likely a rise is present in $S_1 \rightarrow S_2$.

The slow ms changes present at lower wavenumbers – a rise within 1 ms and subsequent decay with 50 ms – unlikely represents recombination, but rather slow forward transfer to PPBQ (a discussion can be found in 7.3).

9.4.2 Global fit and decay associated spectra

In this section a golbal fit approach is presented. As the lower wavenumbers do not show a pronounced flash dependent amplitude pattern and the contributions of quinone related kinetics is higher, only the high wavenumber set will be used. The 1477 cm^{-1} band of the same measurement is included, to allow the discrimination between quinone and donor contributions at 1382 and 1410 cm^{-1}.

The fit results of the multiexponential function are presented in figure 9.5. Transients at 1382, 1394 and 1402 cm^{-1} are presented in figure 9.6. These show that the fit quality is very high. The number of exponential components is rationalized by the following: Using four exponentials in $S_1 \rightarrow S_2$, even when giving starting values for the decay times above 100 µs, always the 2 µs phase is found, leaving the quinone fit unsatisfactory. Thus, five exponential components are used for this transition. When in $S_2 \rightarrow S_3$ only six functions are used, the fit residuum of the quinones will still contain wiggles from 1 to 800 ms (see app. fig. 11.32). Thus, a fit function with seven components is used. In the $S_3 \rightarrow S_0$ weak oscillations are

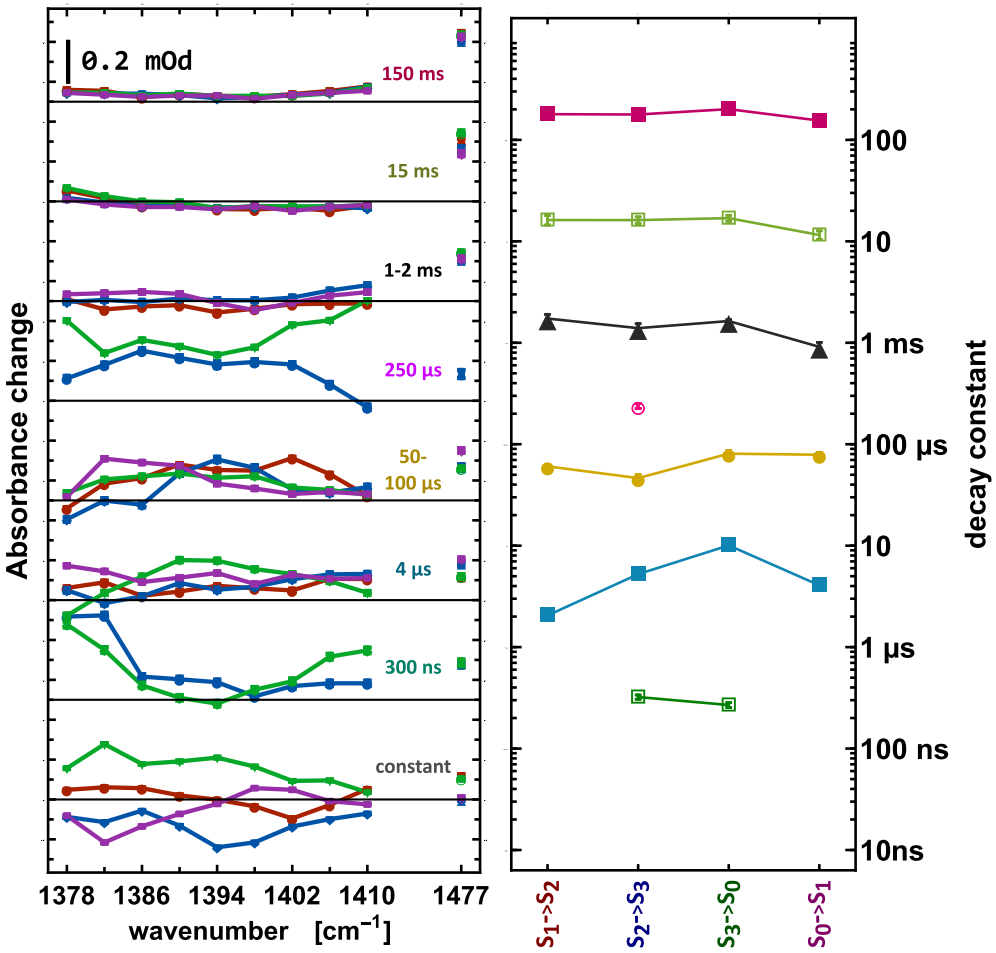

Figure 9.5: Decay associated spectra (*left*) and decay times (*right*) of the symmetric COO^- region of PSII membranes. Amplitudes are plotted on the same height as the corresponding decay times. In the fit the wavenumbers from 1378 to 1410 cm^{-1} of fig. 9.4.1 and the quinone band recorded at 1477 cm^{-1} are included. The number of exponentials used has been chosen to remove as many oscillation in the residuum plot as possible without increasing the fit error dramatically: $S_1 \rightarrow S_2$ (*red*): 5 exp, $S_2 \rightarrow S_3$ (*blue*): 7 exp, $S_3 \rightarrow S_0$ (*green*): 6 exp and $S_0 \rightarrow S_1$: 5 exp (*magenta*). (pH 6.2, 20 °C, +PPBQ)

still present in the residuum function of the used six component simulation – again at later times. A higher order fit is desirable, but it did not converge. In the $S_0 \rightarrow S_1$ the use of up to seven exponential functions was possible, only the fit residuals did not improve by using more. When using more than the presented five exponential, first a 40 ns was found (6 exp), then the 80 µs phase was split into 55 and 200 µs (7 exp).

The sum of the **constant** is close to zero (9.5, except for 1477 cm^{-1}). This means the changes discussed, will be reversed throughout the catalytic cycle: For the band at *1382* cm^{-1}, changes of the first transition are reversed after the second, and the stronger changes of the third reversed after the fourth. It might be that some of these reversal of period two are quinone related. At *1394* cm^{-1} the constants of both the $S_1 \rightarrow S_2$ and $S_0 \rightarrow S_1$ cross zero. The band in the second transition is reversed in the third. At *1402* cm^{-1} this behavior

continues, and smaller changes of the first are reversed in the fourth transition. The constant at *1410* cm^{-1} may be caused by quinone reactions.

In $S_2 \rightarrow S_3$ and $S_3 \rightarrow S_0$ a **300 ns** phase was found (320 ± 15 and 270 ± 15 ns). The spectrum of this phase is very characteristic and shows significant peaks at 1378 to 1382 and at 1402 and 1410 cm^{-1}, which are higher in $S_3 \rightarrow S_0$. Note, that the 1477 cm^{-1} band also senses this process (see section 7.1.10). The phase is present in the raw data as well (app. figure 11.25). Hence, this phase is introduced by the heat artefact correction. The kinetics and S-state dependency strongly argue for a carboxylate group absorbing at **1378-1382** cm^{-1} involved in the **300 ns** phase of the P_{680}^{+} $Y_Z^{\bullet ox}$ reaction. At his position, no band was not found before in Mn depleted PSII (sec. 3.3). This means that only in oxygen evolving centers with a positive charge at the cluster, this change is sensed. A positive signal in the symmetric carboxylate region can resemble a strengthening of the transition dipole moment, a change of bonding leaving either lower absorption in the asymmetric stretch and higher in the symmetric stretch or leading to a band shift or a deprotonation of a carboxylate. This change then is reversed within 300 ns, meaning e.g. a deprotonation followed by reprotonation or a reversible reorientation of the carboxylate group changing the symmetry of the bond.

The next phase of about **4 μs** is present in all transitions. For the individual S-state transitions, values of $2.1 \pm .2$, $5.2 \pm .4$, $10.1 \pm .6$ and $4.1 \pm .2$ µs were obtained. The third flash is significantly slower, because only two phases, which precede the 1.6 ms rise, were found, but three phases are expected (4 µs, 30 µs and 200 µs, scheme in fig. 2.2). With the exception of $S_3 \rightarrow S_0$, where a broad band contributes with a maximum at 1390 to 1394 cm^{-1}, in all transitions the spectral amplitude distribution is devoid of clear bands. In this 4 µs phase the 1477 cm^{-1} band shows a period of two behavior. Known acceptor side kinetics in this time range are the decay of triplet states and the **non-heme iron reduction** by Q_A^-. Light harvesting complexes and PSII centers with a modified Q_A^- binding site (e.g. by detergent) could form triplet states rapidly in each transition and may contribute to this phase. The electron transfer to the non-heme iron on the other hand should show a binary oscillation as observed for the quinone band. The amplitude ratio of even to odd transitions is around 1:0.66 (see 7.3), fitting well the observation at 1477 cm^{-1} in the joint fit. Our group found a halftime of iron reduction of 15 ± 3 µs at 18 °C and pH 6.3 ([Chernev et al., 2011]). This is slightly slower than the decay times found here. On the other hand, when only fitting the 1477 cm^{-1} band decay constants of 10-12 µs were found for all flash transitions. So if this phase represents the non-heme iron reduction then why does it not show a pronounced spectral response (ignoring $S_3 \rightarrow S_0$)? A possibility is that upon Q_A^- formation, also in broken centers, a proton is taken up by a carboxylate cluster at the stromal surface (initial positive change). When the iron becomes oxidized or the charges recombine, the proton is again released. This proton could lead to a feature-less continuum band (reported for the non-heme iron reactions in [Berthomieu and Hienerwadel, 2001]).

The spectra of the next **50 to 100 μs** phase are very diverse, even though the decay times are similar. Resolved it yielded: 61 ± 2 µs in $S_1 \rightarrow S_2$, 46 ± 4 µs in $S_2 \rightarrow S_3$, 81 ± 6 µs in $S_3 \rightarrow S_0$ and 79 ± 4 µs in $S_0 \rightarrow S_1$. The $S_1 \rightarrow S_2$ is sensed strongly at 1390 and 1402 cm^{-1} and weaker at 1382 cm^{-1}. The decay time fits well to the **Mn oxidation**. In the $S_2 \rightarrow S_3$ a decay is only present at 1394 cm^{-1}. The found 45 µs fits very well to the **proton transfer** found in [Klauss et al., 2015]. In $S_3 \rightarrow S_0$ one broad band appears between 1382 and 1302 cm^{-1}. The found 80 µs indicates a **mixture of** the 30 µs **protonic and** the 200 µs **lag phase**. In $S_0 \rightarrow S_1$ mainly the wavenumbers between 1382 and 1390 cm^{-1} show a decay. The found 80 µs are a better match for the **proton transfer**, although a clear separation of the electron and proton transfer in an earlier study was not possible ([Klauss et al., 2015]).

A **240** ± 15 ***µs*** phase was only found in $S_2 \rightarrow S_3$. It shows up with maxima at 1386 and 1398 to 1402 cm^{-1}. The kinetics are in agreement with values known for **Mn oxidation**.

The next three phases are all needed to simulate the reoxidation of the reduced quinone by PPBQ (discussion in sec. 7.3). Weak contributions were found at 1378, 1406 and 1410 cm^{-1}. In the $S_3 \rightarrow S_0$ however, the similar kinetic of **1.64** ± .05 **ms** (compared to 1.73 ± 0.17, 1.39 ± 0.15 and 0.91 ± 0.10 ms for the other S-state transitions) showed a very distinct spectral shape. Maxima of the rise are observed at 1382 and 1394 cm^{-1}. The kinetics match the **Mn oxidation and O-O bond formation** very well.

All in all, one can state that all electron and proton transfer events previously reported were found in the selected spectral region. Some events are difficult to distinguish from another, especially in $S_3 \rightarrow S_0$ and $S_0 \rightarrow S_1$. Although the quinone band at 1477 cm^{-1} was included in the simulation, it did not influence any decay constant.

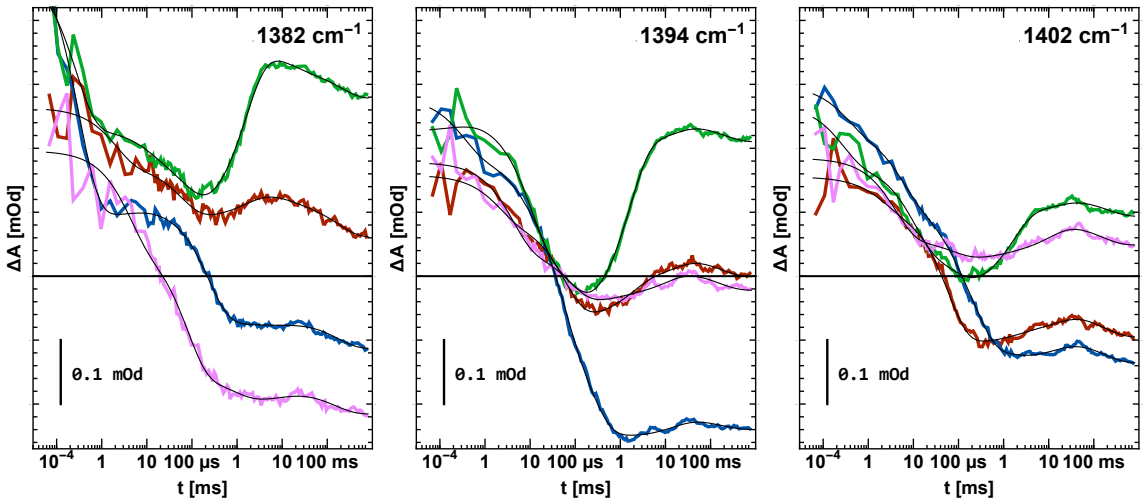

Figure 9.6: Transients showing the electron and proton transfer around the Mn cluster. Wavenumbers are indicated. The color code is: red, blue green, magenta for $S_1 \rightarrow S_2$, $S_2 \rightarrow S_3$, $S_3 \rightarrow S_0$ and $S_0 \rightarrow S_1$, respectively. The deconvoluted transients were obtained at pH 6.2 and 20 °C from PSII membranes of spinach on a 25 µm thick sample. Simulation results are presented in figure 9.5.

9.4.3 A probe of the electron and proton transfer events around the Mn cluster

From the discussion of the global fit results it becomes clear that the spectral range from 1382 to 1406 cm^{-1} is a very valuable tool for investigating the complete photocycle of PSII. If only a limited amount of measurement time or samples are available, the wavenumbers presented in figure 9.6 are a good choice. The band at 1382 cm^{-1} is sensitive to the 300 ns phase of $Y_Z^{\bullet ox}$ formation, the O-O bond formation and the $S_0 \rightarrow S_1$ transition. At 1394 cm^{-1} the 30-100 µs phases of the $S_2 \rightarrow S_3$ and $S_3 \rightarrow S_0$ are pronounced and the O-O bond formation as well as the proton coupled electron transfer of the $S_2 \rightarrow S_3$ are well visible. The band at 1402 cm^{-1} shows a strong $S_1 \rightarrow S_2$ Mn oxidation and senses most other transitions as well. All of the transients show weak rises within some ms, vanishing in the tens to hundreds of ms.

The next question to answer is which of the found decay phases remove the initial positive amplitudes and which are the ones forming the steady state values. This knowledge is important for the reevaluation of all published PSII FTIR studies.

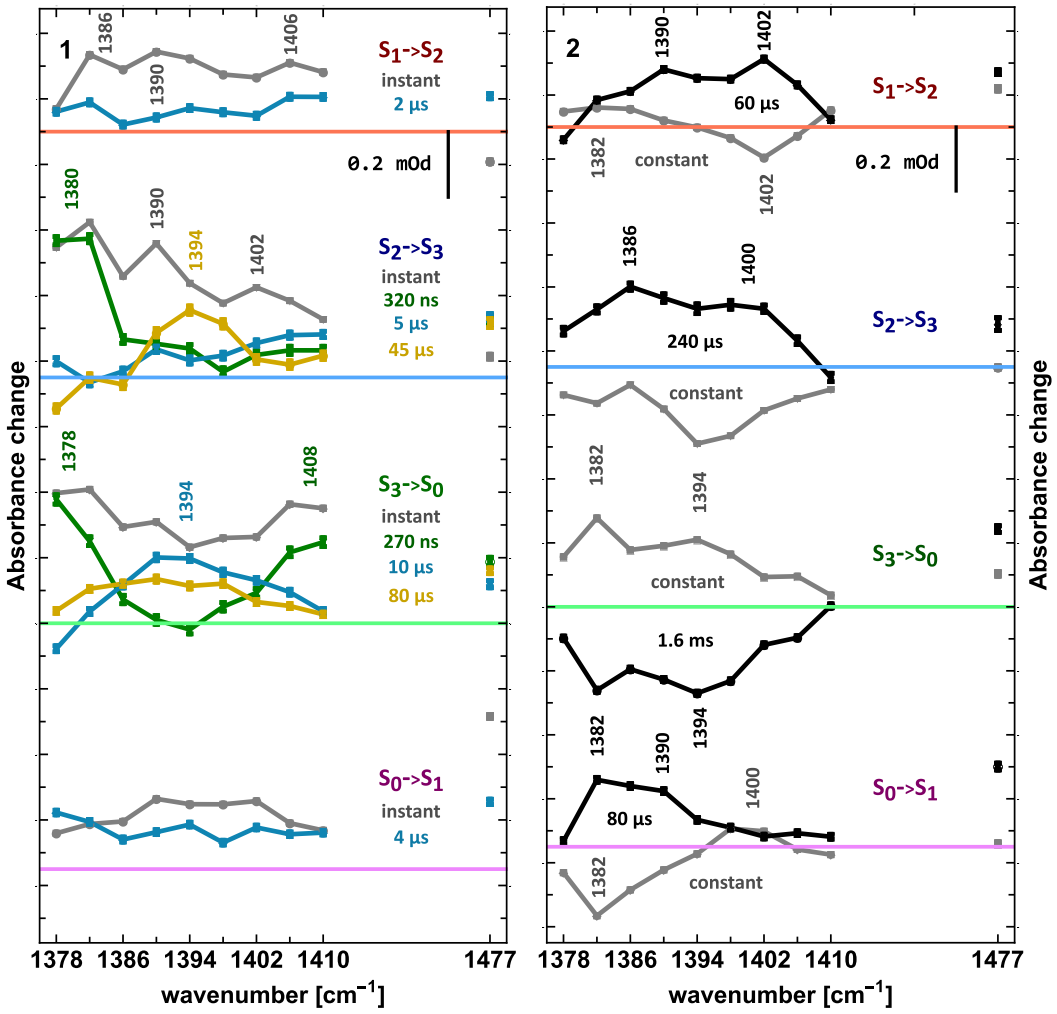

Figure 9.7: Electron and proton transfer decay associated spectra taken from figure 9.5. From top to bottom: $S_1 \rightarrow S_2$ to $S_0 \rightarrow S_1$. In the *left* figure the simulation components preceding known Mn oxidation events are plotted. The gray spectra represents the amplitude change after the flash excluding the amplitudes of the slow ms-quinone phases. The *right* figure shows in gray the fit constant, representing the steady state value, and in black the decay associated spectra of Mn oxidation. In $S_1 \rightarrow S_2$ the 80 µs component is plotted.

To answer this, the left panel of figure 9.7 shows the initial amplitude in gray (sum of all components excluding the quinone phases) and all decay channels faster than the Mn oxidation or in $S_0 \rightarrow S_1$ faster than 80 µs. The right panel shows the steady state spectrum in gray (fit constants) and in black the Mn oxidation events or in $S_0 \rightarrow S_1$ the 80 µs phase.

In $\mathbf{S_1 \rightarrow S_2}$, the initial feature created upon charge separation does not decay within 2 µs (fig. 9.7), but mostly with the Mn oxidation event (60 µs). Some of the initial amplitude remains even around 1382 cm^{-1}. Only at 1402 cm^{-1} the negative feature appears with Mn oxidation[8]. At least **three different chemical groups** seem to contribute: one at 1382 cm^{-1}, formed quickly and decaying afterwards with some changes staying, one around 1394

[8]this feature is far stronger in the not deconvolved first flash transition

cm^{-1}, formed but decaying to zero and one at 1402 cm^{-1}, formed, decaying to even negative values.

In $\mathbf{S_2} \rightarrow \mathbf{S_3}$ (second spectrum), the initial amplitudes largely decay to zero with the 300 ns and 30 µs phases, with bands at 1378 to 1382 and 1394 cm^{-1}, respectively. The steady state spectrum mainly origins from the Mn oxidation events. Only around 1386 and 1402 cm^{-1} some of the initial amplitude decays with the 240 µs phase. At least **five different vibrations** seem to contribute, but some might origin from the same residuum: The two bands of the fast phase at 1382 and 1394 cm^{-1}, the two formed instantly but decaying with Mn oxidation at 1386-1390 and 1402 cm^{-1} and the one silent until Mn oxidation at 1394 cm^{-1}.

In $\mathbf{S_3} \rightarrow \mathbf{S_0}$, a part of the initial amplitude stays at 1386-1390 cm^{-1}, while the rest decays with the mixture of the three phases of 270 ns, 10 µs and 80 µs. This is the only transition where the 10 µs phase shows a wavenumber dependent spectrum. In section 9.4.2 it was concluded, that this phase is a mix of the 4 and 30 µs phase, while the 80 µs is a mix of the 30 µs and a 200 µs phase. The Mn oxidation and O-O bond formation spectrum mirrors the steady state spectrum. In this transition at least **five to six groups** take part: two changing with 300 ns at 1378-1382 and 1406-1410 cm^{-1}, one at 1394 cm^{-1} stemming from the mixed 30 µs phase (position likely as in $S_2 \rightarrow S_3$), a fast one around 1386 cm^{-1}, and two at 1382 and 1394 cm^{-1} sensing Mn oxidation.

In $\mathbf{S_0} \rightarrow \mathbf{S_1}$ the initial spectrum is small and devoid of features compared to the other transitions. It decays nearly completely within 4 µs. This indicates that this phase is not related to the electron transfer event. The steady state values are created in the 80 µs phase. Only **one group** at 1382 to 1386 cm^{-1} is enough to describe the visible changes.

Together this makes: Three groups form rapidly and decay with 300 ns or 30 µs in $S_2 \rightarrow S_3$ and $S_3 \rightarrow S_0$. The number of groups sensing Mn oxidation is $3+3+2+1 = 9$ (approximately at 1382, 1386-1390, 1394 and 1402 cm^{-1}). These describe a catalytic reaction cycle and each formed band needs to be reversed in a later step. For this the gray spectra in right panel of fig. 9.7 are compared: The two groups formed in $S_1 \rightarrow S_2$ are reversed at similar positions in $S_0 \rightarrow S_1$. As both show similar amplitudes, it might be a band shift of one group changing its H-bonding properties. The group changing in $S_2 \rightarrow S_3$ is reversed in $S_3 \rightarrow S_0$. The remaining contribution of $S_3 \rightarrow S_0$ is reversed in $S_0 \rightarrow S_1$.

We end up with the following carboxylate groups sensing events of the photocycle between 1378 and 1410 cm^{-1}[9]:

At least three groups at 1378-1382 (300 ns), 1394 (30 µs) and 1406-1410 cm^{-1} (300 ns) form upon charge separation and vanish upon $Y_Z^{\bullet ox}$ formation in $S_2 \rightarrow S_3$ and $S_3 \rightarrow S_0$.

One group at 1394 cm^{-1} forms upon charge separation but decays with Mn4 oxidation in $S_1 \rightarrow S_2$.

Two groups at 1386 and 1400 cm^{-1} form upon charge separation in $S_2 \rightarrow S_3$ and decay (to zero) with Mn1 oxidation.

A pair of groups at 1382 (+) and 1402 (-) cm^{-1} is created upon Mn3 oxidation or proton release in $S_0 \rightarrow S_1$ and reversed in $S_1 \rightarrow S_2$ upon charge separation. It might reflect a band shift.

One group at 1394 cm^{-1} formed upon Mn oxidation in $S_2 \rightarrow S_3$ and reversed upon Mn oxidation in $S_3 \rightarrow S_0$. In $S_2 \rightarrow S_3$ Mn1 becomes oxidized and the newly bound second substrate water deprotonates. This water binding and deptrotonation might explain the changes sensed over the whole spectral region tested.

[9] This assumes, that no vibrations contribute that cancel or mask the kinetics of the others.

One group at 1382 cm^{-1} formed with Mn oxidation in $S_3 \rightarrow S_0$ and reversed with Mn oxidation in $S_0 \rightarrow S_1$. In $S_0 \rightarrow S_1$ Mn3 becomes oxidized and a proton is possibly released from a hydroxide at position O5 ([Siegbahn, 2013]).

The **identities of the carboxylate groups** are currently under discussion. They can either be located on the protein surface and deprotonate due to electrostatic repulsion ([Junge et al., 2002]). Another option is, that the carboxylate groups are part of the first or second ligation sphere, as indicated by simulations by [Nakamura and Noguchi, 2016]. Or they may belong to residues, which are coupled via an H-bonding network, even further away from the OEC, as suggested by Richard Debus. He saw that point-mutations of the first sphere ligands did not alter the difference spectrum in this region (see fig. 3.4, [Debus, 2016]).

The three carboxylates reacting on $Y_Z^{\bullet ox}$ or P_{680}^+ formation in $S_2 \rightarrow S_3$ and $S_3 \rightarrow S_0$ (1382, 1394 and 1406 cm^{-1}) may fit to either option. If they are located near surface and deprotonate, then they would need to become reprotonated from the protein interior via one of the proton release pathways. Because they are not detected in Mn depleted samples but upon charge separation in S_2 and S_3, either the Mn cluster, its positive charge or the H-bonding network including the cluster is needed to promote the vibration change. Also, they do not appear in the steady state spectra and are therefore not excluded by the point mutation studies. As the origin of the 300 ns and 30 µs phase is unknown, these bands are interesting targets of future research.

9.4.4 The signals at 1400 and 1544 cm^{-1} compared at pH 6.2 and 7.5

Table 9.1: Simulation results of the curves at 1400 cm^{-1}: pH 6.2 and at 1398 cm^{-1}: pH 7.5 of figure 9.8. Errors are given in the order of the last digit of the values. In $S_1 \rightarrow S_2$ two components were forced to be used. This causes the high error in the pH 7.5 simulation.

	$S_1 \rightarrow S_2$		$S_2 \rightarrow S_3$		$S_3 \rightarrow S_0$	
pH	6.2	7.5	6.2	7.5	6.2	7.5
a1 [mOd]			.09 (1)		0.15 (2)	
τ1 [ns]			350 (60)		260 (30)	
a2 [mOd]	0.12 (1)	-.02 (4)	0.13 (0)	0.02 (1)	0.15 (0)	
τ2 [µs]	8.8 (1.2)	22 (35)	17 (1)	20 (13)	18 (1)	
a3 [mOd]	0.13 (1)	0.13 (3)	0.18 (0)	0.21 (1)	0.05 (1)	0.08 (1)
τ3 [µs]	85 (9)	145 (50)	320 (10)	240 (20)	280 (80)	60 (8)
a4 [mOd]					-0.12 (1)	-0.17 (1)
τ4 [ms]					2.2 (2)	2.3 (2)

Proton release phases may become blocked at lower pH ([Zaharieva et al., 2011]). At higher pH, the lag phase of the $S_3 \rightarrow S_0$ transition was reported to accelerate ($\approx$ 200 µs at pH 6.2, and faster than 50 µs at pH 7)). To get a first idea of the origin of the fast 300 µs phases in $S_2 \rightarrow S_3$ and $S_3 \rightarrow S_0$, the transients of the $\nu_S(COO)$ at 1400 cm^{-1} and of the amide II band at 1544 cm^{-1} are compared at pH 6.2 and 7.5 in figure 9.8. Both were measured under similar conditions at 10 °C.

The $\nu_S(CO)$ band at **1400** cm^{-1} (left) shows some stunning features: The steady state values are very similar in both data sets. The initial amplitude, however, is much smaller

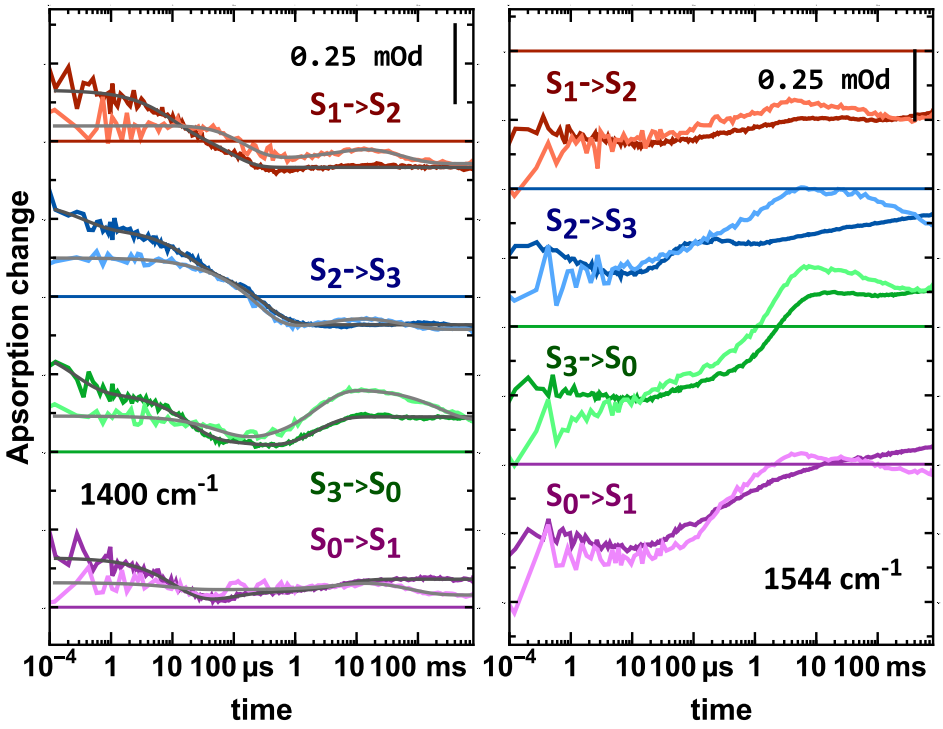

Figure 9.8: Comparison of pH 6.2 (*dark*) and 7.5 (*bright*) measured at: *left*: $\nu_S(COO)$ - 1400 cm^{-1} (pH 6.2) and 1398 cm^{-1} (pH 7.5); *right*: amide II - 1544 cm^{-1}. All sets on 15 µm PSII membranes and 10°C. The simulation results of the curves at 1400 cm^{-1} are presented in table 9.1. A linear plot of the transients at 1400 cm^{-1} up to 400 µs is presented in figure 11.31.

at pH 7.5 (bright). In a simulation all fast decay channels ($\approx 20\mu s$) in the first three transitions are smaller at high pH by a factor of 5-7 (see table 9.1). This is in contrast to the PTB experiment, where the amplitudes of apparent volume changes occurring with 30 µs in $S_2 \rightarrow S_3$ and $S_3 \rightarrow S_0$ were of the very same order in both pH ranges ([Klauss et al., 2015]). On the other hand, a second fast phase in $S_3 \rightarrow S_0$ speeds up, but does not change in amplitude. This shows, that the origin of the 30 µs and 300 µs at pH 6.2 are not from the same chemical groups.

At both pH values the amplitude of the Mn oxidation time are identical within the error range. Only in $S_3 \rightarrow S_0$ the amplitude is higher at higher pH, but the transient later decays back to the same final value. The decay of the first transition seems, on a first glance, to be slowed down at pH 7.5, but the simulation-results shows that within the error the transition is as fast as another. The $S_2 \rightarrow S_3$ is faster at pH 7.5 with 250 ± 20 µs than with 320 ± 10 µs at pH 6.2. In tendency this pH dependence was observed before ([Gerencser and Dau, 2010]) and argues for a proton movement accompanying Mn oxidation.

The amide II band at **1544** cm^{-1} decays within 10 µs in all transitions at pH 6.2. This turns even into a rise in $S_2 \rightarrow S_3$ and $S_3 \rightarrow S_0$ transition at pH 7.5. The possible transient proton sensation in $S_2 \rightarrow S_3$ around 100 µs at pH 6.2 is either hidden or not present at pH 7.5. Here, a continuous rise up to 5-10 ms is present possibly masking this shoulder. Also in $S_0 \rightarrow S_1$ the transient differs. At pH 7.5 the rise is much faster than at pH 6.2. The slow ms decay reverses this stronger rise as in the other transitions. These ms kinetics point to a modification of the quinone reactions.

The PDB experiment in [Klauss et al., 2015] states, that the apparent volume changes of all phases are independent of the pH. The volume changes were explained by electrofriction, meaning the local reorientation of ions and dipoles towards a charge that cause a global attraction of the charged separated states. If the phases are equally large but only differ in kinetics in this experiment, but differ strongly in amplitude in the SFIR experiment the molecular origin needs to differ.

Hypothetically spoken, it might be that a bulk pH sensing carboxylate group (with an apparent pK_a between 6 and 7) increases its absorption at 1400 cm^{-1} upon deprotonation (of itself or a group that it is H-bonded to) forced by the charge separated state. A similar interpretation was found for measurements of the proton release kinetics with a pH sensitive dye ([Junge et al., 2002]). Here the fast proton release (µs) was found to be electrostatic in natur and within 30 µs, it then becomes reprotonated. This proton might come from somewhere within the protein close to the cluster. Now at higher pH, the proton-back-pressure decreases, in turn increasing the deprotonation rate inside and the transfer outside. However, the carboxylate or its H-bonding partner is already deprotonated due to its pK_a, and will therefore not sense the charge seperated state, as can be seen in $S_2 \rightarrow S_3$ and $S_3 \rightarrow S_0$ at 1400 cm^{-1}. If this holds, then the rate limiting step of this reaction is the deprotonation inside the cluster and not the reprotonation of the surface carboxylate or its H-bonding partner. Surface glutamic acids with a pK_a between 6.3 and 6.7 were reported before ([Chen et al., 2000]). It might further be, that this high pK_a group resides on or close to the exit of a proton egress pathway. At lower pH, when it is anyway protonated, it would shield the interior of the channel from the the high proton concentration in the bulk, reducing thereby the proton backpressure sensed by the Mn cluster. A pH series determined pK_as blocking PSII to be at 4.6 ([Zaharieva et al., 2011]). The surface group sensed with the 30 µs phase at pH 6.2 thus might only be important for pH ranges between 5 and 6.

Also for further studies the observations made here become very important: in $S_3 \rightarrow S_0$ the absence of a 30 µs phase reveals the "lag phase", decaying in 60 µs at pH 7.5 with the same amplitude change as at pH 6.2. Because this phase is still present, it means that it origins from a different process involving most likely rearrangements at the cluster. As it speeds up, it may be related to proton movements. This is the first clean observation of a signal related to this phase. In most experiments it only manifests in delayed response of the signals. To study its most interesting nature, one can measure at a higher pH.

9.5 Comparisson of spinach PSII membrane particles and Synechocystis core complexes

In this final chapters the measurements done in conjunction with Richard Debus from UC California are presented. He provided the PSII core complexes extracted from *Synechocystis* sp. 6803. The sample preparation protocol follows his advice, with a main modification of not drying the samples before a measurement. Paul Greife assisted in the sample preparation as well as the measurements.

In this chapter first the similarities and differences between PSII membranes from spinach and the core complexes from wild type *Synechocystis* are compared. Then the first results of the D1-D61A PSII are presented.

The data obtained from concentrated PSII membranes of spinach was measured at 10 °C at pH 6.2. The PSII core complexes in solution from *Synechocystis* sp. PCC6803 were measured at 5-8 °C at pH 6.0 and slightly lower salt concentrations (see se. 4.1).

9.5.1 Events around the Mn cluster

The band at 1400 cm^{-1} is sensitive to most kinetics at the donor side in PSII membranes. It does not change with Q_A^- reoxidation. This is important because we saw that the kinetics of the electron transfer from Q_A^- to PPBQ in PSII membranes differ significantly from the ones of Q_A^- to FeCy in PSIIcc (sec. 7.3). Therefore,we first want to take a look at the $\nu_S(COO)$ band.

The left panel of figure 9.9 shows the four transitions recorded at 1400 cm^{-1}. The data on PSIIcc is multiplied by a factor of 1.5. This is reasonable, because per disk about 50 μg_{Ch} are used in PSII core complexes and 300-500 μg_{Chl} in PSII membranes, giving a factor of 6-10 more chlorophyll in PSII membranes. Per PSII monomer however about 30 chlorophylls are present in PSIIcc whereas about 200 are present in PSII membranes, reducing the signal per chlorophyll by a factor of around 7. In total the signal is expected to be slightly higher in PSII membranes. The fit quality is satisfactory for both data sets. In table 9.2 the results are presented (the ones of PSII membranes are the same as in tab. 9.1).

In $S_1 \rightarrow S_2$, the transients appear very similar. Both the initial (10 µs) and the final absorption changes are equal. The zero crossing takes place at 30 to 60 µs. The fit results in the table (unscaled PSIIcc) show the same main decay component with 85 µs. The amplitude differs only by a factor of 1.3. In the PSII membranes an additional decay with 10 µs was found, similar to the 2 µs phase in the 20 °C data (sec. 9.4.3). The core complex simulation does not require this phase.

The transients of $S_2 \rightarrow S_3$ again are remarkably similar. From 30 µs onward the two curves lie on top of each other. The fit yielded times of 320 ± 10 and 410 ± 25 µs for PSII membranes and PSIIcc, respectively. The amplitude ratio is about 1.6. For this phase in PSII membranes our group previously found a slowdown from 290 ± 10 µs at room temperature to 400 ± 90 µs at 5 °C ([Klauss et al., 2015]). The maximally 5 °C difference between the two measurements presented here is thus unlikely to be the explanation for the slower reaction in PSIIcc. Besides this slow down of the 300 µs phase, the most drastic change is again present in the first µs. In PSII membranes, a 20 µs phase is found with an amplitude of 0.13 mOd and thus nearly as large as the subsequent electron transfer. In PSIIcc it is almost absent. This difference is less pronounced in $S_1 \rightarrow S_2$.

On a first glance the $S_3 \rightarrow S_0$ transition differs much more. Again the early phase is absent in core complexes as in $S_2 \rightarrow S_3$. The next phase ("lag") is more pronounced in PSIIcc. While the unscaled simulated amplitude of 0.05 mOD is as large as for PSII membranes, it is clearly larger when applying a scaling factor of 1.3 to 1.6 as for the other transitions. The kinetics are, within the error range, identical.

The rise sensed during the Mn oxidation and O-O bond formation is weaker in PSIIcc than in PSII membranes. The flash dependent steady state values show a similar period of four oscillation (*not shown*). This means that the miss factor is similar in both samples. Again the kinetics of this step are, within the error range, identical. A possibility of the lower amplitude in PSII membranes might lie in the wavenumber used. The data of PSIIcc is recorded at 1398 cm^{-1}, which is 2 cm^{-1} lower than the one of the PSII membranes. The decay associated spectra obtained on PSII membranes (black spectrum of $S_3 \rightarrow S_0$ in fig. 9.7) states, that the amplitude change should become rather stronger towards 1394 cm^{-1}. This is the same for the steady state value (gray spectrum of the same figure). But when comparing this result to any of the steady state spectra of Richard Debus (e.g. in [Banerjee et al., 2018a]), one notices that, in PSIIcc, the $S_3 \rightarrow S_0$ spectra do show weaker changes at 1392 cm^{-1} and stronger positive signals at 1384 and 1402 cm^{-1}. This means that the environment of the

Table 9.2: Simulation results of the 1400 cm^{-1} transients of figure 9.9. Values in brackets show the fit errors. If the error was smaller then 0.05 mOD it is shown as a 0. Variations in the measurements caused by e.g. the temperature control will yield errors at least in the order of 0.01 mOd. The results obtained on PSIIccs are unscaled.

	$S_1 \rightarrow S_2$		$S_2 \rightarrow S_3$		$S_3 \rightarrow S_0$		$S_0 \rightarrow S_1$	
pH	bby	cc	bby	cc	bby	cc	bby	cc
a1 [mOd]			.09		.15			
			(.01)		(.02)			
τ1 [ns]			350		260			
			(60)		(30)			
a2 [mOd]	.12		.13	.02	.15	.02	0.15	.03
	(.01)		(.00)	(.01)	(.00)	(.01)	(.01)	(.00)
τ2 [µs]	8.8		17	50	18	25	12	25
	(1.2)		(1)	(20)	(1)	(15)	(1)	(5)
a3 [mOd]	.13	.10	.18	.11	.05	.05	-.04	
	(.01)	(.00)	(.00)	(.01)	(.01)	(.01)	(.01)	
τ3 [µs]	85	87	320	410	280	180	100	
	(9)	(4)	(10)	(25)	(80)	(50)	(35)	
a4 [mOd]					-.12	-.03	-.04	-.01
					(.01)	(.00)	(.00)	(.00)
τ4 [ms]					2.2	2.5	6.2	11
					(.2)	(.6)	(.9)	(6)
c [mOd]	-.08	-.06	-.09	-.06	.11	.05	.09	.02
	(.00)	(.00)	(.00)	(.00)	(.00)	(.00)	(.00)	(.00)

carboxylates participating in the H-bonding network differ slightly between PSII membranes of spinach and PSIIcc of *Synechocystis*.

The same holds when comparing the data of $S_0 \rightarrow S_1$ either in figure 9.9 or between the steady state spectra of figure 9.7 with [Banerjee et al., 2018a]. The steady state amplitude at 1400 cm^{-1} is weaker in PSIIcc and no positive absorption is observable around 1394 cm^{-1} in the spectra of PSII membranes. The negative band at 1384 cm^{-1}, however, is very similar in the steady state spectra of both organisms. In $S_0 \rightarrow S_1$, also the change faster than 20 µs is weaker in PSIIcc and the simulated 100 µs kinetics of the PSII membranes is not visible, due to either noise or a weak rise in PSIIcc.

Noguchis presented the 1400 cm^{-1} transients with a spectral resoltution of 16 cm^{-1} and a instrument rise time of 25 µs in $S_1 \rightarrow S_2$, $S_3 \rightarrow S_0$ and $S_0 \rightarrow S_1$ ([Noguchi et al., 2012], [Shimizu et al., 2018]) and with 2.5 µs in $S_2 \rightarrow S_3$ ([Sakamoto et al., 2017]). He measured them on *Thermosynechoccocus elongatus* core complexes kept at 10 °C. In $S_1 \rightarrow S_2$, he found a weak positive signal at 25 µs decaying to -0.4 mOd wit 50 ± 10 µs. Our cyanobacterial signal with 87 ± 4 µs is a bit slower, but stems from a different species as well. In the 2012 paper he fitted the $S_2 \rightarrow S_3$ with one exponential decaying with 350 ± 30 µs. The zero transition was found at about 200-300 µs as in my data. Both compares reasonably well, again with slightly slower kinetics in my data. In his 2017 paper with higher time resolution, he found an additional 13 µs phase. Comparing the transients in $S_3 \rightarrow S_0$, his starts with a

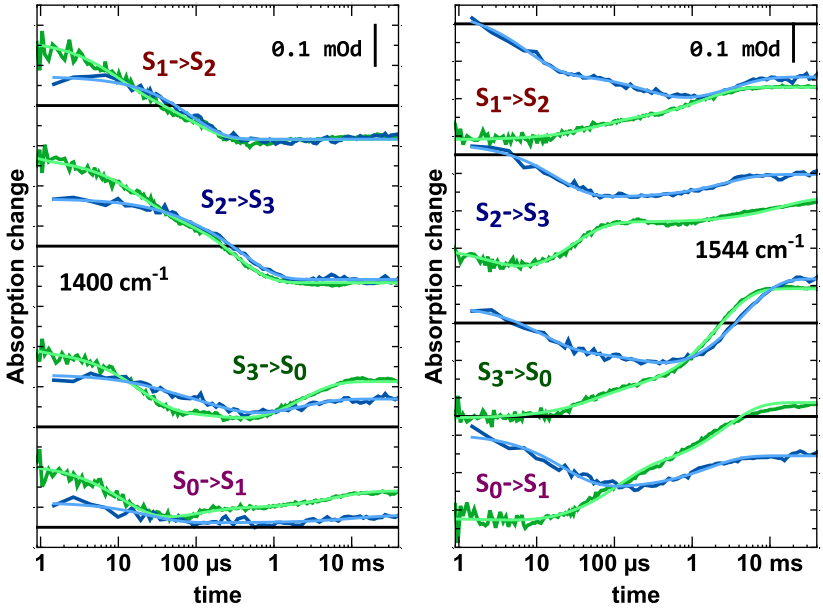

Figure 9.9: Comparison of concentrated PSII membrane particles from spinach (*green*) and core complexes in solution from *Synechocystis* sp. PCC 6803 (*blue*) measured at 1400 cm^{-1} (*left*) and 1544 cm^{-1} (*right*). The spinach data is measured at 10 ° C and the same as in figure 6.1. The measurements of *Synechocystis* is obtained at 6-9 °C and scaled by a factor of 1.5. Electron and proton transfer events are sensed in the transients of the $\nu_S(COO)$ band at 1400 cm^{-1}. The fit results are listed in table 9.2.

positive amplitude that decays within 200 µs (no zero crossing) and then rises until 3-5 ms. This behavior is the same as in the data presented here. Noguchi simulated a consecutive reaction with one silent phase and obtained 60 ± 15 µs, 550 ± 50 µs and a 1550 ± 150 µs. All three phases differ to the ones obtained here. When he fitted the other transient at 2500 cm^{-1} he found a 190 ± 15 µs and a 1200 ± 150 µs phase. The former one fits much better to the 180 ± 50 µs, while the slow one however is still much to fast. In $S_0 \rightarrow S_1$ his early transient at 1400 cm^{-1} rose with 800 ± 100 µs. The *Synechocystis* data might contain this phase, but is too noisy to really extract it. Noguchi's fit at 2500 cm^{-1} returned a phase of 130 ± 10 µs, similar to the one obtained from PSII membranes. In his newest publication, he used a different protocol to obtain the $S_0 \rightarrow S_1$ transition. Here he found only a rise with 45 ± 4 µs (25 µs resolution). In both of my data sets an early decay is present, not matching his data. Overall the transients up to the $S_3 \rightarrow S_0$ compare well. Noguchi's decay constants are typically faster than mine. This might be caused by a species dependency or by a difference in set against reported temperature.

9.5.2 Conformation changes sensed differently in PSII membrane particles and Synechocystis core complexes

Amide modes are typically sensitive to the secondary structure of a protein. Amide I bands (mainly $\nu(CO)$ of the backbone) are relatively well understood. They are used to track folding or unfolding of helices or β sheets during a reaction. Understanding amide II bands

(mainly the out of phase combination of $\nu(CN)$ and $\delta_{inplane}(NH)$) is much more complicated [Barth, 2007]. We can only use it, to track backbone changes in general.

In chapter 6, the band at 1544 cm^{-1} was already shortly introduced. A band at this position is present in nearly all spectra of the redox active cofactors in PSII (see sec. 3.3). This makes the separation of events impossible. For that reason the fit results of the band alone will not be discussed here[10]. Still it is a valuable tool to track changes possibly not sensed by the carboxylates.

The right panel of figure 9.9 compares the amide II band of PSII membranes (green) with that of PSIIcc (blue, factor 1.5). Whereas the 1400 cm^{-1} changes were mainly present at times below 10 µs, the 1544 cm^{-1} differs up to 1 ms. In all transients the PSII membranes show strong negative absorption changes upon charge separation (Q_A^- P_{680}^+). PSIIcc on the other hand starts without any absorption change and only slowly develops in tendency similar changes.

In $S_1 \rightarrow S_2$, the electron transfer at the donor and acceptor side causes a reversal of the initial absorption changes in PSII membranes. This is in line with observation of volume changes done in our group ([Klauss et al., 2015]). The PSIIcc of *Synechocystis* shows the opposite: it continues to decay up to 1 ms. From there on the two transients are similar.

In $S_2 \rightarrow S_3$, the PSII membrane signal shows a rise around 29 ± 2 µs with the proton release at the donor side, possibly mixed with the electron transfer from Q_A^- to the non-heme iron. Because the fit gives an amplitude bigger than in other transitions, a donor side reaction is indicated. In the core complex data this rise is not directly visible. Only when one compares the decay in this transition with the ones of the others, one notices, that it stagnates at 50 µs, while it continues to decay up to 500 µs in the others. This means the same change likely is present but masked. From about 300 µs onward both transients rise in parallel.

In $S_3 \rightarrow S_0$ again a complex rise is observed in PSII membranes, followed by a strong rise with the O-O bond formation step (50 µs and 2.2 ms). No significant phase is found later on. As this band senses most electron and proton transfer events it indicates that Mn oxidation, O-O bond formation and oxygen release happen in a concerted manner. The core complex signal decays until 300 µs and rises slightly delayed (relative to the PSII membranes) to a similar value.

In $S_0 \rightarrow S_1$ the PSII membrane signal rises strongly with 100 µs and 2.7 ms. The slow phase is different to both the $S_2 \rightarrow S_3$ and the $S_3 \rightarrow S_0$ transition. The PSIIcc signal, after reaching its maximal negative value, rises only weakly. Its change is comparable to the $S_2 \rightarrow S_3$ transition.

Summary and hypothesis

The following observation were taken:

1) The amplitude of the 30 µs phase is diminished in PSIIcc.

This point needs to be separated into two sub-points. I tracked transition number independent fast changes in PSII membranes. The kinetics of 4 to 10 µs were similar to the triplet decay in LHCs ([Christen et al., 1998]). The observation that PSIIcc do not sense a fast decay in $S_1 \rightarrow S_2$ points to this explanation. In PSII membranes LHCs are present and can form trimers, that are excited and may cause these signals. A contribution from the quinone side is unlikely because in PSII membranes no binary change was observed (sec. 9.4.3).

[10] for the interested reader the band was included in the global fit in section 8.4.

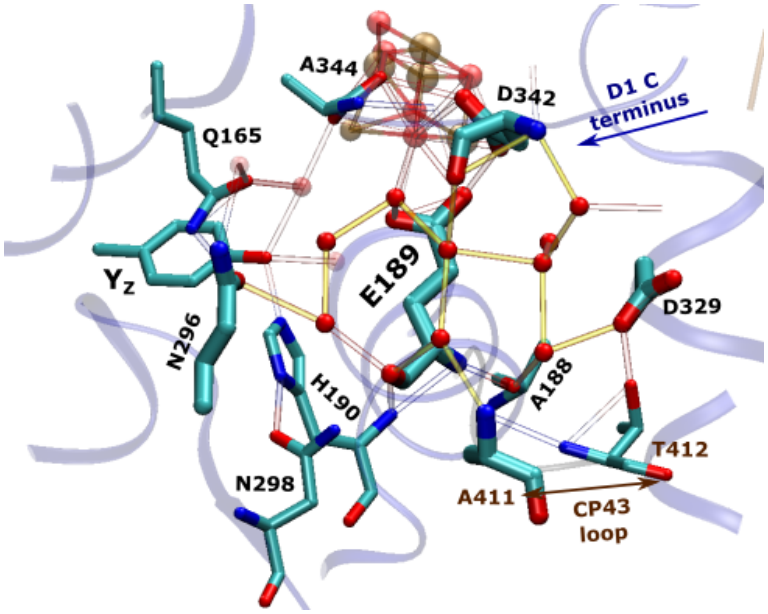

Figure 9.10: Environment of E189 and the breathing waters numbered 26 to 30. These waters are moving in the new flash resolved XFEL structures ([Kern et al., 2018]). E189 is H-bond with them via the carboxylate side chain and the carbonyl group of the backbone. This residue is the most moving one during the S state transitions and might be the source of the amide band changes described here. Partially the shown H-bonding network is part of the "back" proton exit pathway (fig. 9.2). *crystal 4UB6*

The flash number dependent fast amplitude changes are also weaker in PSIIcc than in PSII membranes and similar to the pH effects observed. This might have different origins: either the groups sensing the pH of the solution are not present in PSIIcc, this points to groups at the extrinsic proteins, which differ between the two species ([Nelson and Yocum, 2006]). Alternatively, the groups might be affected by the detergent belt of the core complexes. A third option is that the pK_a of the carboxylate groups differ due to the different adaption and evolution of PSII and the thylakoid lumen. An effect due to the different electric field in the two samples can rather be ruled out as the apparent volume changes at different pH values do not differ ([Klauss et al., 2015]).

2) The kinetics of the S-states are nearly identical.

This is good news, because it allows the usage of most observations obtained in the last decades on either sample type and to transfer them to one another.

3) Changes in $S_3 \rightarrow S_0$ and $S_0 \rightarrow S_1$ are sensed more weakly at 1400 cm^{-1} in PSIIcc than in PSII membranes. Changes in $S_1 \rightarrow S_2$ and $S_2 \rightarrow S_3$ are identical (as reported for $S_1 \rightarrow S_2$ also by [Remy et al., 2004]).

There is still the chance that the differences origin only from the deconvolution procedure, although this is unlikely, because in [Banerjee et al., 2018a] the 1383 cm^{-1} band is positive in $S_3 \rightarrow S_0$ but negative in $S_0 \rightarrow S_1$– like in the SFIR deconvoluted PSII membrane transients. Was there a large effect due to mixing of the S-states, then the change in the $S_0 \rightarrow S_1$ would be masked. Mainly the 1394 cm^{-1} band does differ in both sample types (gray spectra in fig. 9.7). The mutation of N87A mimicking spinach PSII does not restore this change in $S_3 \rightarrow S_0$ ([Banerjee et al., 2018a]). Possibly the difference lies in the extended H-bond network. This

result needs to be kept in mind when comparing the results of PSIIcc from *Synechocystis* and PSII membranes from spinach. A scan of the symmetric carboxylate stretching region of the higher S-state transitions in PSIIcc, similar to the one recorded here on PSII membranes, should be measured to identify other changes.

4) The amide II band reacts differently upon charge separation.
There may several explanations: PSIIcc may be more inert in reacting to the charge separation, the protein conformation changes upon charge separation are less pronounced in PSIIcc or completely different changes take place.

This is not at all easily explained. First there is the question of the origin of this band. A peptide bond is rather rigid and the NH group sensed in amide II is involved in H-bonds forming the secondary structure. The changes also show up at the acceptor side when an electron donor to the cluster was added removing the positive charge (see sec. 3.3). They also appear when an electron acceptor is added and no negative charge is present. Still the changes are more pronounced when both charges are formed and closer to each other (at around 1 µs in PSII membranes). Additionally, in PSII no huge changes are observed in the amide I region. A large scale structural change can therefore be excluded. Also our group found volume changes occuring during the photocycle of the order of water molecules ([Klauss et al., 2012a]). The changes sensed by the amide II band therefore seem to be of local nature.

One thus needs to search for changes present locally around the Mn cluster – changes that are induced by the creation of the positive charge at P_{680}. In recent two flash crystal structures of [Suga et al., 2017] and [Kern et al., 2018] a very fast change of D1-E189 was observed. Its environment is presented in figure 9.10. The H-bonding network contains at least four waters moving as well ([Kern et al., 2018]). These waters connect the backbone of D1-D342 (two residues next to the C-terminus), the backbone of E189, two residues of the CP43 loop and D1-N296. The neighbor of E189 is the histidine 190. The neighbor of N296 is N298 H-bonded to the second nitrogen of the histidine, playing a possible role in proton transfer. Both the E189 and D342 ligate Mn1. This means that when the H-bonding properties of Y_Z-His190 change, the whole region will sense it, including some NH peptide groups and loose structures such as the CP43 loop. Also groups located at the end of three different D1-transmembrane helices are involved: Y_Z, His190 and N296/N298.

All this renders this region a good candidate for causing amide absorption changes upon Y_Z or Mn1 oxidation. Mn1 is proposed to become oxidized in $S_2 \rightarrow S_3$ and to change its oxidation state. In this transition strong changes are sensed at 1544 cm^{-1}. As discussed before, also in PSIIcc this change might be present showing up by a plateau between 50 µs and 1 ms, as opposed to the other transitions. The early rise with the proton release phase reflects a relaxation of the protein, while the – and this is extremly hypothetical – subsequent binding of a water to Mn1 causes tension to this region again by the movement of E189 (as observed from one flash to two flash data in [Kern et al., 2018]), that causes a small decay.

All this might only explain the small rise and decay in $S_2 \rightarrow S_3$ and not at all the differences of the two samples[11].

A difference between the data sets is the different electron acceptor added to the sample. In PSII membranes the quinone reaction follows a binary pattern. In PSIIcc the quinone reaction is the same in all transitions except for the first flash. For them three decay times of the reduced quinone signal were found: a weak 20 µs phase and two equally strong phases with 400 µs and 4 ms. The slowest phase is definitely present and follows a similar direction

[11] The D1-N87 residue is much further away from this region

as in PSII membranes. The 400 µs phase, on the other hand, is not present at 1544 cm^{-1}. This can be seen in $S_1 \rightarrow S_2$ and $S_0 \rightarrow S_1$ in this time regime, where the absorption changes have different signs[12]. Based on the quinone reaction, the only explanation why the initial state causes different signals is a change induced by the binding of FeCy, which may differ a lot from the changes induced by quinone binding – PPBQ or Q_B– at the Q_B pocket (see also sec. 9.6.3).

Another option explaining the differences of the amide II changes are the different extrinsic proteins. PsbO is present in both samples but PsbP and PsbQ are only present in plants, while PsbU and PsbV are only present in cyanobacteria ([Nelson and Yocum, 2006]). The plant subunits show more ordered structures in β sheets (PsbP) or α helix bundles (PsbQ). Possibly this ordered structure lets PSII react in a more directed way onto charge separation in plants.

A last option is a simple one not related to any mechanism at all. PSII core complexes are not embedded in a native membrane but are dissolved in detergent (β-DM). It is known that PSII needs some lipids to function properly, but how much a detergent belt might affect the protein flexibility is unclear.

9.6 Wild type and D1-D61A core complexes of Synechocystis sp. PCC 6803

9.6.1 Introduction

The D1-D61 residue was, and still is, an important target of research when studying the mechanism of oxygen evolution. It is H-bonded to water W1, which in turn is bound to the dangling Mn4 (fig. 9.1). W1 is also connected to a group of waters within H-bonding distance reaching Y_Z. Its second oxygen points away from the cluster towards D1-K317 and D1-E65 (fig. 3.12). Furthermore, it is only two water molecules away from the clorid ion. Cl depletion blocks PSII in its function. This function is restored if D1-K317 is mutated to a non-positive residue, which is interpreted as an H-bond formed between K317 and D61 without Cl ([Pokhrel et al., 2013]).

The H-bonds towards Y_Z and D1-E65 both are connected to two different proposed proton exit pathways (fig. 9.2). D61 is located at the entrance of one of the pathways, which later splits and leads to the stroma along the shortest way via a loop of PsbO ([Ho, 2012]). Its connection to both has been confirmed by FTIR studies where in $S_1 \rightarrow S_2$ a negative feature at 1747 cm^{-1} is eliminated by D61A, E65A and D2-E312A, and in $S_2 \rightarrow S_3$ judged by a positive feature at 1745 cm^{-1} eliminated by D61A, D1-Q165 and D1-E329 [Debus, 2014]. Several simulations pointed to a proton release of W1 via D61 possibly to the bulk upon $Y_Z^{\bullet ox}$ formation in $S_2 \rightarrow S_3$, $S_3 \rightarrow S_0$ and $S_0 \rightarrow S_1$ ([Narzi et al., 2014], [Retegan et al., 2014] and [Siegbahn, 2013]). This has not been verified experimentally. If it holds true, then the gap at W1 might be filled by a proton originating from one of the substrates as suggested by [Siegbahn, 2013]. Also Leonardo Guidoni and Matteo Capone suggested a similar mechanism only towards W2 in $S_3 \rightarrow S_0$ (*talk at BUR meeting 2018*). Either way the arrangements of water molecules also stabilized by D61 might be crucial for the proton release to the bulk and the orchestration of water binding and deprotonation at the cluster.

Kinetic studies of the D61N mutation were conducted by oxygen polarography and UV/VIS changes of Y_Z ([Hundelt et al., 1998a], [Hundelt et al., 1998b], [Dilbeck et al., 2012]). One

[12]Deconvoluted data: excluding first flash, i.e. the quinone reactions in each transition are the same

outcome was that P^+_{680} reduction by Y_Z is unaffected by the mutation but the S-state transitions are slowed, especially strong the $S_3 \rightarrow S_0$. On D61A only polarographic measurements exist ([Bao and Burnap, 2015]). The kinetics of the lag phase were retarded by a factor of two while the ones of oxygen evolution by a factor of 30 (at 27 °C). By varying the temperature, this study found that the activation enthalpy of the transition was lowered: $\Delta H_{D61,lag} \approx 1/2\Delta H_{WT,lag}$ and $\Delta H_{D61,O2} \approx 2/3\Delta H_{WT,O2}$. The large slow down is related to an enormous entropy penalty $\Delta S_{D61A,lag,O-O} \approx 2 * \Delta WT$. Because this was found for both the O-O bond formation and the lag phase (summarizing all preceding events) it was concluded that both the transient and the ground state are altered.

Richard Debus measured the FTIR steady state spectra on D61A (with better S/N in [Debus, 2014]. Among others, he found the following two effects:

First, D61A eliminates the negative band of a weakly H-bonded water in $S_1 \rightarrow S_2$ at 3660 cm^{-1} and alters the negative signal of one in $S_2 \rightarrow S_3$ (3606 cm^{-1}). If such a signal appears, it means that a water either deprotonates or forms a strong H-bond. The one in $S_1 \rightarrow S_2$ is also eliminated in spectra of E333Q (ligates Mn4, Mn3) and K317A (binds to Cl) but not D170H (ligates Mn4, Ca). This speaks for the change of a water around the chloride site in $S_1 \rightarrow S_2$ (one shown in fig. 3.12)[13]. In $S_2 \rightarrow S_3$ an absorption loss unique to D61A was found, meaning the water needs to be close to D61[14]. The $\delta(DOD)$ vibrations indicate, that two waters change in $S_1 \rightarrow S_2$: one of them is eliminated in D61A. This could mean that the water was H-bonded to D61 before (here no change in $S_2 \rightarrow S_3$ was observed).

Second, in all S_{i+1} minus S_i spectra there is a broad positive features around 2000-3000 cm^{-1} indicating the creation of a polarizable network of water and amino acids. It is strongest in $S_1 \rightarrow S_2$ (at 2600-3000 cm^{-1}), where the charge of the Mn cluster changes. In $S_1 \rightarrow S_2$ this is absent in D61A, indicative for an altered H-bond network in later transitions. Because it stays present in $S_2 \rightarrow S_3$ the increase of polarizibility of another H-bond system does not comprise D61.

9.6.2 WT and D-D61A transients at 1478, 1384, 1400, 1514 and 1544 cm^{-1}

Before looking onto the kinetics of the donor side, we need to make sure that the **quinone reactions** are unaltered. Figure 9.11 shows the direct comparison of the flash transients of the WT and mutant recorded at 1478 cm^{-1}. Bright curves represent the D61A data. In all four transitions, the Q_A^- reoxidation kinetics are unaltered. All quinones are also reoxidized in the mutant and the amount of charge separated PSII stays at the same level at 1 µs. 1/4 of the signals decay within 20-30 µs, about 3/8 within 400-500 µs and the remaining 3/8 within 4-6 ms (see sec. 7.3).

Now let us take a look at the bands sensing the Mn cluster's photocycle. Figure 9.12 shows the bands at 1384, 1400, 1514 and 1544 cm^{-1} for the WT (dark) and the D1-D61A (bright) and figure 9.13 the flash dependent amplitude pattern at various times. This data is *not deconvolved* and the colors represent flash transitions. The reason why I did not simulate the S-state transitions can best be seen in the transients at 1384 and 1400 cm^{-1}: Both data sets show similar initial changes but the state reached at 800 ms is close to zero in the third and fourth flash transient of the mutant. A proper deconvolution thus is not possible. This behavior and the extent of flash number dependent steady state pattern decreased

[13] *speculation:* in [Siegbahn, 2013] possibly water W2 (bound to W1) or water between W2-S, D61 and K317, rather not W-SB (W2, close to D170)

[14] W1 or W2-S

over the time of measurements (less activity after 6 h, *not shown*). Typically up to seven measurements could be used on the same sample.

At **1383 cm^{-1}**, shown in figure 9.12 and 9.13, the D61A data starts at 1 µs in each flash at slightly elevated positive signals. In the WT a quaternary pattern is visible, weakly at 4 µs and strongly at 30 µs with a maximum after the second and sixth flash. In the mutant no pattern is visible at 4 µs and the pattern at 30 µs is delayed by one flash and remains until 200 µs. This is also visible in the transients. The very early decay (20 µs) in flash one to three is hardly slowed down in D61A. The following decay in the WT finishes between 100 µs and 1 ms, whereas it continues in D61A up to 10 ms in all flashes. The final quaternary pattern in the WT develops in flash 1 between 30 µs and 200 µs and in flash 2 and 3 between 30 µs and 5 ms. In flash 3 also a rise of the Mn cluster is present starting at 1 ms. This rise is very weakly present and starts maybe around 50 ms in D61A. The flash pattern at 500 ms of the mutant shows rather a binary oscillation with positive amplitudes after odd flashes and slightly higher amplitudes after flash 3 and 7.

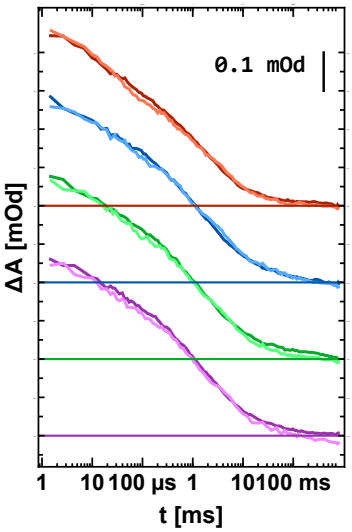

Figure 9.11: Quinone reactions in WT (*dark*) and D61A (*bright*) monitored at 1478 cm^{-1}- the reduced quinone band. From top to bottom: flash 1-4. Simulation results can be found in figure 7.18. The data was recorded at 6-9 °C and pH 6.0. The mutant transients are multiplied by factor of 1.2.

At **1400 cm^{-1}** only in flash 1 the amplitude at 1 µs is higher in D61A. In flash two and three, the initial amplitude is by the same amount smaller. In flash four it is again identical. This is nicely visible in the flash pattern. Here, the WT pattern shows a very nice $Y_Z^{\bullet ox}$ pattern (compare fig. 8.4). The mutant exhibits maxima at the first and fifth flash and rather a minimum after the third flash. Still it follows at 4 µs and at 30 µs a quaternary pattern, indicative for (modified) cycling. Looking at the transients the mutant seems to follow in the first two flashes the behavior of the WT. It is slowed in the first flash and drastically slowed in the second flash. Still, the final negative changes of the WT are reached. In the first and second flash with a similar offset as the initial values. The flash amplitudes at 100 and 500 ms after flash 5 and 6 are also slightly negative in the mutant indicating cycling. Opposed to this, the rise with Mn oxidation in $S_3 \rightarrow S_0$ is not present in the mutant. Possibly a small rise starts at 100 ms in flash 3 and 4. In flash 4 the late rise looks similar to dark drifts, but no dark drift is observed at this wavenumber. This can be seen at flash 0 and minus 1, which are dark measurements, in the 500 ms pattern. The absence of the 2 ms rise is similar as at 1383 cm^{-1}.

The first and second flash transition at **1514 cm^{-1}** appear on a first glance very similar. Like at 1384 cm^{-1} the amplitude at 1 µs is in the mutant higher than in the WT. This additional signal decays in all flashes within 100 µs. All single data sets recorded on D61A show this early decay (average of three different measurements on two different samples). Besides this the third flash data differs. Here the WT decays with the known Mn oxidation time. The D61A transient starts to decay from 10 ms onward. Looking at the flash pattern, surprisingly the 4 µs trace shows very similar behavior to the WT. The latter develops its final shape by the decay of the second and sixth flash, which starts at 30 µs and a decay of

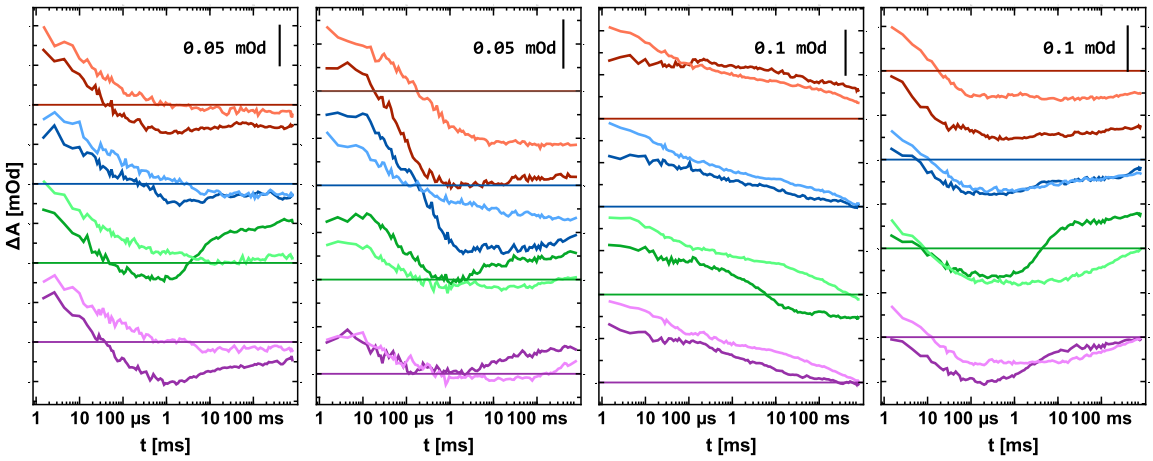

Figure 9.12: Comparisson of WT (*dark*) and D1-D61A (*bright*) at 1383, 1400 (avg of 1398 and 1400 cm^{-1}), 1514 and 1544 cm^{-1}. Data taken at 6-9 °C and pH 6.0 of core complexes from *Synechocystis* sp. PCC 6803 in solution. FeCy was added as an electron acceptor. The different colors represent flash induced transitions, from top to bottom: flash one to four.

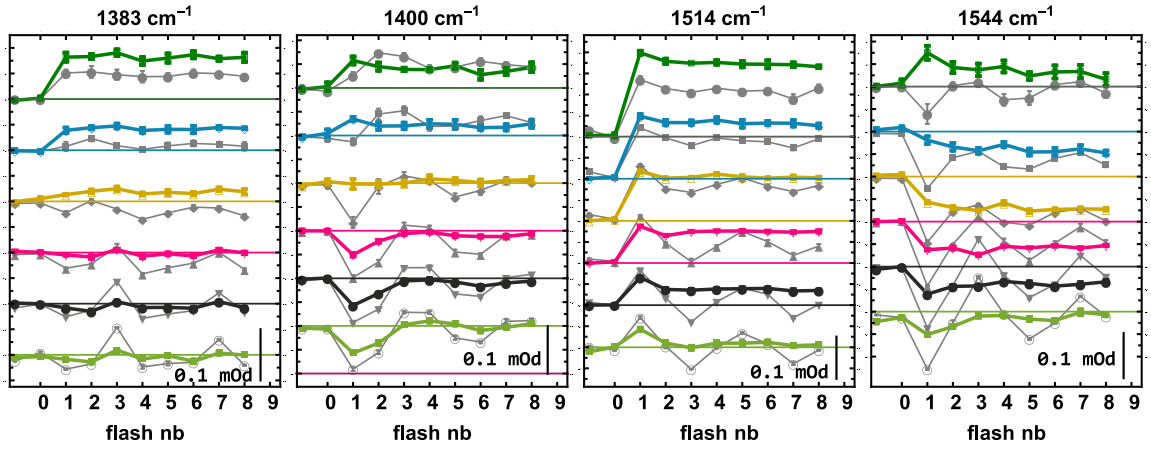

Figure 9.13: Comparisson of WT (gray) and D1-D61A (colored) flash number dependent amplitude patterns at 1383, 1400 (avg of 1398 and 1400 cm^{-1}), 1514 and 1544 cm^{-1}. Data taken at 6-9 °C and pH 6.0 of core complexes from *Synechocystis* sp. PCC 6803 in solution. FeCy was added as an electron acceptor. From top to bottom the time increases. Averaged has been in the interval of 0.75 to 1.5 of the following values: **green: 4 µs, blue: 30 µs, yellow: 200 µs, pink: 5 ms, black: 100 ms** and **light green: 500 ms.**

the third and seventh flash, which at 200 µs. Both features are absent in D61A, leaving the early amplitude pattern similar in shape to the final.

Looking at **1544 cm^{-1}**, the first flash is kinetically identical, just shifted by 0.1 mOd. The second flash looks alike in both sets. The beginning of the third flash also seems to be equal, but the onset of the rise is delayed from 1 ms to about 30 ms. The 4 µs flash pattern of the WT looks identical to the one at 1400 cm^{-1}- only shifted to negative values. The shape of the pattern stays conserved over time and only shifts with the quinone reactions.

Only the distinctive rise in the third flash modifies it. Therefore,it is no wonder that the mutant can not recreate the same pattern, it shows positive features in the first flash and only a weak rise in the third. Nonetheless a flat pattern is developing between 100 and 500 ms.

Comparison with Steady State spectra of D61A and with the cycling of D61N

The **steady state spectra** were obtained with a flash spacing of 13 s and a spectral resolution of 4 cm^{-1} by [Debus, 2014]. The values can be best compared when using the flash pattern at 500 ms (fig. 9.13). The values of flash 1 and 3 at 1383 cm^{-1} match in both data set. In flash 2 his spectrum shows a negative dip at 1380 cm^{-1} giving a more negative feature at 1383 cm^{-1} in D61A. In the SFIR data both show the same change.

The 1400 cm^{-1} data of D61A is similarly negative after the first two flashes in both data sets and no absorption is seen after flash 3.

At 1514 and 1544 cm^{-1}, the two data sets differ in the first two flashes, which is explainable by the spectral resolution of the FTIR data, and in the third flash, where the decay of the SFIR experiment seems to be not finished.

Taking into account the spectral resolution all bands match pretty well. Only flash 2 at 1384 cm^{-1} might differ slightly.

The **cycling** of the D1-D61A mutation compares well to the one obtained of cells and the D61N replacement with flash resolved oxygen release by [Hundelt et al., 1998a] (20 °C, 3 Hz). It compares rather with the low pH (5, 5.5) than with the pH 6.5 oxygen release pattern of thylakoids measured by [Dilbeck et al., 2012] (20 °C, 1 Hz). It might be that because the O-O bond formation starts in our measurement between 50 and 100 ms and has not finished (see transition at 1514 or 1544 cm^{-1}) a higher flash spacing might be necessary at lower temperatures. Also it might be due to the long duration of the measurements presented here (8 h). It was observed that the flash pattern becomes worse after 8 h, however the acceptor side was not hindered (data not shown). Thus the damage might happen at the less stable donor side with D61A present.

9.6.3 The effect of D61A on the kinetics of the S-state transitions

Several approaches were tried to extract the kinetics of all S-state transitions in the D1-D61A PSIIcc. One problem is that the $S_3 \rightarrow S_0$ transition is very slow and kinetically overlapping with slow drifts present in some dark measurements. The other problem is that the carboxylate vibrations are not as sensitive to this transition as in WT or PSII membranes. In addition bands in the amide I/II and $\nu_{AS}(COO)$ are sensing the acceptor side and other kinetics as well, making it difficult to separate the donor side from these (sec. 6). A first approach was to extract only the changes associated with the Mn photocycle by subtracting from each flash's transient the average over the first four flashes. This will remove the quinone contribution, which is the same in each flash. The results are not as convincing as hoped and difficult to interpret. One can find them in the appendix (fig. 11.36). Global fits of various selections of wavenumbers were performed as well. Two are shown in figure 11.35 of the appendix. The amplitudes yielded only small S-state dependence. The extractable information are limited and include the higher amount of electron transfer from Q_A^- to the iron in the first flash. Also the clear slowdown of $S_3 \rightarrow S_0$ becomes visible. It will be used as a comparison below. To find better results, solely the changes sensed at 1400 cm^{-1} were used for the flash 1 and 2 transition. In the O-O bond formation transition other wavenumbers are used as well. Because in the D1-D61A data the two measurements at 1398 cm^{-1} and the

one measurement at 1401 cm^{-1} differed slightly, we will discuss the observed changes for the two wavenumbers and their average separately.

Effect on the $S_1 \rightarrow S_2$ transition

In section 9.6.2 and figure 11.36, we found that the band at 1400 cm^{-1} best describes the possible $S_1 \rightarrow S_2$ state. The first flash transients are shown in figure 9.14 (average of 1398 and 1400 cm^{-1} for WT: red and D1-D61A: orange). The left figure shows the data as measured. Zooming into the shown rectangle and normalizing gives the middle pannel. Between 5 and 200 µs the kinetics seem to be the same. A monophasic decay of the WT yields a decay with 90 µs (see table 9.3). However when *shifting* the D61A transient by 0.03 mOd the right figure is obtained: The overall amplitude change is now apparently the same, but it is slower in the mutant slower. The question arises whether Mn oxidation is slowed down in the mutant or, as the middle panel suggests, two phases are present.

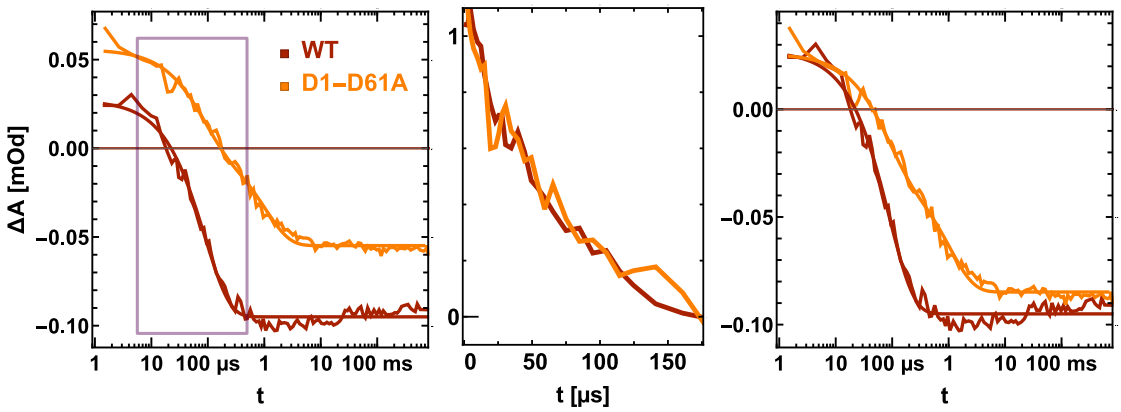

Figure 9.14: Comparison of WT and D61A at 1400 cm^{-1} in the $S_1 \rightarrow S_2$ transition. *left*: unscaled logarithmic plot. *center*: the transients are normalized to the values at 10 and 90 µs. *right*: D61A transient shifted by 0.03 mOd. The transient of the mutant is the average of both wavenumbers presented in figures 9.15. The kinetics of the 80 µs electron release phase are unaltered. An additional slow phase seems to be present.

Table 9.3: Fit results of the first flash data of WT and D1-D61A PSIIcc at pH 6.0 and 6-9 °C. First two columns at 1400 cm^{-1} as shown in fig. 9.14. D61A: jf represents the results of the joint simulation as shown in fig. 9.15.

	$S_1 \rightarrow S_2$					
	WT	**D61A**	D1-D61A: jf			
	1400 cm^{-1} avg		1398 I	1400 I	1398 II	1400 II
c [mOd]	-.095 (1)	-.055 (1)	-.066 (1)	-.041(1)	-.069 (1)	-.042 (1)
a1 [mOd]	.122 (2)	.054 (3)	.118 (2)	.074 (2)	.065 (4)	.051 (3)
τ1 [µs]	89 (3)	79 (8)	410 (20)		95 (9)	
a2 [mOd]		.057 (3)			.068 (3)	.036 (3)
τ2 [ms]		1.0 (0.1)			1.2 (1)	

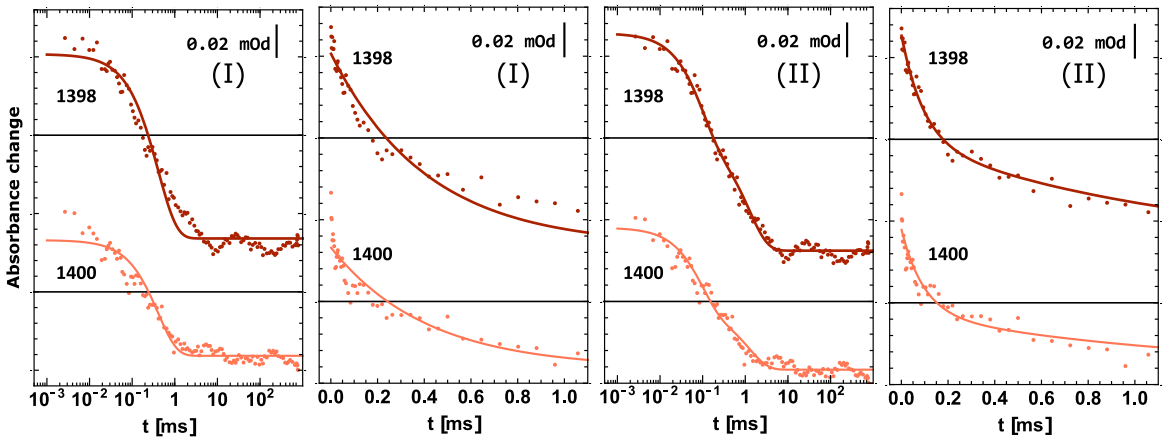

Figure 9.15: Joint fit results of the $S_1 \rightarrow S_2$ transition of D61A at 1398 cm^{-1} (*top*) and 1400 cm^{-1} (*bottom*). First two panels from left: one exponential joint fit with a time constant of $409 \pm 18\,\mu s$. Last two panels: two exponential joint fit with time constants of $95 \pm 9\,\mu s$ and $1.2 \pm 0.1\,ms$.

The simulations of D1-D61A at the averaged 1400 cm^{-1} transient in figure 9.14 consists of two exponentials. Taking only the single measurements at 1398 and 1400 cm^{-1} and fitting them jointly with one or two exponential functions yields the results presented in figure 9.15 (fit I or II, respectively). The plots are shown once on the linear and once on the logarithmic scale. With one exponential function the 1400 cm^{-1} transient is fitted fine (I), when ignoring the first 100 µs. The 1398 cm^{-1} transient on the other hand is not fitted well at all. The decay time is found to be 410 ± 20 µs (see tab. 9.3). This value lies in between the older ones found for D1-D61N by transient absorption changes at 360 nm at 20 °C[15]: [Dilbeck et al., 2012] obtained 505±30 µs. The fit quality seems to be fine. [Hundelt et al., 1998a] found 340±70 µs at the same temperature and with the same method. The fit is also fine.

The double exponential simulation (II) presented on the right side of figure 9.15 however fits our data much better. Now both wavenumbers are fitted well. The found 95 µs component is as strong as the 1.2 ms component at 1398 cm^{-1}. At 1400 cm^{-1} the fast component is slightly more pronounced. This result and the average of both in figure 9.14 state that there is a second process causing half of the changes observed and which is slowed down by a factor of ten. The first component is kinetically unaltered.

Effect on the $S_2 \rightarrow S_3$ transition

In the following, the second flash transients obtained from the measurements around 1400 cm^{-1} for WT and D1-D61A will be compared. For simplicity the results will be discussed as the ones of $S_2 \rightarrow S_3$ assuming from the flash pattern obtained in figure 9.13 that most photosystem reached the S_2 state.

In figure 9.16 the average of the measurements at 1398 and 1400 cm^{-1} are presented. The brighter colors represent D61A. As seen before, the D61A transient starts at a lower positive absorption change and ends at a less negative value. The WT data shows clearly two phases up to 1 ms (like PSII membranes, see fig 9.6). It also seems to contain a slow phase in the hundreds of ms. It is present in nearly all single measurements and in opposed direction

[15] quinones are also sensed

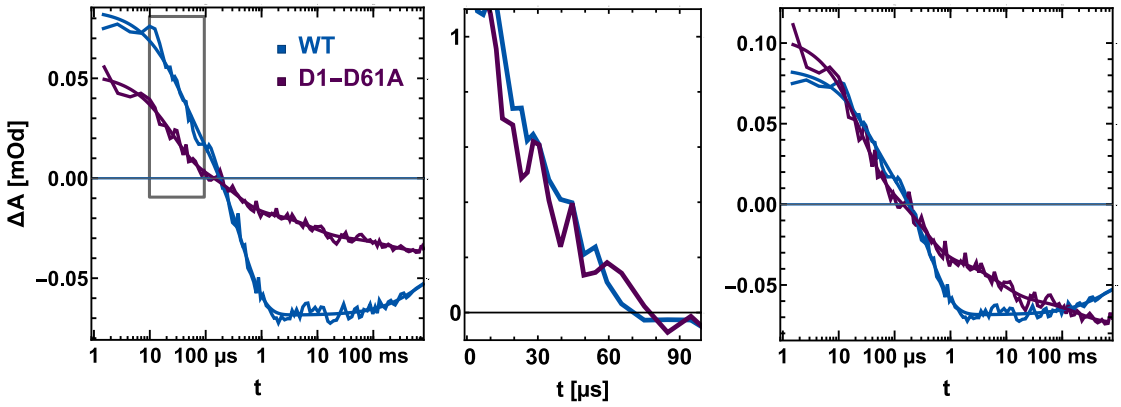

Figure 9.16: Comparison of WT and D61A at 1400 cm^{-1} in the $S_2 \rightarrow S_3$ transition. *left*: unscaled logarithmic plot. *center*: the transients are normalized to the values at 10 and 90 µs. *right*: D61A transient scaled by a factor of two. The transient of the mutant is the average of both wavenumbers presented in figures 9.17. The kinetics of the 30 µs proton release phase are unaltered. Judging from the right figure, the electron transfer phase seems to be split into two phases.

Table 9.4: Fit results of the second flash data of WT and D1-D61A PSIIcc at pH 6.0 and 6-9 °C. First two columns at 1400 cm^{-1} as shown in fig. 9.16. D61A: jf represents the results of the joint simulation as shown in fig. 9.17.

	$S_2 \rightarrow S_3$					
	WT	**D61A**	D1-D61A: jf			
	1400 cm^{-1} avg		1398 I	1400 I	1398 II	1400 II
c [mOd]	-.046 (13)	-.037 (2)	-.050 (1)	-.021 (1)	-.052 (1)	-.020 (1)
a1 [mOd]	.049 (3)	.043 (2)	.056 (2)	.038 (2)	.052 (3)	.035 (3)
τ1 [µs]	31 (4)	24 (3)	31 (3)		27 (3)	
a2 [mOd]	.103 (3)	.025 (2)	.027 (2)	.024 (2)	.024 (3)	.022 (2)
τ2 [µs]	420 (20)	310 (60)	690 (95)		340 (70)	
a3 [mOd]		.013 (2)			.015 (2)	.011 (2)
τ3 [ms]		7.5 (2.3)			7.5 (2.3)	
a4 [mOd]	-.022 (13)	.008 (1)	.021 (1)	.005 (1)	.015 (2)	-.001 (1)
τ4 [ms]	650 (550)	190 (110)	65 (11)		170 (55)	

to the dark drift (not shown). The D61A transient shows one fast phase ending at around 100 µs. From there on, it decays over the whole time range. As discussed before the steady state of the FTIR measurements by [Debus, 2014] is similar in WT and D61A.

When looking at the indicated rectangle and normalizing the transients (*middle panel*), the two transients show the same kinetics up to 90 µs. When scaling the D61A data by a factor of two - without any shift - the *right* figure is obtained. Even when ignoring the points later than 100 ms a different kinetic behavior is found between 1 and 10 ms.

To find the kinetic components of the D61A sample, first the single wavenumbers are fitted. This is shown in figure 9.17 for three exponetials on the left and four exponentials on the right, both in linear and logarithmic scale. A two exponential decay fitted none of

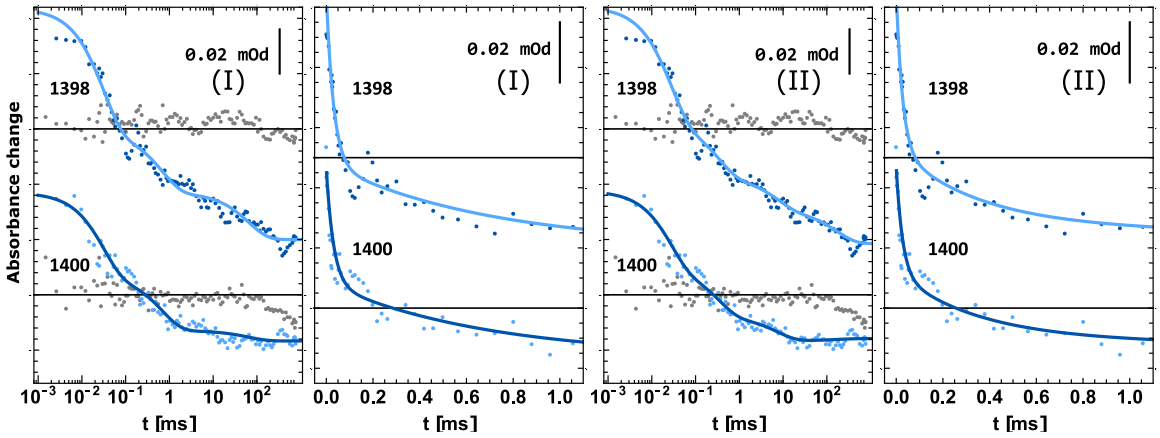

Figure 9.17: Joint fit results of the $S_2 \rightarrow S_3$ transition of D61A at 1398 cm^{-1} (*top*) and 1400 cm^{-1} (*bottom*). *Left*: full logarithmic and linear view with a three exponential fit. The time constants are $31 \pm 2\,\mu s$, $688 \pm 95\,\mu s$ and $65 \pm 11\,ms$. The latter fits the dark drift (plotted in gray). An additional phase might be present with 5-10 ms. *Right*: linear and logarithmic plot simulated with four exponentials. The time constants are $27 \pm 3\,\mu s$, $340 \pm 70 \mu s$, $7.5 \pm 2\,ms$ and $170 \pm 60\,ms$.

the two satisfactorily. In the logarithmic plots it becomes apparent why I separated the two data sets: After 10 ms the 1398 cm^{-1} decays clearly much stronger than the 1400 cm^{-1} measurement. The dark measurement is plotted as well in gray. The drift present in the dark[16] starts around 100 ms and follows the same direction as the 1398 cm^{-1} transient.

In the linear plot we see that both simulations describe the data well until 1 ms. A 30 µs and a 690 ± 95 or a 340 ± 70 µs phase are found in the three or four exponential fit, respectively. The amplitudes of either phase stay about the same at both simulations (tab. 9.4). The difference between the simulations starts later than 1 ms. The quality of the fit is better with four exponentials. However, the quality is a question of judging what is noise and what is real. In the dark trace of 1398 cm^{-1} (top gray) similar oscillations are present as in the data, suggesting that the wiggles of the decay are noise. Without them, the curve would decay linearly in the logarithmic plot from 500 µs to 200 ms. This range is too big to fit it with only one exponential. The dark measurement at 1400 cm^{-1} does not show the oscillations but a drift starting at 100 ms. Up to 100 ms this transient (bottom, light blue) is therefore the most trustworthy. To simulate it well until 100 ms, the four exponential fit is needed, that inturn also fits the 1398 cm^{-1} trace.

The size of the amplitudes in the four exponential fit is more or less the same at 1398 and 1400 cm^{-1}. Only the 170 ms component is absent at 1400 cm^{-1}, causing the steady state values to differ as well. This is another indication, that this phase stems from drifts. The fastest phase with 30 µs is slightly larger at 1398 cm^{-1}.

Now that I explained the choice of the four exponential fit we can compare the D61A to the WT. The amplitude and kinetics of the 30 µs phase are identical. The kinetics of Mn oxidation in WT seem to be unaltered with D61A present (300-400 µs, within the error of joint fit). The amplitude is only 1/4 of the one of the wild type. The mutated PSII needs a further phase with 7.5 ± 2.3 ms to finish this transition. Both measurements show a small slow drift, most likely an artefact. The observation, that the amplitude of the 400 µs phase

[16] possibly due to heat up by the QCL or varying water vapor

is much smaller holds also for the three exponetial fit. Here a decay constant of 690 ± 95 µs was found.

[Dilbeck et al., 2012] found a 645 ± 80 µs phase in the second flash with D61N present. The fit and data quality is less good than in flash one or the WT, and an extra phase could be present. [Hundelt et al., 1998a] found a rise time of 750 ± 70 µs. The data is only present up to 2 ms and from 1.5 ms onward the fit quality becomes bad. Also in the SFIR data, the data is well fitted until 1.1 ms by both functions (linear scale of fig. 9.17). Although, they studied another mutation the kinetics are similar to my three exponetial fit. Their data quality or presentation is not at all conclusive. Therefore, an additional decay channel – as found here – is not in contradiction to the reports of D1-D61N.

Effect on the $S_3 \rightarrow S_0$ transition

In section 9.6.2 it was found that the $\nu_S(COO)$ vibrations around 1400 cm^{-1} are not as sensitive to the O-O bond formation in the mutant as in the WT, but that this step still takes place as judged by other bands and the flash pattern.

Therefore, the approach to extract the kinetics differs in this section. First we want to know how the fast kinetics differ with D61A present. For this the 1400 cm^{-1} band is presented in figure 9.18. The left part shows the transients of both, mutant an WT as measured. The initial absorption change is smaller in the mutant. By zooming into the region from 10 to 600 µs and normalizing, the middle panel is obtained. Again WT and D61A do not differ, only before 10 µs the transients seem to differ. But the simulation of the transients yields a 20 µs phase in both with a similar amplitude of D61A as the WT. When scaling the D61A transient by a factor of two and shifting the result by 0.015 mOd the transients compare as in the right figure. Apparently the very fast decay is over-scaled in the mutant. The slow rise upon O-O bond formation is present in the mutant but drastically slowed down. In this range the QCL induced drift is present in dark measurements, but in the opposite direction. Still, to judge whether this immense slow down is real, we want to look at other wavenumbers as well.

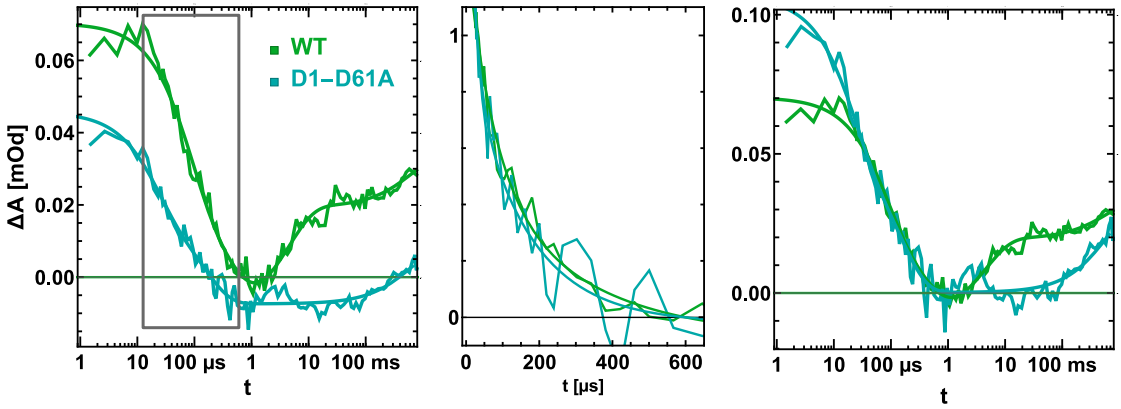

Figure 9.18: Comparison of WT and D61A at 1400 cm^{-1} in the $S_3 \rightarrow S_0$ transition. *left*: unscaled logarithmic plot. *center*: the transients are normalized to the values at 30 and 600 µs. *right*: D61A transient scaled by a factor of two and shifted by 0.015 mOd. The transient of the mutant is the average of both wavenumbers presented in figures 9.20. The kinetics of the 200 µs proton release phase are unaltered.

When looking at the 1544 cm^{-1} amide II transients in figure 9.19, a similar behavior can be observed. The absorption change at 1 µs is slightly lower in the WT. Both are a little bit above zero and decay in conjunction. The strong rise sensed by the WT starting around 500 µs (red to orange arrow) is not observed at all in D61A. The transient of the mutant starts to rise at 10 ms up to the hundreds of ms (purple arrow). Looking at the flash number dependent amplitude pattern of both data sets (right panel), the final quaternary pattern develops within these time intervals. This is in the 3rd and 7th flash in the WT and 3rd, 4th and 7th and 8th flash in D1-D61A. In the mutant also the 5th and 6th flash amplitudes rise causing the flash pattern to flatten out. This indicates a much higher miss factor for this transition, possibly due to too short flash spacing.

Because the WT transient shows a drift above 100 ms and the 1544 cm^{-1} band senses basically all of PSII's cofactors, a joint simulation is done on several wavenumbers to determine the delay in the rise.

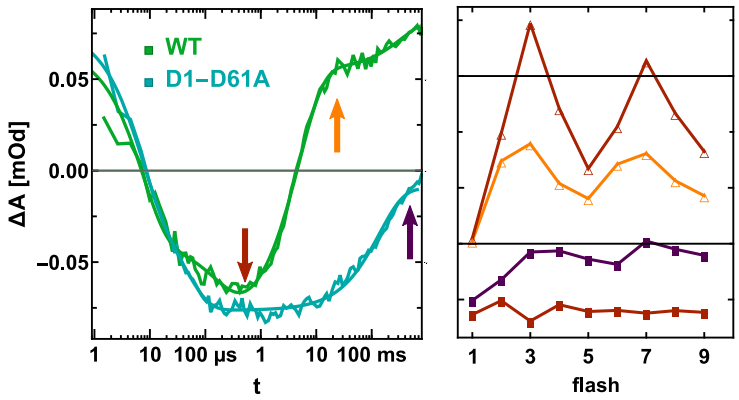

Figure 9.19: Comparison of WT and D61A at 1544 cm^{-1} in the $S_3 \rightarrow S_0$ transition. *left:* transients as measured. *right:* flash number dependent amplitude pattern averaged at the times indicated by an arrow: yellow 500 µs, red 20 ms, purple 600 ms. The conformation changes sensed at this amide II band are created equally fast. The rise time due to Mn oxidation, O-O bond formation and the proton rearrangement are strongly slowed down by a factor of around 30.

The joint fit was conducted of the transients at 1383, 1398, 1400 and 1544 cm^{-1}. These wavenumbers were chosen for their small quinone contribution and their strong contribution to the ms step in $S_3 \rightarrow S_0$ in the WT. The results are presented in figure 9.20 and table 9.5. A four exponential fit function was chosen. A lower number decreased the fit residual and a higher did not improve them significantly. The 10 µs phase is especially strong at 1383 and 1544 cm^{-1} (green). This might indicate stronger non-heme iron sensing at these wavenumbers and cause the time constants to decrease compared to the fits on only the 1400 cm^{-1} bands. The 100 µs decay is equal at all wavenumbers (blue). A 6 ms phase is mainly sensed at 1383 and 1544 cm^{-1} and reflects the Q_A^- reoxidation by FeCy (4-6 ms, sec. 7.3). The last phase was found to be 180 ± 10 ms. It is strongly sensed at 1544 cm^{-1} and weakly as a rise in the symmetric carboxylate stretching region. When decreasing the number of exponentials by one, the rise time changes to 150 ms. When increasing the components it slows down to 240 ms while a 23 ms phase is found additionally. [Bao and Burnap, 2015] measured temperature dependent oxygen release and found for D1-D61A $149 \pm 15\,ms$ for T = 8 °C. This compares well to the values found here.

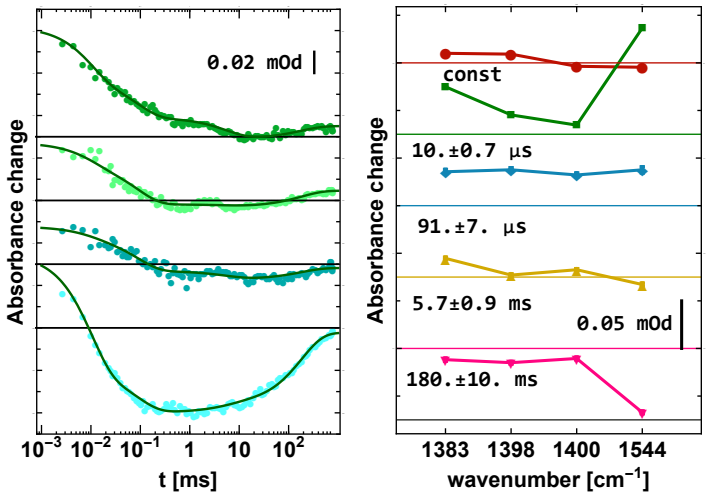

Figure 9.20: Joint fit results of the $S_3 \rightarrow S_0$ transition of D61A. *left*: transients measured at 1383, 1398, 1400 and 1544 cm^{-1}. *right*: The amplitudes of the constant and the four exponential components.

Table 9.5: Fit results of the third flash. The WT results are taken from the simulation of the deconvoluted data presented in fig. 9.2. The results of D1-D61A 1400 cm^{-1} from fig. 9.18 and the D1-D61A: jf origins from a joint fit of the transients presented in fig. 9.20. All measurements taken at pH 6.0 and 6-9 °C.

	$S_3 \rightarrow S_0$			
	WT	**D61A**	D1-D61A: jf	
	1400 cm^{-1} avg		1398	1400
c [mOd]	.046 (1)	.008 (8)	.009 (1)	-.004 (1)
a1 [mOd]	.022 (9)	.027 (4)	.020 (4)	.010 (4)
τ1 [µs]	26 (15)	21 (5)	10 (1)	
a2 [mOd]	.050 (8)	.026 (4)	.038 (2)	.032 (2)
τ2 [µs]	180 (50)	160 (30)	91 (7)	
a3 [mOd]	-.031 (4)		.002 (1)	.008 (1)
τ3 [ms]	2.5 (6)		5.7 (.9)	
a54 [mOd]		-.015 (8)	-.015 (1)	-.011 (1)
τ54 [ms]		590 (470)	185 (10)	

Effect on the $S_0 \rightarrow S_1$ transition

The $S_0 \rightarrow S_1$ transition is already difficult to study in the WT. With D1-D61A present, the flash resolved data becomes even more demanding to deconvolve. In the raw data the fourth flash transition contains mainly signals from the third flash (see fig. 9.13). Therefore, no statements on the kinetics of this transition can be made.

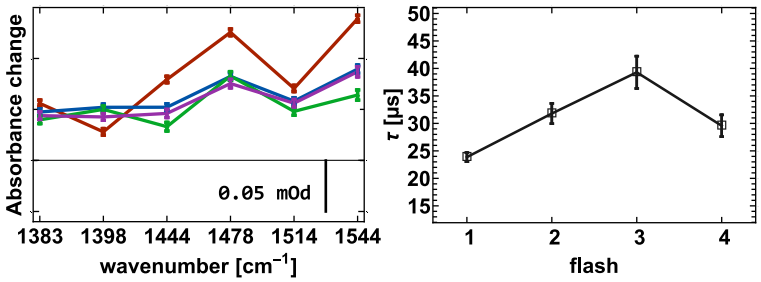

Figure 9.21: Joint fit results of the 30 µs phase including the quinone bands at 1444 and 1478 cm^{-1} as well as one at 1514 cm^{-1}. Flash one in red, 2 in blue, 3 in green and flash 4 in magenta. Bands with strong quinone contributions as the ones at 1444, 1478 or 1544 cm^{-1} show higher amplitudes in the first flash. On the contrary the band without quinone contributions at 1398 cm^{-1} shows the smallest amplitude after the first flash and highest after the second and third flash.

Does the 30 µs phase origin from the donor side?

Because it is a very strong result that the 30 µs phase in S_2 and $S_3 \rightarrow S_0$ is kinetically unaltered and only the amplitudes decrease in D1-D61A, it shall be tested, whether it does not originate from a different source than the proton release phase. There are two possible contributions:

a) quinones

Simulating the quinone band at 1478 cm^{-1} individually, resulted in a 20 to 30 µs phase in all flashes. The amplitude is highest after the first flash, because more iron got oxidized by FeCy in the dark. In later flashes the contribution stays constant.

The fit included the wavenumbers at 1383, 1398, 1444, 1478, 1514 and 1544 cm^{-1}. The complete results are shown in the appendix (fig. 11.35). Figure 9.21 only shows the components of the 25 and 40 µs phase. In the third flash it is slowest, possibly because of donor side contributions (10 and 90 µs in joint fit, see tab. 9.5). The amplitude of the first flash (red) is much higher at 1444, 1478 and 1544 cm^{-1}. We learn from that that the **strong early decay of the amide II** band in PSIIcc **stems from the acceptor side**. At 1398 cm^{-1} the opposite is observed. The phase is weakest after flash 1. This clearly speaks for an origin at the donor side.

b) high misses

It was found that the flash pattern at 1544 cm^{-1} shows nearly no rise after 500 µs after the first and second flash, but all later flashes do. This means that the rise of $S_3 \rightarrow S_0$ is present at later flashes and we have a high miss-factor of this transition under the conditions of the measurement. It remains possible that also the efficiency of earlier transitions is affected.

Figure 9.22 shows the transients measured at 1398 cm^{-1} in the first, second and third flash transition (dark). After

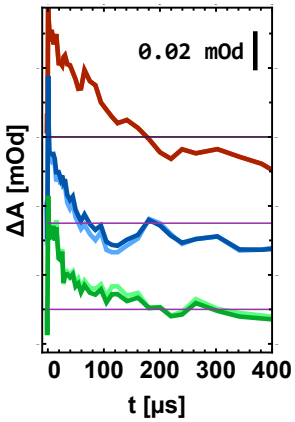

Figure 9.22: A miss correction of the transients at 1398 cm^{-1} keeps fast phases after the first three flashes (red, blue, green). The miss factor is assumed to be 15 %. Brighter traces are corrected.

the subtraction of 15 % of flash 1 from flash 2 and rescaling to 100 % the brighter curve is obtained. Before and after it does not show strong contributions from the first flash. The fast phase stays present. Using the newly obtained transient to apply it likewise to flash 3 also no change of the very fast phase is found. Only the slower 100-200 µs phase is enlarged.

This means the 30 µs phase is exclusively present in $S_2 \rightarrow S_3$ and $S_3 \rightarrow S_0$ and stems from the donor side.

9.6.4 Summary of effects observed in D1-D61A PSIIcc

The **fast proton release** phases are unaltered in $S_2 \rightarrow S_3$ and $S_3 \rightarrow S_0$, both in amplitude and kinetically. It means that the carboxylate at position D1-D61 does not take part in the event of this phase, meaning it is not contributing directly to the absorption change or modifies the H-bonding network. Because the kinetics are unaltered, it can be concluded that the rate determining step of this reaction stays the same during these 30 µs. One can say that this phase is not localized around D61. This is surprising as W1 was proposed to become deprotonated ([Siegbahn, 2012]) and the D1-D61 to take part in a prominent proton channel and a H-bonding network including the connection to Y_Z.

The **lag phase** in $S_3 \rightarrow S_0$ is kinetically unaltered. The amplitude is, however, halved, while the 30 µs amplitude remains the same. When the kinetics are unaltered it means that the rate determining step of the reaction is not modified. Because the amplitude changes, it means that either D61 contributes directly (sensed around 1400 cm^{-1}) or the H-bonding network transmitting is disrupted so that less carboxylate can react onto the changes. This may be the extended H-bonding network reported in [Service et al., 2014a], in which the Mn cluster region is connected via D1-D61 to D1-E65 up to D2-E310. Either way the processes during the lag phase are localized in the vicinity of D61. [Bao and Burnap, 2015] found a retardation of the lag phase. To reproduce this, one would need to include a silent phase in the simulation of the SFIR flash 3 data, that needs to be finished before the onset of the rise at 1400 or 1544 cm^{-1}. In any event this means that the lag phase is of more complicated nature. It consists of an (kinetically) unaltered (SFIR) and an altered component ([Bao and Burnap, 2015]).

The **kinetics of Mn oxidation** in D1-D61A PSIIcc are slowed down in all transitions. In $S_1 \rightarrow S_2$ either a similar retardation from 89 ± 3 µs to 410 ± 20 µs as in the literature is sensed ([Hundelt et al., 1998a], [Dilbeck et al., 2012]) or one phase stays the same with 79 ± 8 µs and halved amplitude and another phase with 1.2 ± 0.1 ms appears. The latter is favored by our data. In $S_2 \rightarrow S_3$ our data clearly favors a multiphasic transition with the 420 ± 20 µs phase of the WT split into one 310 ± 60 µs and one 7.5 ± 2.3 ms phase. The total absorption change is decreased. Reviewing the literature of D1-D61N, I found indications that a second phase is present in their data as well ([Hundelt et al., 1998a],[Dilbeck et al., 2012]). The $S_3 \rightarrow S_0$ transition is with 150-240 ms equally slow as estimated from a D1-D61A study by [Bao and Burnap, 2015].

Judging from the temporal development of the flash pattern at 1544 cm^{-1}, the **miss factor** is very high in $S_3 \rightarrow S_0$ under conditions of the measurement. Because of the slow $S_3 \rightarrow S_0$ transition this might be mainly due to too the flash spacing.

A joint fit including the quinones clearly stated that the **early difference of the amide II** between PSII membranes and PSIIcc band at 1544 cm^{-1} origins from the acceptor side. Possibly it involved the binding of FeCy or different flexibility due to a different adaption to the antenna system.

The amplitude **change upon charge separation** is bigger after the first flash at all wavenumbers and smaller at 1400 cm^{-1}, similar at 1544 cm^{-1} and bigger at 1383 and 1514 cm^{-1} after later flashes. This indicates that either the dark stable state S_1 is already modified or that some center do not contain a functional Mn cluster. The latter I consider as less likely because the bands at 1400 cm^{-1} shows a weak flash amplitude pattern with the first and fifth flash showing a maximum.

9.6.5 Hypothesis on the effect of the D1-D61A mutation

Additionally to the observations just listed it was reported for D1-D61A that in $S_1 \rightarrow S_2$ a water molecule close to the chloride site, does not deprotonate or form a stronger H-bond and that a polarizable H-bonding network does not evolve. Also in $S_2 \rightarrow S_3$ another water close to D61 does not form a stronger H-bond or deprotonate ([Debus, 2014]). In $S_3 \rightarrow S_0$ the activation enthalpy is lowered in the lag phase and in O_2 release, but there is an immense enthalpy penalty in D61A. Because it is in the lag phase as well either preceding transient states or the S_2 state are altered [Bao and Burnap, 2015].

Our data shows that the 30 µs phase is unaltered upon mutation in both $S_2 \rightarrow S_3$ and $S_3 \rightarrow S_0$. This suggests that neither the polarizable H-bonding network formed in $S_1 \rightarrow S_2$ nor the changes of the single water molecules in $S_1 \rightarrow S_2$ or $S_2 \rightarrow S_3$ are important for this phase. This strengthens the idea of a deprotonation further remote from D1-D61. On the other hand, the deprotonation in S_2 is described to be highly exergonic after $Y_Z^{\bullet ox}$ formation ([Siegbahn, 2013]) and might not require D61 as a base. This does not exclude the broad channel of figure 9.2, yet, as it might be flexible enough to conduct the proton via other water molecules or along the chloride site.

Our D61A transients suggests a biphasic reaction of $S_2 \rightarrow S_3$ and possibly $S_1 \rightarrow S_2$. In the WT they were monophasic. The $S_3 \rightarrow S_0$ stays monophasic but is slowed down dramatically. The **biphasic behavior** in $S_1 \rightarrow S_2$ and $S_2 \rightarrow S_3$ may be explainabe in two ways:

I) the reaction is heterogeneous

In his recent review [Pantazis, 2018] highlights the possibility of different conformations in most S-states of the WT. These correlate in S_2 and S_3 with open and closed cubane forms of the cluster but also with various reaction pathways, i.e. water binding, shuffling and de- and re-protonation events. Whether or not the S_1 is heterogeneous is still under discussion. In any event, with no carboxylate keeping W1 in place, the H-bonding network will surely be altered and different S_1 conformations might become stable. If for example in the mutant the closed cubane was slightly preferred and W1 was not stabilized by D61 then the dangling Mn could be more flexible, slowing the water binding entropicaly ([Askerka et al., 2017]). This could cause the slow 7.5 ± 2.3 ms phase observed. A cluster in the open cubane in S_2 might not be influenced as Mn4 is stabilized by two µ-oxo bridges.

II) subsequent reaction steps

I will use the model introduced by [Siegbahn, 2013] to explain a possibility how a biphasic $S_2 \rightarrow S_3$ transition might look like. This is not at all a unique explanation and not based on any observation besides the biphasic behavior in $S_2 \rightarrow S_3$ and the monophasic reaction in $S_3 \rightarrow S_0$. However basic components of this mechanism can be applied to several reported alternatives (review by [Pantazis, 2018]). To explain the idea we need some key-players not discussed yet. In his model we start in a open cubane with O5 at Mn4 and a non-crystal water Wx ligating Mn1 (see figure 9.23). This water is connected to W1 between Mn4 and D61 via three waters, of which one is bound to the chloride anion.

Upon $Y_Z^{\bullet ox}$ formation a proton is released at W1[17]. This might be our 30 µs phase. After the proton is released Mn1 is oxidized leading to the binding of Wx, which in turn releases a proton from position A to B with a low barrier. To finish the transition the proton needs to be transferred from position B to C which also shows a low barrier. This was calculated for the WT. If now no deprotonated carboxylate is H-bonded to W1, but rather another water fills the empty space, the transfer from position A to B will hardly be affected. As this is the important step to oxidize Mn, Mn oxidation will also not be affected. As mentioned before, in $S_1 \rightarrow S_2$ a water close to the chloride does not form a strong H-bond nor deprotonates. This will directly modify the transfer from B to C either by a higher barrier when the proton stays close to the chloride or by enthalpic considerations when there is no stable water wire connecting this site to the deprotonated water W1.

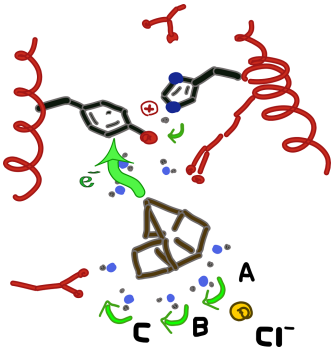

Figure 9.23: Water groups involved in the proton transfer from substrate water in $S_2 \rightarrow S_3$ or the substrate hydroxide in $S_3 \rightarrow S_0$ at position A to a hydroxide group formed upon $Y_Z^{\bullet ox}$ formation at position C. Mechanism proposed by [Siegbahn, 2013]. The proton moves step wise from the binding water at Mn1 via three water molecules to the hydroxo group. It passes a water bound to the chloride anion.

In $S_3 \rightarrow S_0$ no mulitphasic behavior is found and in D61A the step is limited by a much higher entropic penalty. In the WT the KIE is very low with 1.2 and proton rearrangements are not rate limiting. I will first try to explain this again by the model of Siegbahn. He suggests a similar mechanism as in $S_2 \rightarrow S_3$: first W1 deprotonates (C), then the substrate – now a hydroxo – at Mn1 (A) needs to deprotonate (A to B) in order to be oxidized in a concerted step. This state is stabilized by the necessary transfer of the proton from B to C. However, this step already possesses a very high barrier (similar as the O-O bond formation). If additionally the (entropic) penalty of D61A is added, the reaction will become very slow and proton movement limited. Therefore, this can be tested, by measuring the kinetic isotope effect in D_2O.

However, other reasons can not be excluded at all. A very difficult step in this reaction is also the release of oxygen which needs to be replaced by water. In the disturbed arrangement of the mutant this might cause the slow down as well.

9.7 Conclusion and outlook

First measurements in the symmetric carboxylate stretching region were presented, introducing these changes as a reliable tool to study most events of the photocycle. The identified kinetics are in excellent agreement with the ones reported before ([Klauss et al., 2015]). These described an extended reaction cycle, with alternating proton and electron release steps from the oxygen evolving cluster. In the region from 1378 to 1410 cm^{-1} at least ten carboxylate groups contributed to the changes observed. Among these were three prominent bands that

[17] W2 in some alternative mechanisms

sensed either the 300 ns or the 30 µs phase. This shows that the reactions of the two phases happen at distinct sites. The remaining groups sensed Mn oxidation associated events and reversed changes induced upon charge separation or formed the steady state spectra.

At pH 7.5, the amplitude of the 30 µs phase was diminished drastically while the kinetics remained unaltered. This suggests the involvement of surface pH sensing carboxylates in this phase.

Though PSIIcc from *Synechocystis* and PSII membranes from spinach are very different sample types from different species, their kinetics of the photocycle are very similar. When measuring in the amide II region especially kinetics of Q_A^- reoxidation differed. The amide II band at 1544 cm^{-1} sensed in PSII membranes proton release and Mn oxidation during the $S_2 \rightarrow S_3$. A possible H-bonding network causing these changes was discussed. These kinetics were masked in PSIIcc. A global fit showed that some early changes origin from differences at the quinone side of PSII, involving the non-heme iron.

A very first time resolved infrared study of the D1-D61A alteration was conducted. Contrary to what might have been expected, it did not affect the 30 µs phase neither in $S_2 \rightarrow S_3$ nor in $S_3 \rightarrow S_0$, even though it is located directly at the entrance to a proton exit pathway and is H-bonded to a W1 in turn ligating Mn4. This suggests that the fast proton is not released from W1 or a site close by. However it might be that the proton release is not relying on D61 being present as a proton acceptor.

The kinetics of Mn oxidation steps were altered. The most drastic change was the slowdown of the $S_3 \rightarrow S_0$ transition by a factor of more than 30. In $S_1 \rightarrow S_2$ and $S_3 \rightarrow S_0$, two different simulations were preformed. The one fitting less well, yielded kinetics similar to the ones obtained before for D1-D61N. Certainly in $S_2 \rightarrow S_3$ and possibly in $S_1 \rightarrow S_2$ an additional phase was found. Reevaluating the literature data supported this finding for $S_2 \rightarrow S_3$. A hypothesis explaining this behavior was formulated either as two distinct states of the cluster or a multi-step reaction.

Because an unaltered "lag" phase was found, but a study before reported that it is only slowed down, a more complicated mechanism may be underlying, where there is one infrared active phase (at the wavenumbers measured) and one IR-inactive phase, which is slowed down.

Outlook

One very important outcome of this study is that the reduction of the non-heme iron takes place within 25-30 µs and really disturbs the measurements we are targeting for. It can be avoided in PSII membranes by the use of a different quinone as for example the commercially available 2,5-Dichloro-1,4-benzoquinone or decylplastoquinone or with the extracted native plastoquinones (extraction protocol in [Kurreck et al., 1995]). In PSII core complexes the addition of the right amount of ferrocyanide is supposed to keep the iron oxidized by decreasing the redox potential of the ferri/ferro couple ([Iizasa et al., 2010]). A redox tuning of the bicarbonate was also found ([Brinkert et al., 2016]). When depleting PSII of bicarbonate possibly the electron transfer from Q_A^- will slow down as well.

In PSII membranes two bands at 1378-1382 and 1394 cm^{-1} are identified that either sense the 300 ns or the 30 µs phase in $S_2 \rightarrow S_3$ and $S_3 \rightarrow S_0$ especially strongly. As the nature of the associated events is still unclear, these bands are interesting research targets. The latter was found to be sensitive to the pH of the solution. One could measure the pK_a of this band and try to find its location. A good comparison will be the NMR study of the pK_a of surface

carboxylates in PsbO (*unpublished, group of Oschkinat*). These groups might be especially interesting because one of the proton channels exits at the interface of PsbO.

The high pH measurement showed that most of the 30 µs phase disappeared in PSII membranes. This unveiled the "lag" phase in $S_3 \rightarrow S_0$. One can search for the optimal pH value where the two signals are well separated and get a clean access fur further studies.

Without a question, it is most interesting to study the dynamics of water itself: It is the water that rearranges, binds, deprotonates and gets oxidized. Infrared spectroscopy gives access to these dynamics (reviewed by [Nakamura et al., 2016]). One option to access this region is to buy another laser module. Unfortunate the QCL modules cover a spectral region of only 100-200 cm^{-1}[18]. Another option is to use our Vertex80v and either measure in the Step-Scan mode or use the broad band source and the sensitive detector together with narrow band filters. Another possibility might work as well. Richard Debus uses D_2O to shift the $\delta(D/HOD/H)$ to 1100 to 1300 cm^{-1}. When using a mix to also have δDOH vibrations present, the current setup can be used to measure them. Only these bands are very weak. Debus found signals in the order of 2.5 µOd while the one at 1400 cm^{-1} was as big as the data reported here. The S/N ratio of the SFIR-setup is around 5 µOd with 300 samples averaged, but limited by systematic noise. The outcome would be to have time resolved signals of the proposed substrate waters at 1238 cm^{-1} in $S_2 \rightarrow S_3$ and 1254 cm^{-1} in $S_3 \rightarrow S_0$ (in $D_2^{16}O - D_2^{18}O$, [Debus, 2014]).

Reported steady state spectra of the $S_1 \rightarrow S_2$ transition yielded no difference between PSII membranes from spinach and PSIIcc from *Synechocystis* ([Remy et al., 2004]). But the new data suggests differences in the symmetric carboxylate regions in the $S_3 \rightarrow S_0$ and $S_0 \rightarrow S_1$ transitions and possibly changes around 1500-1515 cm^{-1}. To clarify this point first steady state difference spectra of all four transitions should be recorded. Then time resolved spectra as the one obtained for PSII membranes. A larger spectral coverage is recommended.

It was shown that the $S_2 \rightarrow S_3$ transition in PSIIcc of D1-D61A becomes multiphasic. To judge whether it is due to heterogeneity or not measurements in D_2O might help. In heterogenic centers the fast unaltered phase should show a similar kinetic isotope effect as the WT. The slow phase will most likely show a high value as well. To study the $S_3 \rightarrow S_0$ transition the flash spacing may need to be enlarged.

[Pokhrel et al., 2013] suggested that D1-K317 will form a salt bridge with D1-D61 upon chloride depletion. This hinders oxygen evolution. A neutral residue at D1-317 PSII restores the function again. First one could test this hypothesis also with a chloride depleted measurement on D1-D61A. This might produce another outcome: in Siegbahn's mechanism, he involves a chloride binding water as a transient proton transporter, that accepts the proton from the substrate first. If the anion helps to extract these protons then it might also store them without the deprotonated D61 present.

With the new setup it is now possible to study various genetically modified PSII. Many of the first sphere mutations did not alter the difference spectra, but they might modify the kintics allowing to trap certain intermediates. To study the proposed origin of the amide II band at 1544 cm^{-1} the H-bonding network around D1-E189 needs to be broken. A bulky residue at D1-D329 or the loop of CP43 might do so without disturbing the function of the cluster or Y_Z.

[18] Daylight Solutions, 2012

10 Summary

FTIR on PSII – Review

- An **overview of the FTIR spectra of the most relevant cofactors** during their redox chemistry is presented. Additionally, a list of genetically modified amino acids around the Mn cluster which have so far been studied by means of FTIR spectroscopy is added. The influence of these mutations on bands between 1100-1800 cm^{-1} is indicated.

A New Single-Frequency IR Experiment

- A new time resolved single-frequency setup was designed and constructed that employs a tuneable cw Quantum Cascade Laser for the detection of almost all reaction steps of PSII. It is **possible to detect** absorption changes smaller than $\mathbf{10^{-5}}$ **OD** units in the time domain **from 40 ns to seconds** of wavenumbers ranging from 1300 to 1650 cm^{-1}.

- The setup comprises a temperature control system, **automatic sample exchange and data recording**.

- A measurement protocol – adapted to the challenges of PSII – was established. It includes the **synchronization** of the S-states and an **excitation flash sequence that advances all PSII step-wise** in the catalytic cycle, followed by a high energy pulse. The latter **allows to determine** the flash induced **heat artefact and** to **correct** for it, reproducibly.

- A protocol to measure PSII core complexes was established together with Richard Debus from the University of California Riverside.

Quinones

- For the first time, **FTIR steady state difference spectroscopy, variable chlorophyll fluorescence and time resolved single-frequency IR spectroscopy were brought together** to study the quinone electron transfer in PSII. While it was unclear in the steady state spectra why the first flash transition showed much stronger signals, this study was able to directly explain this observation: 30% of Q_A^- does not become reoxidized.

- The **connectivity correction model of the variable chlorophyll fluorescence was verified** by comparing the SFIR data and the fluorescence as well as comparing PSII membranes and thylakoids. This method is the most important probe of photosynthetic function in intact organisms.

- The various kinetics of the electron transfer from Q_A^- to Q_B were investigated. These agreed well with the ones reported in the literature. Q_B^- is stable and does not become protonated before the arrival of the second electron.

- The **absorption of Q_B^- was assigned to 1482** cm^{-1} and the **absorption of** Q_BH_2 tentatively **to 1475** cm^{-1} were found. For the first time, it was possible to extract the **neutral quinone vibrations** in functional PSII at room temperature **at 1650 and 1670** cm^{-1}. The vibration at 1650 cm^{-1} might be mixed with the oxidized water bending mode.
- At pH 7.5 the quinone reactions are faster. This pH is closer to the stromal pH of chloroplasts. The average kinetics of 500 µs and 3 ms match the rate limiting steps of the Mn cluster of 1.6 ms.
- **No evidence for** a contribution of $\mathbf{Y_Z^{ox}}$ dynamics **at 1478** cm^{-1} were found. This rules out results obtained by [Guo et al., 2018].
- In intact and oxygen evolving PSII a **recombination spectrum** was obtained. This definitely includes signals from Q_A^-. The recombination partner is still unclear. The dynamics either point to $Y_Z^{\bullet ox}$ or Cytochrome b559. Bands at 1364 and 1399 cm^{-1} indicate a contribution from a possibly modified or premature Mn cluster.
- The **electron transfer rates** from Q_A^- **to PPBQ** in PSII membranes of spinach **and to FeCy** in PSII core complexes of *Synechocystis* were determined and the individual phases were assigned.

P_{680}^+ Decay and Fast Proton Release Phases

- At pH 6.2 **the reduced quinone band** at 1478 cm^{-1} **shows P_{680}^+ reduction kinetics** with 300 ns and 30 µs. A weak band at this wavenumber was reported also in the $P_{680}^+ - P_{680}$ spectra. Charge recombination between P_{680}^+ and Q_A^- was reported to be slower with 150 µs ([Christen and Renger, 1999]).
- **Bands at 1378-1384 and 1504** cm^{-1}, and more weakly at 1406-1410 cm^{-1}, **sense the 300 ns** $Y_Z^{\bullet ox}$ **stabilization** phase in $S_2 \rightarrow S_3$ and $S_3 \rightarrow S_0$. **At 1394** cm^{-1} **a broad band decays within 50 µs** in $S_2 \rightarrow S_3$ and 10-100 µs in $S_3 \rightarrow S_0$. These bands are not assigned yet, but are likely carboxylates, as they cannot be vibrations of P_{680}^+, which would sense both phases. Two subsequent rearrangements at distinct sites may be an explanation.
- **At pH 7.5 the amplitudes** of the 30 µs phase at 1400 and 1544 cm^{-1} and of both phases at 1478 cm^{-1} **become much smaller**. This might be related to a deprotonation event upon charge separation and subsequent reprotonations of a bulk-pH sensing (possibly protein-interior) group.
- A band around **1310** cm^{-1} **is a good marker for the** P_{680} **reactions**, of both the triplet and the oxidized form.
- An early 4 µs phase found in PSII membranes likely reflects triplet state quenching mainly in the light harvesting complexes.

The Band Position of the Redox Active Tyrosine Radical $Y_Z^{\bullet ox}$ at pH 7.5

- **Between 1510 and 1515** cm^{-1} **a band is formed upon charge separation in all S-state transitions** at pH 7.5. It is overlapping with a carboxylate/amide II band at 1509 cm^{-1} and influenced by a Q_B band at 1520 cm^{-1}.

- In $S_2 \rightarrow S_3$ and $S_3 \rightarrow S_0$, the **decay with Mn oxidation kinetics** could be clearly extracted. In $S_1 \rightarrow S_2$ a similar behavior was found, but the band position is obscured. In $S_0 \rightarrow S_1$ it decays only slightly.

- A **rise** with the 300 ns and 30 µs phase was **not found**. A residual **decay**, earlier than the specific Mn oxidation times, is present that origins from a neighboring band.

- Overall this behavior lets us **assign the band to** the CO stretching vibration of $\mathbf{Y_Z^{ox}}$. The band position is the same as in Mn depleted PSII ([Nakamura et al., 2014], pH 5.5-7.5). This indicates a neutral tyrosine strongly H-bonded to D1-H190.

- The band is not shifting with 100 µs in the $S_2 \rightarrow S_3$ transition, as was stated by [Sakamoto et al., 2017]. It decays with Mn oxidation.

Catalytic reaction cycle

- The **symmetric carboxylates stretching region between 1382 and 1406** cm^{-1} **senses all** kinetic **components of** the previously proposed **extended reaction cycle** of PSII water oxidation, which is characterized by alternating removal of electrons and protons from the catalytic site of water oxidation ([Klauss et al., 2015]).

- In $S_0 \rightarrow S_1$ only one phase of 78±4 µs was found at 20 °C and pH 6.2 in PSII membranes. At some bands a phase around 1 ms was present, but it most likely reflects quinone reactions that were masked by the stronger protein rearrangements of the other S-state transitions.

- At pH 7.5 the amplitude of the **30 µs phase** monitored at 1400 cm^{-1} in $S_3 \rightarrow S_0$ vanishes, while the slower **lag phase** only becomes faster. In PSIIcc at pH 6.0, only the 30 µs phase is diminished at 1400 cm^{-1}. This observation points to two subsequent processes, which **involve two distinct sites**.

- PSII core complexes from *Synechocystis* sp. PCC 6803 and PSII membranes from spinach showed overall similar kinetics of the reaction cycle. The spectra in the symmetric carboxylate region differs slightly in $S_3 \rightarrow S_0$ and possibly in $S_0 \rightarrow S_1$. The amplitude of the fast 30 µs phase is smaller at 1400 cm^{-1} in PSIIcc.

- The study of the **genetically introduced alanine at the position D1-D61 did not alter the kinetics nor the amplitude of the 30 µs phase in** $S_2 \rightarrow S_3$ **and** $S_3 \rightarrow S_0$. This is surprising, as many studies suggested a deprotonation event either of water W1, H-bonded to D61, or the proton release via a pathway to the bulk including D61. However, this observation only states that the carboxylate residuum is not crucial for this step in the reaction. A proton may still be conducted along the altered H-bonding network.

- The **D61A slowed the Mn oxidation in all observed transitions** and modified the changes of the carboxylates: the oxidation in $S_1 \rightarrow S_2$ is slowed down. In $S_2 \rightarrow S_3$ it seemingly becomes biphasic.

- In $S_3 \rightarrow S_0$ the so called "lag phase" was kinetically not altered by D61A but halved in the response by the carboxylate at 1400 cm^{-1}. The Mn oxidation was slowed down by more than a factor of 30.

- Overall, the analysis of the quinone dynamics at pH 7.5 – closer to the stroma pH – gave decay time of about 0.5 and 3.5 ms for bound and unbound Q_B, respectively. An amplitude ratio was found to be 0.65:0.15, taken from the measurements of thylakoids at pH 6.2. This results in an average reaction time for processing of about 4 ms four photons in the native environment. The analysis of the symmetric carboxylate region at 6.2 – closer to the lumen pH – suggests a reaction time for a complete catalytic cycle of $60 + 240 + 1600 + 80 \approx 2$ ms. The **rate limiting reaction of PSII is therefore not the water oxidation but the directed transfer of the electrons**.

10.1 Outlook

- The new time resolved IR setup facilitated new insights and opens up a variety of new avenues in PSII research. Fast automatized measurements and a high signal to noise ratio allow to systematically study various bands sensing the different reaction steps separately.
- Many further improvements were suggested (section 5.4). The most crucial one is to overcome the need to realign after changing the wavenumber.
- New Quantum Cascade Laser Diodes were suggested. The spectral ranges of the protonated carboxylates around 1750 cm^{-1}, OH vibrations at high wavenumbers and the region of tyrosines and histidines might be interesting next targets.
- The bands, sensing the 300 ns and 30 µs phase, should be studied systematically to get access to their origin. A series of measurements at various pH values could be used to determine the (apparent) pK_a of these groups.
- The strength of the new setup is the measurement of carboxylate groups that are involved in the proton release pathways. A reinvestigation of genetically modified PSII will yield insights of possible transient changes not visible in the steady state FTIR spectra.
- The study of D1-D61A presented here, is only a beginning. Next, the kinetic isotope effects upon H_2O – D_2O exchange should be determined and the biphasic behavior in $S_2 \rightarrow S_3$ investigated.
- Because the new setup allows to study various processes within PSII in a short time, the effect of natural variations can easily be accessed. Protein isoforms but also PSII from various organisms can be studied.
- Additionally to the measurements of purified PSII, the high sensitivity and high IR power allows to measure thicker samples and also the time resolved interaction of various photosynthetic proteins. A very next step may be to track the Q_BH_2 oxidation reaction at the cytochrome, induced by activating PSII. This type of measurement may now be possible in thylakoids, cells and maybe even leaves.

List of Figures

Bibliography

[A. Maxime, 2012] A. Maxime, R. v. G. (2012). *Time-Resolved FTIR Difference Spectroscopy Reveals the Structure and Dynamics of Carotenoid and Chlorophyll Triplets in Photosynthetic Light-Harvesting Complexes*. Infrared Spectroscopy. IntechOpen.

[Andersen and Ogilby, 2002] Andersen, L. K. and Ogilby, P. R. (2002). A nanosecond near-infrared step-scan fourier transform absorption spectrometer: Monitoring singlet oxygen, organic molecule triplet states, and associated thermal effects upon pulsed-laser irradiation of a photosensitizer. *Review of Scientific Instruments*, 73(12):4313–4325.

[Anderson et al., 2012] Anderson, J. M., Horton, P., Kim, E.-H., and Chow, W. S. (2012). Towards elucidation of dynamic structural changes of plant thylakoid architecture. *Philosophical Transactions of the Royal Society B: Biological Sciences*, 367(1608):3515–3524.

[Antal et al., 2013] Antal, T. K., Kovalenko, I. B., Rubin, A. B., and Tyystjarvi, E. (2013). Photosynthesis-related quantities for education and modeling. *Photosynth Res*, 117(1-3):1–30.

[Ashizawa and Noguchi, 2014] Ashizawa, R. and Noguchi, T. (2014). Effects of hydrogen bonding interactions on the redox potential and molecular vibrations of plastoquinone as studied using density functional theory calculations. *Physical Chemistry Chemical Physics*, 16(24):11864–11876.

[Askerka et al., 2017] Askerka, M., Brudvig, G. W., and Batista, V. S. (2017). The o2-evolving complex of photosystem ii: Recent insights from quantum mechanics/molecular mechanics (qm/mm), extended x-ray absorption fine structure (exafs), and femtosecond x-ray crystallography data. *Accounts of Chemical Research*, 50(1):41–48.

[Banerjee et al., 2018a] Banerjee, G., Ghosh, I., Kim, C. J., Debus, R. J., and Brudvig, G. W. (2018a). Substitution of the d1-asn(87) site in photosystem ii of cyanobacteria mimics the chloride-binding characteristics of spinach photosystem ii. *Journal of Biological Chemistry*, 293(7):2487–2497.

[Banerjee et al., 2018b] Banerjee, G., Ghosh, I., Kim, C. J., Debus, R. J., and Brudvig, G. W. (2018b). Substitution of the d1-asn(87) site in photosystem ii of cyanobacteria mimics the chloride-binding characteristics of spinach photosystem ii. *Journal of Biological Chemistry*, 293(7):2487–2497.

[Bao and Burnap, 2015] Bao, H. and Burnap, R. L. (2015). Structural rearrangements preceding dioxygen formation by the water oxidation complex of photosystem ii. *Proceedings of the National Academy of Sciences of the United States of America*, 112(45):E6139–E6147.

[Barth, 2000] Barth, A. (2000). The infrared absorption of amino acid side chains. *Progress in Biophysics and Molecular Biology*, 74(3):141–173.

[Barth, 2007] Barth, A. (2007). Infrared spectroscopy of proteins. *Biochimica Et Biophysica Acta-Bioenergetics*, 1767(9):1073–1101.

[Barth and Zscherp, 2002] Barth, A. and Zscherp, C. (2002). What vibrations tell us about proteins. *Quarterly Reviews of Biophysics*, 35(4):369–430.

[Berthold et al., 1981] Berthold, D. A., Babcock, G. T., and Yocum, C. F. (1981). A highly resolved, oxygen-evolving photosystem-ii preparation from spinach thylakoid membranes - electron-paramagnetic-res and electron-transport properties. *Febs Letters*, 134(2):231–234.

[Berthomieu and Hienerwadel, 2001] Berthomieu, C. and Hienerwadel, R. (2001). Iron coordination in photosystem ii: interaction between bicarbonate and the qb pocket studied by fourier transform infrared spectroscopy. *Biochemistry*, 40(13):4044–4052.

[Berthomieu and Hienerwadel, 2005] Berthomieu, C. and Hienerwadel, R. (2005). Vibrational spectroscopy to study the properties of redox-active tyrosines in photosystem ii and other proteins. *Biochimica et Biophysica Acta*, 1707(1):51–66.

[Berthomieu and Hienerwadel, 2009] Berthomieu, C. and Hienerwadel, R. (2009). Fourier transform infrared (ftir) spectroscopy. *Photosynthesis Research*, 101(2):157–170.

[Berthomieu et al., 1998] Berthomieu, C., Hienerwadel, R., Boussac, A., Breton, J., and Diner, B. A. (1998). Hydrogen bonding of redox-active tyrosine z of photosystem ii probed by ftir difference spectroscopy. *Biochemistry*, 37(30):10547–10554.

[Berthomieu et al., 1990] Berthomieu, C., Nabedryk, E., Mantele, W., and Breton, J. (1990). Characterization by ftir spectroscopy of the photoreduction of the primary quinone acceptor qa in photosystem-ii. *Febs Letters*, 269(2):363–367.

[Boussac et al., 2012] Boussac, A., Ishida, N., Sugiura, M., and Rappaport, F. (2012). Probing the role of chloride in photosystem ii from thermosynechococcus elongatus by exchanging chloride for iodide. *Biochimica et Biophysica Acta (BBA) - Bioenergetics*, 1817(5):802–810.

[Brinkert et al., 2016] Brinkert, K., De Causmaecker, S., Krieger-Liszkay, A., Fantuzzi, A., and Rutherford, A. W. (2016). Bicarbonate-induced redox tuning in photosystem ii for regulation and protection. *Proceedings of the National Academy of Sciences*, 113(43):12144–12149.

[Brünig, 2013] Brünig, F. (2013). *Die Photosystem II Rekombinationsfluoreszenz unter Einfluss von DMSO*. Thesis.

[Burie et al., 1995] Burie, J. R., Boussac, A., Boullais, C., Berger, G., Mattioli, T., Mioskowski, C., Nabedryk, E., and Breton, J. (1995). Ftir spectroscopy of uv-generated quinone radicals - evidence for an intramolecular hydrogen-atom transfer in ubiquinone, naphthoquinone, and plastoquinone. *Journal of Physical Chemistry*, 99(12):4059–4070.

[Chen et al., 2000] Chen, H. A., Pfuhl, M., McAlister, M. S. B., and Driscoll, P. C. (2000). Determination of pka values of carboxyl groups in the n-terminal domain of rat cd2: Anomalous pka of a glutamate on the ligand-binding surface. *Biochemistry*, 39(23):6814–6824.

[Chernev et al., 2011] Chernev, P., Zaharieva, I., Dau, H., and Haumann, M. (2011). Carboxylate shifts steer inter-quinone electron transfer in photosynthesis. *J Biol Chem*, 286(7):5368–5374.

[Chernev et al., 2013] Chernev, P., Zaharieva, I., Dau, H., and Haumann, M. (2013). *Coordination changes of carboxyl ligands at the QAFeQB triad in photosynthetic reaction centers studied by density-function theory*, pages 95–101. Springer, Heidelberg.

[Christen et al., 1998] Christen, G., Reifarth, F., and Renger, G. (1998). On the origin of the '35-µs kinetics' of p680+ reduction in photosystem ii with an intact water oxidising complex. *FEBS Letters*, 429(1):49–52.

[Christen and Renger, 1999] Christen, G. and Renger, G. (1999). The role of hydrogen bonds for the multiphasic p680(+)* reduction by yz in photosystem ii with intact oxyen evolution capacity. analysis of kinetic h/d isotope exchange effects. *Biochemistry*, 38(7):2068–77.

[Christen et al., 1999] Christen, G., Seeliger, A., and Renger, G. (1999). P680+• reduction kinetics and redox transition probability of the water oxidizing complex as a function of ph and h d isotope exchange in spinach thylakoids. *Biochemistry*, 38(19):6082–6092.

[Chu, 2013] Chu, H.-A. (2013). Fourier transform infrared difference spectroscopy for studying the molecular mechanism of photosynthetic water oxidation. *Frontiers in Plant Science*, 4(146).

[Chu et al., 2001] Chu, H. A., Debus, R. J., and Babcock, G. T. (2001). D1-asp170 is structurally coupled to the oxygen evolving complex in photosystem ii as revealed by light-induced fourier transform infrared difference spectroscopy. *Biochemistry*, 40(7):2314–2316.

[Chu et al., 2004] Chu, H. A., Hillier, W., and Debus, R. J. (2004). Evidence that the c-terminus of the d1 polypeptide of photosystem ii is ligated to the manganese ion that undergoes oxidation during the s1 to s2 transition: an isotope-edited ftir study. *Biochemistry*, 43(11):3152–66.

[Daldrop et al., 2018] Daldrop, J. O., Saita, M., Heyden, M., Lorenz-Fonfria, V. A., Heberle, J., and Netz, R. R. (2018). Orientation of non-spherical protonated water clusters revealed by infrared absorption dichroism. *Nature Communications*, 9(1):311.

[Danielsson et al., 2004] Danielsson, R., Albertsson, P.-k., Mamedov, F., and Styring, S. (2004). Quantification of photosystem i and ii in different parts of the thylakoid membrane from spinach. *Biochimica et Biophysica Acta (BBA) - Bioenergetics*, 1608(1):53–61.

[Dau, 1994] Dau, H. (1994). Molecular mechanisms and quantitative models of variable photosystem ii fluorescence. *Photochemistry and Photobiology*, 60(1):1–23.

[Dau and Zaharieva, 2009] Dau, H. and Zaharieva, I. (2009). Principles, efficiency, and blueprint character of solar-energy conversion in photosynthetic water oxidation. *Accounts of Chemical Research*, 42(12):1861–1870.

[de Wijn et al., 2001] de Wijn, R., Schrama, T., and van Gorkom, H. J. (2001). Secondary stabilization reactions and proton-coupled electron transport in photosystem ii investigated by electroluminescence and fluorescence spectroscopy. *Biochemistry*, 40(19):5821–5834.

[de Wijn and van Gorkom, 2001] de Wijn, R. and van Gorkom, H. J. (2001). Kinetics of electron transfer from qa to qb in photosystem ii. *Biochemistry*, 40(39):11912–11922.

[Debus, 2014] Debus, R. J. (2014). Evidence from ftir difference spectroscopy that d1-asp61 influences the water reactions of the oxygen-evolving mn4cao5 cluster of photosystem ii. *Biochemistry*, 53(18):2941–2955.

[Debus, 2015] Debus, R. J. (2015). Ftir studies of metal ligands, networks of hydrogen bonds, and water molecules near the active site mn4cao5 cluster in photosystem ii. *Biochimica et Biophysica Acta (BBA) - Bioenergetics*, 1847(1):19–34.

[Debus, 2016] Debus, R. J. (2016). Identifying carboxylate ligand vibrational modes in photosystem ii with qm/mm methods. *Proceedings of the National Academy of Sciences*, 113(45):12613.

[Debus et al., 2005] Debus, R. J., Strickler, M. A., Walker, L. M., and Hillier, W. (2005). No evidence from ftir difference spectroscopy that aspartate-170 of the d1 polypeptide ligates a manganese ion that undergoes oxidation during the s0 to s1, s1 to s2, or s2 to s3 transitions in photosystem ii. *Biochemistry*, 44(5):1367–74.

[Demmig and Winter, 1986] Demmig, B. and Winter, K. (1986). Sodium, potassium, chloride and proline concentrations of chloroplasts isolated from a halophyte, mesembryanthemum crystallinum l. *Planta*, 168(3):421–426.

[Dilbeck et al., 2012] Dilbeck, P. L., Hwang, H. J., Zaharieva, I., Gerencser, L., Dau, H., and Burnap, R. L. (2012). The mutation d1-d61n in synechocystis sp. pcc 6803 allows the observation of ph-sensitive intermediates in the formation and release of o2 from photosystem ii. *Biochemistry*, 51(6):1079–1091.

[Diner and Rappaport, 2002] Diner, B. A. and Rappaport, F. (2002). Structure, dynamics, and energetics of the primary photochemistry of photosystem ii of oxygenic photosynthesis. *Annu Rev Plant Biol*, 53:551–80.

[Eckert and Renger, 1988] Eckert, H. J. and Renger, G. (1988). Temperature dependence of p680+ reduction in o2-evolving ps ii membrane fragments at different redox states si of the water oxidizing system. *FEBS Letters*, 236(2):425–431.

[Gerencser and Dau, 2010] Gerencser, L. and Dau, H. (2010). Water oxidation by photosystem ii: H2o-d2o exchange and the influence of ph support formation of an intermediate by removal of a proton before dioxygen creation. *Biochemistry*, 49(47):10098–10106.

[Giuffrida et al., 2017] Giuffrida, S., Cottone, G., and Cordone, L. (2017). The water association band as a marker of hydrogen bonds in trehalose amorphous matrices. *Physical Chemistry Chemical Physics*, 19(6):4251–4265.

[Grabolle, 2005] Grabolle, M. (2005). Die donorseite des photosystems ii: Rekombinationsfluoreszenz- und röntgenabsorptionsstudien (thesis). *Fachbereich Physik, Freie Univ. Berlin, http://www.diss.fu-berlin.de/2005/174/.*

[Görlin, 2012] Görlin, M. (2012). *"Light-induced and time-resolved FTIR difference spectroscopy of Photosystem II"*. Thesis.

[Grundmeier and Dau, 2012] Grundmeier, A. and Dau, H. (2012). Structural models of the manganese complex of photosystem ii and mechanistic implications. *Biochimica et Biophysica Acta*, 1817(1):88–105.

[Guerra et al., 2018] Guerra, F., Siemers, M., Mielack, C., and Bondar, A.-N. (2018). Dynamics of long-distance hydrogen-bond networks in photosystem ii. *The Journal of Physical Chemistry B*, 122(17):4625–4641.

[Guo et al., 2018] Guo, Z. J., He, J. Y., and Barry, B. A. (2018). Calcium, conformational selection, and redox-active tyrosine yz in the photosynthetic oxygen-evolving cluster. *Proceedings of the National Academy of Sciences of the United States of America*, 115(22):5658–5663.

[Guskov et al., 2009] Guskov, A., Kern, J., Gabdulkhakov, A., Broser, M., Zouni, A., and Saenger, W. (2009). Cyanobacterial photosystem ii at 2.9-Å resolution and the role of quinones, lipids, channels and chloride. *Nature Structural & Molecular Biology*, 16(3):334–342.

[Haumann and Junge, 1994a] Haumann, M. and Junge, W. (1994a). Extent and rate of proton release by photosynthetic water oxidation in thylakoids: electrostatic relaxation versus chemical production. *Biochemistry*, 33(4):864–72.

[Haumann and Junge, 1994b] Haumann, M. and Junge, W. (1994b). The rates of proton uptake and electron transfer at the reducing side of photosystem ii in thylakoids. *FEBS Lett*, 347(1):45–50.

[Haumann and Junge, 1999] Haumann, M. and Junge, W. (1999). Evidence for impaired hydrogen-bonding of tyrosine yz in calcium-depleted photosystem ii. *Biochimica et Biophysica Acta*, 1411(1):121–33.

[Haumann et al., 1999] Haumann, M., Mulkidjanian, A., and Junge, W. (1999). Tyrosine-z in oxygen-evolving photosystem ii: A hydrogen-bonded tyrosinate. *Biochemistry*, 38(4):1258–1267.

[Hellwig et al., 1999] Hellwig, P., Mogi, T., Tomson, F. L., Gennis, R. B., Iwata, J., Miyoshi, H., and Mantele, W. (1999). Vibrational modes of ubiquinone in cytochrome bo(3) from escherichia coli identified by fourier transform infrared difference spectroscopy and specific c-13 labeling. *Biochemistry*, 38(44):14683–14689.

[Hienerwadel and Berthomieu, 1995] Hienerwadel, R. and Berthomieu, C. (1995). Bicarbonate binding to the non-heme iron of photosystem ii, investigated by fourier transform infrared difference spectroscopy and 13c-labeled bicarbonate. *Biochemistry*, 34(50):16288–16297.

[Hienerwadel et al., 1996] Hienerwadel, R., Boussac, A., Breton, J., and Berthomieu, C. (1996). Fourier transform infrared difference study of tyrosined oxidation and plastoquinone qa reduction in photosystem ii. *Biochemistry*, 35(48):15447–15460.

[Ho, 2012] Ho, F. M. (2012). Structural and mechanistic investigations of photosystem ii through computational methods. *Biochim Biophys Acta*, 1817(1):106–20.

[Hochmal et al., 2015] Hochmal, A. K., Schulze, S., Trompelt, K., and Hippler, M. (2015). Calcium-dependent regulation of photosynthesis. *Biochimica et Biophysica Acta (BBA) - Bioenergetics*, 1847(9):993–1003.

[Hundelt et al., 1998a] Hundelt, M., Hays, A. M., Debus, R. J., and Junge, W. (1998a). Oxygenic photosystem ii: the mutation d1-d61n in synechocystis sp. pcc 6803 retards s-state transitions without affecting electron transfer from yz to p680+. *Biochemistry*, 37(41):14450–6.

[Hundelt et al., 1998b] Hundelt, M., Hays, A.-M. A., Debus, R. J., and Junge, W. (1998b). *The Mutation D1-D61N in PS II of Synechocystis: Retardation of et from Oec→YZOXand No Effect on YZ→P680+*, pages 1387–1390. Springer Netherlands, Dordrecht.

[Ifuku and Noguchi, 2016] Ifuku, K. and Noguchi, T. (2016). Structural coupling of extrinsic proteins with the oxygen-evolving center in photosystem ii. *Front Plant Sci*, 7:84.

[Iizasa et al., 2010] Iizasa, M., Suzuki, H., and Noguchi, T. (2010). Orientations of carboxylate groups coupled to the mn cluster in the photosynthetic oxygen-evolving center as studied by polarized atr-ftir spectroscopy. *Biochemistry*, 49(14):3074–3082.

[Ishikita et al., 2007] Ishikita, H., Galstyan, A., and Knapp, E.-W. (2007). Redox potential of the non-heme iron complex in bacterial photosynthetic reaction center. *Biochimica et Biophysica Acta (BBA) - Bioenergetics*, 1767(11):1300–1309.

[Junge et al., 2002] Junge, W., Haumann, M., Ahlbrink, R., Mulkidjanian, A., and Clausen, J. (2002). Electrostatics and proton transfer in photosynthetic water oxidation. *Philosophical Transactions of the Royal Society B-Biological Sciences*, 357(1426):1407 – 1418.

[Kato et al., 2016] Kato, Y., Ishii, R., and Noguchi, T. (2016). Comparative analysis of the interaction of the primary quinone qa in intact and mn-depleted photosystem ii membranes using light-induced atr-ftir spectroscopy. *Biochemistry*, 55(46):6355–6358.

[Kato and Noguchi, 2016] Kato, Y. and Noguchi, T. (2016). Ftir spectroelectrochemistry combined with a light-induced difference technique: Application to the iron-quinone electron acceptor in photosystem ii. *Biomedical Spectroscopy and Imaging*, 5(3):269–282.

[Kern et al., 2018] Kern, J., Chatterjee, R., Young, I. D., Fuller, F. D., Lassalle, L., Ibrahim, M., Gul, S., Fransson, T., Brewster, A. S., Alonso-Mori, R., Hussein, R., Zhang, M., Douthit, L., de Lichtenberg, C., Cheah, M. H., Shevela, D., Wersig, J., Seuffert, I., Sokaras, D., Pastor, E., Weninger, C., Kroll, T., Sierra, R. G., Aller, P., Butryn, A., Orville, A. M., Liang, M., Batyuk, A., Koglin, J. E., Carbajo, S., Boutet, S., Moriarty, N. W., Holton, J. M., Dobbek, H., Adams, P. D., Bergmann, U., Sauter, N. K., Zouni, A., Messinger, J., Yano, J., and Yachandra, V. K. (2018). Structures of the intermediates of kok's photosynthetic water oxidation clock. *Nature*, 563(7731):421–425.

[Kim et al., 2018] Kim, C. J., Bao, H., Burnap, R. L., and Debus, R. J. (2018). Impact of d1-v185 on the water molecules that facilitate o2 formation by the catalytic mn4cao5 cluster in photosystem ii. *Biochemistry*.

[Kimura et al., 2005a] Kimura, Y., Mizusawa, N., Ishii, A., Nakazawa, S., and Ono, T. A. (2005a). Changes in structural and functional properties of oxygen-evolving complex induced by replacement of d1-glutamate 189 with glutamine in photosystem ii: ligation of glutamate 189 carboxylate to the manganese cluster. *J Biol Chem*, 280(45):37895–900.

[Kimura et al., 2005b] Kimura, Y., Mizusawa, N., Ishii, A., and Ono, T. (2005b). Ftir detection of structural changes in a histidine ligand during s-state cycling of photosynthetic oxygen-evolving complex. *Biochemistry*, 44(49):16072–16078.

[Kimura et al., 2003] Kimura, Y., Mizusawa, N., Ishii, A., Yamanari, T., and Ono, T. A. (2003). Changes of low-frequency vibrational modes induced by universal n-15- and c-15-isotope labeling in s-2/s-1 ftir difference spectrum of oxygen-evolving complex. *Biochemistry*, 42(45):13170–13177.

[Klauss et al., 2012a] Klauss, A., Haumann, M., and Dau, H. (2012a). Alternating electron and proton transfer steps in photosynthetic water oxidation. *Proceedings of the National Academy of Sciences of the United States of America*, 109(40):16035–40.

[Klauss et al., 2015] Klauss, A., Haumann, M., and Dau, H. (2015). Seven steps of alternating electron and proton transfer in photosystem ii water oxidation traced by time-resolved photothermal beam deflection at improved sensitivity. *J Phys Chem B*, 119(6):2677–89.

[Klauss et al., 2012b] Klauss, A., Sikora, T., Suss, B., and Dau, H. (2012b). Fast structural changes (200-900ns) may prepare the photosynthetic manganese complex for oxidation by the adjacent tyrosine radical. *Biochim Biophys Acta*, 1817:1196–1207.

[Krejtschi et al., 2008] Krejtschi, C., Huang, R., Keiderling, T. A., and Hauser, K. (2008). Time-resolved temperature-jump infrared spectroscopy of peptides with well-defined secondary structure: A trpzip β-hairpin variant as an example. *Vibrational Spectroscopy*, 48(1):1–7.

[Krivanek et al., 2008] Krivanek, R., Dau, H., and Haumann, M. (2008). Enthalpy changes during photosynthetic water oxidation tracked by time-resolved calorimetry using a photothermal beam deflection technique. *Biophysical Journal*, 94(5):1890–903.

[Krivanek et al., 2007] Krivanek, R., Kern, J., Zouni, A., Dau, H., and Haumann, M. (2007). Spare quinones in the qb cavity of crystallized photosystem ii from thermosynechococcus elongatus. *Biochimica et Biophysica Acta*, 1767(6):520–7.

[Kurreck et al., 1995] Kurreck, J., Seeliger, A. G., Reifarth, F., Karge, M., and Renger, G. (1995). Reconstitution of the endogenous plastoquinone pool in photosystem ii (ps ii) membrane fragments, inside-out-vesicles, and ps ii core complexes from spinach. *Biochemistry*, 34(48):15721–31.

[Libnau et al., 1994] Libnau, F. O., Kvalheim, O. M., Christy, A. A., and Toft, J. (1994). Spectra of water in the near- and mid-infrared region. *Vibrational Spectroscopy*, 7(3):243–254.

[Linke et al., 2008] Linke, M., Lauer, A., von Haimberger, T., Zacarias, A., and Heyne, K. (2008). Three-dimensional orientation of the qy electronic transition dipole moment within the chlorophyll a molecule determined by femtosecond polarization resolved vis pump-ir probe spectroscopy. *J Am Chem Soc*, 130(45):14904–5.

[Mathis and Haveman, 1977] Mathis, P. and Haveman, J. (1977). Analysis of absorption changes in uv related to charge-accumulating electron carriers in photosystem-ii of chloroplasts. *Biochimica Et Biophysica Acta*, 461(2):167–181.

[Metz et al., 1989] Metz, J. G., Nixon, P. J., Rogner, M., Brudvig, G. W., and Diner, B. A. (1989). Directed alteration of the d1 polypeptide of photosystem ii: evidence that tyrosine-161 is the redox component, z, connecting the oxygen-evolving complex to the primary electron donor, p680. *Biochemistry*, 28(17):6960–6969.

[Mezzetti et al., 2011] Mezzetti, A., Blanchet, L., de Juan, A., Leibl, W., and Ruckebusch, C. (2011). Ubiquinol formation in isolated photosynthetic reaction centres monitored by time-resolved differential ftir in combination with 2d correlation spectroscopy and multivariate curve resolution. *Analytical and Bioanalytical Chemistry*, 399(6):1999–2014.

[Mezzetti and Leibl, 2005] Mezzetti, A. and Leibl, W. (2005). Investigation of ubiquinol formation in isolated photosynthetic reaction centers by rapid-scan fourier transform ir spectroscopy. *European Biophysics Journal with Biophysics Letters*, 34(7):921–936.

[Mezzetti and Leibl, 2017] Mezzetti, A. and Leibl, W. (2017). Time-resolved infrared spectroscopy in the study of photosynthetic systems. *Photosynthesis Research*, 131(2):121–144.

[Mezzetti et al., 2003] Mezzetti, A., Leibl, W., Breton, J., and Nabedryk, E. (2003). Photoreduction of the quinone pool in the bacterial photosynthetic membrane: identification of infrared marker bands for quinol formation. *Febs Letters*, 537(1-3):161–165.

[Miller and Brudvig, 1991] Miller, A. F. and Brudvig, G. W. (1991). A guide to electron paramagnetic resonance spectroscopy of photosystem ii membranes. *Biochimica et Biophysica Acta*, 1056(1):1–18.

[Montoya et al., 1994] Montoya, G., Cases, R., Rodriguez, R., Aured, M., and Picorel, R. (1994). Detergent-induced reversible denaturation of the photosystem-ii reaction-center - implications for pigment-protein interactions. *Biochemistry*, 33(39):11798–11804.

[Muh et al., 2012] Muh, F., Glockner, C., Hellmich, J., and Zouni, A. (2012). Light-induced quinone reduction in photosystem ii. *Biochim Biophys Acta*, 1817(1):44–65.

[Nabedryk et al., 1990] Nabedryk, E., Leonhard, M., Maentele, W., and Breton, J. (1990). Fourier transform infrared difference spectroscopy shows no evidence for an enolization of chlorophyll a upon cation formation either in vitro or during p700 photooxidation. *Biochemistry*, 29(13):3242–3247.

[Nagao et al., 2018] Nagao, R., Kitazaki, S., and Noguchi, T. (2018). Evaluation of photosynthetic activities in thylakoid membranes by means of fourier transform infrared spectroscopy. *Biochimica et Biophysica Acta (BBA) - Bioenergetics*, 1859(2):129–136.

[Nagao et al., 2017a] Nagao, R., Ueoka-Nakanishi, H., and Noguchi, T. (2017a). D1-asn-298 in photosystem ii is involved in a hydrogen-bond network near the redox-active tyrosine yz for proton exit during water oxidation. *Journal of Biological Chemistry*.

[Nagao et al., 2017b] Nagao, R., Yamaguchi, M., Nakamura, S., Ueoka-Nakanishi, H., and Noguchi, T. (2017b). Genetically introduced hydrogen bond interactions reveal an asymmetric charge distribution on the radical cation of the special-pair chlorophyll p680. *Journal of Biological Chemistry*.

[Nakamura et al., 2014] Nakamura, S., Nagao, R., Takahashi, R., and Noguchi, T. (2014). Fourier transform infrared detection of a polarizable proton trapped between photooxidized tyrosine yz and a coupled histidine in photosystem ii: Relevance to the proton transfer mechanism of water oxidation. *Biochemistry*, 53(19):3131–3144.

[Nakamura and Noguchi, 2016] Nakamura, S. and Noguchi, T. (2016). Quantum mechanics/molecular mechanics simulation of the ligand vibrations of the water-oxidizing mn4cao5 cluster in photosystem ii. *Proceedings of the National Academy of Sciences*, 113(45):12727.

[Nakamura and Noguchi, 2017] Nakamura, S. and Noguchi, T. (2017). Infrared determination of the protonation state of a key histidine residue in the photosynthetic water oxidizing center. *Journal of the American Chemical Society*, 139(27):9364–9375.

[Nakamura et al., 2016] Nakamura, S., Ota, K., Shibuya, Y., and Noguchi, T. (2016). Role of a water network around the mn4cao5 cluster in photosynthetic water oxidation: A fourier transform infrared spectroscopy and quantum mechanics/molecular mechanics calculation study. *Biochemistry*, 55(3):597–607.

[Narzi et al., 2014] Narzi, D., Bovi, D., and Guidoni, L. (2014). Pathway for mn-cluster oxidation by tyrosine-z in the s-2 state of photosystem ii. *Proceedings of the National Academy of Sciences of the United States of America*, 111(24):8723–8728.

[Nelson and Yocum, 2006] Nelson, N. and Yocum, C. F. (2006). Structure and function of photosystems i and ii. *Annual Review of Plant Biology*, 57:521–567.

[Nilsson et al., 2014] Nilsson, H., Rappaport, F., Boussac, A., and Messinger, J. (2014). Substrate-water exchange in photosystem ii is arrested before dioxygen formation. *Nat Commun*, 5:4305.

[Noguchi, 2008] Noguchi, T. (2008). Fourier transform infrared analysis of the photosynthetic oxygen-evolving center. *Coordination Chemistry Reviews*, 252(3-4):336–346.

[Noguchi, 2015] Noguchi, T. (2015). Fourier transform infrared difference and time-resolved infrared detection of the electron and proton transfer dynamics in photosynthetic water oxidation. *Biochimica et Biophysica Acta (BBA) - Bioenergetics*, 1847(1):35–45.

[Noguchi et al., 1993] Noguchi, T., Inoue, Y., and Satoh, K. (1993). Ft-ir studies on the triplet state of p680 in the photosystem ii reaction center: Triplet equilibrium within a chlorophyll dimer. *Biochemistry*, 32(28):7186–7195.

[Noguchi et al., 1999] Noguchi, T., Inoue, Y., and Tang, X.-S. (1999). Structure of a histidine ligand in the photosynthetic oxygen-evolving complex as studied by light-induced fourier transform infrared difference spectroscopy. *Biochemistry*, 38(31):10187–10195.

[Noguchi et al., 1994] Noguchi, T., Mitsuka, T., and Inoue, Y. (1994). Fourier transform infrared spectrum of the radical cation of β-carotene photoinduced in photosystem ii. *FEBS Letters*, 356(2-3):179–182.

[Noguchi and Sugiura, 2003] Noguchi, T. and Sugiura, M. (2003). Analysis of flash-induced ftir difference spectra of the s-state cycle in the photosynthetic water-oxidizing complex by uniform n-15 and c-13 isotope labeling. *Biochemistry*, 42(20):6035–6042.

[Noguchi et al., 2012] Noguchi, T., Suzuki, H., Tsuno, M., Sugiura, M., and Kato, C. (2012). Time-resolved infrared detection of the proton and protein dynamics during photosynthetic oxygen evolution. *Biochemistry*, 51(15):3205–14.

[Noguchi et al., 1998] Noguchi, T., Tomo, T., and Inoue, Y. (1998). Fourier transform infrared study of the cation radical of p680 in the photosystem ii reaction center: Evidence for charge delocalization on the chlorophyll dimer. *Biochemistry*, 37(39):13614–13625.

[Noguchi et al., 2001] Noguchi, T., Tomo, T., and Kato, C. (2001). Triplet formation on a monomeric chlorophyll in the photosystem ii reaction center as studied by time-resolved infrared spectroscopy. *Biochemistry*, 40(7):2176–2185.

[Okubo and Noguchi, 2006] Okubo, T. and Noguchi, T. (2006). Selective detection of the structural changes upon photoreactions of several redox cofactors in photosystem ii by means of light-induced atr-ftir difference spectroscopy. *Spectrochim Acta A Mol Biomol Spectrosc*.

[Okubo and Noguchi, 2007] Okubo, T. and Noguchi, T. (2007). Selective detection of the structural changes upon photoreactions of several redox cofactors in photosystem ii by means of light-induced atr-ftir difference spectroscopy. *Spectrochimica Acta Part a-Molecular and Biomolecular Spectroscopy*, 66(4-5):863–868.

[Okubo et al., 2007] Okubo, T., Tomo, T., Sugiura, M., and Noguchi, T. (2007). Perturbation of the structure of p680 and the charge distribution on its radical cation in isolated reaction center complexes of photosystem ii as revealed by fourier transform infrared spectroscopy. *Biochemistry*, 46(14):4390–4397.

[Onoda et al., 2000] Onoda, K., Mino, H., Inoue, Y., and Noguchi, T. (2000). An ftir study on the structure of the oxygen-evolving mn-cluster of photosystem ii in different spin forms of the s2 state. *Photosynthesis Research*, 63(1):47–57.

[Pantazis, 2018] Pantazis, D. A. (2018). Missing pieces in the puzzle of biological water oxidation. *ACS Catalysis*, 8(10):9477–9507.

[Petrouleas and Crofts, 2005] Petrouleas, V. and Crofts, A. (2005). *The Iron-Quinone Acceptor Complex*, volume 22 of *Advances in Photosynthesis and Respiration*, pages 177–206. Springer Netherlands.

[Petrouleas and Diner, 1987] Petrouleas, V. and Diner, B. A. (1987). Light-induced oxidation of the acceptor-side fe(ii) of photosystem ii by exogenous quinones acting through the qb binding site. i. quinones, kinetics and ph-dependence. *Biochimica et Biophysica Acta (BBA) - Bioenergetics*, 893(2):126–137.

[Pham and Messinger, 2016] Pham, L. V. and Messinger, J. (2016). Probing s-state advancements and recombination pathways in photosystem ii with a global fit program for flash-induced oxygen evolution pattern. *Biochimica et Biophysica Acta (BBA) - Bioenergetics*, 1857(6):848–859.

[Pokhrel et al., 2015] Pokhrel, R., Debus, R. J., and Brudvig, G. W. (2015). Probing the effect of mutations of asparagine 181 in the d1 subunit of photosystem ii. *Biochemistry*, 54(8):1663–1672.

[Pokhrel et al., 2013] Pokhrel, R., Service, R. J., Debus, R. J., and Brudvig, G. W. (2013). Mutation of lysine 317 in the d2 subunit of photosystem ii alters chloride binding and proton transport. *Biochemistry*, 52(28):4758–4773.

[Portis, 1981] Portis, A. R. (1981). Evidence of a low stromal mg(2+) concentration in intact chloroplasts in the dark: I. studies with the ionophore a23187. *Plant Physiology*, 67(5):985–989.

[Putrenko et al., 1999] Putrenko, I., Vasil'ev, S., and Bruce, D. (1999). Modulation of flash-induced photosystem ii fluorescence by events occurring at the water oxidizing complex. *Biochemistry*, 38(33):10632–41.

[Rantamäki and Tyystjärvi, 2011] Rantamäki, S. and Tyystjärvi, E. (2011). Analysis of s2qa- charge recombination with the arrhenius, eyring and marcus theories. *Journal of Photochemistry and Photobiology B: Biology*, 104(1):292–300.

[Rappaport et al., 2005] Rappaport, F., Cuni, A., Xiong, L., Sayre, R., and Lavergne, J. (2005). Charge recombination and thermoluminescence in photosystem ii. *Biophysical Journal*, 88(3):1948–58.

[Razeghifard et al., 1999] Razeghifard, M. R., Kim, S., Patzlaff, J. S., Hutchison, R. S., Krick, T., Ayala, I., Steenhuis, J. J., Boesch, S. E., Wheeler, R. A., and Barry, B. A. (1999). In vivo, in vitro, and calculated vibrational spectra of plastoquinone and the plastosemiquinone anion radical. *Journal of Physical Chemistry B*, 103(44):9790–9800.

[Remy and Gerwert, 2003] Remy, A. and Gerwert, K. (2003). Coupling of light-induced electron transfer to proton uptake in photosynthesis. *Nature Structural Biology*, 10(8):637–644.

[Remy et al., 2004] Remy, A., Niklas, J., Kuhl, H., Kellers, P., Schott, T., Rogner, M., and Gerwert, K. (2004). Ftir spectroscopy shows structural similarities between photosystems ii from cyanobacteria and spinach. *European Journal of Biochemistry*, 271(3):563–567.

[Renger, 2004] Renger, G. (2004). Coupling of electron and proton transfer in oxidative water cleavage in photosynthesis. *Biochimica et Biophysica Acta (BBA) - Bioenergetics*, 1655(0):195–204.

[Retegan et al., 2014] Retegan, M., Cox, N., Lubitz, W., Neese, F., and Pantazis, D. A. (2014). The first tyrosyl radical intermediate formed in the s-2-s-3 transition of photosystem ii. *Physical Chemistry Chemical Physics*, 16(24):11901–11910.

[Ruan et al., 2002] Ruan, X., Li, D. H., Xu, Q., Mao, H. B., Li, G. F., Gong, Y. D., Kuang, T. Y., and Zhao, N. M. (2002). Phosphatidylcholine-induced reactivation of photosystem ii membranes pretreated with triton x-100. *Journal of Photochemistry and Photobiology B-Biology*, 67(2):109–115.

[Süß, 2011] Süß, B. (2011). *"Entwicklung eines Step-Scan FTIR-Experiments zur Untersuchung der lichtinduzierten Wasserspaltung der oxygenen Photosynthese"*. Thesis.

[Saito et al., 2013] Saito, K., Rutherford, A. W., and Ishikita, H. (2013). Mechanism of proton-coupled quinone reduction in photosystem ii. *Proceedings of the National Academy of Sciences of the United States of America*, 110(3):954–959.

[Sakamoto et al., 2017] Sakamoto, H., Shimizu, T., Nagao, R., and Noguchi, T. (2017). Monitoring the reaction process during the s2 → s3 transition in photosynthetic water oxidation using time-resolved infrared spectroscopy. *Journal of the American Chemical Society*, 139(5):2022–2029.

[Schiller and Dau, 2000] Schiller, H. and Dau, H. (2000). Preparation protocols for high-activity photosystem ii membrane particles of green algae and higher plants, ph dependence of oxygen evolution and comparison of the s2-state multiline signal by x-band epr spectroscopy. *J Photochem Photobiol B*, 55(2-3):138–44.

[Schilstra et al., 1998] Schilstra, M., Rappaport, F., Nugent, J., Barnett, C., and Klug, D. (1998). Proton/hydrogen transfer affects the s-state-dependent microsecond phases of 680+ reduction during water splitting. *Biochemistry*, 37(11):3974–3981.

[Schlodder et al., 1985] Schlodder, E., Brettel, K., and Witt, H. (1985). Relation between microsecond reduction kinetics of photooxidized chlorophyll aii (p-680) and photosynthetic water oxidation. *Biochimica et Biophysica Acta*, 808:123–131.

[Schönborn, 2017] Schönborn, M. (2017). *"Time-resolved step-scan FTIR spectroscopy on photosystem II"*. Thesis.

[Service et al., 2010] Service, R. J., Hillier, W., and Debus, R. J. (2010). Evidence from ftir difference spectroscopy of an extensive network of hydrogen bonds near the oxygen-evolving mn(4)ca cluster of photosystem ii involving d1-glu65, d2-glu312, and d1-glu329. *Biochemistry*, 49(31):6655–69.

[Service et al., 2014a] Service, R. J., Hillier, W., and Debus, R. J. (2014a). Network of hydrogen bonds near the oxygen-evolving mn4cao5 cluster of photosystem ii probed with ftir difference spectroscopy. *Biochemistry*, 53(6):1001–1017.

[Service et al., 2014b] Service, R. J., Hillier, W., and Debus, R. J. (2014b). Network of hydrogen bonds near the oxygen-evolving mn4cao5 cluster of photosystem ii probed with ftir difference spectroscopy. *Biochemistry*, 53(6):1001–1017.

[Service et al., 2013] Service, R. J., Yano, J., Dilbeck, P. L., Burnap, R. L., Hillier, W., and Debus, R. J. (2013). Participation of glutamate-333 of the d1 polypeptide in the ligation of the mn4cao5 cluster in photosystem ii. *Biochemistry*, 52(47):8452–8464.

[Service et al., 2011] Service, R. J., Yano, J., McConnell, I., Hwang, H. J., Niks, D., Hille, R., Wydrzynski, T., Burnap, R. L., Hillier, W., and Debus, R. J. (2011). Participation of glutamate-354 of the cp43 polypeptide in the ligation of manganese and the binding of substrate water in photosystem ii. *Biochemistry*, 50(1):63–81.

[Shevela and Messinger, 2012] Shevela, D. and Messinger, J. (2012). Probing the turnover efficiency of photosystem ii membrane fragments with different electron acceptors. *Biochimica et Biophysica Acta (BBA) - Bioenergetics*, 1817(8):1208–1212.

[Shimada et al., 2011] Shimada, Y., Suzuki, H., Tsuchiya, T., Mimuro, M., and Noguchi, T. (2011). Structural coupling of an arginine side chain with the oxygen-evolving mn4ca cluster in photosystem ii as revealed by isotope-edited fourier transform infrared spectroscopy. *Journal of the American Chemical Society*, 133(11):3808–3811.

[Shimada et al., 2009] Shimada, Y., Suzuki, H., Tsuchiya, T., Tomo, T., Noguchi, T., and Mimuro, M. (2009). Effect of a single-amino acid substitution of the 43 kda chlorophyll protein on the oxygen-evolving reaction of the cyanobacterium synechocystis sp. pcc 6803: Analysis of the glu354gln mutation. *Biochemistry*, 48(26):6095–6103.

[Shimizu et al., 2018] Shimizu, T., Sugiura, M., and Noguchi, T. (2018). Mechanism of proton-coupled electron transfer in the s0-to-s1 transition of photosynthetic water oxidation as revealed by time-resolved infrared spectroscopy. *The Journal of Physical Chemistry B*, 122(41):9460–9470.

[Siegbahn, 2008] Siegbahn, P. E. (2008). A structure-consistent mechanism for dioxygen formation in photosystem ii. *Chemistry–A European Journal*, 14(27):8290–302.

[Siegbahn, 2012] Siegbahn, P. E. (2012). Mechanisms for proton release during water oxidation in the s2 to s3 and s3 to s4 transitions in photosystem ii. *Phys Chem Chem Phys*, 14(14):4849–56.

[Siegbahn, 2013] Siegbahn, P. E. M. (2013). Water oxidation mechanism in photosystem ii, including oxidations, proton release pathways, o—o bond formation and o2 release. *Biochimica et Biophysica Acta (BBA) - Bioenergetics*, 1827(8–9):1003–1019.

[Siegbahn, 2017] Siegbahn, P. E. M. (2017). Nucleophilic water attack is not a possible mechanism for o-o bond formation in photosystem ii. *Proceedings of the National Academy of Sciences of the United States of America*, 114(19):4966–4968.

[Sproviero et al., 2008] Sproviero, E. M., Gascon, J. A., McEvoy, J. P., Brudvig, G. W., and Batista, V. S. (2008). Computational studies of the o2-evolving complex of photosystem ii and biomimetic oxomanganese complexes. *Coordination Chemistry Reviews*, 252(3-4):395–415.

[Strickler et al., 2006] Strickler, M. A., Hillier, W., and Debus, R. J. (2006). No evidence from ftir difference spectroscopy that glutamate-189 of the d1 polypeptide ligates a mn ion that undergoes oxidation during the s0 to s1, s1 to s2, or s2 to s3 transitions in photosystem ii. *Biochemistry*, 45(29):8801–11.

[Strickler et al., 2007] Strickler, M. A., Walker, L. M., Hillier, W., Britt, R. D., and Debus, R. J. (2007). No evidence from ftir difference spectroscopy that aspartate-342 of the d1 polypeptide ligates a mn ion that undergoes oxidation during the s0 to s1, s1 to s2, or s2 to s3 transitions in photosystem ii. *Biochemistry*, 46(11):3151–3160.

[Strickler et al., 2005] Strickler, M. A., Walker, L. M., Hillier, W., and Debus, R. J. (2005). Evidence from biosynthetically incorporated strontium and ftir difference spectroscopy that the c-terminus of the d1 polypeptide of photosystem ii does not ligate calcium. *Biochemistry*, 44(24):8571–7.

[Styring et al., 2012] Styring, S., Sjöholm, J., and Mamedov, F. (2012). Two tyrosines that changed the world: Interfacing the oxidizing power of photochemistry to water splitting in photosystem ii. *Biochimica et Biophysica Acta*, 1817(1):76–87.

[Suga et al., 2015] Suga, M., Akita, F., Hirata, K., Ueno, G., Murakami, H., Nakajima, Y., Shimizu, T., Yamashita, K., Yamamoto, M., Ago, H., and Shen, J.-R. (2015). Native structure of photosystem ii at 1.95 a resolution viewed by femtosecond x-ray pulses. *Nature*, 517(7532):99–103.

[Suga et al., 2017] Suga, M., Akita, F., Sugahara, M., Kubo, M., Nakajima, Y., Nakane, T., Yamashita, K., Umena, Y., Nakabayashi, M., Yamane, T., Nakano, T., Suzuki, M., Masuda, T., Inoue, S., Kimura, T., Nomura, T., Yonekura, S., Yu, L. J., Sakamoto, T., Motomura, T., Chen, J. H., Kato, Y., Noguchi, T., Tono, K., Joti, Y., Kameshima, T., Hatsui, T., Nango, E., Tanaka, R., Naitow, H., Matsuura, Y., Yamashita, A., Yamamoto, M., Nureki, O., Yabashi, M., Ishikawa, T., Iwata, S., and Shen, J. R. (2017). Light-induced structural changes and the site of o=o bond formation in psii caught by xfel. *Nature*, 543(7643):131–135.

[Suzuki et al., 2005] Suzuki, H., Nagasaka, M.-a., Sugiura, M., and Noguchi, T. (2005). Fourier transform infrared spectrum of the secondary quinone electron acceptor qb in photosystem ii†. *Biochemistry*, 44(34):11323–11328.

[Suzuki et al., 2013] Suzuki, H., Yu, J., Kobayashi, T., Nakanishi, H., Nixon, P. J., and Noguchi, T. (2013). Functional roles of d2-lys317 and the interacting chloride ion in the water oxidation reaction of photosystem ii as revealed by fourier transform infrared analysis. *Biochemistry*, 52(28):4748–4757.

[Takahashi et al., 2009] Takahashi, R., Boussac, A., Sugiura, M., and Noguchi, T. (2009). Structural coupling of a tyrosine side chain with the non-heme iron center in photosystem ii as revealed by light-induced fourier transform infrared difference spectroscopy. *Biochemistry*, 48(38):8994–9001.

[Takahashi et al., 1987] Takahashi, Y., Hansson, r., Mathis, P., and Satoh, K. (1987). Primary radical pair in the photosystem ii reaction centre. *Biochimica et Biophysica Acta (BBA) - Bioenergetics*, 893(1):49–59.

[Takei et al., 2008] Takei, K.-i., Takahashi, R., and Noguchi, T. (2008). Correlation between the hydrogen-bond structures and the c=o stretching frequencies of carboxylic acids as studied by density functional theory calculations: Theoretical basis for interpretation of infrared bands of carboxylic groups in proteins. *The Journal of Physical Chemistry B*, 112(21):6725–6731.

[Tamm and Tatulian, 1997] Tamm, L. K. and Tatulian, S. A. (1997). Infrared spectroscopy of proteins and peptides in lipid bilayers. *Quarterly Reviews of Biophysics*, 30(4):365–429.

[Umena et al., 2011] Umena, Y., Kawakami, K., Shen, J.-R., and Kamiya, N. (2011). Crystal structure of oxygen-evolving photosystem ii at a resolution of 1.9 Å. *Nature*, 473:55–60.

[Utschig and Thurnauer, 2004] Utschig, L. M. and Thurnauer, M. C. (2004). Metal ion modulated electron transfer in photosynthetic proteins. *Accounts of Chemical Research*, 37(7):439–447.

[Van Eerden et al., 2017] Van Eerden, F. J., Melo, M. N., Frederix, P. W. J. M., Periole, X., and Marrink, S. J. (2017). Exchange pathways of plastoquinone and plastoquinol in the photosystem ii complex. *Nature Communications*, 8:15214.

[Vass et al., 1992] Vass, I., Styring, S., Hundal, T., Koivuniemi, A., Aro, E., and Andersson, B. (1992). Reversible and irreversible intermediates during photoinhibition of photosystem ii: stable reduced qa species promote chlorophyll triplet formation. *Proceedings of the National Academy of Sciences of the United States of America*, 89(4):1408–12.

[Venyaminov and Kalnin, 1990] Venyaminov, S. Y. and Kalnin, N. N. (1990). Quantitative ir spectrophotometry of peptide compounds in water (h2o) solutions. i. spectral parameters of amino acid residue absorption bands. *Biopolymers*, 30(13-14):1243–1257.

[Wei et al., 2016] Wei, X., Su, X., Cao, P., Liu, X., Chang, W., Li, M., Zhang, X., and Liu, Z. (2016). Structure of spinach photosystem ii–lhcii supercomplex at 3.2 Å resolution. *Nature*, 534:69.

[Wellburn, 1994] Wellburn, A. R. (1994). The spectral determination of chlorophylls a and b, as well as total carotenoids, using various solvents with spectrophotometers of different resolution. *Journal of Plant Physiology*, 144(3):307–313.

[Young et al., 2016] Young, I. D., Ibrahim, M., Chatterjee, R., Gul, S., Fuller, F. D., Koroidov, S., Brewster, A. S., Tran, R., Alonso-Mori, R., Kroll, T., Michels-Clark, T., Laksmono, H., Sierra, R. G., Stan, C. A., Hussein, R., Zhang, M., Douthit, L., Kubin, M., de Lichtenberg, C., Vo Pham, L., Nilsson, H., Cheah, M. H., Shevela, D., Saracini, C., Bean, M. A., Seuffert, I., Sokaras, D., Weng, T. C., Pastor, E., Weninger, C., Fransson, T., Lassalle, L., Brauer, P., Aller, P., Docker, P. T., Andi, B., Orville, A. M., Glownia, J. M., Nelson, S., Sikorski, M., Zhu, D., Hunter, M. S., Lane, T. J., Aquila, A., Koglin, J. E., Robinson, J., Liang, M., Boutet, S., Lyubimov, A. Y., Uervirojnangkoorn, M., Moriarty, N. W., Liebschner, D., Afonine, P. V., Waterman, D. G., Evans, G., Wernet, P., Dobbek, H., Weis, W. I., Brunger, A. T., Zwart, P. H., Adams, P. D., Zouni, A., Messinger, J., Bergmann, U., Sauter, N. K., Kern, J., Yachandra, V. K., and Yano, J. (2016). Structure of photosystem ii and substrate binding at room temperature. *Nature*, 540(7633):453–457.

[Zaharieva et al., 2016] Zaharieva, I., Chernev, P., Berggren, G., Anderlund, M., Styring, S., Dau, H., and Haumann, M. (2016). Room-temperature energy-sampling kbeta x-ray emission spectroscopy of the mn4ca complex of photosynthesis reveals three manganese-centered oxidation steps and suggests a coordination change prior to o2 formation. *Biochemistry*, 55(30):4197–211.

[Zaharieva et al., 2011] Zaharieva, I., Wichmann, J. M., and Dau, H. (2011). Thermodynamic limitations of photosynthetic water oxidation at high proton concentrations. *J Biol Chem*, 286:18222–18228.

[Zhang et al., 1998] Zhang, H. M., Fischer, G., and Wydrzynski, T. (1998). Room-temperature vibrational difference spectrum for s(2)q(b)(-)/s(1)q(b) of photosystem ii determined by time-resolved fourier transform infrared spectroscopy. *Biochemistry*, 37(16):5511–5517.

[Zhang et al., 1997] Zhang, H. M., Razeghifard, M. R., Fischer, G., and Wydrzynski, T. (1997). A time-resolved ftir difference study of the plastoquinone q(a) and redox-active tyrosine y-z interactions in photosystem ii. *Biochemistry*, 36(39):11762–11768.

[Zhang et al., 2002] Zhang, J., Oettmeier, W., Gennis, R. B., and Hellwig, P. (2002). Ftir spectroscopic evidence for the involvement of an acidic residue in quinone binding in cytochrome bd from escherichia coli. *Biochemistry*, 41(14):4612–4617.

[Zhang et al., 2017] Zhang, M., Bommer, M., Chatterjee, R., Hussein, R., Yano, J., Dau, H., Kern, J., Dobbek, H., and Zouni, A. (2017). Structural insights into the light-driven auto-assembly process of the water-oxidizing mn4cao5-cluster in photosystem ii. *eLife*, 6:e26933.

[Zobnina et al., 2017] Zobnina, V., Lambreva, M. D., Rea, G., Campi, G., Antonacci, A., Scognamiglio, V., Giardi, M. T., and Polticelli, F. (2017). The plastoquinol-plastoquinone exchange mechanism in photosystem ii: insight from molecular dynamics simulations. *Photosynthesis Research*, 131(1):15–30.

11 Appendix

11.0.1 Programs controlling the setup

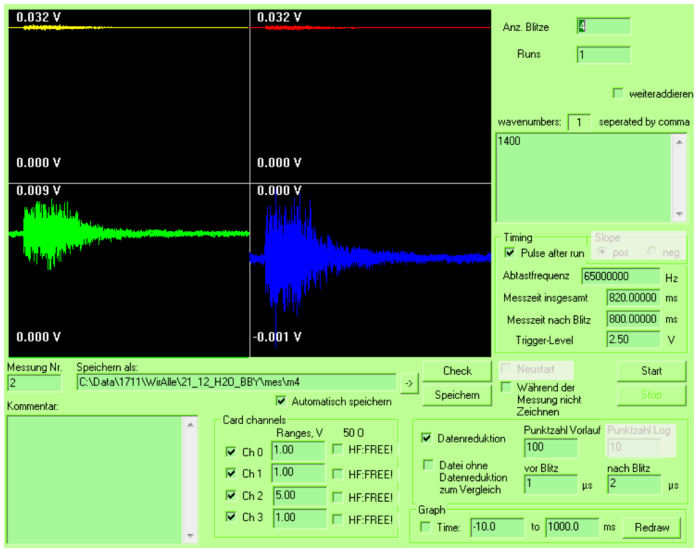

Figure 11.1: Program controlling the data sampling. *Details in text.* Gray boxes cover parts without any function.

The **data recording program** is based on a program of the delayed chlorophyll fluorescence setup written in C++ and adapted to this setup first by Dr. Petko Chernev and by myself. It sets the A/D conversion card, records and stores the data and is capable of automating the sequential acquisition of multiple flashes, repetitions and wavenumbers.

The user interface is shown in figure 11.1. The top left corner shows the recorded transients of the first four flashes, autoscaled after the measurement finishes. Below, the file path is specified, an index representing the measurement number is appended to the filename to differentiate sequential measurements. This index can be set manually in the corresponding box. Measurements are saved only when the tick box 'Automatisch Speichern' is marked. Comments written in the bottom left text box are added to the preamble of the text file following the date and time. The channel number and flash number are both preceded by the pound sign '#' as an identifier.

In the field in the top right the number of recorded flashes is entered. Below in "Runs" the number of measurements (=*number of spots in the linear stage program*). An optional check box below would automatically average all measurements. A list of the measured wavenumbers is entered in the large text box. The system runs through all sample spots and desired flashes for each wavenumber. The wavenumber is appended to the filename to differentiate different measurements.

In order for the sample stage to begin movement a flag needs to be raised. Since the stage control software is a separate program, this flag needs to be communicated externally. The data recording program creates a dummy folder which the stage control program waits for. Once triggered, the program deletes the folder and moves the sample holder to the next position.

Below, the "Abtastfrequenz" meaning sampling frequency is set, with possible values restricted by the A/D card. Next, the total total measurement time is entered, this value should be set such that at least 20 ms are recorded before the flash. Note that logarithmic

averaging starts after the difference of the two and needs to be agree with the pulse generator (see section 5.2.1). With the button “Während der Messung Zeichnen” one can switch the drawing function on or off.

The buttons “Start” and “Stop” starts and stops the measurements. If one presses the stop button and there are still runs to record it will take a while until the program resets.

In the bottom line next to the comment field one can select the number of channels. The card will only allow 1, 2 or 4 channels. The range needs to match the allowed values. If the tick below 50 Ω is empty the lines will be terminated with 50 Ω utilizing the high frequency mode. High an low frequency modes allow the selection of different voltage ranges of each channel.

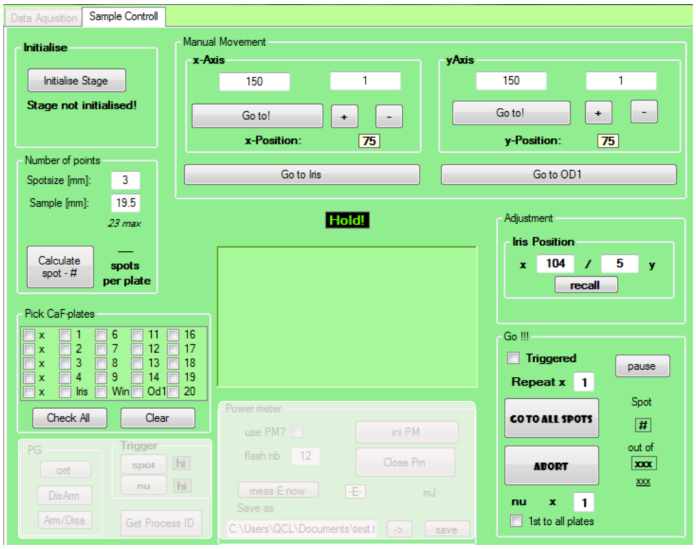

Figure 11.2: Program controlling the movement of the linear stage. *Details in text.* Gray boxes cover parts without any function.

In the lower right corner one can select how the data is averaged in time. Without a tick the full 65 MS/s will be saved. A tick at “Datenreduktion” allows to save already averaged data. The field below will additionally save the raw data. The four fields to the right modify the averaging. “Punktzahl Vorlauf” determines into how many equidistant points the time before the flash will be averaged. “vor Blitz” and “nach Blitz” define how many µs will be saved with the full time resolution before the flash and after the flash respectively. The number of points after the flash also defines the point number after which the averaging is doubled (e.g. 1 µs: 65 points raw, next 65 avg into 32...).

The **program controlling the linear stage** is based on a program of the FTIR setup written by Björn Süß ([Süß, 2011]) in C# and adapted to this setup by myself with the assistance of Dr. Petko Chernev. It allows manual control of the translation stages, assists in the alignment and calculates the total number of spots on all samples.

The user interface is shown in figure 11.2. The button “Initialise Stage” initialises the stages by driving them to the central reference point at 75 mm. Whenever the stages are moving or have reached the desired position this is displayed in the center (in figure “Hold”).

The two boxes in the top enable manual control over the stages. In each the first white box gives the position in mm, “Go to!” moves the stages. With“+” or “-” the stage moves one step with the entered distance. With “Go to Iris/OD1” the stages drive to the center of the iris used to align the lasers or to an IR neutral density filter mounted on the sample board.

The position of the IR beam is aligned at the iris. The coordinates are entered in the “Iris Position” box. These coordinates serve as the reference point for the automatised movement. Also the excitation laser can be aligned onto this position.

All other boxes are used to handle the automised measurement. The settings of the box “Number of points” set the distance of the measurement spots and the diameter of the sample

area. When pressing "Calculate spot - #" the corresponding number of spots fitting in a densed packing manner in the sample diameter is calculated. The positions on each plate relative to the center will be displayed in the middle box[1].

In the raster below one can select the loaded CaF_2 positions. When pressing the calculate spots button with checked CaF_2 plates the total number of spots is displayed in the "Go !!!" box on the right.

In the "Go !!!" box the measurement is started or aborted. After pressing the "Start" button all spots on the plate are moved into the IR beam at the former iris location. After reaching one spot and "Triggered" is checked the program will continuously search for a temporary file (created by the data recording program) before moving on. The number of repetitions per wavenumber and the number of wavenumbers determine the total number of repetitions. The difference between repetitions and wavenumbers is whether or not a trigger pulse will be sent to the QCL to change the wavenumber.

11.0.2 IR spectra

Table 11.1: Specifications of the QCL MIRcat given by Daylight Solutions

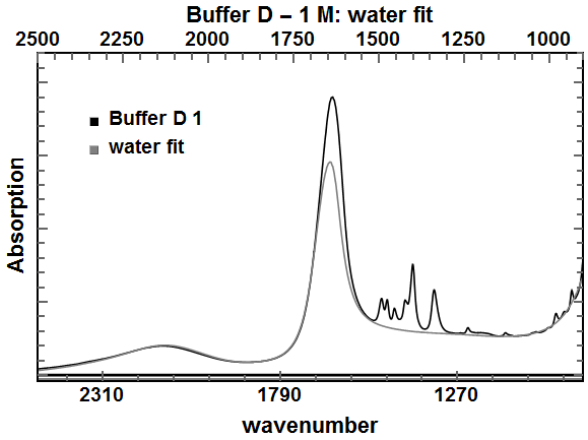

Figure 11.3: IR spectrum: buffer D with 1 M betaine. To extract the pure betaine spectrum the spectrum of water has been simulated to the 2200 cm^{-1} band.

The extracted lines of dried buffer D with 1 M betaine fit the spectra of the NIST database for betaine in the condensed phase with local maxima above 1000 cm^{-1} at 1128 cm^{-1}, merging bands from 1185 to 1236 cm^{-1}, 1334 cm^{-1}, merging bands from 1400 to 1500 cm^{-1} (NIST database), 1600, 1690 and 2220 cm^{-1}.

Band position in solution shift and the ratio of absorption varies with molecular interaction, as in some PSII data sets a good subtraction was not achievable. Solubelized betaine bands appear at 1125, 1237, 1337, 1404, 1450 - 1495 and 1608 cm^{-1}. The latter might be the merging of the two separated bands of the dry sample at 1600 and 1690 cm^{-1}. Both might be due to remaining tightly bond water molecules. The band at 2220 cm^{-1} disappears in solution.

[1] At the time writing there is a bug in the program causing a crash when the calculated position is not exact at two digits

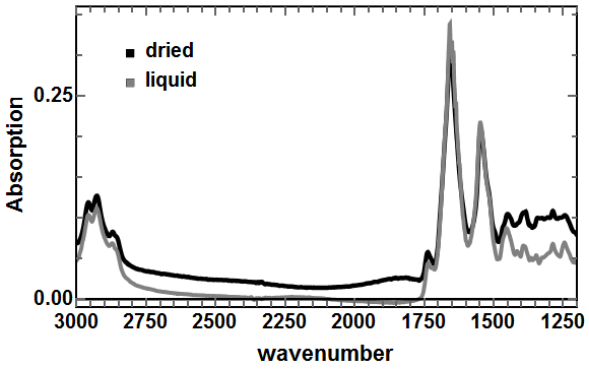

Figure 11.4: IR spectrum of a dried and a liquid sample (15 µm, not concentrated, absorption of PSII in solution doubled). To remove the water absorption it has been fitted to the water association peak at 2200 cm^{-1} of the untreated spectrum (*see appendix fig. 11.8*). All peak positions also in the amide I / water bend region match very well.

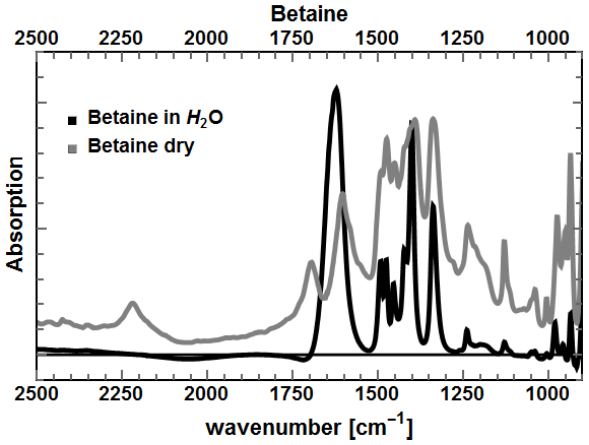

Figure 11.5: IR spectrum of betaine dried and in solution.

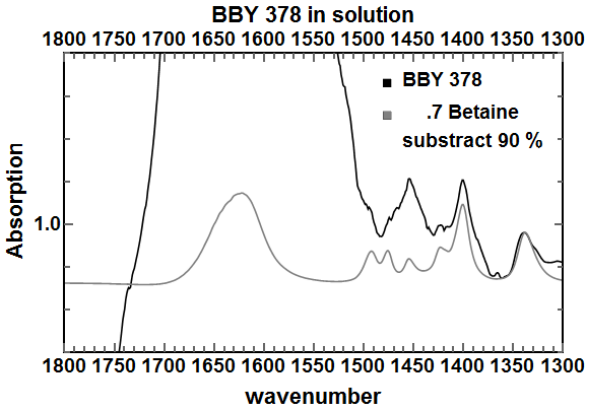

Figure 11.6: IR spectrum of PSII membranes and betaine buffer.

The variation of the relative peak heights of different measurements might explain some of the small discrepancies of the dried spectrum to the one accessible at the NIST data base.

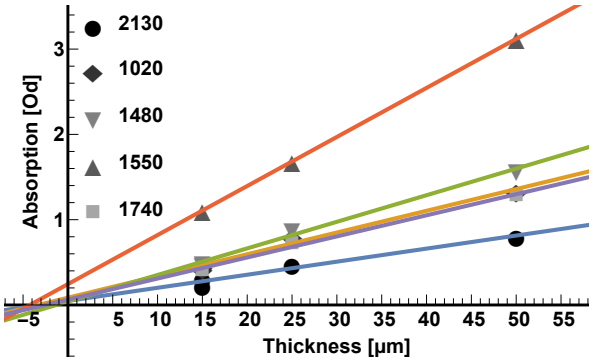

Figure 11.7: At the indicated wavenumbers the absorption of samples created with spacers of a certain thickness has been simulated with a linear function. The corresponding spectra are presented in figure 4.6. None of the curves crosses zero absorption at 0 µm thickness indicative for 2 to 5 µm additional thickness to due to the high amount of samples.

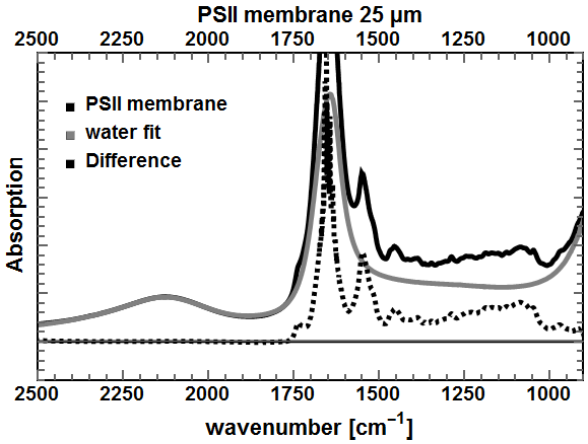

Figure 11.8: IR spectrum of PSII membranes from spinach. The spectrum of water can be sutracted to obtain the dashed spectrum.

11.1 Heat artefact

11.2 Quinones

In figure 11.15 the single frequency amplitudes are shown with the corresponding FTIR data averaged from 360-480 ms. Both data sets are in good agreement and exhibit at this time a pure binary pattern, slightly more pronounced in the SF-measurement. We can therefore exclude contributions from the OEC. Comparing the first and the third flash data the absorption change of the first flash is about 2-4 times stronger in both data sets.

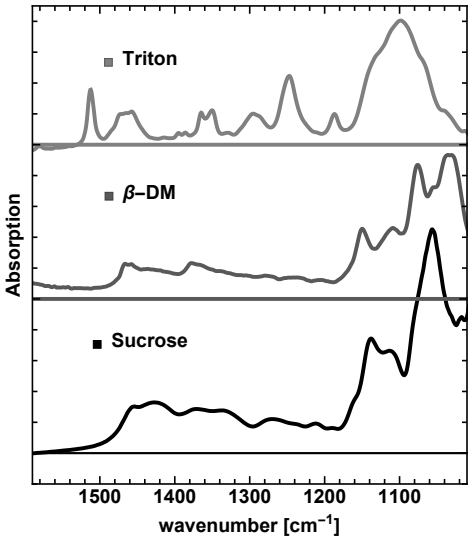

Figure 11.9: IR spectrum: triton, sucrose β-DM in the fingerprint region.

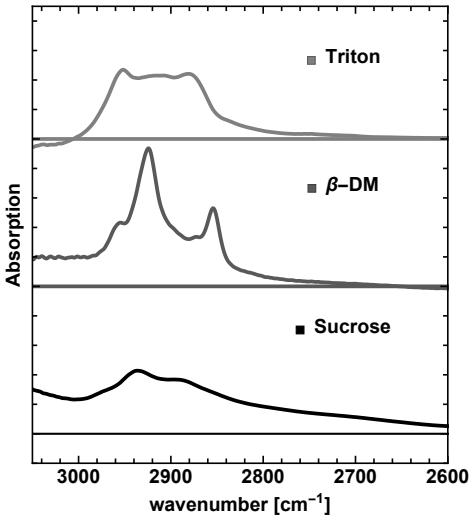

Figure 11.10: IR spectrum: triton, sucrose β-DM, in the high wavenumber region.

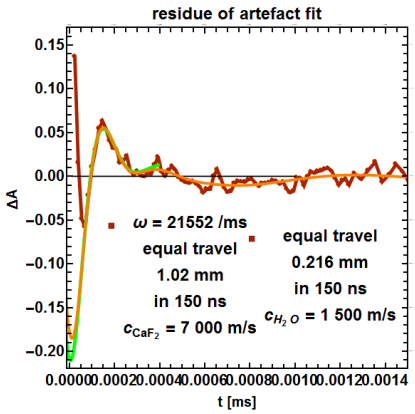

Figure 11.11: Fit approach of the pressure wave. Assuming the speed of sound in CaF2 or water.

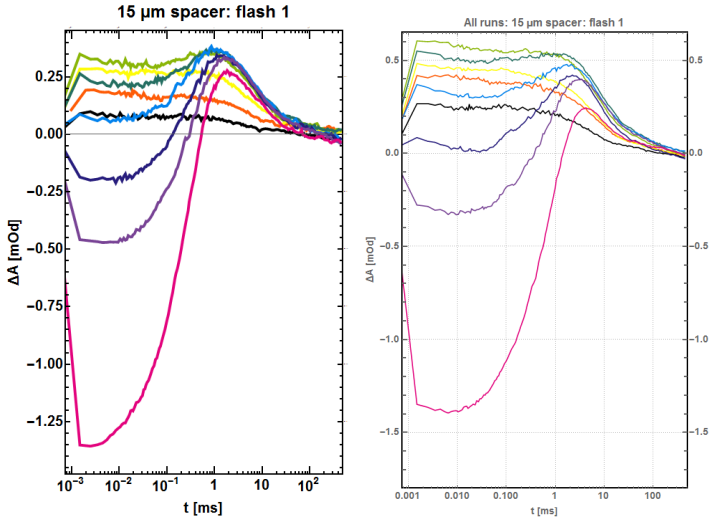

Figure 11.12: Transients of the saturation curves in fig. 5.13 measured at 1478 cm^{-1} for 15 µm on the *left* and 25 µm on the *right*. The heat relaxation is faster with 15 µm thickness. The overall quinone signal higher at 25 µm.

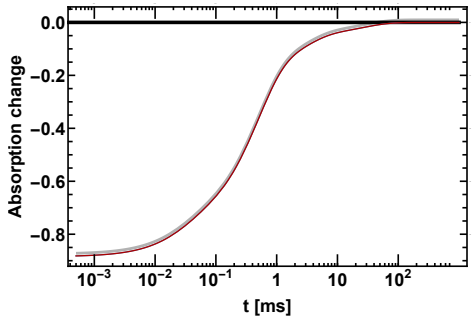

Figure 11.13: Three normalized heat artefacts measured at 1478 cm^{-1}. Two of which are recorded at 10 °C and one at 20 °C. The normalized kinetics are not distinguishable and therefor the heat correction very reproducible.

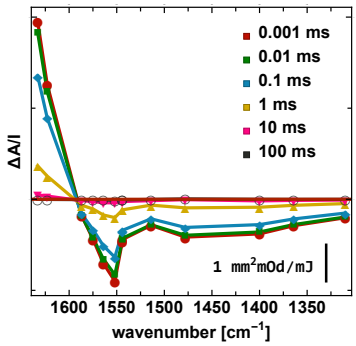

Figure 11.14: Heat signal extracted from the measurements presented in chapter 6. Recorded on spinach PSII membranes at 10 °C and pH 6.2.

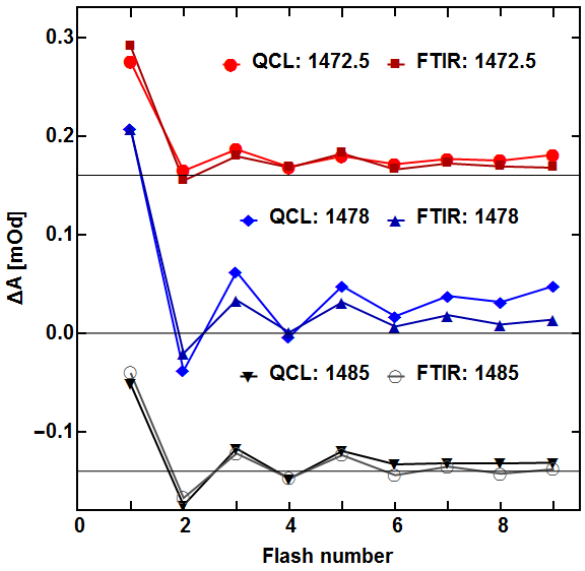

Figure 11.15: Flash patterns of single frequency data in comparison with the steady state FTIR data (see fig. 7.5, pH 6.2 and 20 °C). The data points are obtained by averaging over 360-480 ms. A scaling factor for the single frequency data is calculated for the first flash. A clear binary pattern is present in both data sets.

The changes of the second flash at 1472.5 and 1478 cm-1 stay positive in the steady state data set. Just in later times when QA- recombines the expected negative peak, caused by the uptake of a 2nd electron and coupled protons by QB-, becomes present (compare figure 7.5). In both sets already in the 4th flash nearly no negative signals are observed within 480 ms. As the 1472.5 cm-1 band never crosses the zero line one can safely assume that the formed quinol contributes here as observed for ubiquinol-10 at 1470 cm-1 by Mezzetti et al. in photosynthetic membranes [Mezzetti et al., 2003].

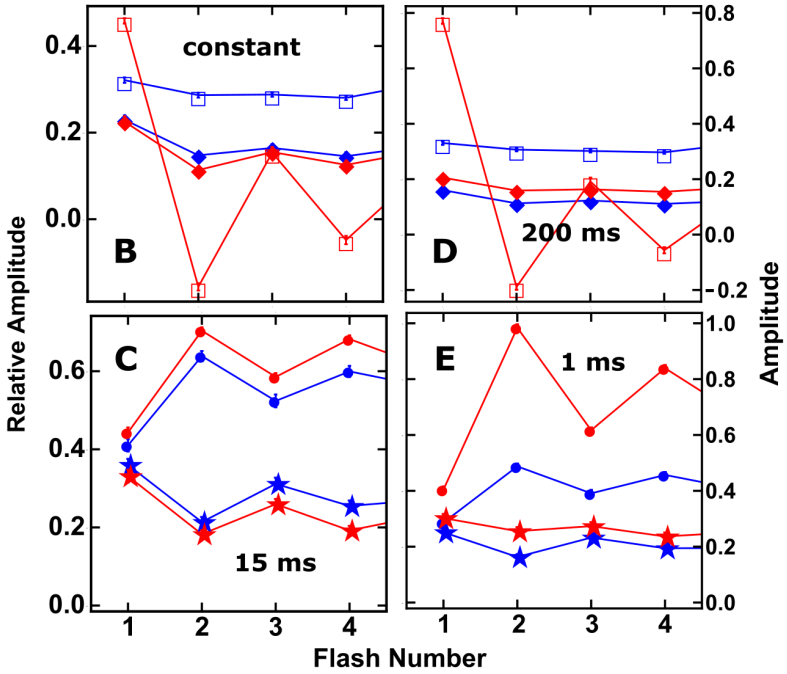

Figure 11.16: Simulation parameters of the amplitudes related to the time courses of Q_A^- re oxidation in PSII membranes at pH 6.2 and 20 °C. Panel B and C as in figure 7.8 of the main text: the amplitude relative to the total decay related to the quinones. Fluorescence and SF-IR data fit well. Panel D and E belong to the absolute amplitudes. The IR data senses stronger the decay related to Q_BH_2 formation as the vanishing reduced form absorbs as well. Whereas the 15 and 200 ms amplitudes fit reasonably well.

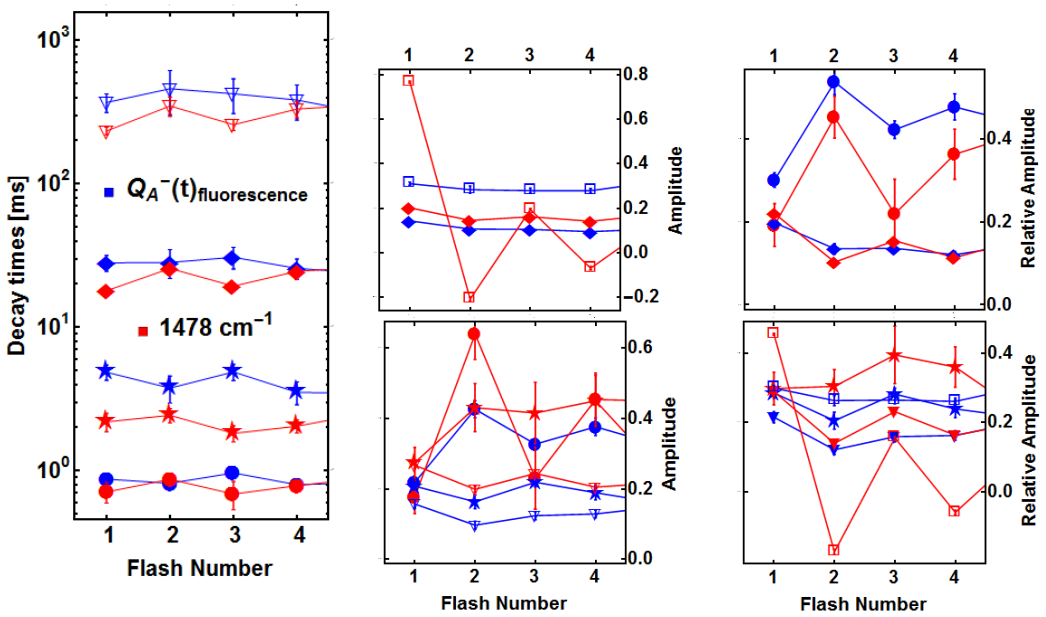

Figure 11.17: 1478 cm^{-1} and variable fluorescence simulated with 4 simulated exponential functions. Measurement at pH 6.2 and 20°C on PSII membranes. *left*: decay times, *middle:* relative amplitudes (amplitude of component over total decaying amplitude), *right* absolute amplitudes

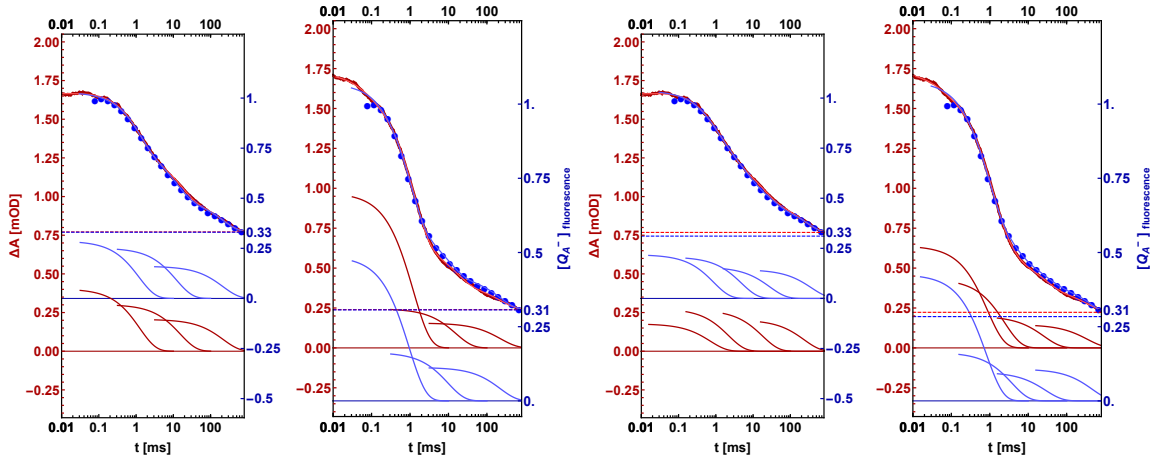

Figure 11.18: Dynamics of the transients at 1478 cm^{-1} (blue) and the amount of reduced Q_A extracted from the variable fluorescence (red) for the 1st and 2nd flash for PSII membranes at pH 6.2. The *left* figure transients are fitted with three exponents for the Q_A^- decay, the *right* ones with four functions. The fluorescence fit started at 100 µs whereas the sf-IR fit at 10 µs. The components of the 3 or 4-exponential fits (global fit for the single frequency data) are shown as thin lines in the corresponding color. The dashed lines resembles the fit constants. With one component more, the fast component (1-1.2 ms) splits into a faster one with 0.7-0.9 ms and a slower one with 2-4 ms.

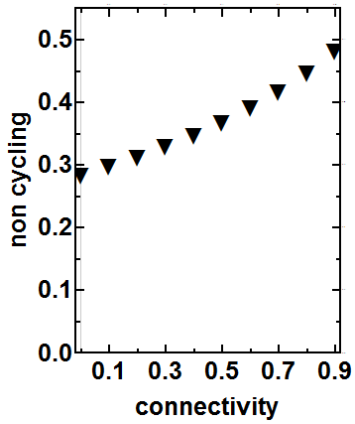

Figure 11.19: Influence of the connectivity parameter on the amount of non-cycling PSII. The values at 700 ms are obtained when the connectivity parameter p is varied in the correction model of the variable chlorophyll fluorescence. Measurement at room temperature and pH 6.2 on PSII membranes of spinach.

11.3 P_{680} and Y_Z

11.3.1 Slow phases: bands corresponding to Y_D, quinone and recombination kinetics

A positive band in the 450 minus 700 ms double difference spectrum is present around 1505 cm^{-1} in the first transition. The band position is expected for bands relfecting $Y_D^{\bullet ox}$ Y_D redox changes. After dark adaption most clusters are present in the S_1 state. The clusters that were in the S_0 state before could donate an electron to $Y_D^{\bullet ox}$ forming a neutral Y_D. This Y_D can then donate once after flash excitation an electron to S_2 (or S_3) with slow kinetics (biphasic: 500 ms to 1 s and many seconds).

Thus a negative signal due to $Y_D^{\bullet ox}$ is expected at 1504 cm^{-1} and a positive at 1512 cm^{-1} due to the creation of Y_D when calculating the difference between 450 ms minus 700 ms ($Y_D^{\bullet ox}$ formation, Mn cluster reduction). It would only be present in the first flash transition when S_2 is formed for the first time. In the deconvoluted data this flash transition is omitted and the electron donation not visible whereas all other transition as quinone contributions will be present. This explains why only the red trace shows clear singals above zero.

On the other hand also the Mn oxidation of $S_1 \rightarrow S_2$ is reversed. The decay asociated spectrum is present as the yellow line (120 µs) in the top left panel of figure 8.11. Only the contribution of carboxylates and amide II bands will be reversed when an electron is extracted from Y_D- and no Y_Z redox state changes will be observed. Therefore,the S_2 reduction will cause decaying bands from 1495 to 1512.5 cm^{-1} leading to positive bands in the difference spectrum between 450 ms minus 700 ms in figure 11.29.

One explanation for strong positive bands at 1505 and 1507.5 cm^{-1}[2] is therefore the S_2 to S_1 back-reaction. The only negative signal present is located at 1500 cm^{-1}. It might reflect the contributions of $Y_D^{\bullet ox}$ minus the expected positive signals of the cluster. If this was true the H-bonding strength might be slightly weaker than in the measurements of the $Y_D^{\bullet ox}$ minus Y_D spectra measured in Mn depleted samples presented in the introduction.

[2]neglecting more complicated mechanisms including Cyt b556 etc.

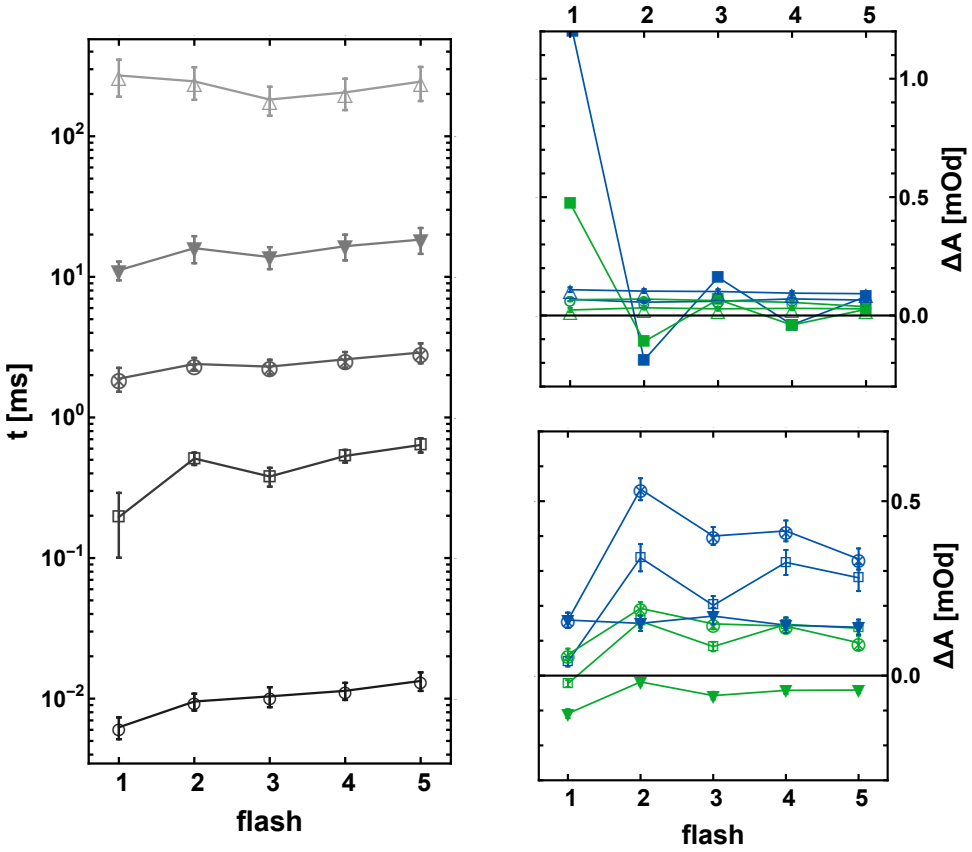

Figure 11.20: Simulation results of Q_A^- decay at pH 7.5 in PSII membranes without the addition of electron acceptor: visualization of the simulation presented in table 7.2. Flash pattern of the decay times (A), corresponding quaternary cycling decay amplitudes and constants (B) and binary cycling decay amplitudes (C) are shown of the transient at 1478 and 1485 cm^{-1} (global fit results). The same plot markers in A, B and C correspond to each other. The fit constants are shown as circles.

Another explanation does not involve Y_D at all. Assuming a different relaxed state of PSII possibly the first flash transition involves a conformational change of amino acids, some subunits or the protein backbone. Then the negative signal at 1500 cm^{-1} and the positive at 1505 cm^{-1} might be a shift of an asymmetric carbocylate or an amide II band during the dark to light transition.

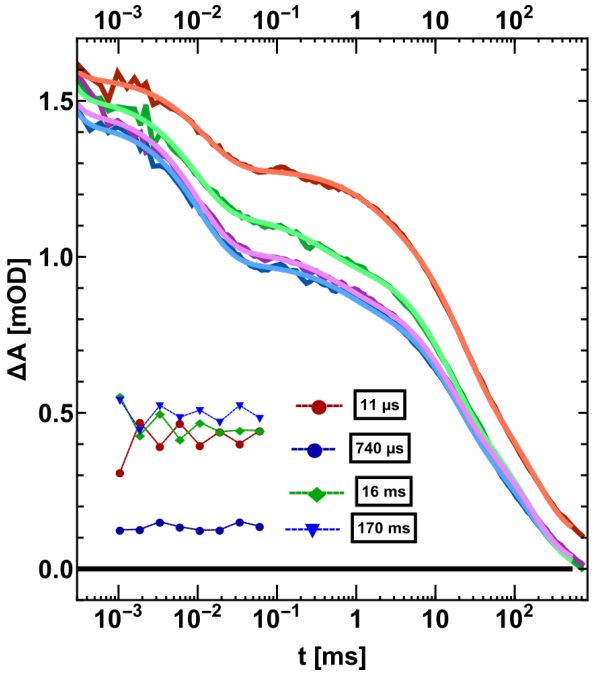

Figure 11.21: Fit results of the electron transfer to PPBQ at pH 6.2 and 20 °C in PSII membranes from spinach. In red: flash 1, blue: flash 2, green: flash 3, magenta: flash 4. Measurement taken from the scan at 1378-1410 cm^{-1} of section 9.4.3. Not shown is a fast 100 ns phase close to the time resolution. The inset shows the amplitude contribution per flash.

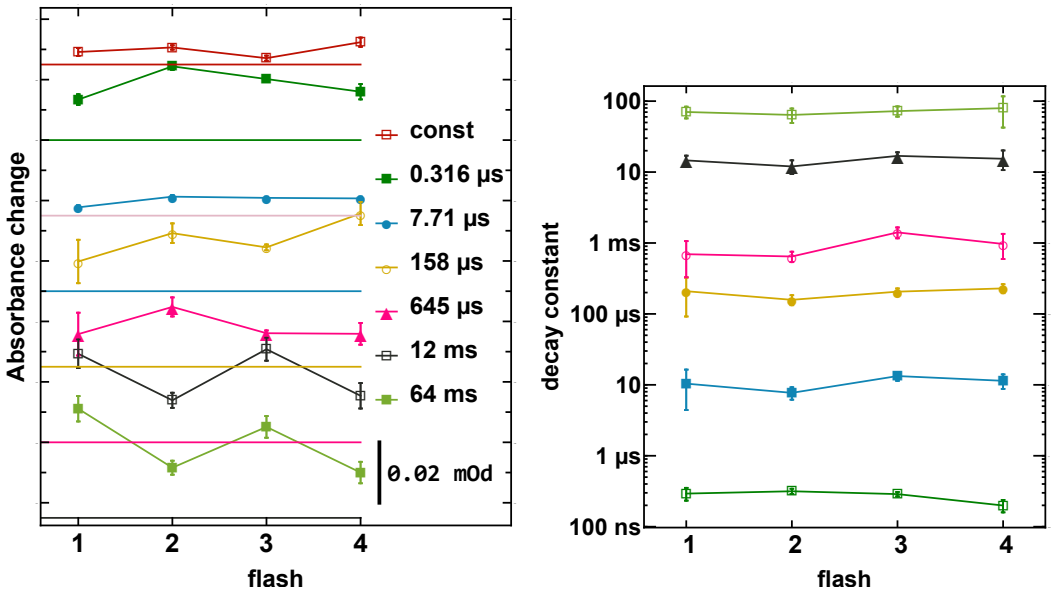

Figure 11.22: Fit results of the electron transfer to PPBQ at pH 7.5 and 10 °C in PSII membranes. Measurement taken from the scan at 1495-1520 cm^{-1} of section 8.4.

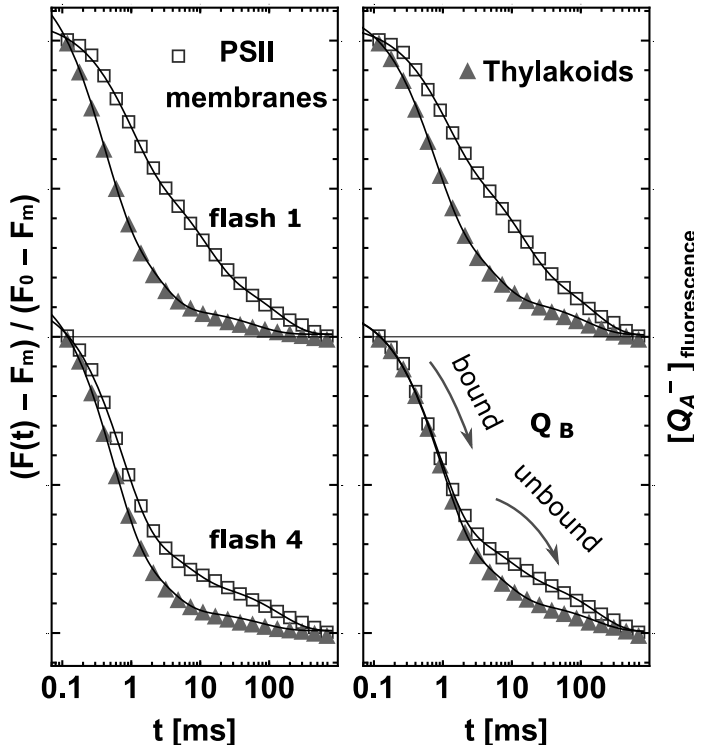

Figure 11.23: Normalized fluorescence transients of the first and fourth flash data for PSII membranes (empty squares) and thylakoid membranes (triangles) at pH 6.2 and room temperature. Left: no correction in Q_A^- nonlinearity has been applied (p=0). Right: connectivity parameter of p=.3 and p= .7 for PSII membranes and thylakoids respectively and equation 4.2 has been used. Shown is also a three exponential fit. The second fourth transients match well after correction. The first flash on the first glance not. The decay times and amplitudes of the simulation match after correction and only the ratio between fast and slow decay changes with less forward electron transfer to Q_B bound.

11.4 Water oxidation

To judge whether the very fast pronounced changes of the lower wavenumber set are real, in figure 11.30 this measurement is compared with a measurement obtained at 10 °and a 15 µm spacer (from sec. 6). Overall the kinetics and amplitudes are identical. Even the flash dependent amplitude pattern are the same. Only the decay in the first 10 µs is much higher in the data set discussed here. At 1365 cm^{-1} a carotenoid anion band is present, at 1380 cm^{-1} a band of the P_{680} triplet. The triplet state of carotenoids is known to decay in LHCs with about 4 µs [Christen et al., 1998]. It might be possible that this phase is then stemming from damaged centers.

Here, mainly the measurements at 1378 and 1382 cm^{-1} bands show different kinetics in flashes 2, 3, 6 and 7, whereas in most other bands like at 1402 cm^{-1} no difference to the high energy flash is visible.

D1-D61A

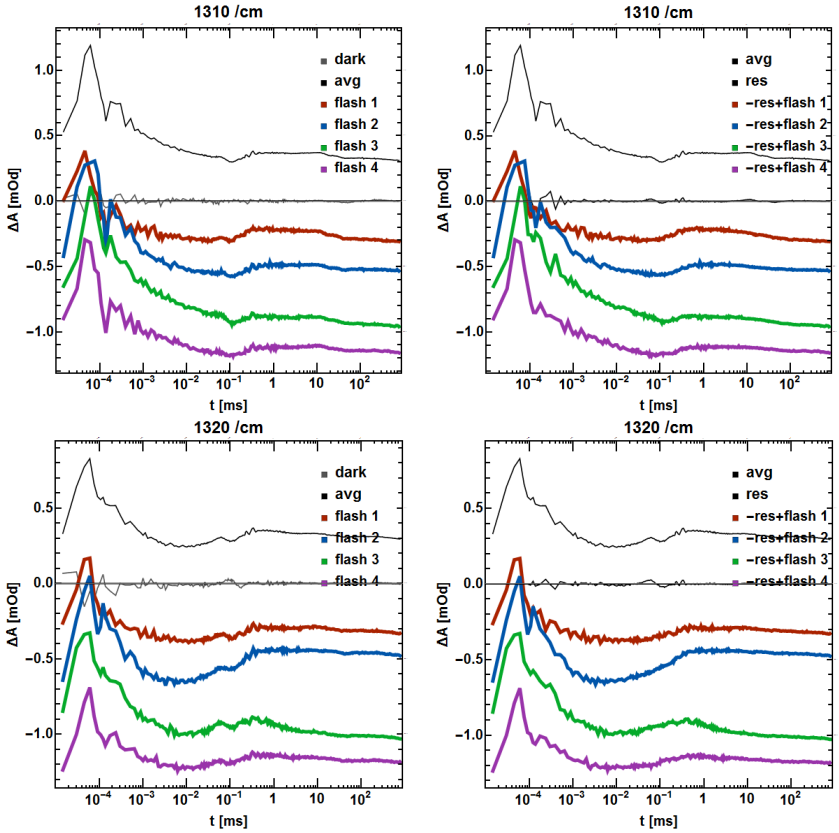

Figure 11.24: Extraction of the QCL noise for the set recorded between 1300 and 1320 cm^{-1} at pH 6.2 and 10°C in chapter 8.3: *left*: before correction, *right*: after correction. The left figure shows the transients after heat artefact correction and sampling in time. The black curve in the top is the average of all flashes. The dark curve around zero is the dark measurement recorded right before the first flash. On the right the curve around zero is the extracted residuum of a six exponential function of the all flash average. The four flash transients in the right figure were corrected with this residuum. The results are beautiful.

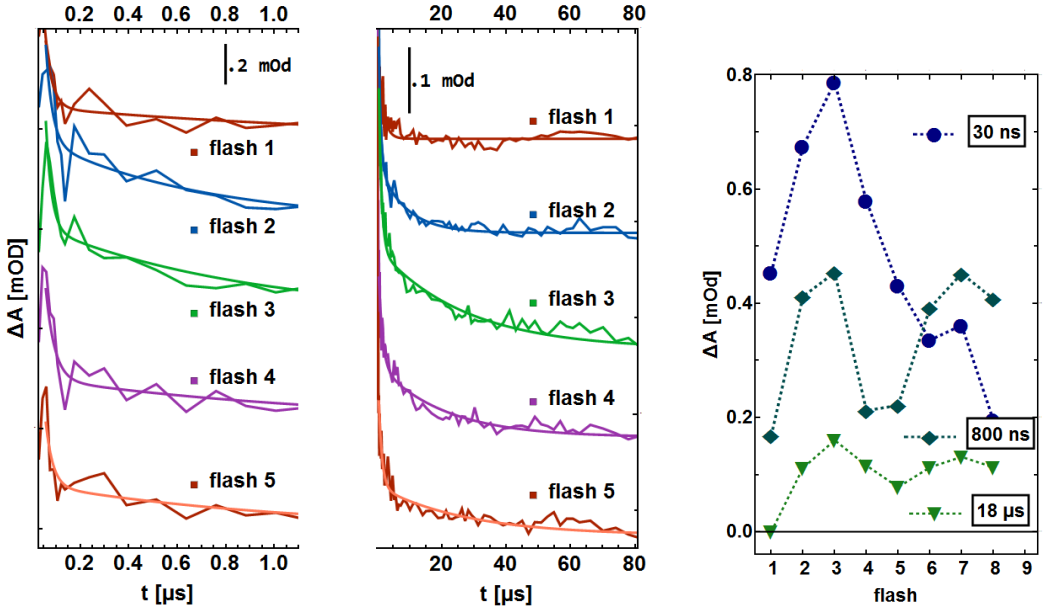

Figure 11.25: P_{680}^{+} reduction by Y_Z measured at 1310 cm^{-1} and pH 6.2 and 10 °. The data set is the same as the result of the averaged transients in figure 8.5, only here before deconvolution and only the one wavenumber at 1310 cm^{-1}. *Right*: 30 ns difference flash pattern of the fit evaluated at 50 ns minus the value evaluated at 50 µs. 800 ns and 18 µs amplitude pattern of the fit components.

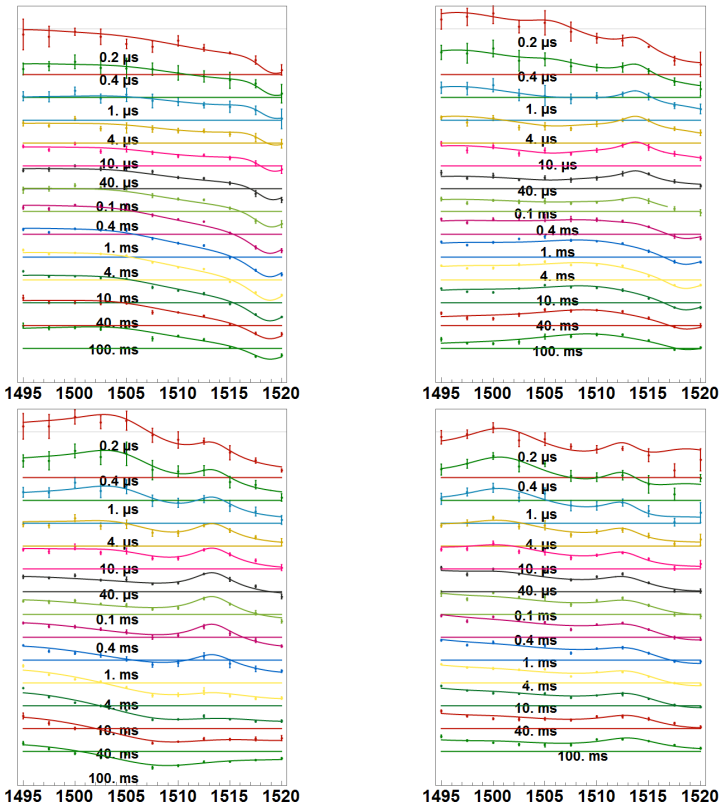

Figure 11.26: Decaying spectra of the fit around 1510 cm^{-1} at pH 7.5 and 10 °C of PSII membranes. The fit is the result from five lorentzians as described in section 8.4.2. top left: $S_1 \rightarrow S_2$, top right: $S_2 \rightarrow S_3$, bottom left: $S_3 \rightarrow S_0$, bottom right: $S_0 \rightarrow S_1$.

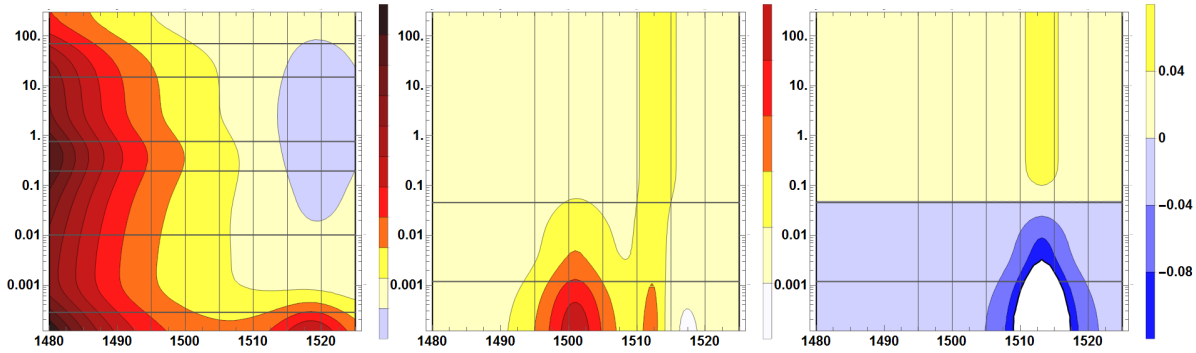

Figure 11.27: Peak fit $S_0 \rightarrow S_1$ of the pH 7.5, 10 °C data on PSII membranes. Left: all components plotted. The decay of a peak at 1512.5 cm^{-1} is present. Middle: P680, $Y_Z^{\bullet ox}$ and carboxylate peak. Right: carboxylate peak. As one can see, the contribtuions of $Y_Z^{\bullet ox}$ and the carboxylate cancel each other. The decay of the band at 1512.5 cm^{-1} together with the fits of the other transitions indicates a contribution of $Y_Z^{\bullet ox}$ in this transition as well.

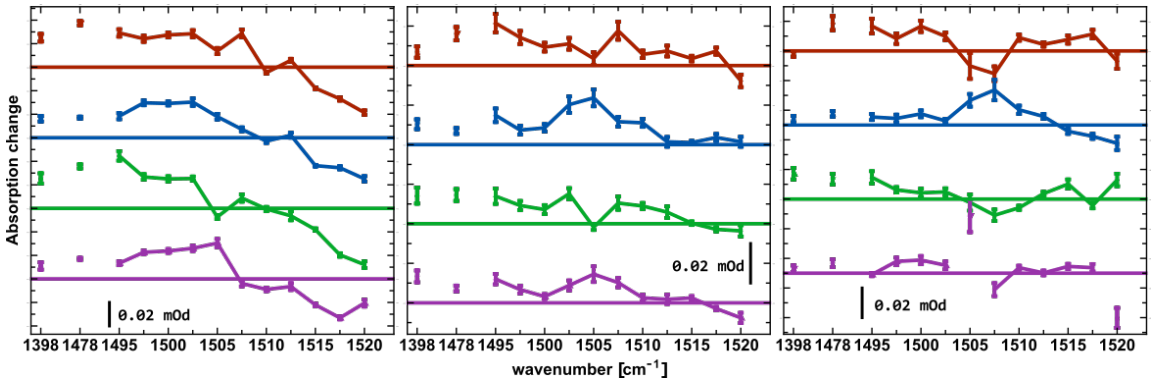

Figure 11.28: Slow changes occurring around 1505 cm^{-1} in the deconvoluted pH 7.5 data (excluding the first flash transition). The colours of the spectra correspond to Red: $S_1 \rightarrow S_2$, blue: $S_2 \rightarrow S_3$, green: $S_3 \rightarrow S_0$ and magenta: $S_0 \rightarrow S_1$. *left*: 5-10 ms minus 50-100 ms. Within this difference in time the electron from Q_A to Q_B and PPBQ takes place visible in the binary behaviour at 1478 cm^{-1} (1478 cm^{-1} scaled by .1). *middle*: 50-100 ms minus 100-200 ms. Here possible recombination with $Y_Z^{\bullet ox}$ (or P_{680}^+?) and Q_A^- or possibly electron transfer to PPBQ might take place. (1478 cm^{-1} scaled by 0.2) *right*: 300-600 ms minus 600-800 ms. In this range of time drifts are strongest. Possible other contributions include recombination and electron transfer to and fro Y_D. A binary pattern at 1507.5 and 1478 cm^{-1} seems to be present. (no 1478 cm^{-1} scaling).

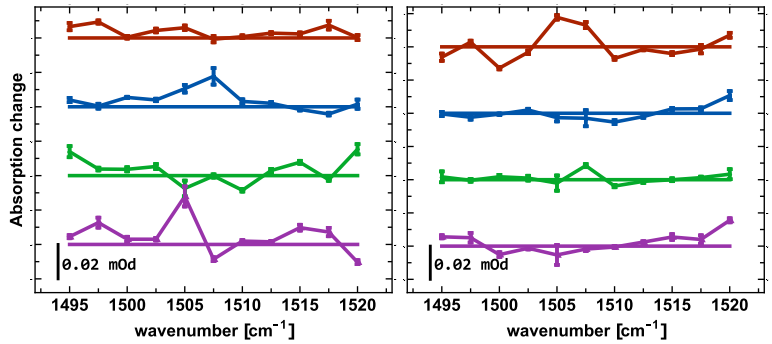

Figure 11.29: Compared are the changes from 300-600 ms minus 600-800 ms in the flash induced data (*left*) and (*right*) the double difference of this and the deconvoluted data shown in the right pannel of figure 11.28. The colours of the spectra correspond to Red: $S_1 \rightarrow S_2$, blue: $S_2 \rightarrow S_3$, green: $S_3 \rightarrow S_0$ and magenta: $S_0 \rightarrow S_1$. Except for the first flash transition the spectra represent the deconvoluted ones. In the double difference spectrum of the first flash minus the $S_1 \rightarrow S_2$ transition clear signals are present in between 1500 and 1510 cm^{-1}.

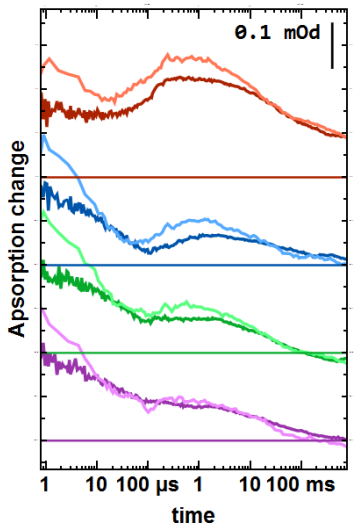

Figure 11.30: Signals of the transient at 1362 cm^{-1} of the measurements in figures 9.4 (bright) and figure 6.1 (dark). The bright was measured at 20 °C and with 25 µm thickness, the dark transients at 10 °C with 15 µm.

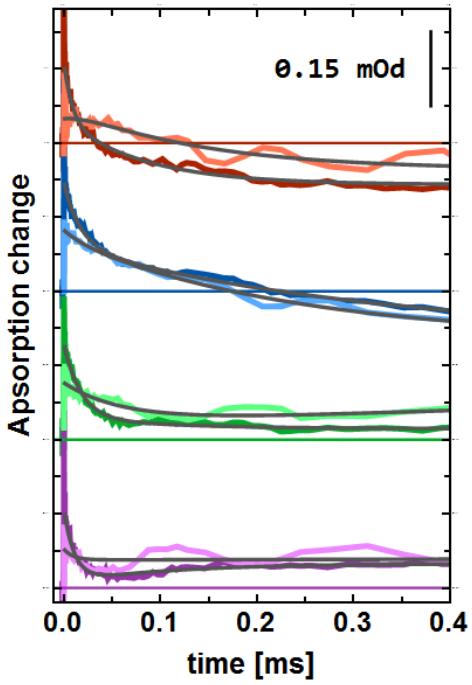

Figure 11.31: Linear plot of the transients at 1400 cm^{-1} at pH 6.2 (dark) and 7.5 (bright) plotted in figure 9.8. From top to bottom: $S_1 \rightarrow S_2$, $S_2 \rightarrow S_3$, $S_3 \rightarrow S_0$ and $S_0 \rightarrow S_1$. 10 °C on PSII membranes from spinach.

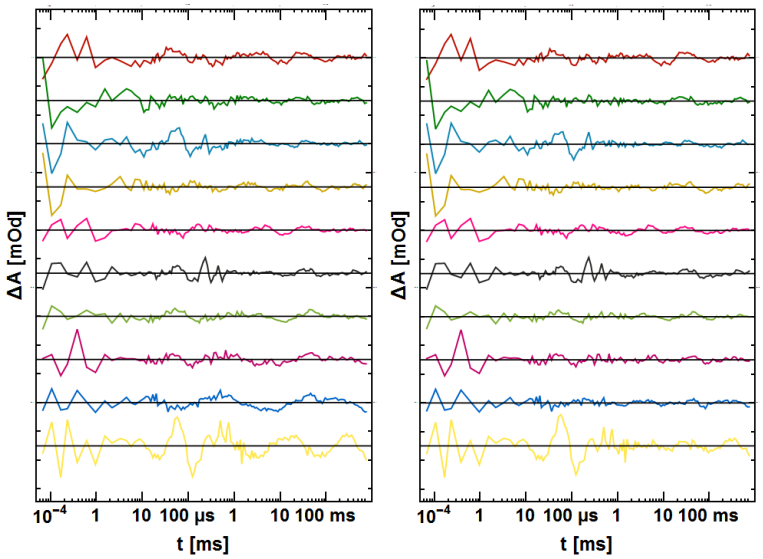

Figure 11.32: $S_2 \rightarrow S_3$ fit residuals of the global fit including 1378 to 1410 cm^{-1} (*top to bottom*) in steps of 4 cm^{-1} (section 9.4.2). *Left*: 6 exponential function, *right:* 7 exp. The quinone vibration at 1478 cm^{-1} (*yellow*) is only well simulated with a 7 exponential function. Measurement at 20 °C and pH 6.2 on PSII membranes from spinach.

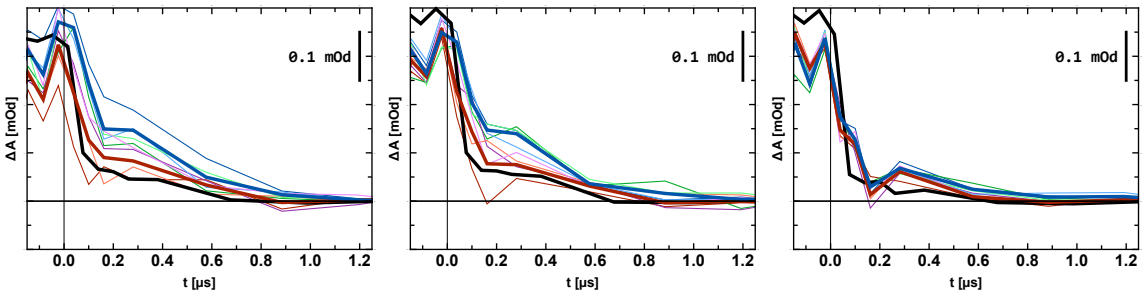

Figure 11.33: Raw data of PSII membranes measured at 20 °C and pH 6.2 - before artefact correction and deconvolution, but after reference detector correction and binning. The transients measured at 1378 (*left*), 1382 (*middle*) and 1402 cm^{-1} (*right*) of the scan from 1378 to 1410 cm^{-1} from section 9.4.3. The *black* transient represents the scaled heat artefact, thin blue and green traces are the transients after the 2nd, 3rd, 6th and 7th flash, the *thick blue* the average of them. Thin red and magenta transients are measured after the 1st, 4th, 5th and 8th flash, the *thick red* trace is the average of them. At 1378 and 1482 cm^{-1} the blue thick line shows clearly a fast decay component with about 300 ns whereas the thick red line follows rather the heat artefact. At 1402 cm^{-1} all traces look alike. Therefore, the decay component shown in green in the decay associated spectra in figure 9.5 is real and not a result from bad heat artefact correction

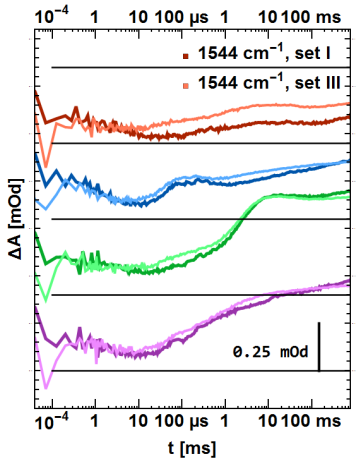

Figure 11.34: The data is measured at 10 °C and pH 6.2 on 15 µm thick PSII membrane samples. The data in chapter 6 was recorded in two sets and the band at 1544 cm^{-1} measured in both shows that no scaling is necessary. The transients of the first four flashes at 1544 cm^{-1} are plotted from top to bottom. Their amplitudes and dynamics are identical.

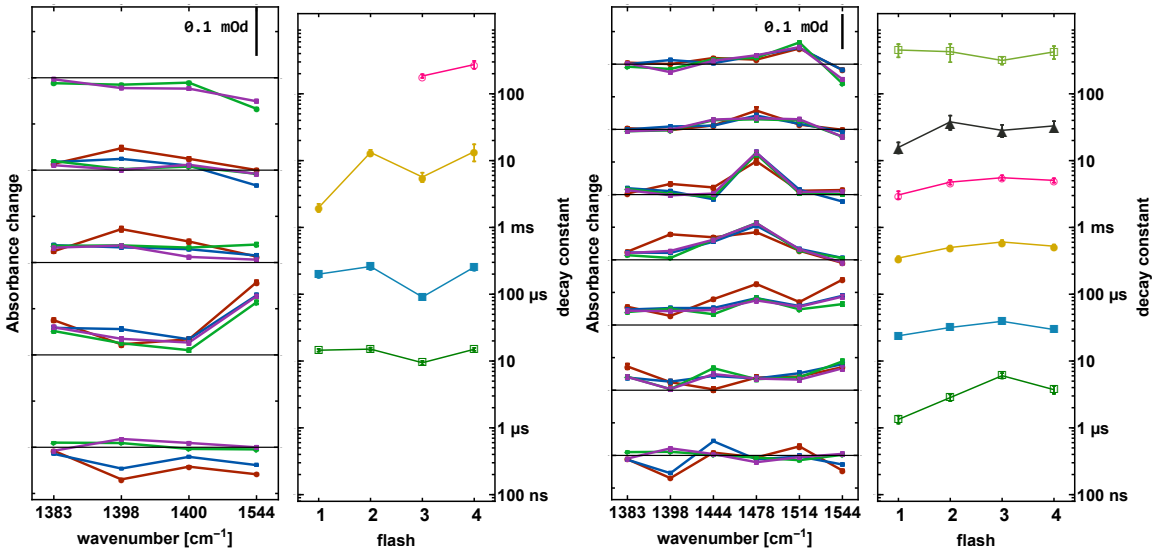

Figure 11.35: Joint fit results of D1-D61A data. The amplitudes on the left panels correspond to the decay times plotted on the same heights. The bottom line of amplitudes represents the fit constant. Amplitude color-code: red: $S_1 \rightarrow S_2$, blue: $S_2 \rightarrow S_3$, green: $S_3 \rightarrow S_0$, magenta: $S_0 \rightarrow S_1$. E.g. the top left rise times in green and magenta belong to the 200-300 ms decay time - also in magenta. *Left:* only wavenumbers are included, which in the WT are dominated by donor side reactions. *Right:* Additional quinone bands are included. Measurements of the D1-D61A PSII core complexes at pH 6.0 and 6-9 °C.

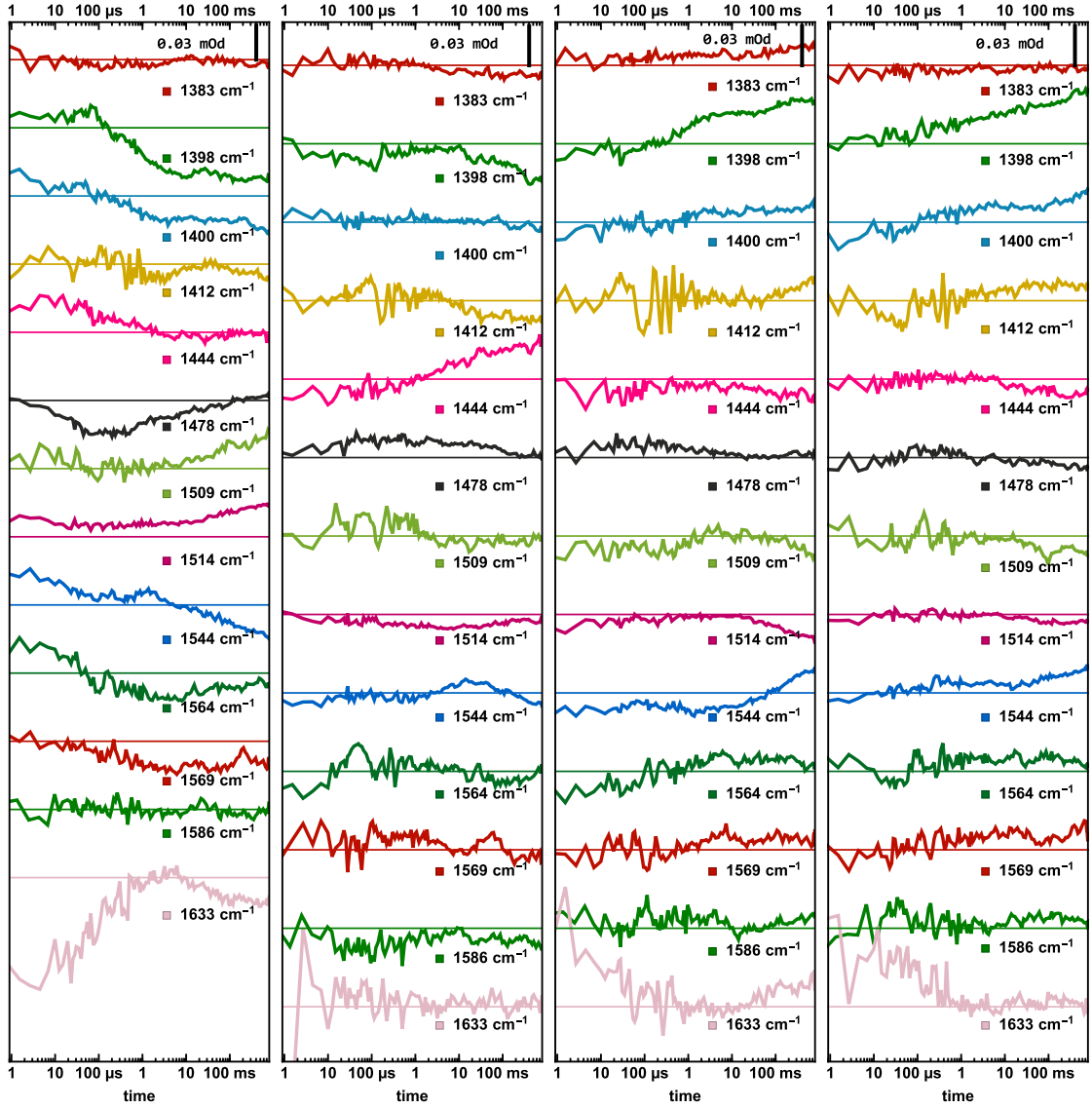

Figure 11.36: Transient of flash one to four (left to right) minus the average of flash 1 to 4. Measurements of the D1-D61A PSII core complexes at pH 6.0 and 6-9 °C.

List of publications

both in preparation

"Combined time-resolved single-frequency, steady-state infrared absorption spectroscopy and variable chlorophyll fluorescence for the investigation of interquinone electron transfer in PSII",
P. Simon, P. Chernev, H. Dau, manuscript in preparation

"Photodynamics of Al-corroles investigated with time-resolved techniques",
contribution: SFIR measurements of the long-living triplet state
Y. Yang, T. Stensitzki, P. Simon, C. Zahn, Z. Gross, K. Heyne, manuscript in preparation

List of presentations on conferences and meetings

talks on international conferences

1st European Congress on Photosynthesis Research, Uppsala, Sweden, 2018:
"Time-resolved IR absorption spectroscopy tracking electron and proton transfer in photosystem II from spinach and cyanobacteria"

17th European Conference on the Spectroscopy of Biological Molecules in Amsterdam, Netherlands, 2017:
"Tracking photosynthetic water oxidation from ns to s"

Posters on national and international conferences

Annual Meeting of the German Biophysical Society in Düsseldorf, 2018

Gordon Research Conference and Seminar on photosynthesis, Newry, USA, 2017

17th International Congress on Photosynthesis in Maastricht, Netherlands, 2016

Protonation Dynamics in Redox Protein, Symposium, Berlin, 2015

16th European Conference on the Spectroscopy of Biological Molecules in Bochum, 2015

DPG Frühjahrstagung, Berlin, 2015

Annual Meeting of the German Biophysical Society in Lübeck, 2014

11.5 Kurzfassung

Dank der vor Kurzem erschienenen strahlungsschädenfreien, hochaufgelösten Kristallstrukturen gab es rasante Fortschritte im Verständnis der photosynthetischen Wasserspaltung im Photosystem II. Dennoch verbleiben noch offene Fragestellungen, vor allem bezüglich des eigentlichen O-O Bindungsmechanismuses, der Identifikation der Substratwassermoleküle, sowie der jeweiligen Protonenfreisetzungsschritte und -pfade. Mit zeitaufgelöster Infrarotspektroskopie können Bindungsänderungen von beteiligten Aminosäuren und Kofaktoren detektiert werden, die wiederum empfindlich gegenüber den Protonierungszustand und Stärke der Wasserstoffbrückenbindungen sind. Bisher sind jedoch weniger als fünf mit einer ungenügenden Auflösung von 16 cm^{-1} gemessen Publikationen an Sauerstoff entwickelndem Photosystem II veröffentlicht worden. Das messzeitintensive Step Scan Experiment unsrer Gruppe ist dagegen nicht frei von einem Anregungslaser induziertem Hitzeartefakt.

In der hier präsentierten Arbeit stelle ich einen von mir entwickelten, dauerstrich Quantenkaskadenlaser basierten Einzelfrequenz-IR-Aufbau (EFIR) vor, der es erlaubt, Transienten mit einer zeitlichen Auflösung von 40 ns und Absorptionsänderungen von weniger als 10^{-5} OD im Bereich von 1300 bis 1650 cm^{-1} zu messen. Der Probenaustausch und die Datenaufnahme funktionieren voll automatisch. Dazu habe ich ein Messprotokoll entwickelt, das es ermöglicht den vom Anregungslaser induzierten Hitzeartefakt reproduzierbar zu korrigieren.

(1) Im ersten Projekt wurden FTIR Differenzspektroskopie mit der variablen Chlorophyll a Fluoreszenz und dem neuen EFIR kombiniert, um den Elektronentransfer zwischen den beiden Chinonen zu vermessen. Es stellte sich heraus, dass die Kinetiken im EFIR und in der Fluoreszenz identisch sind. Zusammen mit der Analyse der Anregungsenergieaustausch basierten Fluoreszenskorrektur, konnte ich erstmals direkt die angewandte Korrekturmethode verifizieren, die als eine der Standardmethoden in der Pflanzenphysiologie genutzt wird.

(2) Als Weiteres wurde die CO Streckschwingung des Y_Z Radikals zwischen 1512,5 und 1515 cm^{-1} im $S_2 \rightarrow S_3$ and $S_3 \rightarrow S_0$ gefunden. Die Bande wird innerhalb von 40 ns gebildet und zerfällt mit den charakteristischen Zeiten der Mangan Oxidation. Hiermit konnte ich zu einer anhaltenden Diskussion mehrerer Gruppen beitragen und diese (eventuell) lösen.

(3) Es wurde eine Region der symmetrischen Carboxylatstreckschwingungen von 25 cm^{-1} identifiziert, in der alle bisher bekannten Schritte des erweiterten Reaktionszykluses des Mn_4Ca-µ-oxo-Clusters beobachtet werden können. Drei bisher nicht zugeordnete Banden wurden gefunden, die entweder mit 300 ns oder 30 µs zerfallen. Diese könnten zu vorübergehend deprotnoierten Carboxylaten gehören. Zusammen mit Richard Debus von der UC Riverside konnte ich feststellen, dass PSII Kernkomplexe von *Synechocystis* sp. PCC 6803 nur leicht veränderte Kinetiken und Spektren des Photozykluses aufweisen.

(4) Als letztes konnten die ersten zeitaufgelösten Infrarotmessungen an genetisch verändertem PSII aufgenommen werden. Das durch Alanin ersetzte Carboxylat (D1-D61) bindet über eine Wasserstoffbrücke zu einem Mn ligierendem Wasser und befindet sich am Beginn eines vorgeschlagenem Protonenkanals. Die Kinetik zeigte keine Verzögerungen der Protonenfreisetzungsdynamiken, was einen Einschluss der Umgebung und des Kanals zu diesen Zeiten ausschließt. Die Mn Oxidierung dagegen zeigte komplexes und verlangsamtes Zeitverhalten und eine Änderung der Amplituden. Dies verwirft einige vorgeschlagenen Hypothesen, erzeugt aber umso mehr neue Fragen über den Mechanismus der Wasseroxidation.

Zusammenfassend kann festgehalten werden, dass ein neuer, vielversprechender experimenteller Ansatz zur zeitaufgelösten Messung der einzelnen Reaktionschritte des Photosystems II entwickelt wurde, der bereits neue Erkenntnisse lieferte und eine Reihe an Möglichkeiten zukünftiger Forschung eröffnet.

11.6 Selbstständigkeitserklärung

Hiermit versichere ich gegenüber der Freien Universität Berlin, dass ich alle von mir genutzten Quellen und Hilfmittel, sowie Zitate kenntlich gemacht habe. Auf dieser Grundlage habe ich die Arbeit selbsständig verfasst.